**Volume II**

# proceedings of the 1968 AIR FORCE
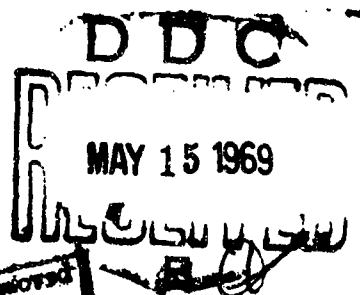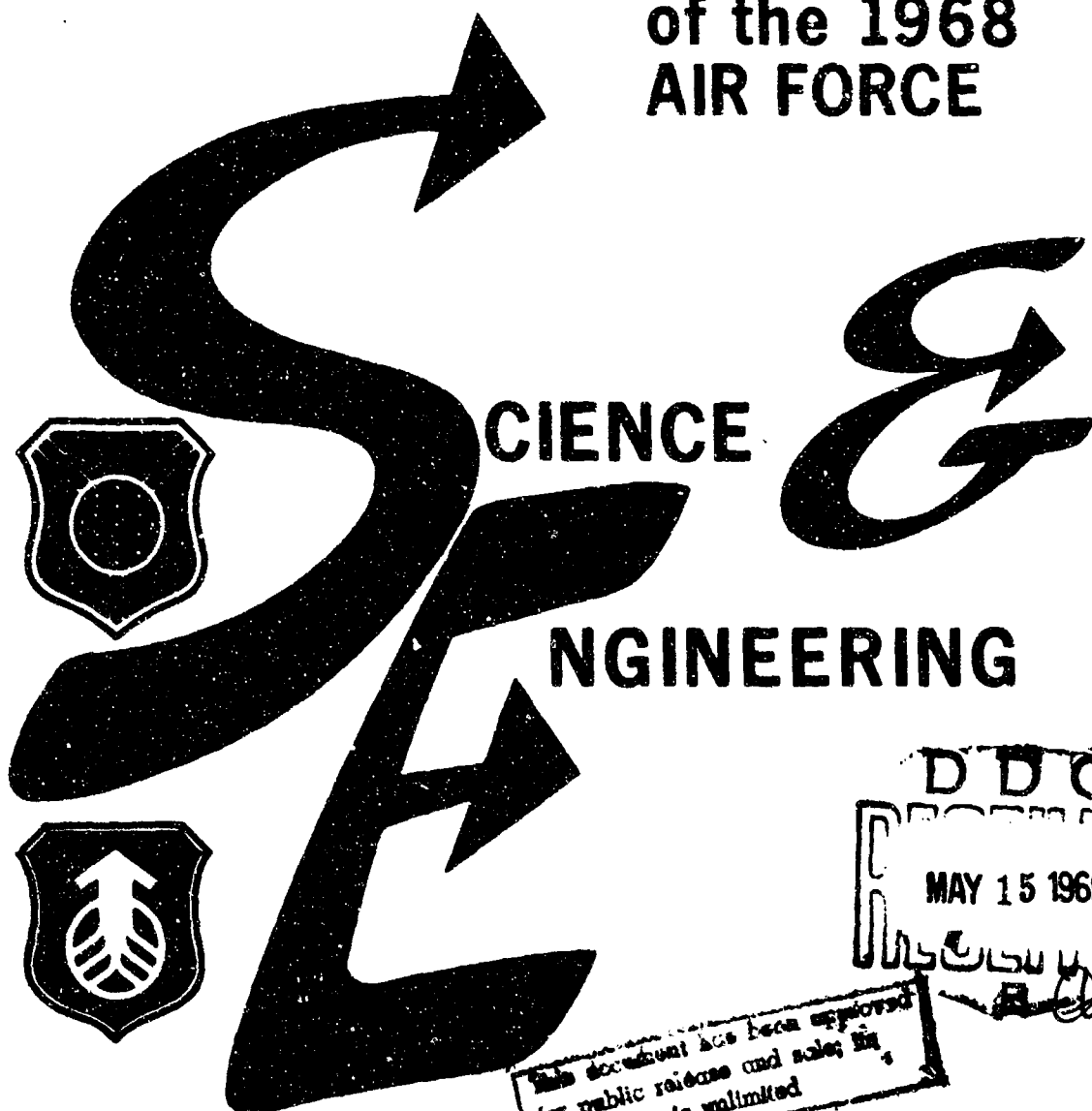
# SCIENCE & ENGINEERING

# SYMPOSIUM

## AIR FORCE ACADEMY ★ 30-31 October • 1 November 1968

## Office of Aerospace Research ★ Air Force Systems Command

PROCEEDINGS

of the

1968 AIR FORCE SCIENCE AND ENGINEERING SYMPOSIUM

30-31 October and 1 November 1968

UNITED STATES AIR FORCE ACADEMY
COLORADO SPRINGS, COLORADO

VOLUME II

Sponsored by

OFFICE OF AEROSPACE RESEARCH

and

AIR FORCE SYSTEMS COMMAND

## PREFACE

The purpose of the Symposium was to review the science and engineering activities of the Air Force, and to reflect representative achievements in science, engineering and technical management. A concomitant aim was to provide a balanced program of maximum interest. Toward this end, the Program Committee selected papers which ran the full gamut of Air Force scientific effort.

The papers included here have four specific objectives:

a. To stimulate the involvement of scientific and engineering talent within the Air Force.

b. To demonstrate Air Force competence in research, development, and evaluation.

c. To provide a forum wherein Air Force personnel can demonstrate the full scope and depth of their current projects.

d. To promote the interchange of ideas among members of the Air Force science and engineering community.

In addition to these specific objectives, the Symposium was held to emphasize particularly the overall in-house capabilities of OAR and AFSC, and to illustrate the effectiveness of the Air Force laboratories.

# TABLE OF CONTENTS

## VOLUME I

# SYMPOSIUM PAPERS

FIRE PROTECTION IN OXYGEN-ENRICHED ATMOSPHERES -

PREVENTION AND EXTINGUISHMENT


BY


DONALD I. CARTER, CAPT, USAF (BSC)


DIRECTORATE OF RESEARCH AND DEVELOPMENT
AEROSPACE MEDICAL DIVISION
AIR FORCE SYSTEMS COMMAND
BROOKS AFB, TEXAS

Fire Protection in Oxygen Enriched Atmospheres -
Prevention and Extinguishment

Captain Donald I. Carter, USAF (BSC)
Aerospace Medical Division

## ABSTRACT

Fire prevention and extinguishment in oxygen enriched atmospheres
present problems significantly greater than are encountered in air at one
atmosphere. This is readily apparent when the ignition temperatures
and burning rates of various materials in these atmospheres are compared.
The Aerospace Medical Division has implemented a program to minimize
these potential hazards. This program entails removal of all unnecessary
potential ignition sources and combustible materials, installation of
fire extinguishing systems and emphasis on operational, maintenance
and training procedures. The removal of combustible materials required
research and development to obtain satisfactory substitutes as did the
fire extinguishing system. Thirteen Aerospace Medical Division chambers
have undergone these modifications and have been returned to commission.
Four additional chambers are in varying states of modification. Slides
and movies of some of the developed items will be shown.

# BIOGRAPHY

Captain Donald I. Carter, a native of Mississippi, obtained a Bachelor of Science degree in civil engineering from Mississippi State University in 1958. He has completed the Air Force Squadron Officers School. He is a member of the Society of American Military Engineers, Aerospace Medical Association, American Industrial Hygiene Association and Health Physics Society. He is a registered professional engineer. His recognitions include the Air Force Commendation Medal, the AFSC Scientific Achievement Award and listing in the 1968 edition of Outstanding Young Men of America. His Air Force assignments have included Bioenvironmental Engineering duties at Little Rock Air Force Base, Arkansas, Vandenberg Air Force Base, California, and Brooks Air Force Base, Texas. He was extensively involved in the development of fire extinguishing systems and protective clothing for oxygen enriched atmospheres. He is currently Chief of the Life Support Division in the Directorate of Research and Development at Aerospace Medical Division Headquarters.

The ignition point of materials in 100% oxygen at 1 atmosphere is much lower than the same material in air at 1 atmosphere. The burning rate of filter paper in air at 1 atmosphere is approximately 1 cm/sec as compared to approximately 4.3 cm/sec in 100% oxygen at 1 atmosphere. [1] A unique characteristic of fire in 100% oxygen is the extremely rapid surface burning characteristic or "nap" fire which instantaneously spreads over the surface of the combustible material and initiates multiple point sources. [2] (Figure 1) The Aerospace Medical Division conducts many experiments in which man is exposed to oxygen enriched atmospheres either as a human test subject or during the course of tending experimental animals or equipment. These potential hazards have caused the Aerospace Medical Division to modify significantly the fire prevention and extinguishment aspects of its simulators which use these atmospheres. This paper will describe some of the modifications which have been accomplished.

Fire prevention in oxygen enriched atmospheres should follow the basic axioms of fire prevention -- minimum combustible materials, minimum ignition sources and adherence to good practices in operation, maintenance and training. The first of these axioms is difficult to implement, however, as most nonmetallic materials will burn in 100% oxygen. Combustibles which should receive close scrutiny include, among others, uniforms, bedding, helmets and insulation on electrical wiring. Materials which were evaluated as replacement items included Nomex, Polybenzamidazole, asbestos, Beta Fiberglas, Teflon, Kapton and combinations of these. Each of the materials had advantages and disadvantages when compared to the criteria for selection: noncombustibility in 100% oxygen at 380 mm Hg, ability to be fabricated into a useful item, compatibility with personnel (present no dermatological problems), cost and durability. Initial problems with these materials included incompatibility with personnel, lack of sufficient material strength, cost and general unavailability. (Figure 2) The material finally chosen for the development of the uniform is a 9 oz/sq yd modified crows foot woven white Beta Fiberglas fabricated into a two piece outfit with fiberglas braid at the waist of the shirt and trousers as well as at the neck and hood closures. The sleeves and legs have a small piece of elastic inside the cuffs to hold the material tightly against the body to prevent a fire from propagating up the arm or leg.

The shirt has a small piece of leather sewn to the chest to accommodate an alligator clip for the oxygen hose and communications wire. The seams are modified fell seams sewn with fiberglas thread with no loose ends exposed. The uniform is worn with cotton undershirt and shorts. These uniforms have proven successful for short "flights" to tend experimental animals as well as for long duration (32 days, continuous) human feeding studies.

The same basic material (Beta Fiberglas) and sewing techniques are used in fabricating helmets to replace leather flying helmets and in fabricating personal effects bags. The personal effects bags can be used to store necessary combustibles such as kleenex, toilet tissue, food packaging materials, books, etc., when these materials are not in use. A slightly different 6 oz/sq yd fiberglas material is used in sheets, pillowcases, blankets, mattress covers and seat cushions. The stuffing in the pillows, mattresses and cushions is woven and matted fiberglas with a small amount of organic binder. This organic binder will burn, however, it is improbable that a fire could penetrate the outer layers of such articles to ignite the binder. Kapton or Teflon insulation has proven effective on electrical wiring.

Some combustible materials have not been replaced either because the degree of hazard presented is small or because no satisfactory substitutes have been found. Some of these items include shoes, socks, oxygen hoses and masks and wooden shavings for animal cages.

Removal of ignition sources primarily entailed modification of the chamber electrical systems. Electrical power is used in the chambers for illumination, environmental control systems, atmospheric sample pumps, fire extinguishing system detectors and for various experimental devices such as treadmills and performance measuring devices. Electrical power is brought into the chambers through a fuse box and then cannon plugs to a junction box. From the junction box it is transmitted in either Teflon or Kapton insulated wiring protected by conduit or cable tray to its point of use. The wiring is derated by a factor of two. All switching which cannot be accomplished external to the chamber is hermetically sealed. Only those electrical devices which are essential to the experiment in progress are permitted within the chamber. In some chambers where devices which potentially overheat are not readily visible, an overheat detection and alarm system has been installed.

It should be recognized that it is impossible to remove all combustible materials and all ignition sources from oxygen enriched atmospheres used in human experimentation or operations.[3] Indeed, the hair on the surface of the human body is combustible. To cope with this potentiality, a fire extinguishing system using water as the extinguishing agent has been designed, fabricated and tested. This system will extinguish fires in cotton materials in 100% oxygen at 1 atmosphere. Such a fire extinguishing system has been installed in 13 Aerospace Medical Division space environment simulators and is programmed for installation in four additional simulators.

The fire extinguishing system consists of three basic integrated subsystems -- fire detection, control circuitry and extinguishing. The detection subsystem uses an ultraviolet (UV) light detector (Figure 3) which sends a signal into the control subsystem when light in the UV (1900Å - 2900Å) region is emitted by the fire. Smoke detectors (Figure 4) using either the ionization or the light path occulsion technique are also used to sound an alarm. The UV detector is less sensitive to false activation than other rapid response detectors (such as infrared detectors) and the smoke detector could give an alarm of an overheat and impending fire condition. Other types of detectors such as preset temperature or rate of temperature rise do not have the needed response time.

The signal from the smoke detector is routed through the control circuitry to energize only visual and audible local alarms due to the possibility of false activation of the detector from fog (produced as a result of rapid decompression of the chamber) or from several other nonfire conditions. (Figure 5) The signal from the UV detector is routed through the control circuitry and performs several functions. If the control circuitry is in the "manual-electric" mode, visible and audible local alarms are energized and a light which designates the "sensing" detector is energized. The chamber operator or the chamber occupants can then decide whether or not to flow the water. If the water flow is actuated, the functions described in the "automatic" mode occur. If the control circuitry is in the "automatic" mode, electrical power to the chamber (other than emergency illumination, communications and fire detectors) is deenergized, normally closed solenoid valves are opened to initiate the water flow, local audible and visual alarms are energized, the Base Fire Department and

Dispensary are summoned and a 20 second timer is energized. After
20 seconds have elapsed the water is automatically turned off and the
system resets itself within 5 seconds for a second application, if
necessary. The control circuitry has other alarms which alert the
chamber operator to such conditions as low water pressure, inoperative
fire detectors, low battery power (backup power mode), valves in the
wrong position, etc. "Manual-electric" mode switches for initiating
the water flow are located at the chamber operator's console as well
as within each compartment of the chamber. The control circuitry is
designed so that the detectors and alarms can be tested without flowing
water.

The water extinguishing subsystem is supplied either from the
base water distribution system or, if the demand cannot be satisfied,
from a pressurized tank. (Figure 6) The system is designed to flow
at the rate of 7.5 gallons per minute per square foot of chamber floor
area (4) through a series of nozzles to disperse the water in a spray/
fog so as to cover the horizontal and vertical planes from both directions.
If a pressurized tank serves as the source, it should have sufficient
capacity for at least two and preferably three 20 second applications.
The water extinguishing subsystem is integrated with the detectors and
control circuitry so that initial water flow occurs v..thin 0.2 seconds
subsequent to the initial appearance of flame within the chamber. The
water flow is stabilized at maximum rate within 0.5 seconds. (Figure 7)
To meet this criterion the water is piped from the source into the chamber
and through the distribution system inside the chamber to differential
hydraulic pressure valves which are located adjacent to each nozzle.
(Figure 8) Locating the valve adjacent to the nozzle decreases the
distance the water must flow subsequent to opening the valve and thus
decreases the reaction time. The control pressure on the opposite side
of the valve is taken from the same water source so that fluctuations
in the supply pressure will not falsely activate the system. The water
flow is initiated by a signal from the control circuitry subsystem
energizing a normally closed solenoid valve in the control line. This
decreases the control pressure and the hydraulic valve opens permitting
the water to flow. When the solenoid valve is deenergized the control
line pressure increases and closes the valve thus stopping the water
flow. The control line pressure can also be released by either of
several strategically located manually activated quick opening ball
valves so that the chamber can be protected even if all electrical power
is lost.

Several fire extinguishing systems of this basic design have been tested subsequent to the initial research and development in 1967. The reaction times and water flow rates have proven effective in extinguishing fires in 100% oxygen at pressures up to 600 torr. Although the water flow rate is approximately 10 times as much as is designed for extreme fire hazards in commercial warehouses no difficulty with human compatibility has been experienced.

(Motion picture - 2 minutes in duration)

Good practices in operation, maintenance and training are similar to those established for aircraft by the Air Force. These include definitive assignment of responsibility, standardizing operating and maintenance procedures, maintaining updated schematics, flow diagrams and wiring diagrams for each chamber, periodic exercising emergency procedures and providing sufficient formal and on-the-job training.

Thirteen Aerospace Medical Division chambers have been modified as described above and have returned to commissioned status. The modifications have proven effective.

1. Cook, G. A.: Meierer, R. E.; Shields, B. M.: "Screening of Flame-Resistant Materials and Comparison of Helium with Nitrogen for Use in Diving Atmospheres." First Annual Summary Report on Combustion Safety in Diving Atmospheres, Contract No. N00014-66-CO149, Office of Naval Research, U. S. Navy, Union Carbide Corporation, March 31, 1967.

2. Denison, D. M.: "Further Studies on the Problems of Fire in Artificial Gas Environments." AMD-TR 67-2, pp 155-167, May 23, 1967.

3. Swan, A. G.: "Two Man Space Environment Simulator Accident." AMD-TR 67-2, pp 4-38, May 23, 1967.

4. Botteri, B. P.: Manheim, J.: "Fire and Explosion Suppression Techniques." Air Force Aero Propulsion Laboratory, Wright-Patterson AFB, Ohio

Figures

1. Typical Space Environment Simulator

2. Beta Fiberglas Uniform

3. UV Detector

4. Smoke Detector

5. Fire Extinguishing System Monitoring Console

6. External Water Supply System

7. Internal Water Distribution System

8. Valve and Nozzle

Figure 1



Figure 2
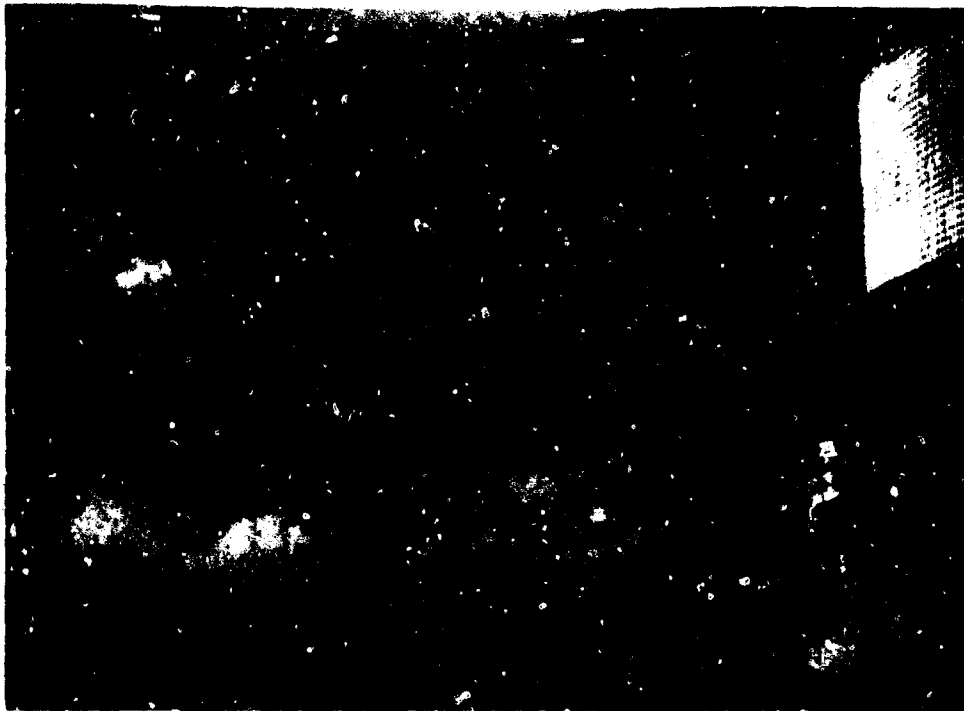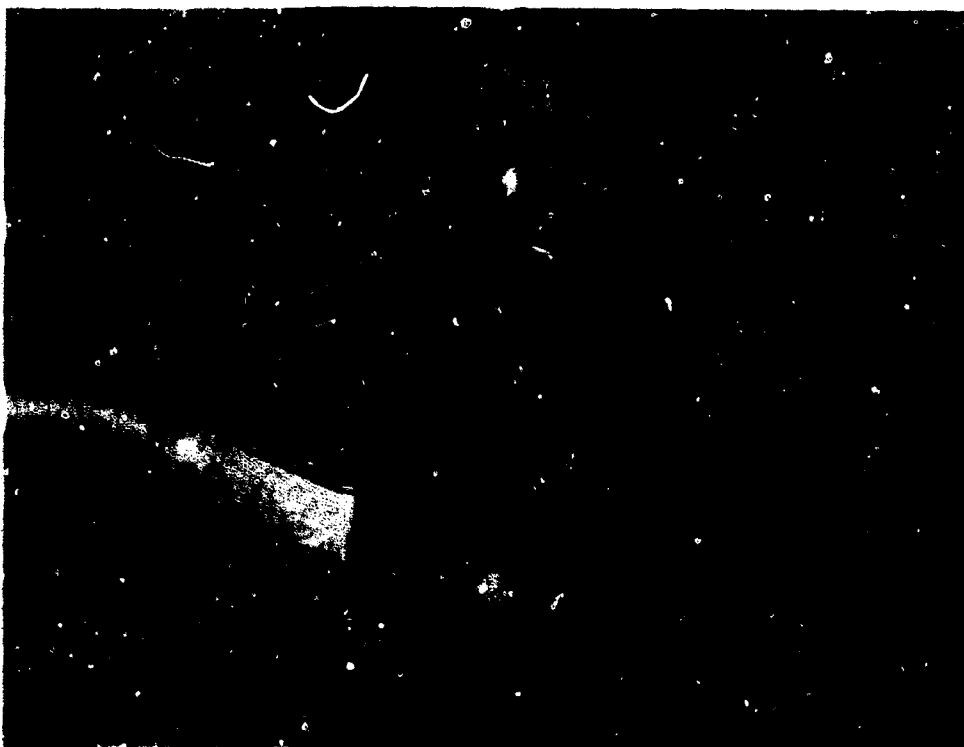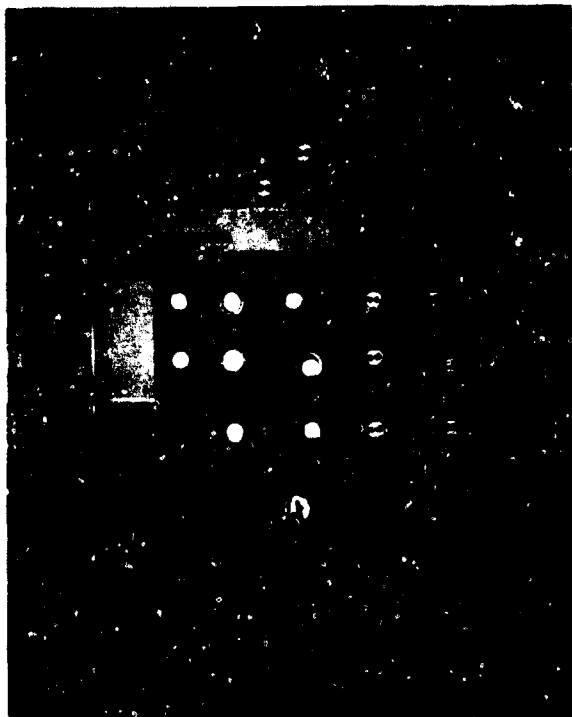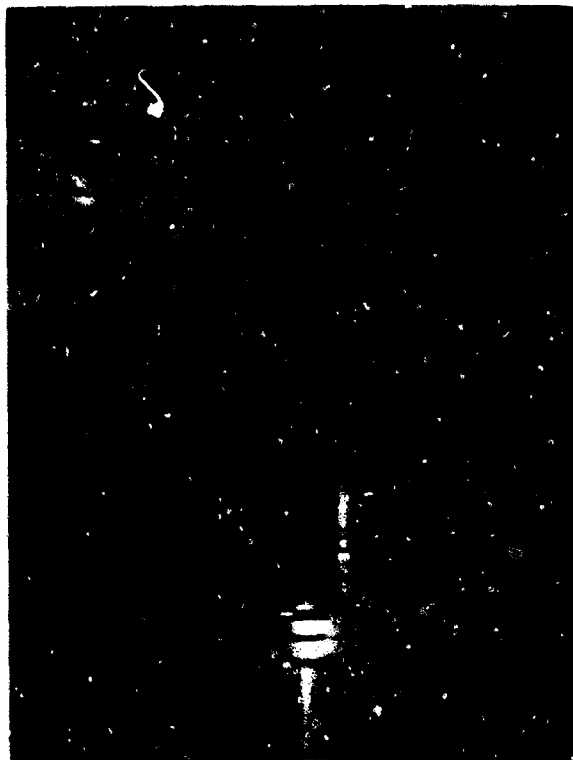
P-11

Figure 3



Figure 4

P-12

Figure 5



Figure 6

P-13

Figure 7



Figure 8

P-14

IN-HOUSE CONTRIBUTIONS TO DESIGN AND CONSTRUCTION OF DEVICES
FOR BIOMEDICAL MONITORING, TRAINING AND EXPERIMENTAL SUPPORT

By

Henry B. Whitmore, Master Sergeant, USAF

Aerospace Medical Division
USAF School of Aerospace Medicine
Air Force Systems Command
Brooks AFB, Texas

# ABSTRACT

In the fields of biomedical monitoring and training, there has always been and there will continue to be, the need for new and better devices. In the area of biomedical monitoring, I have invented such devices as the miniature electrode, respiratory transducer, blood pressure transducer, blood pressure cuff inflation device, and the autonomous blood pressure recording device.

In the area of training, I have invented such devices as the parachute drag release, a spatial disorientation demonstrator, a compressed air ejection seat catapult, a chamber level-off regulator and a hyperbaric chamber ascent valve. Along with these inventions, there has also been an electrical isolation speaker for hyperbaric chambers, a cardiovascular conditioning device, a passive pressure suit (Boyle's Law suit), a soft fabric helmet, and a capability for providing in-flight feeding for air and space crew members wearing pressure suits.

# BIOGRAPHY

Master Sergeant Henry B. Whitmore was born in McKenny, Virginia on 5 June 1930. He is a graduate of Sunnyside McKenny High School, studying general education courses, welding, and shop. Service schools include basic military training, basic medical course, medical technician, altitude chamber technician, aeromedical technician, technical instructor, USAF management training course, OJT administrative course, physiological training supervisor, and pressure suit course.

Sergeant Whitmore's service career has included duty assignments at Randolph AFB, Texas, Gunter AFB, Alabama, Korea, back to Gunter AFB, and in 1959 to his present duty station, Brooks AFB, Texas.

In his present duty position, he is NCOIC of the Medical Support Section, Aeromedical Indoctrination Branch, Education Division, USAF School of Aerospace Medicine, Brooks AFB, Texas.

# AEROSPACE ENGINEERING RELATED TO PRESSURE SUIT DESIGN AND DEVELOPMENT, BIOMEDICAL MONITORING, AND SPECIAL TRAINING DEVICES

Good evening distinguished guests and ladies and gentlemen. I would first like to thank all concerned for this opportunity to be here under these circumstances. I briefly would like to explain a few of my inventions and their significant values. In the fields of biomedical monitoring and training, there has always been the need for new and better devices. Some of the devices I have invented in this field are as follows:

1. **Miniature Electrode** - A low impedence-high sensitivity electrode which utilized small areas of skin contact by using coiled electrode providing greater overall surface area. These electrodes provide a readout comparable to clinical electrodes while being only 1/8 inch in diameter.

Slide #1: Miniature Electrode

2. **Respiratory Transducer** - A transducer for measuring respiratory activity. Unlike the uncomfortable thermistor type of transducer which had previously been in use. The new type transducer is strapped across the subject's chest and could be adjusted so it was hardly noticeable. It is also used in telemetry monitoring. This transducer is also used to measure animal activity as well.

Slide #2: Respiration Transducer

3. **Blood Pressure Transducer** - A miniaturized transducer which is used to monitor blood pressures of subjects wearing pressure suits. The transducer is readily adaptable to existing recording systems, providing excellent results, and at a greatly reduced cost.

Slide #3: Blood Pressure Transducer

4. **Blood Pressure Cuff Inflation Device** - In conjunction with high altitude biomedical monitoring of blood pressures, a method was needed to automatically inflate blood pressure cuffs, either with or without the subject in a pressure suit. I built and tested such a device which met the requirements regardless of altitude variation. Later an additional benefit of linear blood pressure cuff depressurization was developed and incorporated into the device. These units are currently being used in rotational flight simulators and high altitude chambers.

Slide #4: Blood Pressure Cuff Inflation Device

Q-4

5. **Autonomous Blood Pressure Recording Device** - Although the preceding devices were developed for specific and independent purposes, I decided to incorporate the blood pressure cuff inflation device, linear bleed and a digital print system which I designed. The result was a completely portable and autonomous blood pressure recorder with digital write-out. This device is in the process of further development and miniaturization at the present time.

Slide #5:  Autonomous Blood Pressure Recorder

6. **Parachute Drag Release** - In the Aeromedical Indoctrination program, a parachute landing system is used for parachute landing fall procedures. Part of the training requires the student to be dragged. simulating a post-landing situation. The old wind-induced parachute drag procedure was felt to be unpredictable and unsafe from the viewpoint of immediate man-riser release. A quick release mechanism for this purpose which separates the dragged student from a tractor (which provides a controlled drag rate) in a more positive and safe manner.

Slide #6:  Parachute Drag Release

7. **Spatial Disorientation Demonstrator** - A training device which proved to be valuable for demonstrating the vestibular effects of spatial disorientation was the spatial disorientation simulator. With the help of co-workers, I developed a controllable disorientation device which can be programmed to show the effects of disorientation and the unreliability of one's postural senses in various aircraft maneuvers. The device was very well received by the Tactical Air Command, and other models are being procured for the Air Force inventory. This device was constructed at very minimal expense to the government.

Slide #7:  Spatial Disorientation Demonstrator

8. **Compressed Air Ejection Seat Catapult** - One of the most critical training aids used by the Aeromedical Indoctrination Branch is the ejection seat simulator. The old system uses a cartridge catapult to propel the ejection seat up a tract at speeds and "G" loads similar to actual aircraft ejection. However, there are obvious hazards using live cartridges and resultant maintenance, cleaning, and inspections of the system which hold up training operations. My associates and I developed a low pressure air operated catapult system which is much safer, easier to operate, relatively maintenance free and provides a drop-in conversion capability. It has been conservatively estimated that this unit could save the Air Force 1.5 million dollars annually while providing considerably more rapid and safer training.

Slide #8:  Compressed Air Ejection Seat Catapult

9. **Chamber Level-Off Regulator** - The Aeromedical Indoctrination Branch mission entails much low pressure altitude chamber work. It became desirable to have a device which could automatically maintain the chamber at a fixed altitude and simultaneously vent the chamber. I devised such a chamber vent and level-off control. It provides the amazing reliability of plus or minus 25 feet, requires no chamber modification, and can be made for less than $100 in comparison to existing commercial units costing many times more.

Slide #9:  Chamber Level-Off Regulator

10. **Ascent Valve** - One of the factors in hyperbaric chamber work which provides a potentially hazardous situation is the chamber ascent rate of one foot per minute which is desired to provide a safe ascent but is quite difficult to control manually. I designed and built a pressure compensating linear ascent valve which will more than satisfy the requirements.

Slide #10:  Ascent Valve

11. **Electrical Isolation Speaker** - A constant hazard in the operation of the hyperbaric chamber is that of fire. I came up with the idea of removing the burnable materials in the chamber intercommunication system with an all-metal and asbestos speaker system. The system also has the advantage that the wiring is on the outside of the chamber, thus removing the possibility of electrical fire. These speakers are undergoing further development for future Air Force acceptance.

Slide #11:  Electrical Isolation Speaker

12. **Cardiovascular Conditioning Device** - The problem of cardiovascular deconditioning presented itself in human subjects exposed to prolonged weightlessness, which is experienced during orbital missions. I was consulted by Dr. Paul Stevens of the USAFSAM Pulmonary Science Division in a search for a solution to this problem. I designed and fabricated a cardiovascular conditioning device which embodies a vest and helmet providing pooling of blood in the extremities which increases cardiovascular activity, and stimulates the physiological effects of gravity. This device can be incorporated in a space suit. It can also be used as a fabric respiratory, and excellent results have been attained in preliminary testing.

Slide #12:  Cardiovascular Conditioning Device

13. <u>Passive Pressure Suit</u> - Probably the most significant contribution
in research and development is that of the passive pressure suit. This
system pressurizes by means of trapped gas, sealed in a network of
longitudinal tubes which provide counter pressure when ambient pressure
decreases. This system has inherent cooling and ventilation features as
well as excellent high altitude protection. I designed and, with co-
workers, fabricated three test model pressure suits which were tested
by human subjects to altitudes of 80,000 feet. Refinements of these
test models were accomplished by myself. This required: elimination of
torso breathing bladder by changing horizontal tubes to longitudinal
tubes, reducing tube areas while uninflated by accordion tube design
which increases passive ventilation and reduces suit bulk; modification
of existing pressure suit helmets and regulators to integrate with the
passive pressure suit. Consultations with AMRL and UniRoyal personnel
and myself enhanced the fabrication of the first factory model incor-
porating improvements as per my recommendations. During the testing of
this suit I, acting as human subject attained a simulated altitude in
excess of 112,000 feet.

Slide #13:  Passive Pressure Suit


14. <u>Soft Fabric Helmet</u> - Along with my co-workers, I designed and
fabricated a fabric pressure suit helmet to be used with the passive
pressure suit and cardiovascular conditioning device. This helmet was
tested with excellent results and was used as primary test helmet in
the preliminary evaluation of the above mentioned devices.

Slide #12:  Fabric Helmet


15. <u>In-Flight Feeding Capability</u> - The problem of providing a feeding
capability for air crew and space crew members wearing pressure suits
under pressurized configurations for long term exposures and high alti-
tude environments were presented to me in search of a solution. To
correct this problem I modified a full pressure suit helmet by in-
stalling a feeding port in the visor. I also designed a container with
an adapter which could be integrated with the feeding port without loss
of helmet pressure. This feeding device has been used on all USAFSAM
long term altitude pressure suit chamber flights.

Slide #14:  In-Flight Feeding Capability


Again, I thank you for the opportunity of presenting to you some of my
achievements. Sorry that time did not permit me to entertain each of
these in detail but I will be available following this program to answer
any questions generated by this discussion.


Q-7

**EEG/ECG ELECTRODE**

METAL-COIL ELECTRODE

CONTACT PIN

PLASTIC HOLDER

ELECTRODE LEAD

H.B WHITMORE
26 MARCH 1964
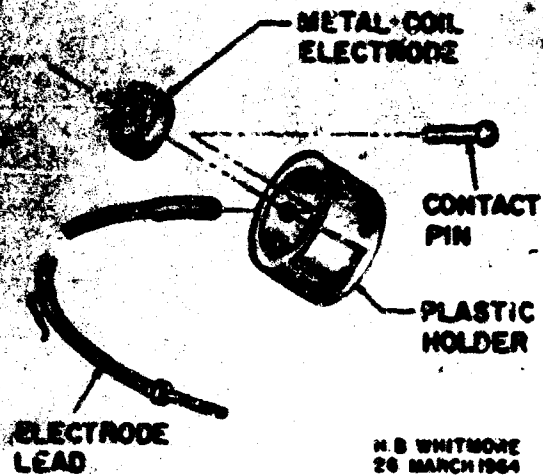
Slide 1



**RESPIRATION TRANSDUCER**

ELECTRODE

CHEST STRAP
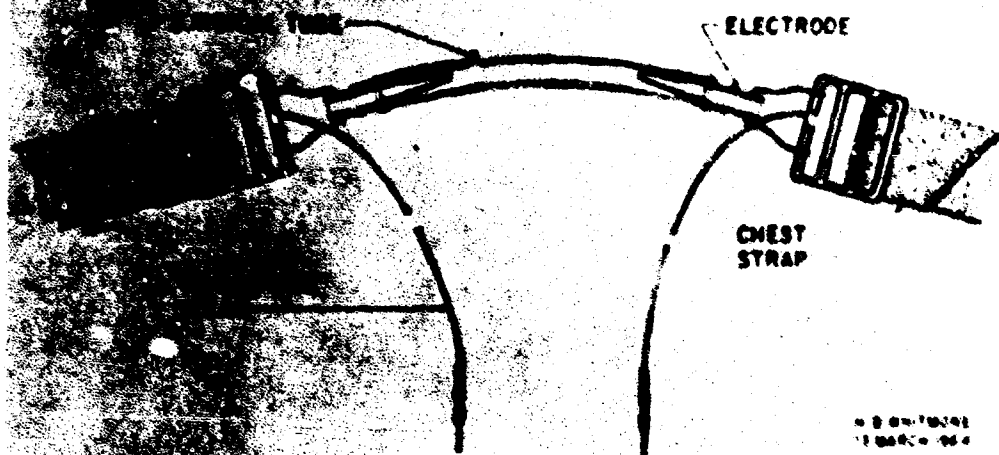
Slide 2

# TRANSDUCER
## (0 TO 30 mm PRESSURE DIFFERENTIAL)



Slide 3



Slide 4

Slide 5



Slide 6

Q-10
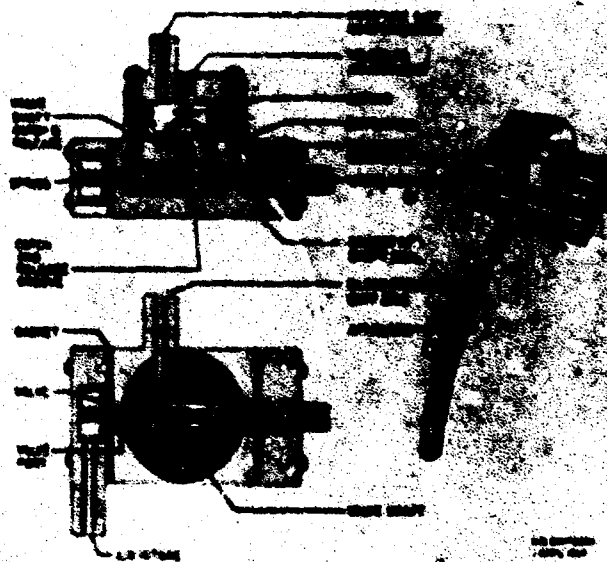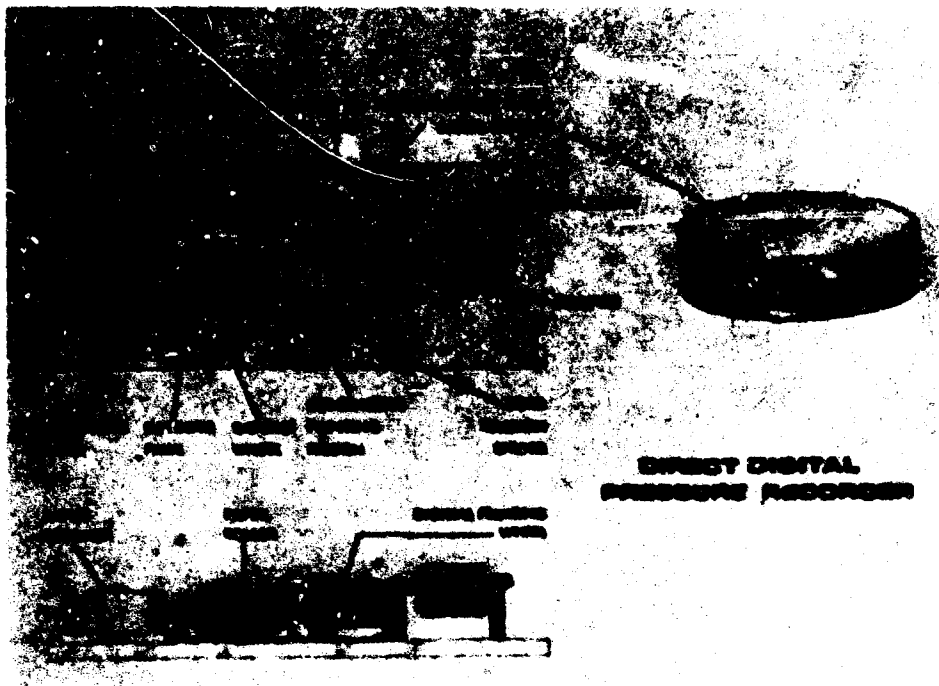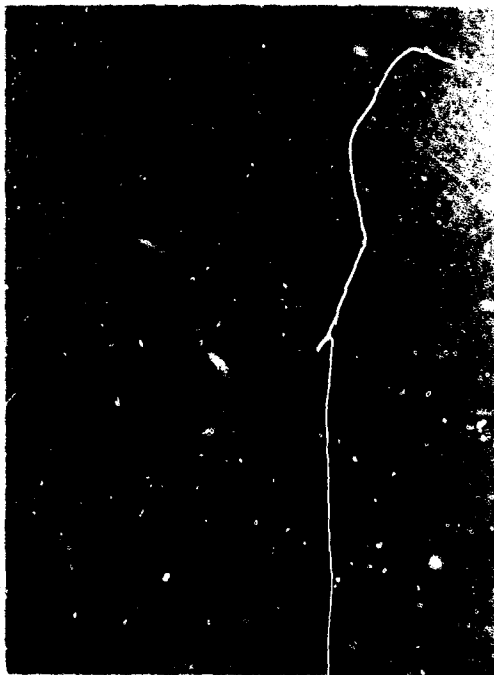
**SPATIAL DISORIENTATION DEVICE**
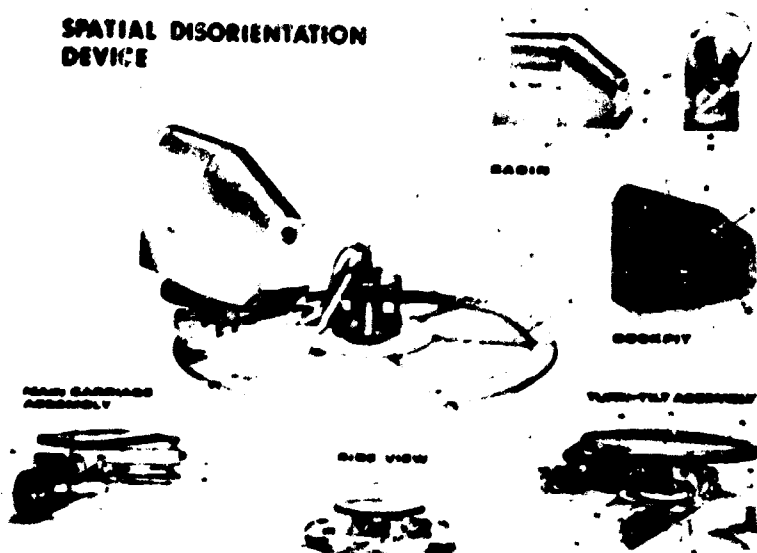
Slide 7

**AIR CATAPULT**
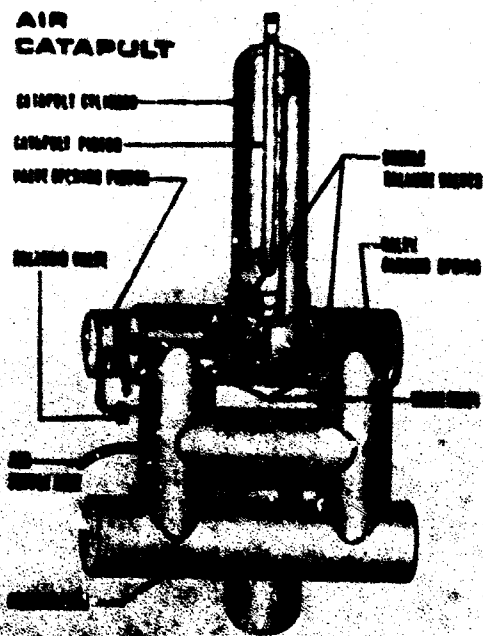
Slide 8

AUTOMATIC VENT AND LEVEL OFF VALVE
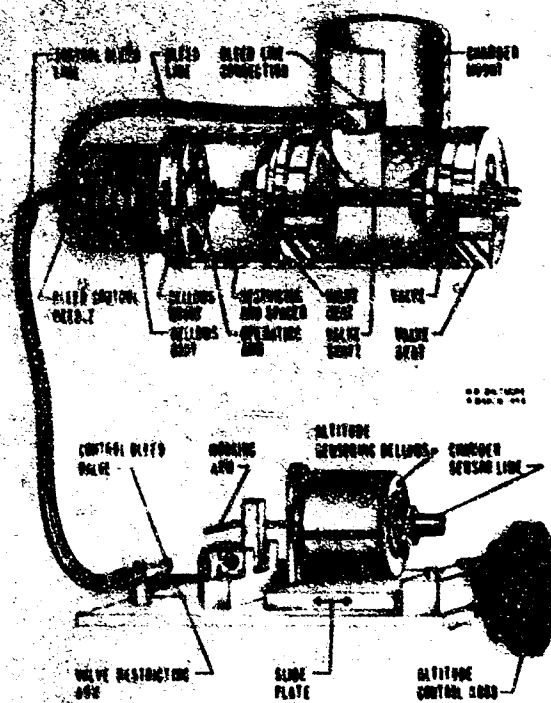
Slide 9
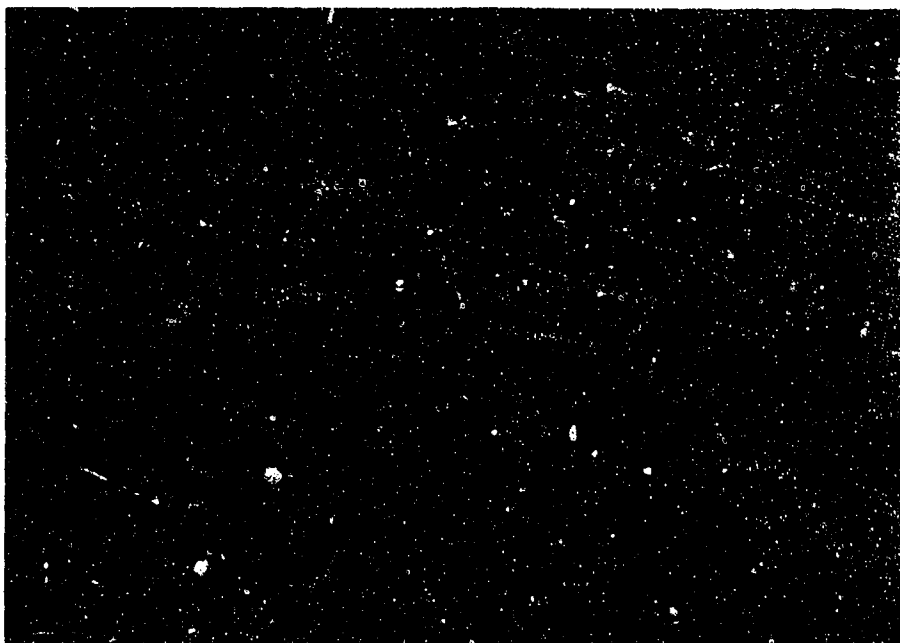


Slide 10

**FIRE PROOF ELECTRICAL ISOLATION SPEAKER**
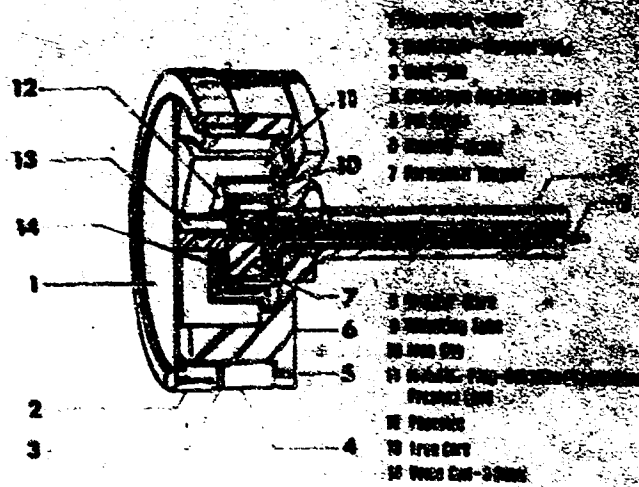
Slide 11

Slide 12

Slide 13


Slide 14

A NEW METHOD FOR DETERMINING

GYROSCOPE SHORT-TERM-DRIFT CHARACTERISTICS

BY

JUDITH G. KOESTLER

CENTRAL INERTIAL GUIDANCE TEST FACILITY
AIR FORCE MISSILE DEVELOPMENT CENTER
AIR FORCE SYSTEMS COMMAND
HOLLOMAN AFB, NEW MEXICO

R-1

# BIOGRAPHY

Judith G. Koestler received a B.S. degree from Baylor University in 1958, majoring in physics and mathematics. After a year of teaching high school mathematics she returned to Baylor to study for a M.S. degree in Physics which she received in 1962. The next two years she served as the Chairman of the Science, Mathematics, and Engineering Department at Hillsboro Junior College in Hillsboro, Texas. Since 1964 she has been employed in the Components Analysis Branch, Analysis Division, of the Central Inertial Guidance Test Facility at Holloman Air Force Base, New Mexico. Her work there has been principally in the analysis associated with laboratory testing of inertial quality gyroscopes to be used in aircraft and missile guidance systems.

In 1967 she was awarded the Patricia Kayes Glass Award, an award given annually to honor outstanding contributions by women working in Air Force Systems Command laboratories, and in 1968 she was one of two women nominated by the Air Force for "Federal Woman of the Year."

Mrs. Koestler's publications include a technical report "Gyroscope Standard Gyrocompassing Accuracy Test" and an article in The American Journal of Physics entitled "Some Developments in Generalized Classical Mechanics."

## ABSTRACT

An important part of the work of an analyst at the Central Inertial
Guidance Test Facility at Holloman Air Force Base, New Mexico, involves
a constant search for improved techniques of testing inertial quality
gyroscopes used in aircraft and missile guidance systems. Once the
initial idea for such a test is formalized, the analyst must design the
test; determine the most efficient data reduction techniques for extracting
the desired information; and examine the practicality of the test con-
sidering the time and effort expended in relation to the quality of the
results obtained.

This paper describes the development of such a test from the time
the need for an improved procedure was recognized through the actual
performance of the test and the analysis of the resulting data. The test
in question is a "two-axis tumble test" which reduces by a factor of five
the test time required to estimate the drift coefficients in the gyro
performance model. The previous method required ten hours of test time
to obtain data for an estimation of the coefficients; the two-axis tumble
test requires only about two hours. Reduced test time provides insta-
bility values which are more nearly "short-term" and which more closely
approximate the instabilities to be expected over a few minutes of boost
phase for a missile or over the few hours of an aircraft flight. The new
procedure also allows a more realistic estimation of any time dependent
characteristics of the coefficients.

## LIST OF FIGURES

## 1. INTRODUCTION

At the Central Inertial Guidance Test Facility (CIGTF) a constant search is underway for improved techniques of testing gyroscopes used in aircraft and missile guidance systems. This paper describes a unique test method called a "two-axis tumble test" developed at the CIGTF. The primary goal of this effort was to establish a test which provides a significant increase of efficiency with respect to test time and manpower and a more realistic estimation of the short-term drift characteristics of gyroscopes than previously available.

After a brief discussion of the gyroscope performance model and of the gyro test now in most common use, a description of the new two-axis tumble test is presented. This includes a discussion of the method used to obtain a solution for the gyro drift coefficients. Finally, the results of a two-axis tumble test performed at the CIGTF are presented.

## 2. GYROSCOPE PERFORMANCE MODEL

A gyroscope performance model is an equation which is assumed to describe the drift rate of a gyroscope when it is subjected to various accelerations and angular input rates. A single degree-of-freedom gyro would be considered perfect if it conformed to the following performance model:

$$S_T i = \omega_I$$

where $S_T$ is the torque generator scale factor, $i$ is the torquer input current, and $\omega_I$ is the angular rate sensed by the gyro input axis. Unfortunately, the perfect gyro does not exist and other terms, designated as "drift terms," must be added to the model to describe the performance of a real gyro. These additional terms are composed of drift coefficients and their respective coordinate functions. The coordinate func-

tions are known quantities consisting of the unit constant and functions of acceleration components along each of the three orthogonal gyro axes (see Figure 1). The drift coefficients are constants which when multiplied by appropriate coordinate functions yield terms expressing gyro drift rate.
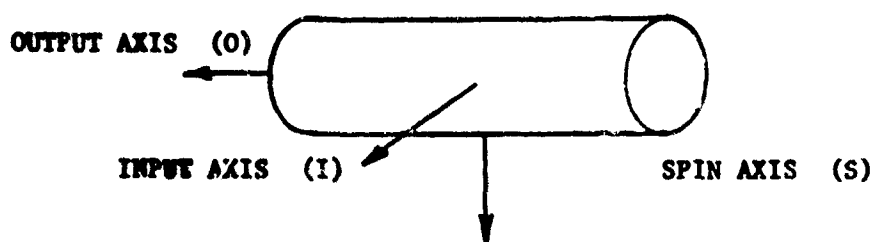


FIGURE 1

AXES OF A SINGLE DEGREE-OF-FREEDOM GYRO

The steady-state performance model assumed for all single degree-of-freedom gyros at the CIGTF is:

$$S_T i = D_F + D_I a_I + D_O a_O + D_S a_S + D_{II} a_I^2 + D_{SS} a_S^2$$

$$+ D_{IO} a_I a_O + D_{IS} a_I a_S + D_{OS} a_O a_S + \omega_I$$

where

$i$      current flow through the torquer (ma)

$S_T$      torquer scale factor (°/hr/ma)

$a_I$      acceleration, with respect to inertial space, of the gyro case along the input axis (g)

$a_O$      acceleration, with respect to inertial space, of the gyro case along the output axis (g)

$a_S$      acceleration, with respect to inertial space, of the gyro case along the spin axis (g)

$D_F$      gyro drift (°/hr) which is insensitive to acceleration

$D_I a_I$     gyro drift (°/hr) attributable to acceleration along the input axis, where $D_I$ (°/hr/g) is a drift coefficient

$D_O a_O$     gyro drift (°/hr) attributable to acceleration along the output axis, where $D_O$ (°/hr/g) is a drift coefficient

$D_S a_S$     gyro drift (°/hr) attributable to acceleration along the spin axis, where $D_S$ (°/hr/g) is a drift coefficient

$D_{II} a_I^2$     gyro drift (°/hr) attributable to the square of acceleration along the input axis, where $D_{II}$ (°/hr/g$^2$) is a drift coefficient

$D_{SS} a_S^2$     gyro drift (°/hr) attributable to the square of acceleration along the spin axis, where $D_{SS}$ (°/hr/g$^2$) is a drift coefficient

$D_{IO} a_I a_I$     gyro drift (°/hr) attributable to the product of accelerations along the input axis and output axis, where $D_{IO}$ (°/hr/g$^2$) is a drift coefficient

$D_{IS} a_I a_S$     gyro drift (°/hr) attributable to the product of accelerations along the input axis and spin axis, where $D_{IS}$ (°/hr/g$^2$) is a drift coefficient

$D_{OS} a_O a_S$     gyro drift (°/hr) attributable to the product of accelerations along the output axis and spin axis, where $D_{OS}$ (°/hr/g$^2$) is a drift coefficient

$\omega_I$     angular velocity, with respect to inertial space, of the gyro case about the input axis (°/hr)

hr     sidereal hour

g     local acceleration of gravity, defined positive upward

## 3. THE STANDARD TORQUE-TO-BALANCE TEST

### 3.1 Torque-to-Balance Mode

"Torque-to-Balance" refers to the mode of gyro operation. In this mode a torque is produced which counteracts and nulls the gyroscopic torque due to the motion of the gyro in inertial space. This counter-torque is measured and constitutes the gyro output.

### 3.2 Test Description

The gyroscope Standard Torque-to-Balance test presently in use

at the CIGTF is the product of several years of development aimed at improving the accuracy of test results. The test was chosen as the fundamental laboratory test because it provides a solution for all nine gyro performance model coefficients in an easy-to-perform, repeatable test which can be performed on most present day gyros. Since the test is repeatable, instabilities of each drift coefficient can also be calculated. The "instability" is a measure of the variation in a drift coefficient over some period of time and is arbitrarily defined as the standard deviation of five independent determinations of the coefficient.

In order to obtain the data necessary for one determination of all nine coefficients about ten hours of testing time is required. The gyro is rotated through $360°$, both clockwise and counterclockwise, about an axis paralleled to the polar axis of the earth at a rate of $300°/hr$. These two rotations are performed for three different gyro orientations: spin axis parallel to axis of rotation, spin axis $90°$ to axis of rotation, and spin axis $180°$ to axis of rotation. The counterclockwise rotation is necessary to eliminate the effects of any input axis misalignment from the plane perpendicular to the axis of rotation. This procedure must be repeated four times to acquire enough data for one instability determination. A complete discussion of the Standard Torque-to-Balance Test is presented in Reference 1.

## 4. THE TWO-AXIS TUMBLE TEST

### 4.1 Need for Improved Procedure

Since the Standard Torque-to-Balance Test requires approximately two days of testing to obtain the data necessary for determination of instability values for the nine drift coefficients, a need for an improved

procedure was apparent. Instability estimates which more nearly correspond to those that would be expected over the few hours of an aircraft flight or over the few minutes of a boost phase for a missile must be obtained. The two-axis tumble test was conceived and developed with that goal.

## 4.2 Test Configuration

Essential to the two-axis tumble est is a fixture which is capable of simultaneously positioning the gyro about two orthogonal axes. In the test configuration, the principal fixture axis is parallel to the earth rate vector. The gyro is mounted so that its input axis is parallel to the secondary fixture axis and therefore senses no earth rate. The starting position for the test is arbitrarily chosen as input axis west and spin axis parallel to negative earth rate.

## 4.3 Comparison of Continuous and Pause Tumbling

.4.3.1 In the continuous tumble mode, the fixture axes are driven at different constant rates. The rates used depend upon the maximum allowable input rate to the gyro and the chosen ratio of motion between the axes. The advantage of this mode is that an increase in data density does not increase the total test time. However, orthogonality and rate drive accuracies become critical considerations in this mode, and a rotation in the opposite direction is necessary to eliminate the effect of input misalignment.

4.3.2 Pause tumbling differs from continuous tumbling in that the rotation about the fixture axes is halted at predetermined positions while the data are collected. The disadvantage of this method is that the gyro drift must be allowed to stabilize in each position before the torquer current is sampled. An advantage, however, is that the misalign-

ment of the input axis has negligible effect since no high rotation rates are sensed by the gyro.

### 4.4 Advantages over Standard-Torque-to-Balance Test

The advantages of the two-axis pause tumble test over the currently used Standard Torque-to-Balance Test are:

a. A solution for the drift coefficients of a gyro with a settling time of two minutes can be obtained in less than two hours as compared to ten hours using the present test method.

b. The need for counterclockwise rotations is eliminated.

c. There is no need to stop the rotation once the sequence required for one solution is completed. Each additional data point, when combined with data from the previous sequence, provides a new solution for the drift coefficients. Therefore, with certain precautions, it is possible to obtain an estimate of how the drift coefficients vary over short periods of time.

## 5. SOLUTION FOR DRIFT COEFFICIENTS

### 5.1 Introduction

A proper solution for the nine performance model drift coefficients depends on two factors. First, no solution is possible unless an appropriate ratio of motion between the two fixture axes is chosen. Next, an analysis method must be selected which provides an optimum solution and then checks this solution for significance.

Following the initial solution for the drift coefficients, a "continuous" solution of the coefficients versus time may also be obtained. Properly interpreted, this solution can be an extremely valuable tool to both gyro and system designers.

## 5.2 Ratio of Motion about the Two Fixture Axes

The first step in obtaining a proper drift coefficient solution is to choose a proper tumble ratio. Let this ratio of angular positions about the two axes be:

$$\frac{m\theta}{n\theta} = \frac{m}{n}$$

where

$m\theta$ is the angle of rotation about an axis parallel and opposite to the axis of the earth, and perpendicular to the gyro input axis. This axis is the principal fixture axis (see Figure 2).

$n\theta$ is the angle of rotation about an axis parallel to the gyro input axis. This is the secondary fixture axis.

The components of the acceleration of gravity along the gyro input, output, and spin axes in terms of $\theta$ are:

$$a_I = -g \cos\lambda \ \sin m\theta$$

$$a_O = -g \cos\lambda \ \cos m\theta \ \cos n\theta - g \sin\lambda \sin n\theta$$

$$a_S = g \cos\lambda \ \cos m\theta \ \sin n\theta - g \sin\lambda \cos n\theta$$

where g is the acceleration of gravity and $\lambda$ is the astronomic latitude angle.

When the values of m and n are properly chosen, correlation among coordinate functions can be reduced to a minimum to obtain optimum separability of the coefficients to be evaluated; however, the coordinate functions for $D_F$, $D_{II}$, and $D_{SS}$ will be correlated independently of the choice of m and n since their coordinate functions contain bias components. Correlation is also dependent upon the number of data points used for solution of the coefficients. This is true because $\sin a\theta$ is correlated with $\sin b\theta$, and $\cos a\theta$ is correlated with $\cos b\theta$ when $|a \pm b|$ equals the number of data points.

R-11

EARTH POLAR AXIS

NORTH

PLANE OF MOTION OF THE
SECONDARY FIXTURE AXIS

PRINCIPAL FIXTURE AXIS

SECONDARY FIXTURE AXIS
(PARALLEL TO THE GYRO
INPUT AXIS)
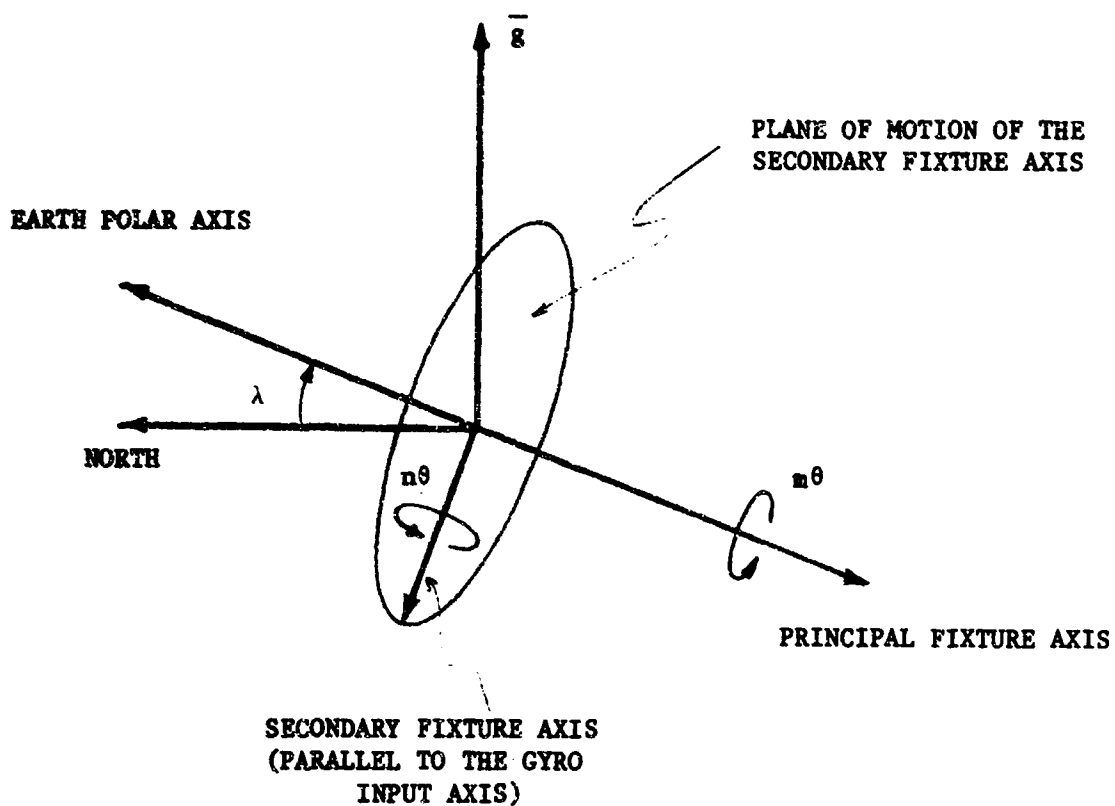
FIGURE 2

ALIGNMENT OF THE TWO FIXTURE AXES
FOR THE TWO-AXIS TUMBLE TEST

To determine which values of m and n yield minimum correlation solutions for a given number of data points computer simulations were used. The results indicated that for a 36-data-point cycle* examples of low correlation ratios are: 5/2, 5/3, 5/4, 6/1, 6/5, 7/1, 7/2, 7/3, 7/4. Other ratios such as 4/3 and 7/5 do not permit separation of the coefficients due to high correlation. Therefore, a continuous tumble test using rotation rates about the two axes of 600°/hr and 450°/hr, respectively, would be unsuitable, while 750°/hr and 300°/hr would make separation possible.

## 5.3 Least Squares Method

### 5.3.1 Drift Coefficients

If the error in the data is normally distributed and uncorrelated with mean zero, the least squares fit of the performance model to the data yields the maximum likelihood, minimum variance estimate of the drift coefficients. In matrix notation the least squares solution is as follows:

$$Y = XD$$

where:

Y     matrix of data (n x 1)

X     matrix of coordinate functions (n x 9)

D     matrix of drift coefficients (9 x 1)

When both sides of the equation are multiplied by the transpose of X

$$X^T Y = [X^T X] D$$

---

* A complete cycle is defined to be a rotation through $\theta = 2\pi$. Therefore, when $\frac{m}{n} = 5/2$, the gyro is rotated through $10\pi$ about the principal fixture axis and through $4\pi$ about the secondary fixture axis.

R-13

Solving for D yields

$$D = [X^T X]^{-1} [X^T Y]$$

### 5.3.2 Standard Error

The standard error of a drift coefficient is an estimate of the standard deviation of the error in the drift coefficient if the mean of the error is assumed to be zero. It is a useful statistic in that it permits a t-test in order to determine the significance of the estimated coefficient. For the $j^{th}$ coefficient the standard error is

$$SE = \sigma_r \sqrt{a_{jj}}$$

where $a_{jj}$ is the term on the $j^{th}$ row and $j^{th}$ column of $[X^T X]^{-1}$; and the standard deviation of the residuals is defined

$$\sigma_r = \sqrt{\frac{\sum_{k=1}^{n} (y_{ok} - y_{ck})^2}{n - 9}}$$

where $y_{ok}$ is the observed $k^{th}$ data point and $y_{ck}$ is the $k^{th}$ data point computed by substituting the nine estimated drift coefficients into the performance model. The magnitude of $a_{jj}$ decreases as the number of data points is increased. Hence, the standard error may be decreased to some extent as the density of the data points for a cycle is increased, allowing recovery of smaller drift coefficients.

### 5.4 Drift Coefficients as a Function of Time

After the gyro is rotated through a complete cycle each additional data point allows a new solution. This type of sliding fit of the performance model to the data permits a number of solutions in a short period of time; however, the new solution is not independent of the previous one. Although several independent solutions are necessary to measure drift coefficient instability, a plot of the non-independent solutions indicates time

R-14

dependent characteristics over shorter periods of time. If any time dependent characteristics can be detected and modeled, a true operating instability of the coefficient can be determined. Present methods of determining operating instability are based upon the assumption that the drift coefficients are stationary during the time required to take enough data for one solution (about 10 hours). Since the time required for one two-axis tumble test cycle is under 2 hours, this assumption is more nearly valid.

## 6. TWO-AXIS TUMBLE TEST PERFORMED AT THE CIGTF

### 6.1 Test Description

To investigate the feasibility of the two-axis tumble test, a test was performed on a Century Detroit two-axis test platform at the CIGTF. Since this fixture has no provision for automatic positioning, the positioning was accomplished manually to an accuracy of 0.1 degree. It was not possible to control closely the time between data samples; thus the data were not equally spaced in time. The test was performed using a 5:2 ratio. The torquer current was sampled for ten seconds at 50° intervals about the principal axis and at 20° intervals about the secondary axis. The time required for each cycle (36 data samples) was 5 to 5 1/2 hours.

### 6.2 Test Results

In Figure 3 a sample of the gyro output is shown for four consecutive cycles. The first solution for coefficients could not be obtained until a full cycle was completed. Thereafter, each new position made possible a new (though not independent) solution. Three representative coefficients recovered from these four cycles of data are shown in Figure 4. A new estimate of each coefficient was made at 8 to 9 minute
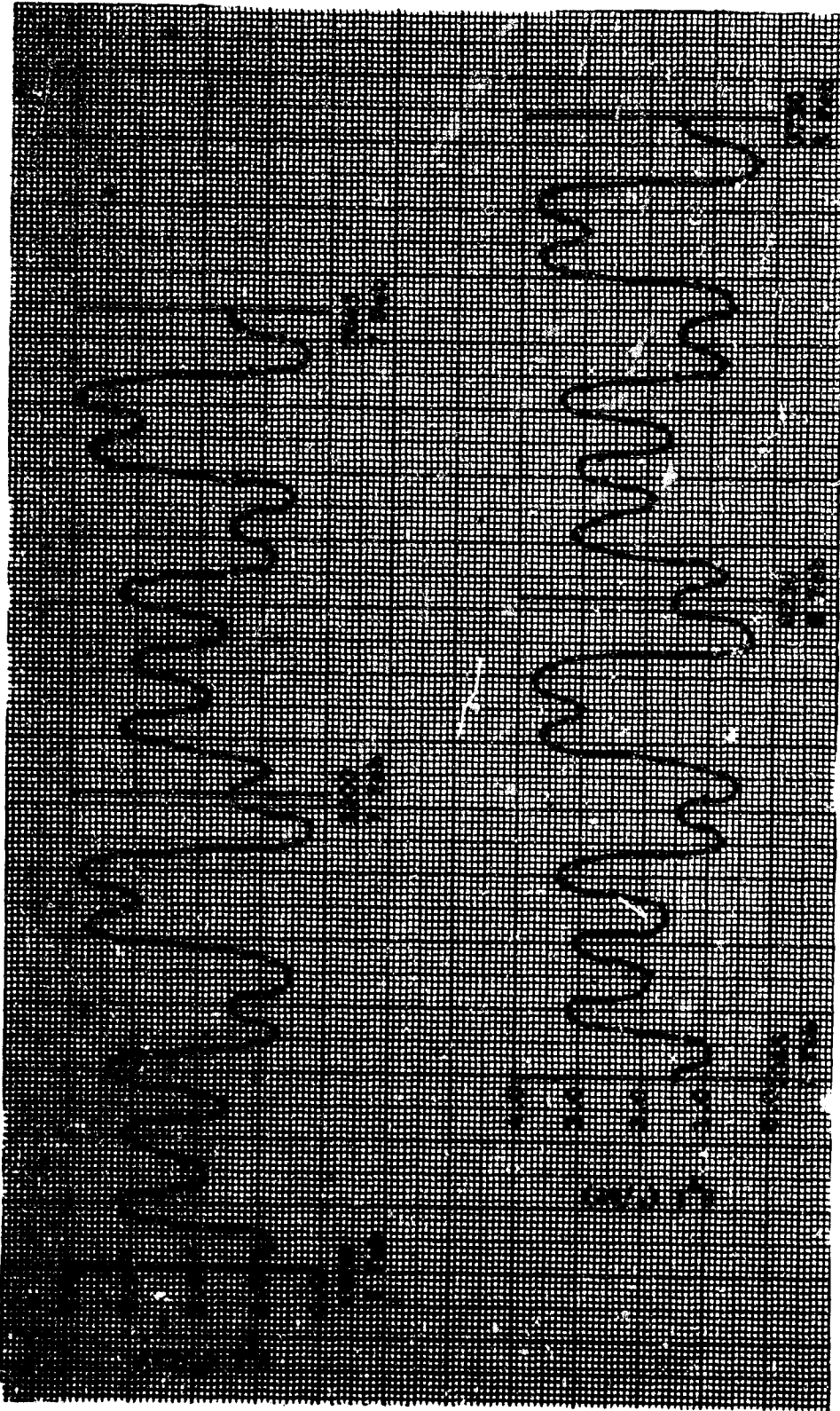
**FIGURE 3**

**GYRO OUTPUT FROM TWO-AXIS TUMBLE TEST**
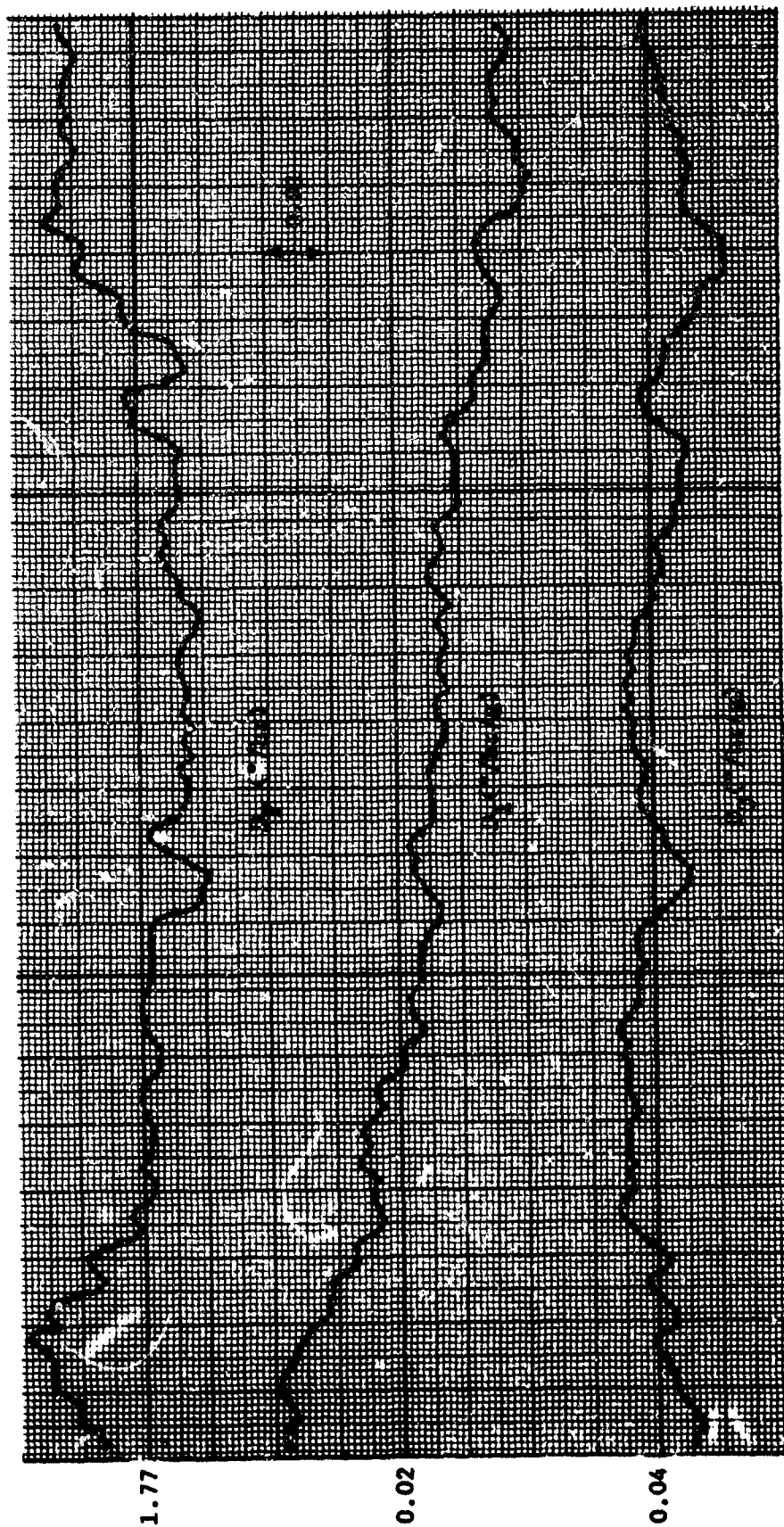
FIGURE 4

VARIATION IN $D_P$, $D_I$, AND $D_O$ DURING 16 1/2 HOURS

R-17

intervals, thus providing a plot of the coefficient versus an approximate time. These plots show trending for some coefficients while others appear to have a long periodic variation. The fact that no coefficient demonstrates a variation with a period equal to that of one test cycle indicates that these variations are not test or position dependent.

## 6.3 Conclusions

The results indicate that the two-axis tumble test is feasible and that a pre-programmed, automatically positioned test fixture would yield drift coefficients as a function of time with data samples at intervals as small as two minutes. The reduced test time will provide instability values which are more nearly "short term." Long term tests such as 60 hour tests would yield information concerning the time varying characteristics of the drift coefficients which would aid in the prediction of gyro drift.

# REFERENCE

Russell, J. F., <u>Gyroscope Standard Torque-to-Balance Test, Technical</u> Report, Holloman Air Force Base, New Mexico:  Air Force Missile Development Center, June 1967.  Unclassified

PROBING THE ELECTRONIC PROPERTIES OF
CRYSTALS BY PRESSURE

By

Dietrich W. J. Langer

# PROBING THE ELECTRONIC PROPERTIES
## OF CRYSTALS BY PRESSURE

Dietrich W. Langer

## ABSTRACT

The determination of the electronic energy levels in crystaline sub-
stances is of prime importance for the description and prediction of such
properties as electrical conductivity, mobility of charge carriers, photo-
conductive response and optical absorption and emission spectra. The
location of these energy levels is determined by the chemical elements
which compose the crystal under consideration, as well as by the separa-
tion of these elements; i.e., the distance between atoms in a given lattice.
In order to separate these two effects experiments were carried out in
which the inner atomic distance was changed and the resulting effects on
the energy levels were studied. Changes in the lattice constant were
introduced by uniaxial extension or compression and by hydrostatic com-
pression (up to 20000 atm.) Systems studied were the band edges and
excitons in II-VI compounds (CdS, ZnS, ZnSe, TnTe and ZnO) as well as
the levels of localized ions (H0, Tm, Mn) in II-VI compounds and Cr in
$Al_2O_3$ (ruby). The experimental results are compared with band struc-
ture and crystal field calculations.

# BIOGRAPHY

Dr. Dietrich W. J. Langer has been a Senior Physicist in the Aerospace Research Laboratories, Solid State Physics Research Laboratory, since September 1957.

Born and raised in Berlin, Germany, Dr. Langer attended the Technische Universitat (Institute of Technology) in Berlin where he received the "Diplom-Ingenieur" degree (the equivalent to the M.S.) in 1957. Under the Paperclip program he then immigrated to the United States and was employed by the Aeronautical Research Laboratory, predecessor of the Aerospace Research Laboratories.

Having also completed the necessary course work leading to the Ph.D. at Berlin, Dr. Langer worked on his thesis while employed at ARL and in December 1960, he received his doctorate at the Technische Universitat of Berlin. In 1961, on a leave of absence from ARL, Dr. Langer conducted studies in particular areas of his interest at the Applied Physics Department of the Harvard University, Cambridge, Mass.

Dr. Langer's work at ARL is in the areas of the effects of pressure on semiconductors, and the optical properties of impurities in II-VI compound crystals. He has been a thesis supervisor for AFIT students. He has also taught classes at the University of Dayton and at Antioch College.

Since joining ARL in 1957, Dr. Langer has advanced in grade from GS-9 to GS-14. In 1964 he was awarded an opportunity of conducting a year of post doctoral studies at the Physics Department of the Ecole Normale Superieure, a branch of the University of Paris. Dr. Langer is a member of the American Physical Society and is author or co-author of some twenty technical reports and journal articles in his field. He is well known to the national and international scientific community by his work and his reputation is reflected by his being asked to organize an International Conference on II-VI Semiconducting Compounds in 1967.

Dr. Langer was married in 1961 to the former Anneliese Hausmann of Berlin, Germany. They have two sons.

Probing the Electronic Properties of
Crystals by Pressure

Dietrich W. J. Langer

Aerospace Research Laboratories
Wright-Patterson Air Force Base, Ohio

I. Introduction

In today's technology the properties of single crystals play a very
important role. Think for example of transistors, the ruby laser computer
memories, light from fluorescent lamps or of the cadmium sulfide expo-
sure meter in your modern camera.

These and other applications make use of the motions of electrons,
or their transitions between discrete energy levels in an appropriate cry-
stal. These discrete energy levels are analogous to the allowed energy
levels of electrons in an isolated atom, i.e. to their different possible or-
bitals. Each kind of crystal exhibits an energy level scheme usually called
"band structure" that is characteristic for its chemical composition, and
its crystallographic structure. Impurities, when added to the crystal,
usually cause the presence of additional energy levels. The band structure
and the impurity levels determine all and every electronic and optical pro-
perty of a crystal.

Our knowledge - today - of such energy bands is derived from an
enormous amount of data determined by experiments. Theoreticians, at
present, have all the tools (e.g. quantum mechanics, theory of relativity)
to predict electronic bandstructures in principle. In reality however, even
the biggest computers are not large and fast enough to do these calculations
completely and exactly. Thus their main effort is centered around finding
suitable approximations which make the calculations manageable and which
still furnish reasonably exact results. Therefore calculations are made
by various methods mainly for crystals with relatively well determined ex-
perimental band structure parameters. The degree of agreement with ex-
periments determines the validity of the method which was used for the cal-
culation. In the case of semiconductors such parameters used for com-
parison with theory, or for adjustment of theory, are usually energy differ-
ences between extrema of certain energy levels (i.e. band gaps between
conduction and valence bands at points of high symmetry in the momentum
space). In order to obtain good agreement with experiment, theoreticians
often feel free to adjust one or a few parameters. However plausible and

correct those adjustments may be (they are usually justified as lump sum refinements of previously made approximations) no one can maintain that the resulting agreement with experimental bandstructure may not be purely accidental, i.e. that it is a convincing argument for the validity of theory and the approximations used. A simple and real acid test, however, is possible at this point by considering the effects of pressure on the system. Pressure causes a lattice dilation and a theoretician can proceed to recalculate, e.g. bandgaps, without further adjustments according to his original scheme by changing the lattice parameters by a small amount. Now the degree of agreement between measured and calculated pressure coefficients is a valid test for the value of the theory.

Besides aiding such, let me call them, emerging theories, pressure coefficients are useful in other ways too. Let me summarize in short what we gain by their knowledge:

1) In conjunction with a well established theory we can identify so called "symmetry assignments" of energy levels by observing the way in which they shift and (perhaps) split.

2) Knowledge of the dilation effect on certain levels (in conjunction with thermal expansion and compressibility coefficients) enables us to reduce experimentally determined temperature effects to their true, intrinsic value, because the effect of the thermal expansion is otherwise inseparable.

3) The pressure coefficient directly determines the amount of pressure necessary to obtain a given optical frequency variation e.g. in solid state lasers (say: pressure tunable lasers) or in electro-optical crystals.

4) The pressure coefficient offers an invaluable check on emerging theories, as pointed out above. It will be the primary purpose of this talk to show how our work contributes in this respect. In three examples I will show how our experimental results have interacted with theory and contributed to the present state of the art.

   a) In the area of bandstructure calculations we have measured the pressure coefficients of bandgaps of several II-VI compounds ( ZnO, ZnS, ZnSe, ZnTe, CdS, CdTe). Theory, though able to compute bandgaps pretty well, has not yet come up with the correct pressure coefficients and is thus forced to refine its original approach.

   b) In an area where the crystal field theory is applicable e.g. the energy levels of Cromium in Aluminum Oxide (Ruby), we measured the pressure dependence of the Cromium Levels and found good quantitative agreement of our values for the change of the crystal field with lattice dilation and the value expected according to the theory. Thus we showed

that in this respect the theory in its present state is adequate.

c) The binding theory of excitons is a third area we engaged in. (An exciton is a hole in the valence band and an electron in the conduction band forming a hydrogen like entity). Here we found experimentally a qualitative disagreement with theory. Energy levels split with pressure. This was not expected according to the conventional treatment. The results could be accounted for only after considering a spin exchange term which in turn is relevant also for the zero-pressure binding energy of excitons. The consequences of the presence of "exchange", demonstrated by these experiments, will be highly significant in all large band gap semiconductors.

The last three items, examples of our work at ARL, will be presented in detail in Section III. In Section II some experimental details and difficulties will be discussed.

## II Experimental Procedures

Conceptually the experiments are simple: One observes spectra in luminescence, absorption, or reflection. These spectra can be related to induced transitions of electrons between two energy levels of the crystal. One applies pressure, hydrostatic or uniaxial pressure, and records the shift in energy of said structure as a function of the applied pressure. The difficulties, however, become obvious when one tries to do just this: With those pressures which one can easily achieve there is no noticable energy shift to be observed and with very high pressures the optical accessability of the sample becomes a problem. The minimum shift which is still observable also depends on the "linewidth" of the absorption lines or the reflection characteristics. Furthermore we set ourselves the goal of obtaining coefficients with less than 10% error (in order to be of value for the comparison with theory).

Our approaches were along two different lines, each with its own particular advantages and drawbacks; 1) application of hydrostatic pressure and 2) application of uniaxial pressure. In both cases it is advantageous to work at as low a temperature as possible because the linewidth becomes narrower and therefore the necessary pressure is lower. Also theories are generally worked out without the inclusion of lattice vibrations and thus we would be as close as possible a common basis with theory.

The hydrostatic system designed and built at ARL which finally did the job consisted of a pressure generator capable of compressing gas up to 20,000 atmospheres (about 300,000 PSI), and a testvessel with two windows which when submersed in a specially designed dewar could be used at the

temperature of liquid nitrogen (-320°F).[1]  Measurements with this test chamber have been routinely done at this temperature to about 12,000 atmospheres (about 180,000 PSI). It should be pointed out that optical accessability in this pressure and temperature range by itself was a unique technological achievement. Materials had to be used beyond their conventional design limits and even apart from special problems of window seals the design area was technologically adventurous. The window plug e.g. in the test vessel on Fig. 1 had to withstand a force equivalent to the weight of a B-52 bomber.

As a byproduct, or figure of merit for the system, we could establish the freezing point of helium at liquid nitrogen temperature (14,140 bars = 212,000 PSI).[2]  The point was about 50% higher in pressure (and temperature) than the highest one measured otherwise. The apparatus still marks the design limit. It was copied by workers in the high pressure field and is working presently in Laboratories at Harvard University, University of Cambridge, England, and at the Sarbonne in Paris. Our complete setup, including spectrograph is shown in Figure 2. The hydrostatic pressure coefficients measured were all measured to better than ± 5% error, some to ± 2%.

Uniaxial pressure applications don't have the glamour but also don't involve the difficulties of the hydrostatic techniques. No huge forces are required if the crystal area is reduced. Several different arrangements have been used; 1) placing a crystal at the extension of a hydraulic ramp, 2) bending a thin crystal, thus observing the effects of compression and expansion on the reflection spectra and finally 3) pulling a crystal up to only 1/2 pound maximum. In this last case, for absorption spectra, the crystal was not thicker than 2 micron 0.00004 inches). With a width of about 2 mm (0.08 inches) this again corresponds to a stress of about 5,000 atmospheres (or 75,000 PSI).

The limit here is set by the brittleness of the crystals, which usually break even before this stress is reached. Though we were able to work at still lower temperatures with uniaxial pressures by immersing the stress apparatus with the crystal into liquid helium (4°K or -452°F), the pressure coefficients could not be determined too accurately because of the greater difficulties in determining the stress to better than 10%. Nevertheless this arrangement proved useful because with uniaxial stress, cubic crystals and especially hexagonal crystals (as the wurtzite II-VI compounds which we were most interested in) give several non equivalent directions to apply the stress to, and thus several pressure coefficients to compare with theory. See Fig. 3.

### III Experimental Results

#### a) Bandstructure

In the study of semiconductors we studied band-to-band transitions usually by measuring the characteristic structure in the reflection spectra. Fig. 4 gives an example of such structure and the change, (the energy-shift) as a function of hydrostatic pressure. The electronic transition in this example does not correspond to the fundamental bandgap of CdTe, but to a higher one, the so called $E_1$ gap. Fig. 5 demonstrates the band structure of CdTe as calculated by $k \cdot p$ method. The three heavy arrows $E_o$, $E_1$ and $E_1 + \Delta_1$ indicate the gaps on which we investigated the pressure coefficients. This figure also may serve to indicate how much information the calculated bandstructure may offer. The few parameters which are available as experimental checks are a few vertical band separations and curvatures at the top of the valence band and bottom of the conduction band at the $\Gamma$ point.

Fig. 6 gives you an example of the evaluation of two sets of measurements in CdTe resulting in pressure coefficients for the transition and the $L_{3v} \rightarrow L_{1c}$ transitions, also called $E_1$ and $E_1 + \Delta_1$ where the small splitting $\Delta_1$ is the spin-orbit splitting of the valence band at the L point. This assignment had been supported also by the pressure coefficients, for $E_1 + \Delta_1$ have very similar pressure coefficients. This points to the fact that the transitions do not occur at different symmetry points in the momentum space but at one and the same point between a split band and a single band, because the spin-orbit splitting of the valence band is not expected to change appreciably with pressure.

In a similar fashion, as demonstrated in the above example, we measured the hydrostatic pressure coefficients for a variety of II-VI compounds.[3] They are summarized in Table I.

The significance of these coefficients lies in the fact that theoretical calculations will have to reproduce them. Calculations made according to various methods, which may or may not use a few adjustable parameters, are offered in the form of these coefficients a simple method to check their validity. A recalculation with different lattice constants would not imply new complications or adjustable parameters and thus should furnish a true check of the method of calculation. Unfortunately up until now such agreement has not been found quantitatively, but that is not the fault of the experiments.

that the three unknowns, the three pressure coefficients of Dq, B and C, were equal to 1.05, -0.03 and -0.35 cm$^{-1}$/kbar respectively. The dependence of Dq upon P is also easily estimated theoretically because Dq is inversely proportional to the interatomic distance raised to the fifth power.

Using Bridgeman's value for $\frac{\Delta V/V}{\Delta P}$ we arrived at $\frac{\Delta Dq}{\Delta P}_{theor} = 1.07$ (cm$^{-1}$/kbar) which we find to be in surprisingly good agreement with our measured value of

$$\frac{\Delta Dq}{\Delta P}_{exp} = 1.05 \ (cm^{-1}/kbar)$$

Thus we concluded that the change of the crystal field could be adequately, i.e. qualitative and quantitatively predicted by the classical crystal field theory.[4]

### c) Exciton Theory

In this third example of our work of probing electronic properties of crystals by pressure we first found an experimental disagreement with theory. Consequently we had to implement the theory in order to describe our findings. Finally we succeeded and in turn our implementation showed up consequences for the binding forces of excitons in all large band gap semiconductors.

Applying uniaxial pressure in directions perpendicular or parallel to the c-axis of wurtzite II-VI compound crystals should shift the energy bands and accordingly the exciton ground states if one follows the conventional deformation potential theory.[5] Figure 8, however, shows, that if the pressure is perpendicular to the c-axis and the propagation direction of light is parallel to the c-axis, that the exciton transition energy splits into two components, one completely polarized with E ∥ P and one with E ⊥ P. These results could be explained only after we added to the usual Hamiltonian, which determines the exciton energies, a term $1/2 \ J \ \sigma_h \cdot \sigma_c$ which represents the spin exchange interaction between electron and hole.

Fig. 9 shows the experimental pressure dependences of excitons in ZnO, CdS and CdSe, where the points are fitted to the data according to the augmented theory. The resulting parameters are listed in Table II.

Especially emphasized should be the following two points: 1) It has been only with the help of these uniaxial pressure measurements that the crystal field parameter ($\Delta_1$), and the anisotropic spin-orbit parameters, ($\Delta_2$), and ($\Delta_3$) could be determined. Without pressure one always had to rely on a quasi-cubic model to approximate the actual anisotropic case. 2) The size and the effect of the exchange (J) could be determined. It is shown that its effect increases in large bandgap semiconductors. In the

case of zincoxide it can be shown that the energy separation between the three excitons at the point even at atmospheric pressure is as much determined by the spin orbit interaction as by the exchange interaction ($\Delta_2 \approx J$), which had previously been completely ignored in ZnO and in all other similar crystals.

<div align="center">Table II</div>

<div align="center">Coefficients used for the "best" fit in the $\Gamma_5$ matrix</div>

| | | ZnO | CdS | CdSe |
|---|---|---|---|---|
| Crystal Field | $\Delta_1$ | .0268 | .0460 | .0712 |
| Spin Orbit $\{$ | $\Delta_2$ | .0074 | .0157 | .1286 |
| | $\Delta_3$ | .0155 | .0191 | .1424 |
| Exchange | $J$ | .0066 | .0022 | -.00016 |
| | $C_1$ | -.0040 | -.00091 | -.00078 |
| | $C_2$ | -.0058 | -.0041 | -.0038 |
| Deformation Potentials $\{$ | $C_3$ | -.0010 | -.0035 | -.0039 |
| | $C_4$ | .0037 | .0021 | .0023 |
| | $C_5$ | .0014 | .0015 | .0012 |

## IV Summary

Three examples of my pressure work were selected. Examples were presented to demonstrate their significance and contributions to the state of the art as well in the field of pressure technology as to the theoretical understanding and description of energy levels in crystals.

In example B) we verified the classical crystal field theory as far as its predictions of pressure dependence are concerned. In example A) the experimentally derived pressure coefficients are providing valuable checks for emerging new methods to calculate the band structures of semiconductors. In example C) uniaxial pressure measurements showed up serious deficiencies in the accepted binding theory of excitons. We were successful afterwards in augmenting the theory so that it described the experiments and we were able to deduce important parameters consequently.

Finally I would like to thank here all those who had assisted me in this work over the years: Dr. Warschauser, who interested me in pressure work to begin with, Mr. Sheffield who had so diligently manufactured the apparatus, and finally Dr. Euwema, whom I have been consulting in many theoretical questions.

## List of References

1) D. Langer and D. M. Warschauer, Rev. Sci. Instr. 32, 32 (1961).

2) D. W. J. Langer, J. Phys. Chem. Solids 21, 122 (1961).

3) D. Langer, Proceedings of the International Conference on Semi-conductors, Prague, p. 1042 (1961), Paris p. 241 (1965) and R. L. Knell and D. W. Langer, Physics Letters 21, 370 (1966).

4) D. W. Langer and R. N. Euwema, J. Phys. Chem. Solids 28, 463 (1967).

5) T. Koda and D. W. Langer, Phys. Rev. Letters 20, 50 (1968) and T. Koda, D. W. Langer and R. N. Euwema, Proceedings of International Conference on Semiconductors, Moscow 1968. in press.
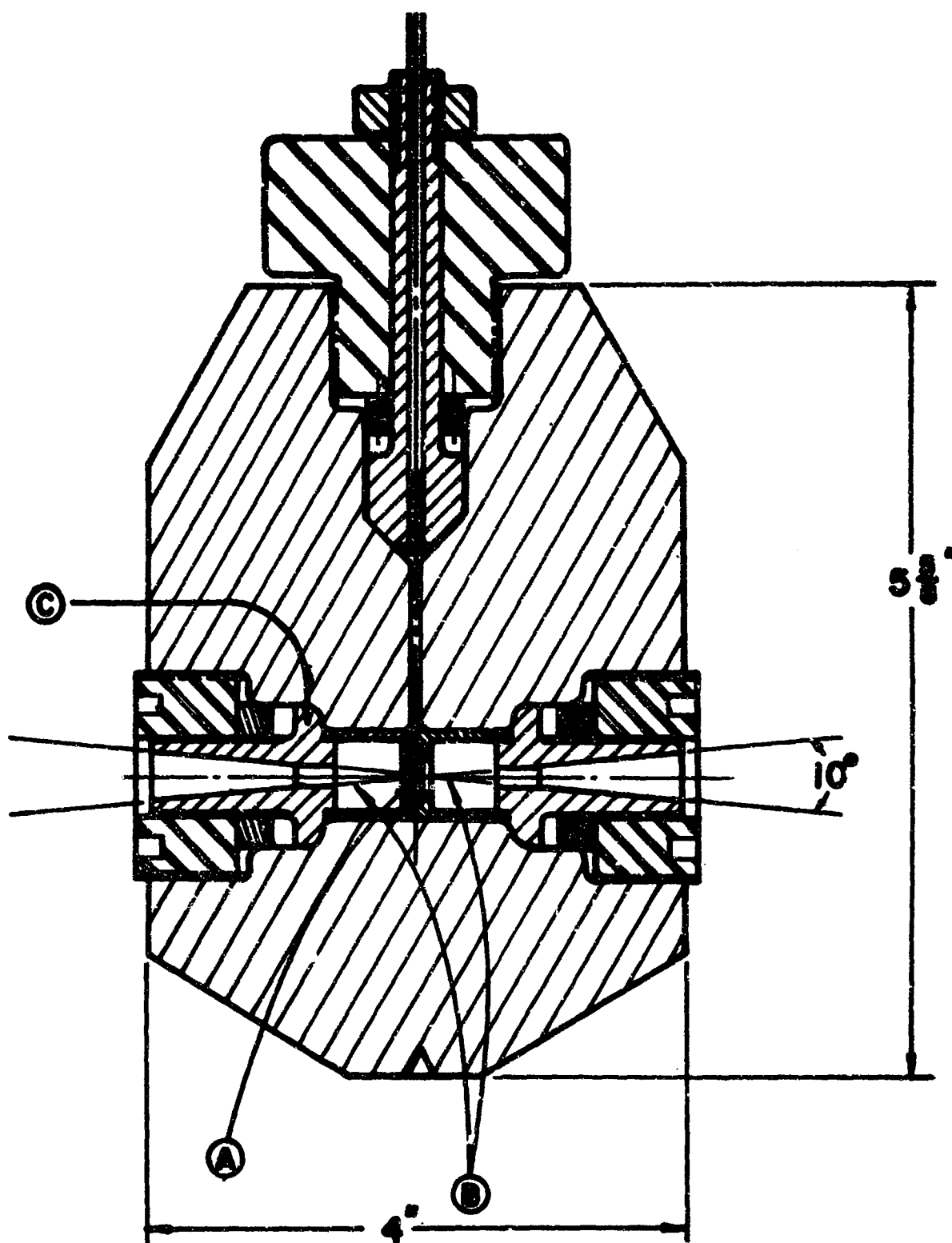
Fig. 1   The test vessel for optical experiments at hydrostatic
pressures up to 12,000 atmospheres at the temperature
of liquid nitrogen.  A) denotes the sample space, B)
two saphire windows and  C) window plugs.

S-13
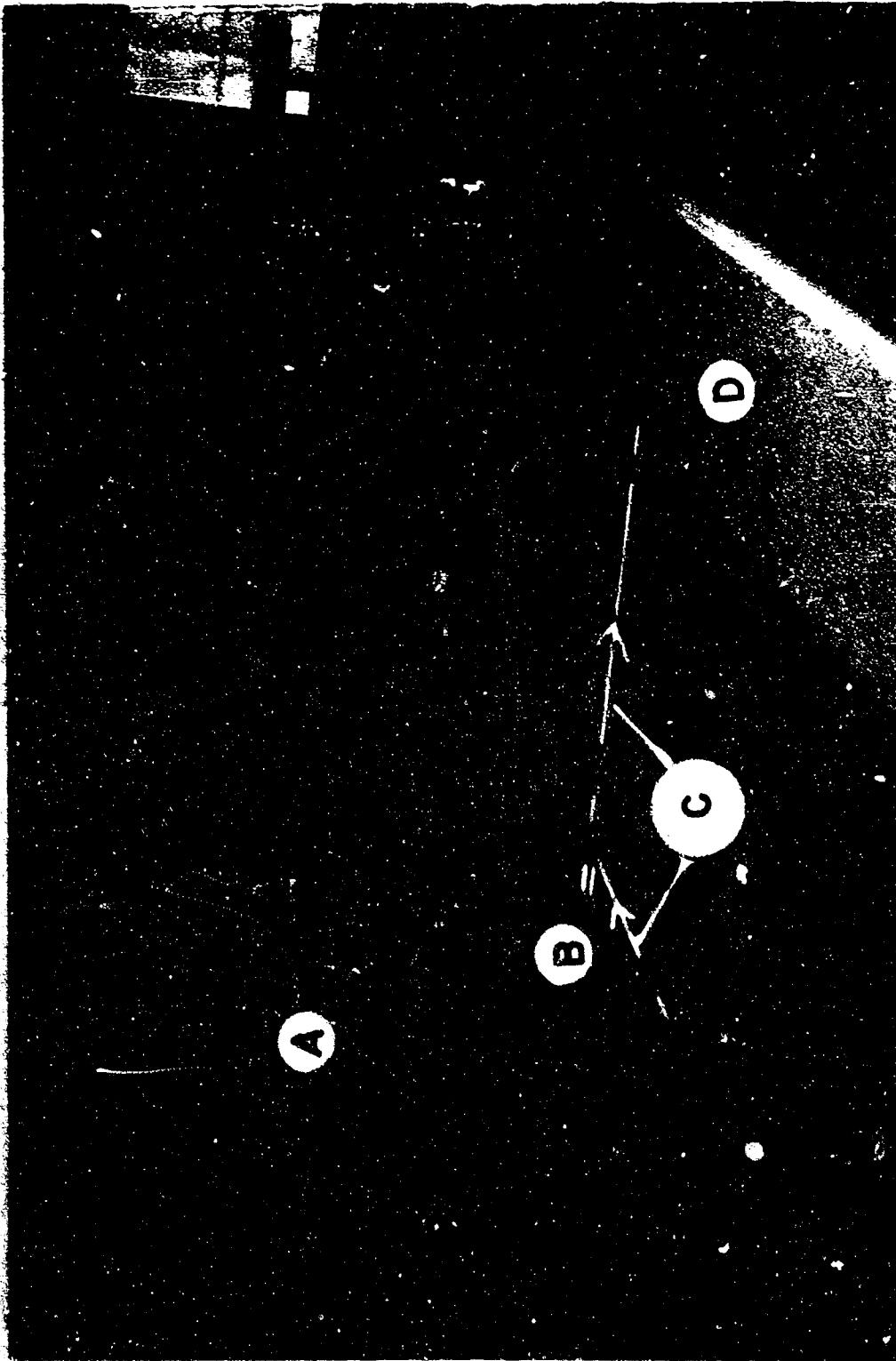
Fig. 2 View of the complete system for reflectivity studies under hydrostatic pressure. A) is the pressure generator, with shield removal, B) Nitrogen Dewar in which test vessel is placed, C) Lightpass, D) Spectrograph.
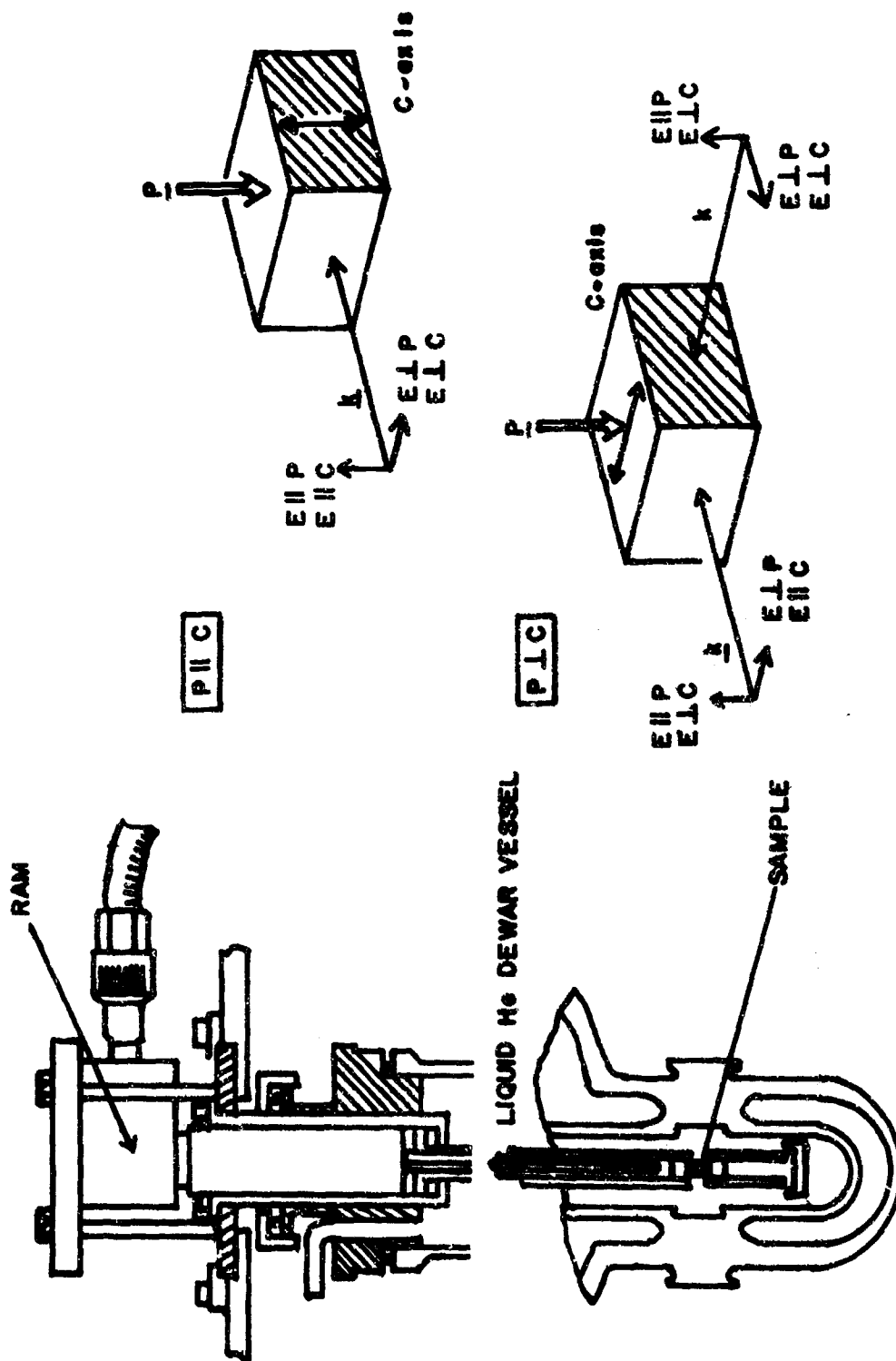
Fig. 3   Schematic of a hydraulic ram type apparatus for applying uniaxial stress to crystals immersed in Liquid Helium. On the right hand side, theoretically significant non-equivalent stress directions for a uniaxial crystal are indicated.
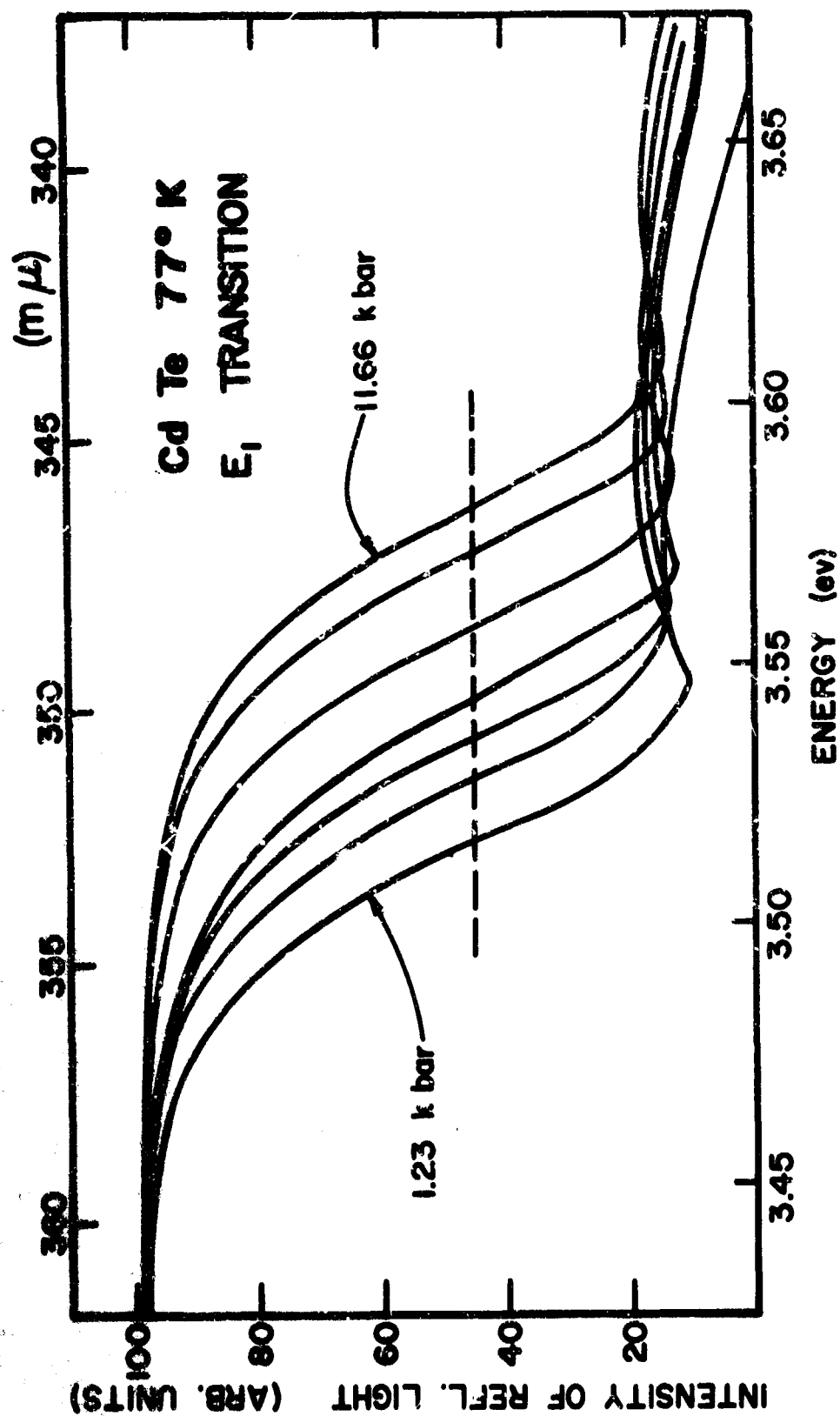
Fig. 4  A typical "reflectivity characteristic" and its dependence on hydrostatic pressure. It corresponds to the $E_1$ transition in Cadmium Telluride.

MOMENTUM

Fig. 5 The Band Structure of Cadmium Telluride as computed by M. Cardona according to the k·p method. Letters designate preferred symmetry points in the momentum space (Brillouin zone). The shaded area is the forbidden gap. The pressure coefficients of the transitions $E_o$, $E_1$ and $E_1 + \Delta_1$ were determined.
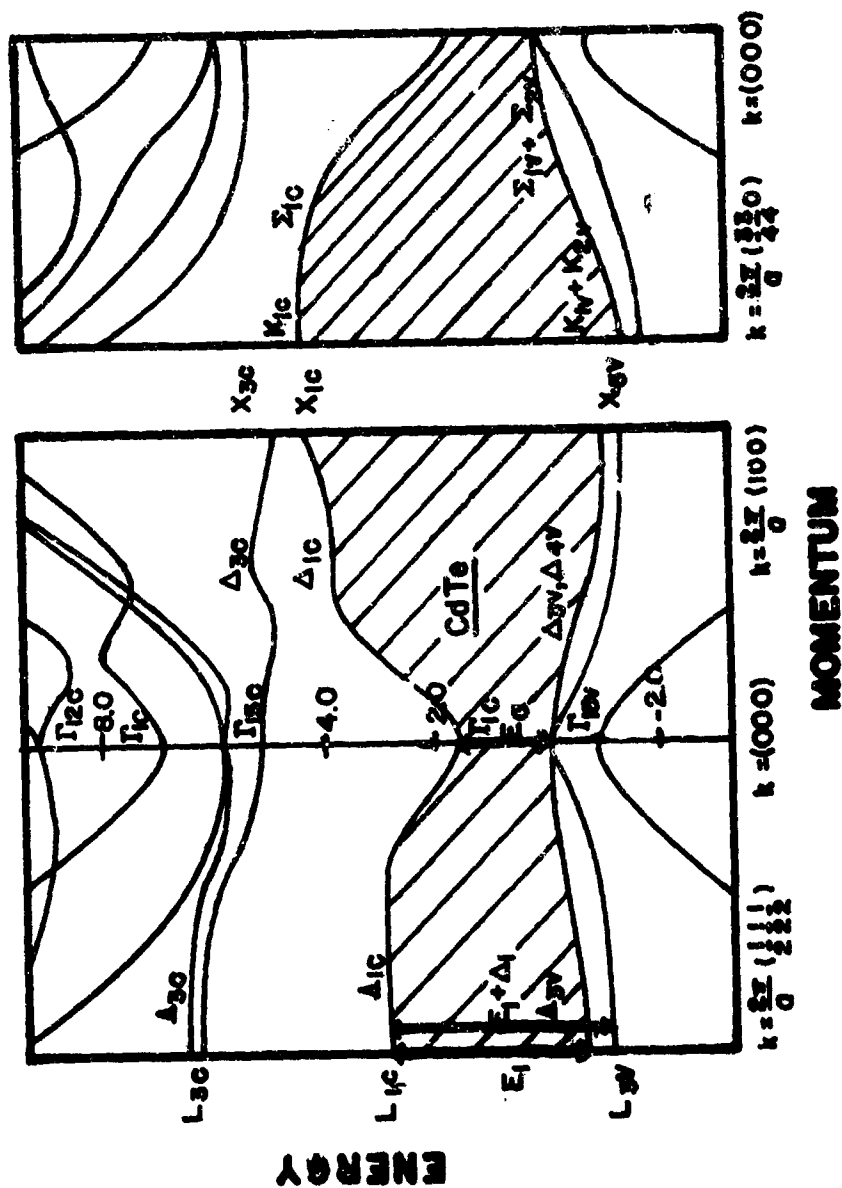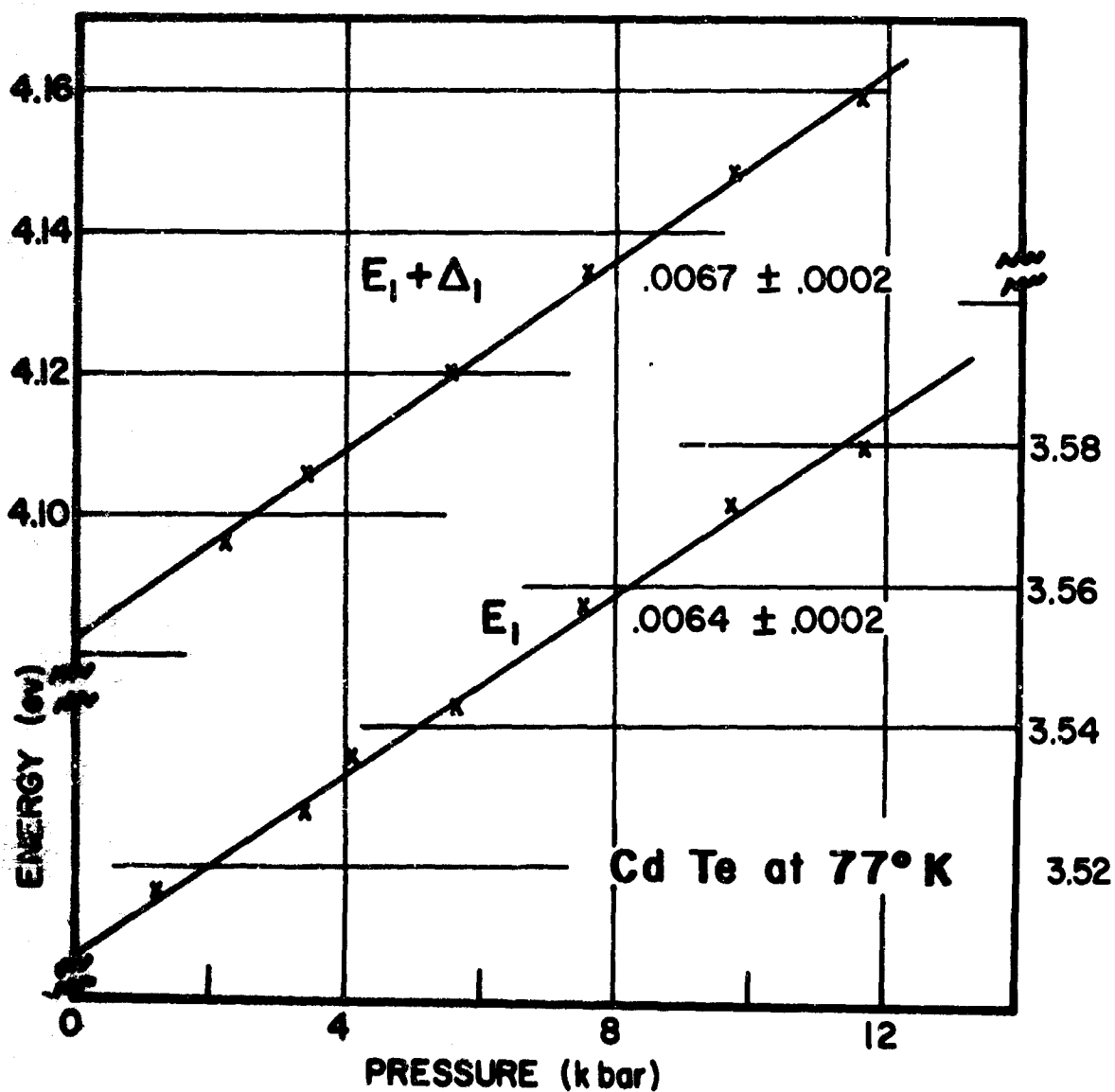
Fig. 6 Plotted are the points of inflection of the set of curves of Fig. 4 and similar ones corresponding to the $E_1 + \Delta_1$ transition in CdTe. The small scatter of points from a straight line is a measure of the accuracy of the linear coefficient.

## Table I

### Pressure coefficients of bandgaps of II-VI compounds

| Compound | Energy gap (eV) | k-point | $(dE/dP)_T$ $(10^{-6} eV/bar)$ |
|----------|-----------------|---------|--------------------------------|
| CdTe     | 1.6             | $\Gamma$ | $8.0 \pm 0.2$                 |
|          | 3.4             | L       | $6.4 \pm 0.3$                  |
|          | 4.0             | L       | $6.7 \pm 0.3$                  |
| ZnTe     | 2.3             | $\Gamma$ | $11.3 \pm 0.2$                |
|          | 3.7             | L       | $5.9 \pm 0.6$                  |
|          | 4.3             | L       | $6.2 \pm 0.6$                  |
| ZnSe     | 2.8             | $\Gamma$ | $10.8 \pm 0.4$                |
| ZnS      | 3.7             | $\Gamma$ | $6.3 \pm 0.2$                  |
| CdS      | 2.6             | $\Gamma$ | $4.5 \pm 0.1$                  |
| ZnO      | 3.4             | $\Gamma$ | $2.7 \pm 0.1$                  |

### b) Crystal field calculations

The conventional crystal field calculations describe the modifications of energy levels of single impurity atoms or ions when surrounded by a crystal matrix. Such calculations usually involve three parameters, B, C and the strength of the crystal field "Dq". Figure 7 shows such a plot for $Cr^{3+}$. The particular value of Dq which is indicated by the dashed line corresponds to the crystal field of Aluminum Oxide ($Al_2O_3$). The intersections of the dashed line with the slanted solid lines represent the energy levels in an $Al_2O_3$:Cr crystal, i.e. ruby crystal. The lowest one, $^2E(G)$, is the familiar upper energy level of the lasing transition. We investigated the shift of the $^4A_2 \rightarrow {}^2E$ transition as a function of hydrostatic pressure and obtained a value of $-0.9 \pm 0.05$ cm$^{-1}$/kbar which means that the lasing line would shift by about 4.3Å or 270 GHz for a pressure of 10 kilobars. In conjunction with the theory and with pressure coefficients for the other transitions previously obtained by other investigators we could derive from four equations for i = 1, 2, 3, 4

$$\frac{\Delta E_i}{\Delta P} = \frac{\partial E_i}{\partial Dq}\bigg|_{theor.} \frac{\Delta Dq}{\Delta P} + \frac{\partial E_i}{\partial B}\bigg|_{theor.} \frac{\Delta B}{\Delta P} + \frac{\partial E_i}{\partial C}\bigg|_{theor.} \frac{\Delta C}{\Delta P}$$
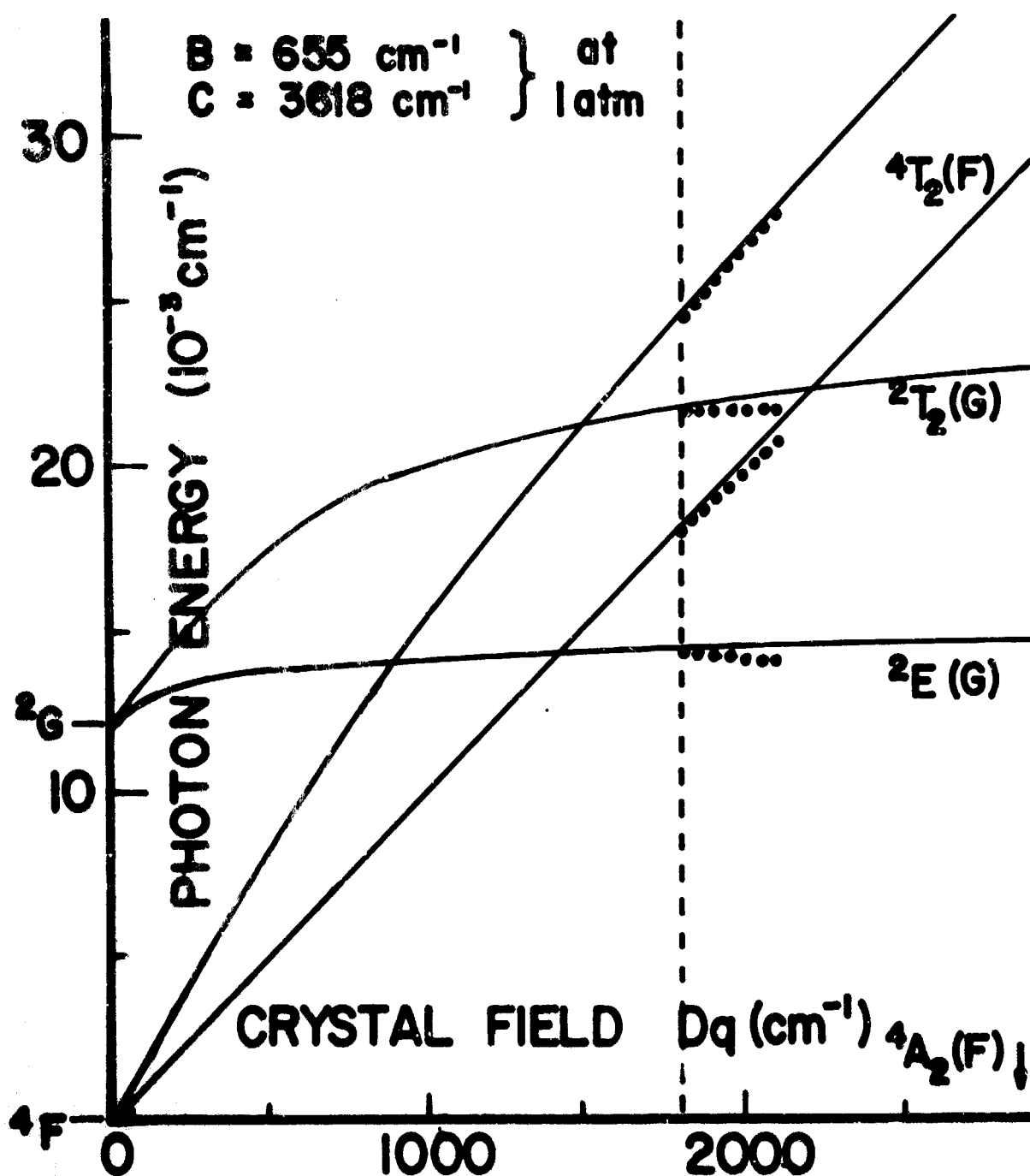
**Fig. 7**  A crystal field plot of $Cr^{3+}$ in an lattice of the $Al_2O_3$ symmetry.  The vertical dashed line corresponds to the exact value of the crystal field in $Al_2O_3$.  The heavy dotted lines indicate the direction of shift of the Cr levels with pressure applied.  The transition from the $^2E$ to the $^4A$ ground state corresponds to the lasing transition in ruby.
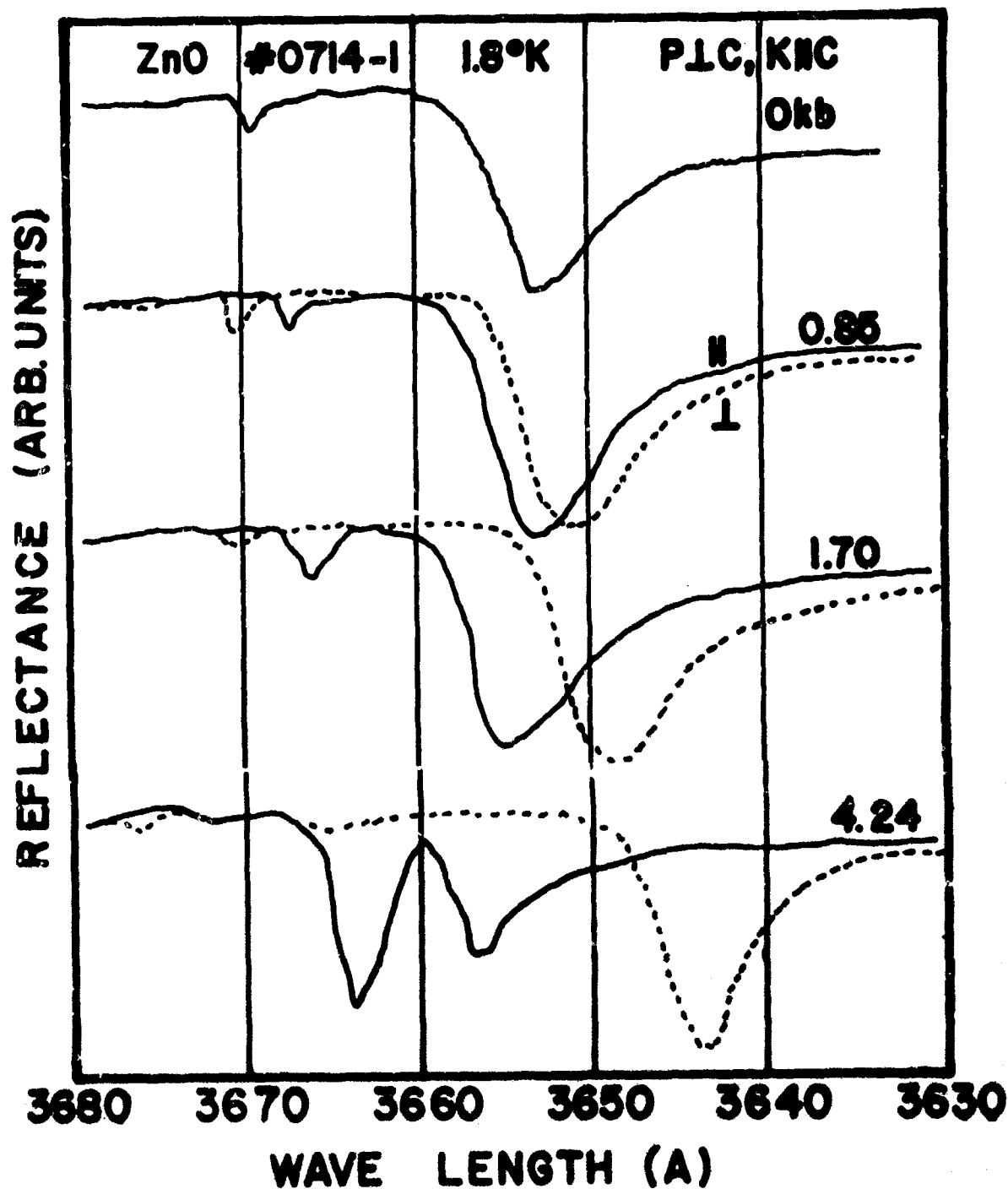
Fig. 8 Variation of the exciton reflection spectra of ZnO under uniaxial stress. Both reflection minima split into two components, completely polarized. The direction of stress is perpendicular to the c-axis of the crystal (P⊥ c) and the direction of lightpropagation is parallel to the c-axis. The splitting is observable only in this configuration.
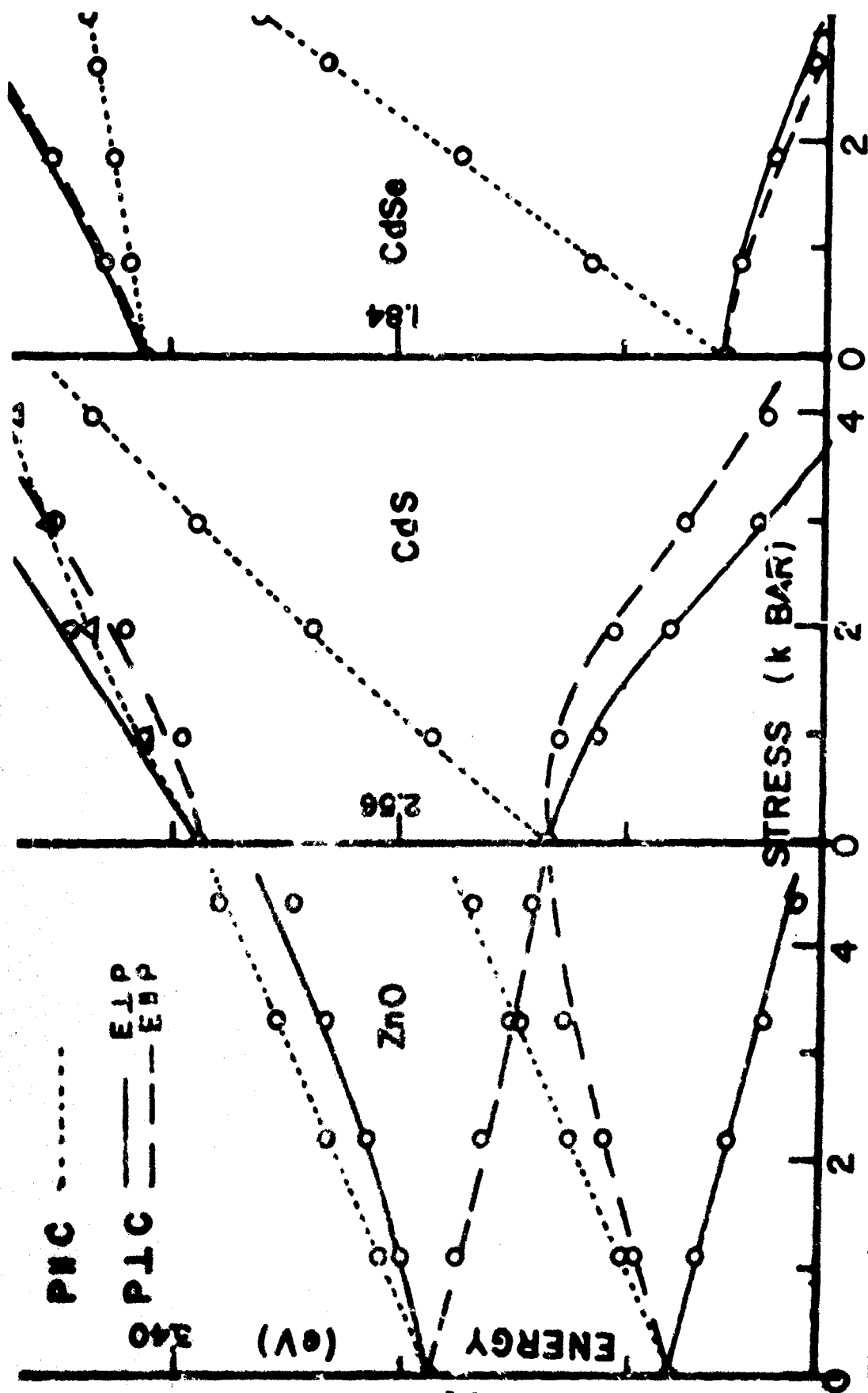
Fig. 9 A comparison of the pressure splittings and shifts of excitons in three similar compounds. The points are fitted to the experimental curves using the deformation potential theory augmented by the spin exchange term.

S-22

# OUTPUT ENERGY DECAY OBSERVATIONS IN RUBY LASERS

By

C. M. Stickley

H. Miller

E. E. Hoell

C. C. Gallagher

R. A. Bradbury

Optical Physics Laboratory
Air Force Cambridge Research Laboratories
Office of Aerospace Research
L. G. Hanscom Field, Bedford, Massachusetts

T-1

# Output Energy Decay Observations in Ruby Lasers

## ABSTRACT

The use of lasers in rangefinding and other applications requires that the laser be capable of being fired many times without its output characteristics changing substantially. We have observed a gradual reduction in ruby ($Cr^{3+}$ in $Al_2O_3$) laser output energy during repeated firing. This reduction is found to occur with varying degrees of severity in all ruby rods tested. We have traced this to the formation of color centers within or on the surface of the ruby rod: defects, impurities, etc., present before exposure can be converted into color centers by the blue and ultraviolet content of the pumplight. Color centers in $Al_2O_3$ have a characteristic absorption vs. wavelength dependence (Levy, 1961); it is on this basis that they were identified. We have shown that the subsequent pumplight absorption by these color centers, which serves to deplete the pumping energy internally in the rod, plus the bulk absorption loss they cause at 6943 Å fully explains the degradation observed to within the limits of experimental error. A reliable indicator of color center formation is the orange-brown appearance which develops in the ruby; only a partial restoration of output energy can be achieved by heating the rods at 900°C for 24 hr, the use of Pyrex to filter the ultraviolet from the pumplight can reduce but not eliminate the rate of energy decay. The principal contribution of this work is that we have determined one mechanism out of five or six which explains the energy decay observed. The complete solution will be known when it is understood how to prevent color center formation in $Al_2O_3$.

T-2

# BIOGRAPHY

Rudolph A. Bradbury attended Harvard University from 1946 to 1949, receiving an A. B. degree in physics. He joined AFCRL in 1951 after working two years with the James Milan Company and received a Master's degree in Electrical Engineering from Northeastern University in 1953. His early work at AFCRL was in the design of transistor circuits. In 1960 he helped construct the first laser at AFCRL and has studied the relationships between material parameters and device specifications since that time.

C. C. Gallagher was born Oct. 2, 1923. His experience previous to The Laser Physics Branch has been in the fields of Ultra High Temperature and Nano-second Non-coherent light sources. A number of papers have been co-authored. He transferred to the Laser Physics group in 1966 where he is engaged in the application of Ultra-High speed pulse techniques to Ruby Lasers.

Edmund E. Hoell was born in Cambridge, Mass. in 1922. Following duty with the U. S. Navy in W. W. 2, he attended Massachusetts Radio School. In 1964 he completed a curriculum in Electronic Engineering Technology at Lowell Technological Institute and received his degree of Associate in Engineering. He has been with AFCRL since 1952 and has worked on data link, scatter, and digital voice communications. He transferred to the Laser Physics Branch in 1962 where he is principally

T-3

engaged in an engineering aide capacity participating in experimental research on lasers and materials.

Harvey Miller joined the Watson Laboratory, the predecessor of the Air Force Cambridge Research Laboratory after service as a navigator and communications officer. He has engaged in the research and development of radar, communications, air traffic control, and digital techniques. He became associated with the Laser Physics Branch in 1963 and has been working in the testing and evaluation of ruby. He has studied at both Mass. State and Northeastern University.

Dr. C. Martin Stickley was born in Washington, D.C. on 30 Oct 1933. He received the E.E. degree from the University of Cincinnati in 1957, the M.S.E.E. from Massachusetts Institute of Technology in 1958, and the Ph.D. in E.E. from Northeastern University in 1964. He joined AFCRL in 1958 at a Lieutenant in the USAF, and was concerned with semiconductor device studies. In 1960 he and Mr. Bradbury started the laser research program at AFCRL. Presently he is Chief of The Laser Physics Branch; he has published numerous articles on laser physics and laser applications.

# 1. INTRODUCTION

In the course of carrying out extensive tests on a number of ruby laser rods of different sizes and origins, we observed that: (a) the energy output of one was considerably less than that of three others similar in size and $Cr^{3+}$ concentration; and (b) the original low threshold energy of two other rods could not be reproduced after they were fired only several times. We have continued the study of this effect because of its obvious importance to all applications of ruby lasers: the maintenance of high energy output. One does not desire to use lasers whose output energy is low or gradually degrades from shot to shot. Examination of the literature showed that Roess (1963) had previously observed this effect in a ruby laser rod which had turned from a reddish-violet color to a "strawberry" color. He commented only that "such a ruby has poorer laser properties than other rubies with the same crystal structure"; his tabulated data shows the threshold energy to be higher for this rod compared to two similar ones. Much more recently Johnson and Grow (1967) reported the results of a study to obtain increased energy output from ruby by prior $\gamma$-irradiation but found instead that the energy output decreased owing to, in their opinion, a reduction in quantum efficiency of the ruby. Also Arkhangelskii et al. (1967) have reported a study of color centers in ruby rods taken from one ruby boule. They observed a threshold increase of 14 percent for one rod along with an increase in absorption in the region of the pumping bands of the sample.

The aim of this paper is to expand upon Roess' observations (1963) by showing that the effects which we have referred to here can be quantitatively accounted for by the gradual development, with firing of the laser, of undesired bulk and surface absorption. We have observed this absorption, and therefore a color change, to varying degrees in all ruby rods tested, and hold that it indicates the presence of color centers that have been filled by the pumplight. This conclusion is based primarily on the fact that the additional absorption as a function of wavelength which develops in the ruby ($Cr_2O_3$ in $Al_2O_3$) agrees with that found by Levy (1961) who studied $\gamma$-irradiation of undoped $\alpha$-$Al_2O_3$. These color centers serve as useless absorbers of pumplight (which reduces the actual pump rate internally in the laser rod) and the laser radiation at 6943 Å, and cause its energy output to drop as color centers are formed. The variation in energy output degradation from sample to sample, the presence of impurities in large quantities, the lack of appreciable conversion of $Cr^{3+}$ to other valence states, and the close similarity of the absorption we have observed with that measured by Levy on undoped $\alpha$-$Al_2O_3$, all suggest that color center formation in the samples we have studied are primarily controlled not by a process which would be common to all ruby rods as suggested by Maruyama and Matsuda (1964), Schultz (1964), and Arkhangelskii, et al. (1967), but by defects and impurities which develop or are implanted during crystal growth. The processes suggested by Arkhangelskii, et al. (1967), Maruyama and Matsuda (1964), and Schultz (1964) might ultimately be applicable in causing energy degradation in the limit of no defects or impurities (of the type which can lead to color center formation) being present in or on the surface of the rod since all ruby rods so far have been

found to have useful life of no more than several hundred thousand shots (Dornitzer, 1966). However, this limited life may well be due to surface contamination occurring during cleaning of the rods rather than by conversion of $Cr^{3+}$ conversion to other valence states.

Section 2 describes the experimental setup for making most of the energy degradation measurements. Section 3 lists the possible mechanisms that could lead to an energy output decay, whereas Section 4 contains a discussion of each, as well as experiments and calculations performed for selection of the ones felt to be responsible for the degradation. Section 5 discusses whether the bulk absorption found is to be attributed to $Cr^{2+}$ or $Cr^{4+}$ or color centers associated with defects and impurities in the ruby; Section 6 states the conclusions of this work.

## 2. LASER ENERGY MEASUREMENT SETUP

Figure 1 is representative of the setup used to irradiate the rods as well as measure the delay to oscillation, the duration of oscillation, and the output energy. The spectral distribution of the pumplight incident on the ruby rods was measured in the 2000 to 4000 Å wavelength region using a calibrated EG&G Model 580/585 Spectroradiometer. In going from 4000 Å to 2000 Å a linear (to within 4 percent) decrease by a factor of 8 units of watts/cm² (unit wavelength) was observed; no Pyrex glass was used between the lamp and the ruby rod. The radiometer was removed to permit alignment of the system with the 6328 Å gas laser and then replaced. A concave mirror and resonant reflector formed the resonant cavity; these were chosen to minimize mechanical instabilities and to reduce the number of dielectric mirror surfaces in the system. For this same reason the rods were not antireflection coated. The mirrors used never had to be re-coated even though they were exposed to tens of thousands of long-pulse laser bursts of several joules per cm² per firing. The flashlamps were changed several times during the course of this work; owing to these changes, as well as occasional mechanical redesign changes of the laser head, the eventual energy decay figures accepted as factual (see Table 1) were obtained by comparing the energy output before to that obtained after annealing the rods. With this technique, the effects of any long term changes in the laser test system were nullified. Cooling was accomplished by Variac control of the power flow into a resistor located in the bottom of a nitrogen dewar; the cooling rate was set so that the laser was fired (about every 1.25 min) when the thermocouple indicated room temperature. An Alzak aluminum pumplight reflector wrapped around the helical flashtube was used initially; after problems with reflectance decay and system contamination, a quartz clamshell-like structure filled with packed MgO powder was substituted for the aluminum reflector. This improved the long term stability of the system considerably. Finally, a four-place digital voltmeter was used across the capacitor bank to monitor accurately the stored energy in the power supply.

## 3. POSSIBLE MECHANISMS LEADING TO OUTPUT ENERGY DECAY

The dependence of the energy output of a ruby laser can be written as

$$E_{out} = N_o h\nu V_{las}(t_{pump} - t_{th}) \left[ \frac{WN_1(t_{th})}{N_o} - \frac{N_2(t_{th})}{\tau N_o} \right] \left[ \frac{|\ln r_1 r_2|}{|\ln r_1 r_2| + 2\beta L} \right],$$

(1)

where

$N_o$    =  $Cr^{3+}$ density in atoms/$cm^3$,

$h\nu$    =  energy of the 6943 Å laser transition, $^2E$ ($\bar{E}$) to $^4A_2$ ground state (the $R_1$ line),

$V_{las}$    =  lasing volume of the ruby rod,

$t_{pump}$    =  duration of pumping pulse,

$t_{th}$    =  delay time to threshold measured from the beginning of the pumping pulse,

$\tau$    =  lifetime of the $R_1$ line,

$N_2$    =  population of the $R_1$, $R_2$, and all higher lying levels, $cm^{-3}$,

$N_1$    =  $N_o - N_2$ = ground state population, $cm^{-3}$

      =  $\dfrac{N_o}{2}\left[ 1 - \dfrac{\beta}{\alpha} - \dfrac{|\ln r_1 r_2|}{2\alpha L} \right]$ at threshold,

$\beta$    =  scatter loss coefficient, $cm^{-1}$,

$\alpha$    =  $R_1$ line absorption coefficient, $cm^{-1}$,

$r_1, r_2$    =  reflectivities of the two mirrors,

$L$    =  length of the laser rod, cm,

$W$    =  actual pump rate within laser rod

      =  $T\eta \dfrac{\bar{\sigma}_\rho \bar{\Delta}_\rho c\overline{\rho(\nu)}}{h\bar{\nu}_\rho n}$,

$\bar{\sigma}_\rho$    =  average pump band cross section, $cm^2$,

$\Delta\bar{\nu}_\rho$    =  average pump band width, Hz,

$h\bar{\nu}_p$    =    average energy of the pump band above ground state,

$c/n$    =    speed of light in the medium,

$\bar{p}(\nu)$    =    average pump power density incident on the rod,

$T$    =    transmission of pump light through rod exclusive of normal transmission losses of pumplight due to pump band absorption

$\eta$    =    efficiency of electron transfer from the pump bands to the R levels.

From this array of parameters upon which the output energy is dependent, eight factors could explain the energy decay: (1) a change in the lasing duration (Siegman and Allen, 1965) $(t_{pump} - t_{th})$; (2) a change in the volume of the rod $V_{las}$ in which laser action is occurring; (3) a decrease in the lifetime $\tau$ as a result of an increase in the nonradiative transition rate from the R lines back to the ground state; (4) a decrease in the average pump power density $\bar{p}(\nu)$ arriving at the rod; (5) a reduction in the density of $Cr^{3+}$ ions $N_0$ by loss of electrons into traps or conversion into other valence states; (6) a reduction in the transfer efficiency $\eta$ resulting from the presence of neighboring impurities or defects which serve to ground state; (7) the development of a competitive absorption mechanism which can reduce the effective pumping rate internally in the rod -- this could be accounted for numerically by a decrease in T away from unity; and (8) an increase in the loss coefficient, $\beta$, either by an increase in internal crystal damage due to the radiation flux (Flowers and Jenney, 1963) or by the development of a bulk absorption at 6943 Å.

## 4. SUMMARY OF EXPERIMENTAL OBSERVATIONS AND INTERPRETATION OF DATA

### 4.1 Explanation of Groupings in Table 1

Table 1 summarizes a large number of the experimental observations. The rods in group I are all about 0.635 cm diameter X 2.6 cm long, of excellent optical quality (one fringe or less in the central region), and of significantly different origins. . The rods in group II are all about 0.635 cm diameter by 2.54 cm long and cut from the same boule. The rods in the remaining groups are all 0.95 cm diameter and 7.5 cm long. The energy output of the group III rods decayed measurably, whereas for the group IV rods only slight (10 to 20 percent) and seemingly nonreproducible decays were seen. Group V rods are those grown more recently by Linde which are core-free. Experiments summarized in groups Vb and VI were carried out by exposing the samples to UV radiation for 2.5 h from an AH-6 Hg lamp.

It should be noted that energy decay was observed to varying degrees in all samples studied independent of their growth method or location. Discussion of these results will be organized primarily by discussing each of the possible mechanisms listed in the foregoing which could produce energy degradation.

## 4.2 Mechanisms Found Not Responsible for Energy Decay

Mechanism (1), a change in the lasing duration, has been observed by Siegman and Allen (1965). It is attributed to the excitation of internally trapped modes in rods having polished sides and attached mirrors; this effect goes away if the rod sides are roughened. For the case of these experiments, all rods had rough sides, and no effect such as those observed by Siegman and Allen were seen. (It should be noted that a decrease in lasing duration due to an increase in threshold will be observed if a constant pump energy is used and some of the following effects develop. This will be a secondary effect which can be taken into account by calculating the average power produced by the laser rather than discussing simply the energy output.)

Mechanism (2), a change in the lasing volume, was examined by taking streak photographs of the near field of group II rods 87 and 106. The lasing diameter was in each case about 0.6 of the rod diameter, in agreement with theory for roughened side walls (Jerrick, to be published).

Mechanism (3), a decrease in the life time $\tau$, was studied by crowbaring the power supply at the end of the pump pulse. This was done for the group I rods before they were annealed. No departure from the value 3 milliseconds was found.

Mechanism (4), a decrease in the lamp output, did occur to some degree in the course of the work. However, most of the energy degradation values quoted were determined by the following methods: (a) by annealing the rods and then measuring the increase in output (group I); (b) by comparing the output with a relatively unfired rod originating from the same boule and cut to the same size and orientation (group II); or (c) by noting the energy decay after illumination with radiation from a mercury lamp (groups Vb and VI). All of these changes would be independent of flash-lamp decay over a long period; thus it is reasonable to discount this as the reason for the decay seen in the groups III and IV rods.

Mechanism (5), a decrease in the $Cr^{3+}$ density, was investigated by measuring the absorption of the ruby samples at 6943 Å with respect to the background transmission before and after firing with a Bausch and Lomb Spectronic 505 Spectrophotometer. As indicated in column IX no definite changes were seen for any of the rods investigated using this measurement technique; the measurement was reproducible to about $\pm 1$ percent corresponding to an uncertainty in $N_0$ of about $\pm 2 \times 10^{17}$ cm$^{-3}$ for the rods in groups I and II. For rod 87 of group II (and rod 86, a mate to it) no large changes in $R_1$ line absorption were seen after annealing at 900°C for 8 hr

in air. Since significant longitudinal $Cr^{3+}$ concentration gradients are known to exist in early Linde Czochralski ruby boules, it is felt that the larger differences in $R_1$ line absorption in the group II rods did not arise from radiation-induced changes but existed prior to rod firing. Measurements made, however, of $E \perp c$ absorption changes at 5600 Å on rod 86 and sample 73 indicate that perhaps a decrease in $Cr^{3+}$ concentration of $2.7 \times 10^{17}$ cm$^{-3}$ did occur (see Section 5) during the flashlamp irradiation (this number is close to the limit of reproducibility of the $R_1$ line absorption measurement and, thus, is felt to be reasonably consistent with it). This represents at the most a reduction in density of only 3 percent of the $Cr^{3+}$ ions and as such, only a small effect, which would not account directly for the degradation seen. However, if these lost electrons from $Cr^{3+}$ ions are converted to absorbing centers having large absorption cross sections, this could be a mechanism that could account for the energy degradation. This will be discussed more fully in Section 5.

Mechanism (6), a decrease in the transfer efficiency, has been suggested by Johnson and Grow (1967) as a possible way to account for the decrease in energy output. Their mechanism requires that electrons associated with $Cr^{3+}$ which are raised to the pump bands by absorption of a pump photon relax into long lived traps rather than to the $^2E$ levels. We suggest that this is unlikely since the transition rate between the pump bands and the $^2E$ levels is fast, being in the neighborhood of $2 \times 10^8$/sec. A more likely mechanism is excitation of electrons from the $^2E$ levels to the conduction band whereupon they are lost in traps. However, the relaxation time out of these traps would have to be less than two min, no absorption change being visible at 6943 Å (two min is the elapsed time in our procedure of measuring the 6943 Å absorption relative to the background transmission as soon as possible after firing the laser rod). In summary, although we cannot positively rule out the possibility that electrons are being lost to traps for perhaps several minutes or less, it seems that all of the energy decays we have seen, with exception of the experimental result summarized in group Vb of Table 1, can be explained by the mechanisms in the following section.

## 4.3 Mechanisms Found Responsible for Energy Decay

### 4.3.1 Bulk Absorption Between 3500-6500 Å

Mechanism (7) is the possibility of development of a competitive bulk absorption mechanism in the same wavelength range as the pump bands of ruby which would reduce the effective pumping rate within the rod. By comparing the transmissions of about identical rods (groups II, III, and IV) or the same rod before and after annealing (groups I, V, and VI) in the neighborhood of 4800 Å (a transmission band of ruby) such absorption was detected. The values found are listed in columns X and XI of Table 1, and the spectral dependence of the induced absorption plotted in Figure 2. Calculations illustrating its effect on the output energy will be given, and the nature of it will be discussed in Section 5.

### 4.3.2 Bulk Absorption at 6943 Å

During the course of this work two methods evolved to determine if mechanism (8), an increase in the loss coefficient $\beta$, could be contributing to the decay observed. Initially, when energy decay and an increase in threshold was observed the fluorescence energy at the threshold voltage (measured with one mirror blocked) was found to be constant, that is, independent of threshold voltage. This procedure was used for the rods in groups III through VIa and would indicate that no increase in $\beta$ was occurring within the sensitivity of the measurement (see column VIII, Table 1; for the group II rods the numbers in this column have large uncertainties due to $Cr^{3+}$ differences making this technique useless for determination of whether a $\beta$ increase occurred for them).

Subsequently, however, background transmission changes at 6943 Å after annealing were detected and directly measured using the Bausch and Lomb Spectrophotometer (see Figure 2). Thus the bulk absorption that develops in the rod upon repeated firing can extend as far into the red as 6943 Å; a detailed calculation performed in the following section will show that even such low absorptions can contribute significantly to an energy output reduction.

### 4.3.3 Sample Calculations of Output Power Decay

To determine if the bulk absorption in the pump band region and at 6943 Å could explain the energy degradation, series of experiments were performed on rod 86, a rod almost identical in size, doping, and state of energy decay to rod 87. These experiments consisted in a series of treatments of the rod interspersed with transmission and energy output measurements to determine what effects the various cleaning and heating steps had on its energy output recovery. These are summarized in Table 2. Note that changes in output energy occurred only when the rod was immersed for 2 hr in boiling nitric acid, chromic acid, and when annealed at 900°C for 24 hr. Since the bulk transmission T and 6943 Å absorption $\beta$ changed only during the annealing treatment, we assume that the output energy increase subsequently observed is to be attributed almost wholly to changes in these factors.

To verify this, a computer program for determining absorbed pump power vs. radius, doping concentration, and diameter in ruby rods with rough sidewalls (Jerrick, to be published) was modified so that the reduction in the absorbed pump power could be computed in the presence of a competing and noninteracting absorption mechanism having the characteristics shown in Figure 2. Calculations were carried out for $R_0 = 0.3$ cm, $F = 0.03$ percent (rod 86), and $R_0 = 0.476$ cm and $F = 0.05$ percent (rod 520) as shown in Figure 3; the ordinate scale is absorption rate of pump energy and equivalent in our terminology to the product $WN_1$; the abscissa is the radial variable $\rho$ normalized to the rod radius R. The light scattering characteristics of the rough sidewalls were assumed to be composed of two factors: 50 percent of the pump flux would be transmitted

according to the laws of reflection and refraction at a polished surface and 50 percent according to those for a Lambertian scattering surface. The spectral distribution of the lamp was taken to be that used by Cooke, McKenna and Skinner (1964); the absorption cross section of the ruby was taken to be an average of those values reported by Dodd, Wood, and Barns (1964), and Cronemeyer (1966). From Figure 3 the expected increase in the product $WN_1$ for rod 86 after annealing is 1.11.

To calculate the change in output energy or power from Eq. (1), it is necessary to determine values for $W$ and $N_1$. The fractional population $n_2 (= N_2/N_0)$ in the $R_1$ level at threshold can be written as

$$n_2 = \frac{1}{2} + \frac{\beta}{2\alpha} + \frac{|\ln r_1 r_2|}{4\alpha L} . \tag{2}$$

For a small diameter, lightly doped ruby rod which is approximately optically thin to the pump radiation, the increase with time of $n_2$ can be described (Sooy, Congleton, Dobratz, and Ng, 1964) as

$$n_2(t) = \left(\frac{W\tau}{W\tau + 1}\right) \left(1 - e^{-(W\tau + 1)t/\tau}\right). \tag{3}$$

Equations (2) and (3) can be equated at $t = t_{th}$ and $W$ can be determined. Knowing $W$, one observes that the fractional ground state population $n_1$ can be determined from Eq. (3) since $n_1 = 1 - n_2$. The expected output power can then be computed from Eq. (1), or the change in output power can be written as

$$\frac{P_{oa}}{P_{ob}} = \frac{E_{oa}/(t_{pump} - t_{tha})}{E_{ob}/(t_{pump} - t_{thb})} = \frac{\left[(W_a\tau + 1)n_{1a} - 1\right]\left[|\ln r_1 r_2| + 2\beta_b L\right]}{\left[(W_b\tau + 1)n_{1b} - 1\right]\left[|\ln r_1 r_2| + 2\beta_a L\right]} . \tag{4}$$

where the "b" and "a" subscripts denote before and after a treatment, such as annealing or UV exposure, which changes the energy output of the rod.

For rod 86, $\alpha = 0.164$ cm$^{-1}$, $L = 2.215$ cm, $r_1 r_2 = 0.92$ (allowance was made here for the resonance between the uncoated end of the rod and the transmitting flat mirror aligned parallel to it); $\beta_a = 0.007$ cm$^{-1}$, determined by the change in rod threshold as a function of temperature (Collins and Nelson, 1963) over the range 296° to 120°K on a similar piece of Czochralski ruby and $\beta_b = 0.007 + (0.006 + 0.003)$cm$^{-1}$ where the increase in $\beta_b$ over $\beta_a$ is taken from the data of Figure 2. The uncertainty in $\beta_b$ is due to the lack of repeatability of the transmission measurement of $\pm 0.5$ percent. Here "a" and "b" denote after and before annealing, respectively.

Table 3 summarizes the laser observations and associated calculations for rod 86. The uncertainty in the observed output powers $P_o$ stems from the lack of a constant pump power over the time $(t_{pump} - t_{th})$. The remainder of the uncertainties originate from the uncertainty in $\beta_b$. In the calculations, method A refers to the procedure outlined, that is,

knowing $t_{th}$, $\beta_a$, $\beta_b$ and the other constants, one can compute $W\tau$, $n_2$, and $P_o$ from Eqs. (1) to (3). Method B uses the computer results shown in Figure 3 to deduce the new pump absorption rate "after annealing" relative to the value calculated by method A for the "before annealing" data. Method B, then, is the one which really tests the deduction that bulk absorption is altering pump rate; both methods test the deduction that bulk absorption at 6943 Å is present before annealing in the amount of $0.006 \pm 0.003$ cm$^{-1}$ for this rod. Note that the absolute values of the observed and calculated output powers do not agree. This is felt to be attributable to the assumption in Eq. (1) that uniformly intense plane waves are depleting the population inversion. In fact (Stickley, 1964), the modes are the multihumped wavefronts characterized by Hermite -- or Laguerre -- Gaussian functions which could lead to incomplete consumption of the population inversion (the unaccounted for power would be lost as fluorescence) and a reduced output power. More applicable, then, is a comparison between the ratios of the observed and calculated output powers. Since the uncertainty in the ratio calculated by method B falls within that of the observed ratio, it is concluded that undesired bulk absorption in the region of the pump bands and 6943 Å can account for the energy degradation in rod 86.

A similar calculation can be made for rod 520 in the experiment summarized in group VI. The pump rate W cannot be calculated exactly since the time-to-threshold is not known. However, Eq. (4) is not very sensitive to it if $W\tau \gg 1$. Since before UV exposure, $E_{ob}$ was about 0.5 joule (for this case b denotes before UV exposure), it is reasonable to assume $W_b\tau \approx 8$, a number which is consistent with other observations and calculations made as outlined and for rods of this diameter. Next, the ratio $W_b N_{1b}/W_a N_{1a}$ could be taken directly from Figure 3. However, that computation used the bulk absorption shown in Figure 2 for rod 86 rather than the lesser amount of absorption which was actually induced in rod 520. To correct this, it is assumed that the above ratio can be linearly reduced by the ratio of the $\Delta\alpha(4800)$ of rod 520 to $\Delta\alpha(4800)$ of rod 86. Also, we assume that the relative duration of laser oscillation of after exposure to before exposure to be 0.95, that $\beta_b = 0.005$ cm$^{-1}$ (a measured value for rod 574 which is similar to rod 520) and that $\beta_a = (0.005 + 0.002)$ cm$^{-1}$ based on the absorption increase seen in rod 521 (a mate to rod 520) after UV exposure. Knowing that $\alpha = 0.20$ and $r_1 r_2 = 0.80$ and carrying through the calculation of method B using Eqs. (2) to (4) we obtain $E_{oa}/E_{ob} = 0.815$ compared to the observed value of $0.79 \pm 0.06$ from Table I.

Similar calculations have not been made for all the other rods, but it is believed that bulk absorption in the region of the pump bands and at 6943 plus surface absorption (discussed in Section 4.3.4) can explain the results with the exception of the one experiment on rod 521 (group Vb); this will be discussed in Section 4.4.

### 4.3.4 Surface Absorption Between 3500 and 6500 Å

It is evident from examination of Table 1 that there are cases where
the color change (column XII) and induced absorption in the center of the
rod (column X) are not well correlated with the energy decay. For rod
99 (group III) it was observed that there was a radial dependence of the
absorption as determined using a 1-mm diameter argon laser beam.
This suggested the possibility that a non-negligible amount of absorption
was occurring immediately at or near the surface of the rough-sided rods
which would not show up with the standard measurement technique for de-
termination of induced absorption. Another factor which gave credence to
this possibility was that rod 87 of group II did not expand at a greater rate
when pumped through a quartz filter compared with the thermal expansion
observed using a Pyrex filter; the other rods in groups I and II did so to
varying degrees. A possible explanation for this observation follows: If
it is assumed that the surface of rod 87 was absorbing so strongly in the
UV (and presumably, then, the visible spectrum) the additional UV which
would be passed by the quartz filter could not get into the center of the
rod to heat it during the time duration (1 millisecond) of both the pump
flash and the measurement.

Furthermore, if strong surface absorption existed, the color change
seen in the rods when viewed from the side might be only a surface rather
than a bulk effect; this would explain the poor correlation between columns
X and XII of Table 1. To test this hypothesis, an outer layer 0.5 mm
thick was ground off the surface of rod 99. The subsequent measurement
of its output energy showed a twentyfold increase along with a drop in its
threshold energy back to the neighborhood of its original value. This
demonstrated conclusively that surface absorption was playing a major
role in some rods in cav ng energy degradation. Also rod 99 after
grinding had an almost pinkish appearance typical of most new ruby; the
small residual orange appearance is explained by the bulk absorption that
still existed in the rod. A third factor that can lead to energy output
degradation must now be stipulated: Much discoloration of various rods
can be explained by changes in surface transmission and reflection rather
than by changes in bulk properties. It is not known what impurities were
introduced onto the surface during the cleaning process normally used
(washing in alconox detergent and hot water with a final cleaning with
ethyl acetate) and which would cause the browning observed.

### 4.4 Further Experimental Observations

The results of testing rod 521 after 2 hr exposure to the light from an
air-cooled AH-6 Hg lamp is summarized in row Vb of Table 1; the rod
was placed 2.5 cm from the lamp. The energy output degradation to 0.35
of the initial value was not expected based on the following three observa-
tions: (a) the flashlamp irradiation tests of rod 521 summarized in row
Va; (b) the performance of rod 520 (row VI) in a similar test at Linde (it
is not known how close rod 520 was to the lamp, however); and (c) the

calculated decay based on the amount of bulk absorption that developed (see column XI). Prior to the UV exposure it was observed that no more than forty flashlamp firings of rod 521 could induce the amount of bulk absorption shown at column X, row Va; rod 86 plus a Verneuil rod not listed on Table 1 showed little, if any, effect of an identical amount of exposure to the Hg lamp radiation. Furthermore, upon annealing in air at 925°C for 24 hr no recovery of the energy output occurred, even though its color became pink and the absorption at 4800 Å dropped to a normal value for annealed ruby. This has never been observed with other rods. A small increase in bulk absorption (0.003 cm$^{-1}$) at 7000 Å was observed after the annealing treatment, although not large enough to account for the lack of rise in the output energy.

Filtering the pumplight through Pyrex for rod 99 (group III), which decayed owing to the development of surface rather than bulk absorption, did not slow down the rate of decay. Schultz (1967) reported that Pyrex filtering of Hg lamp radiation will prevent browning from developing, and that this will prevent output energy decay. Dormitzer (1968) reported that Pyrex filtering also helps to slow down energy decay although not preventing it entirely; it simply extends the useful life of the rods. Our own observations and those of Dormitzer (1968) are that no amount of annealing (at temperatures of 1000°C or less) will fully restore a degraded rod to the same condition as new. Heating for 48 instead of 24 hr at 900°C in air will still bring about an improvement in performance, however. Arkhangelskii, et al. (1967), Maruyama and Matsuda (1964), and Schultz (1964) indicate that annealing at 300°C causes recovery of the pink coloration of ruby. Johnson and Grow (1967) reported that glow curve maxima are reached near 300°K but that the samples must be heated to 800°C to remove all the traps produced by $\gamma$-irradiation. Hunt and Schuler (1953) reported seeing pinkish thermoluminescence at 500°C and that if heated to 1000°C the samples looked identical to those unexposed. Our tests of rod 86 (see Table 2) showed that heating in air at 450°C had no effect. Thus it is likely that the temperature at which appreciable revitalization occurs, as well as to what extent Pyrex will prevent browning from developing, will depend upon the nature of the impurities present in the particular ruby sample.

## 5. NATURE OF THE BULK ABSORPTION

Figure 2 contains plots of induced absorption vs. wavelength for rods 86 and 521, and for a 3 mm thick sample of rod 73, the same larger rod from which rod 87 (a mate to rod 86) was cut. The data for rod 86 and sample 73 were obtained by comparing the absorption vs. wavelength before and after the specimens were annealed at 900°C for 24 hr in air. The data for rod 521 and Levy's (1961) data were obtained by comparing the absorption vs. wavelength before and after the specimens were exposed to AH-6 Hg lamp radiation and $\gamma$-radiation, respectively. Levy's data were normalized to 0.225 cm$^{-1}$ at 4000 Å, for purposes of comparison with the curves for rod 86 and sample 73.

The absorption induced in the sample $\Delta\alpha(\lambda)$ upon irradiation is given by

$$\Delta\alpha(\lambda) = \sigma'(\lambda)N'(\lambda) - \sigma_0(\lambda)\Delta N_0(\lambda) \, ,$$

where $\sigma'(\lambda)$ and $\sigma_0$ and $(\lambda)$ are the absorption cross sections for induced bulk and the $Cr^{3+}$ ground state absorptions, respectively. $N'(\lambda)$ is the density of induced absorbing centers, and $\Delta N_0(\lambda)$ the change in the $Cr^{3+}$ ion density upon irradiation and is positive in sign. Since "holes are eaten out of" the $\Delta\alpha(\lambda)$ curves for the ruby samples in the wavelength regions of maximum ground state absorption of ruby (this is particularly evident at 5600 Å for all samples and at 4100 Å for rod 521 and sample 73; the uncertainty in the values for rod 86 at 4100 Å may have smeared this out), it is likely that some $Cr^{3+}$ was converted to other valence states. An estimate from Figure 2 at 5600 Å of the extent of this gives $\sigma_0(\lambda)\Delta N \simeq 0.04$ $cm^{-1}$ for both sample 73 and rod 86. Using $\sigma_0(\lambda) = 1.47 \times 10^{-19}$ $cm^2$ for $E\perp c$ at 5600 Å (Dodd, Wood, and Barns, 1964) gives $\Delta N_0 \approx 2.7 \times 10^{17}$ $cm^{-3}$ corresponding to a change in $Cr^{3+}$ ion density of about 3 percent; this is similar to the observations of Arkhangelskii, et al. (1967) who saw a density decrease of 2 to 6 percent resulting from optical pumping. Maruyama and Matsuda (1964) reported observing a 52 percent decrease upon $\gamma$-irradiating a sample until the induced absorption saturated.

Since this is good evidence that some $Cr^{3+}$ ions lose electrons, is the absorption in Figure 2 characteristic of other valence states of chromium? In our opinion, it is not, for the reasons which follow.

A study of the literature has shown the type of absorption in Figure 2 to be somewhat similar to what other investigators have found and very similar in some cases. The curves which appear to fit the data for rod 86 very well are from the work of Hunt and Schuler (1953) and Levy (1961). Hunt and Schuler were the first to observe this type of absorption in $\alpha$-$Al_2O_3$; they irradiated thin samples of Linde Verneuil sapphire with x- and $\gamma$-irradiation. The absorption saturated at a value of 0.37 $cm^{-1}$ and peaked at about 4050 Å. They also observed a much stronger band at 2300 Å. Levy's results for $\gamma$-irradiation of Linde Verneuil sapphire, which are very similar (to within 50 Å in terms of the peak locations) to Hunt and Schuler's, are plotted in Figure 2. The saturated peak value he observed was 3.75 $cm^{-1}$; as mentioned in the foregoing, in plotting his data, it was normalized to an approximate average value for the peak transmission of rod 86 and the thin sample of rod 73. Note that its shape and location are in good agreement with our observations particularly for wavelengths longer than 4000 Å. We consider this to be the strongest evidence that the observed absorption is not characteristic of $Cr^{2+}$ or $Cr^{4+}$ since practically the same absorption spectrum is seen in $\gamma$-irradiated sapphire samples containing no $Cr^{3+}$.

Hoskins and Soffer (1964) arrived at a similar conclusion upon the growth of $Al_2O_3$ containing $Cr^{4+}$. They observed an intense absorption somewhat like that in Figure 2 except that the peak value occurred at 4600 Å. They attributed this absorption to a color center associated with the anionic charge compensation rather than $Cr^{4+}$ absorption (the charge

compensation had to be used during the growth to ensure that the chromium would go into the crystal as $Cr^{4+}$ rather than $Cr^{3+}$). Hoskins and Soffer concluded this since (a) they saw it in $\alpha$-$Al_2O_3$ crystals prepared under similar charge compensating conditions but containing no chromium; (b) the strength of the absorption bands would imply an unusually large oscillator strength for $Cr^{4+}$ based on its deduced concentration; and (c) the coloration of the crystal did not change when the $Cr^{4+}$ was converted to $Cr^{3+}$ by blue irradiation.

Maruyama and Matsuda (1964) found a strong dependence of the induced absorption (seen in four bands at 4700 Å, 3700 Å, 2800 Å and 2200 Å with the latter being strongest by a factor of three in absorption) on chromium concentration in Verneuil samples grown by the Shinkosha Company and $\gamma$-irradiated. They proposed that this could be explained by the following mechanism. The difference between starting and final values of $Cr_2O_3$ in ruby growth gets larger as the starting amount increases. The amount that is lost is by vaporization of chromium during the growth. Thus the crystal may contain cation vacancies and, consequently, anion vacancies in order to maintain charge neutrality, and the number of these should be proportional to the amount of $Cr_2O_3$ used in starting to grow the crystal. They suggest that this explanation will hold only when the number of defects and impurities having no dependence on chrome concentration is less than the chrome concentration. ESR measurements made by them showed the $Cr^{3+}$ concentration of their 0.024 percent $Cr^{3+}$ sample to decrease to 52 percent of its initial value after $\gamma$-irradiation of $1 \times 10^5$r. They further suggest that the band they observed which peaks at 4700 Å is due to $Cr^{2+}$. From these data it was possible to calculate that if the band we observed at 4000 Å is due to a loss of $Cr^{3+}$ this should show up as a change in the $R_1$ line absorption after heating. For rod 86 this would have amounted to a change in transmission of 2 percent at 6943 Å, a factor of at least 3 larger than the nonreproducibility of our measurements. Since only changes of the order of the measurement reproducibility were seen, as discussed in the first part of this section, and since the bands do not peak at the same wavelength, it is apparent that this mechanism is not the correct one for the explanation of induced absorption. It should be noted that the saturation absorption value at 4600 Å for Maruyama and Matsuda's lightest doped (0.001 percent) sample was 0.076 $cm^{-1}$, considerably less than the values obtained by Hunt and Schuler (1953) (0.37 $cm^{-1}$) and Levy (1961) (3.75 $cm^{-1}$) for sapphire. This could be interpreted as follows: that Maruyama and Matsuda's samples contained a very low density of defects and impurities, of the sort that lead to color center formation in ruby.

Schultz (1964) also observed a similar absorption in a 0.035 percent Verneuil ruby grown by H. Djevarhirdjian of Switzerland. The absorption strength was 0.17 $cm^{-1}$ at peak wavelength of 4465 Å after only 10 to 20 flashes of a xenon lamp in a laser setup. His tentative conclusion that this absorption was due to a valence change of chromium hinged primarily on the observation that he did not find an EPR signal for the color center at room temperature, whereas some report having seen such a signal, but not in $Al_2O_3$ (see Orton, 1959). Others (Hoskin and Soffer, 1964; Hayes and Jones, 1968; Jolley and McLaughlan, 1963), however, were able to detect such signals only at cryogenic temperatures.

Arkhangelskii et al. (1967) interpret the induced absorption they see in terms of absorption by $Cr^{2+}$ and $Cr^{4+}$. Their conclusion is based on first, the fact that Levy (1961) did not choose to consider small variations in the induced absorption curves for sapphire as meaningful, whereas they did; and second, in the argument given for the observed "bands", that is, absorption by $Cr^{2+}$ or $Cr^{4+}$, one could just as easily suggest it to be a color center of a different nature and the pattern of their logic would not be destroyed.

Finally, mass-spectroscopic impurity concentration measurements were made on rods 79, 84 and 87 of group I to determine if sufficient impurities might be present in order that the color centers could be associated with them rather than with chromium in other valence states. Since the total number of impurities appeared to be four to ten times greater than the $Cr^{3+}$ concentration for the rods (Hunt and Pitha, 1968) it seems possible that there would be enough impurities of the right type present to cause the coloring seen.

In conclusion, we deduce that the absorption which is seen is characteristic of color centers associated predominantly with defects and impurities in the rod rather than $Cr^{2+}$ or $Cr^{4+}$ absorption since (a) the induced absorption shown in Figure 2 is matched best in terms of peak wavelength to the observations made by Hunt and Schuler (1953) and Levy (1961) on $a-Al_2O_3$; (b) the absorption cross section integrated over the visible and UV appears on the order of ten times larger than it does for $Cr^{3+}$, and it seems unreasonable that a change in valence state would be accompanied by such a large change in integrated absorption cross section; (c) there are such significant differences in the peak wavelengths, strengths, and dependence on chromium concentration reported in the literature and between all the various crystals that we have investigated, that it seems unlikely that a simple explanation which would apply to every ruby sample would be valid; and (d) sufficient impurities appear to be present (in the group I rods at least) that the color centers could be associated with them rather than $Cr^{2+}$ or $Cr^{4+}$.

## 6. CONCLUSIONS

We have shown that the gradual output energy decay of ruby lasers upon repeated UV irradiation from typical xenon flashlamps used for pumping can be quantitatively accounted for by a bulk absorption induced in the ruby, which both robs the center of the rod of pumplight and acts as a non-saturating loss mechanism at the laser wavelength. Comparison of the induced absorption vs. wavelength with the absorption curves for $\gamma$-ray induced color centers in undoped $a-Al_2O_3$ shows them to be essentially the same, indicating that the induced absorption does not depend upon the presence of $Cr^{3+}$ for its development. Measurements of ruby sample impurity concentration by mass spectrographic analysis shows that sufficient impurities are present in the samples analyzed to account for the development

of the color centers. Specifically which impurities lead to this are not known.

Contamination of the side surfaces of ruby rods followed by flashlamp irradiation can lead to the development of strong undesired absorption at or near the rod surface and cause energy degradation. Bulk and surface absorption is somewhat reliably detected by an orange-brownish appearance upon comparison with unfired ruby. Heating in air at 900°C for 24 hr will anneal out the color centers, thereby bringing about a useful (but not complete) restoration of the output energy; filtering the UV from the pumplight will reduce the rate of filling of the color centers an thus the rate of output energy decay. Finally, bulk absorption at the laser wavelength can lead to catastrophic damage; the energy densities calculated for this process are of the order of $10^5$ joules per $cm^2$, however, and thus would only be of concern in long, extremely high energy systems where unintentional focussing might occur.

## ACKNOWLEDGMENT

## REFERENCES

Arkhangelskii, Z. L., Morgenshtern, Z. L., and Neustruev, V. B. (1967) Color Centers in Ruby Crystals, Phys. Stat. Sol. 22, 289-295.

Collins, R. J. and Nelson, D. F. (1963) The Pulsed Ruby Optical Maser in Proc. of the Conf. on Optical Instruments and Techniques, K. J. Habell, Ed., Wiley, New York, 441-454.

Cooke, C. H., McKenna, J. and Skinner, J. G. (1964) Distribution of Absorbed Power in a Side-Pumped Ruby Rod, Appl. Optics 3, 957-961.

Cronemeyer, D. C. (1966) Optical Absorption Characteristics of Pink Ruby, J. Opt. Soc. Am. 56, 1703-1706.

Dodd, D. M., Wood, D. L., and Barns, R. L. (1964) Spectrophotometric Determination of Chromium Concentration in Ruby, J. Appl. Phys. 35, 1183-1186.

Dormitzer, H. (1968) Electro Powerpacs, Cambridge, Mass.; private communication; end of life is defined as being an energy output degradation by a factor of three to four.

Flowers, W. and Jenney, J. (1963) Effects of $\gamma$-Irradiation on the Performance of a Ruby Laser, Proc. IEEE 51, 858-860.

Hayes, W. and Jones, D. A. (1968) Paramagnetic Impurities in NaF, Proc. Phys. Soc. 71, 503-505.

Hoskin, R. H. and Soffer, B. H. (1964) Observation of $Cr^{4+}$ in $\alpha-Al_2O_3$, Phys. Rev. 133, A490-A493.

Hunt, M. H. and Pitha, C. A. (1968) AFCRL, Bedford, Mass., and Paul Paulsen, NBS, Gaithersburg, Md., private communication.

Hunt, R. A. and Schuler, R. H. (1953) Saturation in the X-Ray Coloration of Corundum Single Crystals, Phys. Rev. 89, 664.

Jerrick, T. F., "Pump Rate Distribution in Roughened Sidewall Ruby Laser Rods" (to be published).

Johnson, V. R. and Grow, R. W. (1967) Effects of Gamma-Irradiation on the Characteristics of a Ruby Laser, IEEE J. Quan. Elec. QE-3, 1-6.

Jolley, D. G. and McLaughlan, S. D. (1963) Microwave Inversion Efficiency of Orange Ruby, Nature 199, 898-899.

Levy, P. W. (1961) Color Centers and Radiation Induced Defects in $Al_2O_3$, Phys. Rev. 123, 1226-1233.

Maruyama, T. and Matsuda, Y. (1964) Color Centers in $\gamma$-Irradiated Ruby, J. Phys. Soc. Japan 19, 1096-1104.

Orton, J. W. (1959) Paramagnetic Resonance Data, Rep. Prog. Phys. 22, 204-240.

Roess, D. (1963) Untersuchung der Laser-Funktion an roh bearbeitenen Rubinen, Z. angew. Physik 15, 32-33.

Schultz, G. V. (1964) Color Change of a Ruby Crystal When Irradiated by Intense Light, Phys. Letters 9, 301-303.

Schultz, T. (1967) TRG, Inc., Melville, N.Y., private communication.

Siegman, A. E. and Allen, J. W. ('965) Pump Power Dependence of Ruby Laser Starting and Stopping Times, IEEE J. Quantum Elect. QE-1, 386-387.

Sooy, W. R., Congleton, R. S., Dobratz, B. E. and Ng, W. K. (1964) Dynamic Limitations on the Attainable Inversion in Ruby Lasers in Quantum Electronics III, P. Grivet and N. Bloembergen, Ed., Columbia Univ. Press, New York, 1103-1112.

Stickley, C. M. (1964)  A Study of Transverse Modes of Ruby Lasers Using Beat Frequency Detection and Fast Photography. Appl. Optics 3, 967-979.

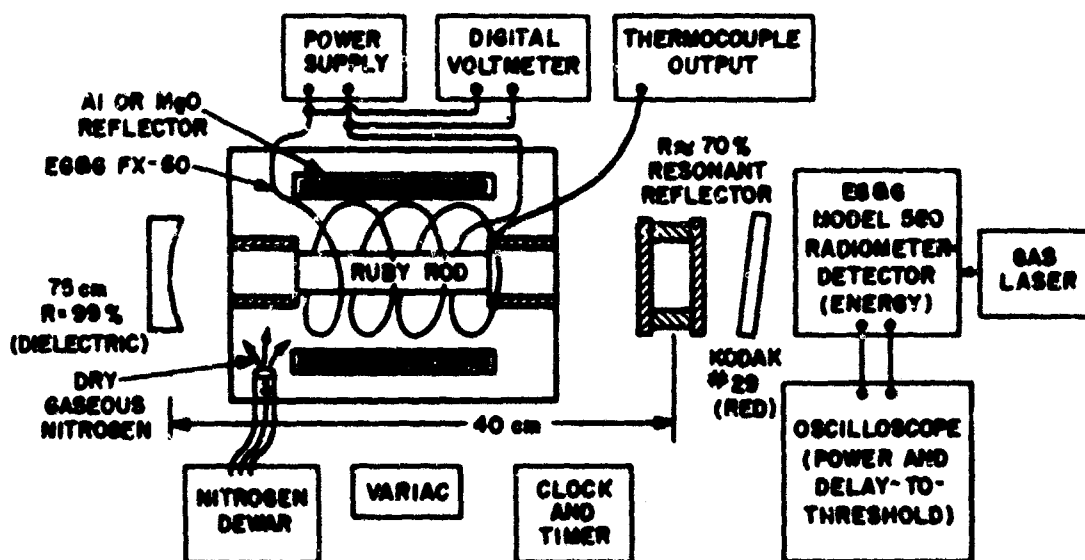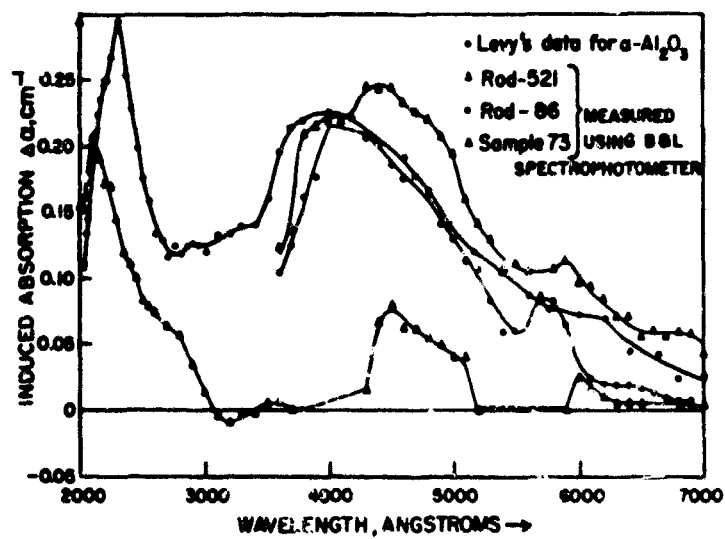## LIST OF FIGURES

## LIST OF TABLES

Figure 1

T-23

Figure 2



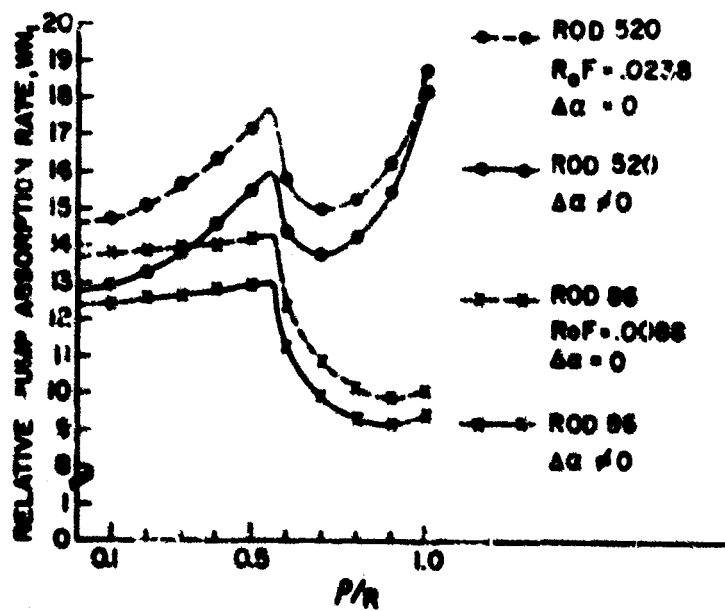Figure 3

Table 1. SUMMARY OF EXPERIMENTAL OBSERVATIONS

| Group | I Red Number | II Origin | III Date Obtained | IV Growth Method | V Number of Firings | VI Energy Decay % | VII Threshold Increase (%) | VIII Fluorescence Change Near Thresh. | IX $R_1$ Line Absorption Change | X Absorption Increase at 4880 Å cm$^{-1}$ Xenon lamp | XI Absorption Increase at 4800 Å cm$^{-1}$ Hg lamp | XII Color Change |
|---|---|---|---|---|---|---|---|---|---|---|---|---|
| I | 21 | Linde | 1961 | VR Vern. | >1000 | 0.5 ± 0.05 | | | No | 0.038 | | Brown |
| | 72 | AFCRL | 1964 | Verneul | >1000 | 0.5 ± 0.05 | | | No | 0.036 | | Slightly brown |
| | 73 | Linde | April 1963 | Duc Vern. | >1000 | 0.7 ± 0.07 | | | No | 0.011 | | Brown |
| | 87 | Linde | 1965 | Czochralski | >1000 | 0.3 ± 0.03 | | | No | 0.143[b] | | Most brown |
| II | 81 | Linde | 1964 | Czochralski | >1000 | 0.26[b] | 14[b] | 0.8[b] | 0.74[b] | 0.143[b] | | Most brown |
| | 100 | Linde | 1964 | Czochralski | 600 | 0.65[b] | 5[b] | 0.8[b] | 0.85[b] | 0.114[b] | | Brown |
| | 106 | Linde | 1964 | Czochralski | 0 | 1.0 | c | 1.0 | 1.0 | None | | Pink |
| III | 98 (810)[b] | Linde | March 1966 | Czochralski | 500 | ~0.5 | 35 | No | No | 0.06 – center[c] / 0.12 – edge | | Brown |
| | 99 (843) | Linde | March 1966 | Czochralski | 1100 | ≤0.10 | 47 | No | No | | | Most brown |
| | 104 | Linde | 1966 | Verneul | 340 | 0.75 | 6 | | No | | | Brown |
| IV | 96 (811) | Linde | March 1966 | Czochralski | 300 | Slight decay but variable | 12 | No | No | 0.030[c] | | Light Pink |
| | 101 (916) | Linde | March 1966 | Czochralski | 330 | | 6 | | No | | | Light Pink |
| V | (530) | Linde | Aug. 1967 | Czochralski | 100 | Small and Uncertain | | No | No | 0.033 | | |
| | (531) | Linde | Aug. 1967 | Czochralski | 100 | | 12 | No | No | 0.046 | | Very Slight Brown |
| | (576) | Linde | Oct. 1967 | Czochralski | 100 | 0.55 | | No | No | 0.015 | | |
| | (531) | Linde | 1967 | Czochralski | | | | | No | | | |
| VI | 98 (810) | Linde | March 1966 | Czochralski | | 0.77 ± 0.06[d] | | | | | 0.04[d] | |
| | (530) | Linde | Aug. 1967 | Czochralski | | 0.79 ± 0.06[d] | | | | | 0.36[d] | |

a. The bracketed number is the Linde rod number; the unbracketed one, AFCRL number.
b. Denotes normalization with respect to rod 106, one which was fired only five times.
c. Denotes normalization with respect to rod 87, one which was used only in 1 standard and not fired.
d. These measurements performed by O. R. Meyer and L. Rothrock of the Linde Co.; energy decay was induced by illumination of rod with Hg lamp for 2-1/2 hours.

T-25

Table 2. EFFECTS OF CLEANING AND ANNEALING ROD 86

|  | Original Condition | After 2 Hr Boil in Water | After 2 Hr Boil in Nitric Acid | After 2 Hr Heat in Air at 450°C | After 2 Hr Boil in Chromic Acid | After 24 Hr Heat in Air at 900°C |
|---|---|---|---|---|---|---|
| % Trans at 4360 Å | 34.0 | 33.0 | 33.2 | 32.5 | 33.0 | 45.4 |
| $E_{out}$ at 2250 $J_{in}$ | 73 mJ | 78 mJ | 102 mJ | 102 mJ | 115 mJ | 211 mJ |
| $E_{out}$ at 2500 $J_{in}$ | 99 mJ | 102 mJ | 143 mJ | · · · | 158 mJ | 266 mJ |

Table 3. LASER OBSERVATIONS AND CALCULATIONS ON ROD 86

|  | Observed | | Calculated | | | | |
|---|---|---|---|---|---|---|---|
|  | $P_0$ watts | $t_{th}$ μsec | Type of Calculation | $W_T$ | $n_2$ | $t_{th}$ μsec | $P_0$ watts |
| Before annealing | 293 ± 15 | 139 | Method A | $22.5^{+0.8}_{-0.7}$ | $0.597^{-0.009}_{-0.013}$ | · · · | $1030^{-70}_{+120}$ |
| After annealing | 443 ± 20 | 111 | Method A | 25. ॒ | 0.597 | · · · | 1520 |
|  |  |  | Method B | $24.1^{+0.6}_{-0.9}$ | 0.597 | $117^{-2}_{+4}$ | $1435^{+35}_{-30}$ |

|  | Observed | Calculated by Method A | Calculated by Method B |
|---|---|---|---|
| $P_{oa}/P_{ob}$ | 1.51 ± 0.04 | $1.48^{+0.10}_{-0.16}$ | $1.39^{+0.14}_{-0.17}$ |

MODERN THERMAL-IMAGING TECHNIQUES

FOR HIGH-TEMPERATURE RESEARCH

By

William G. Field

Robert W. Wagner

Solid State Sciences Laboratory
Air Force Cambridge Research Laboratories
Office of Aerospace Research
L.G. Hanscom Field, Bedford, Massachusetts

U-1

# BIOGRAPHY

Dr. William G. Field received a Bachelor of Science degree in Electrical Engineering from Kansas State College in 1943 and then served as a Radar Officer in the Signal Corps during World War II. He joined what is now AFCRL in 1946. He has worked on high power modulators, magnetic materials and components, single crystal growth, and on ultra-high pressure research including the growth of diamonds. During this time he received a Master of Science degree in Mathematical-Physics from Northeastern University in 1953 and his Ph. D. degree in Geology from Harvard University in 1965. He is currently working on the growth of single crystals at very high temperatures in controlled atmospheres.

Robert W. Wagner was born 3 March 1911 in Reading, Pennsylvania. He attended the Pennsylvania Public Schools, after which he attended Pennsylvania State University, Harvard College and M. I. T. In 1954 he received his B.S. in Electrical Engineering from M. I. T. During World War II he served as a Naval Officer after which he joined AFCRL in 1946. As a Research General Physical Scientist in the Purification and Growth Branch of the Solid State Sciences Laboratory, is presently carrying out experimental research in the field of single crystal growth techniques of highly refractory materials and the correlation of such techniques with resulting crystal structural factors and their ultimate performance in devices such as the laser.

# Modern Thermal-Imaging Techniques for High-Temperature Research

ABSTRACT

Thermal-imaging methods and equipments have improved markedly during the last few years. It is now possible to attain thermal fluxes and temperatures in the laboratory that are comparable to those available when using the sun as a source. This advanced technology has been especially applied to high-temperature crystal growth, but can also be applied to many other problems including: (1) melting, vaporization and ablation studies, (2) fuel ignition, (3) heat blast and burn effects, (4) characterization of windows at optical and microwave frequencies, (5) energy conversion, (6) generation of water, (7) radiative parameters, (8) and many physical and chemical investigations requiring very high temperatures such as phase determination, purification, alloying and X-ray diffraction. Such experiments can be carried out quite easily in the 1500-3000$^{\circ}$C range, and temperatures can be extended well beyond this range.

The basic concept involved in thermal imaging is to produce heating by focusing an image of an intense light source onto a material. This process has two major advantages: the heating process is clean, and essentially any atmosphere can be used. The use of thermal imaging has been limited in the past by the necessity of having adequate sources, optical systems and associated equipments. These restrictions can generally be eliminated by careful design and good experimental technique.

A modern high-performance, dual-compound, thermal-imaging fur-
nace will be described. Its application to materials research, especially
single crystal growth, will be covered together with application to other
problems of importance to the Air Force.

## 1. INTRODUCTION

Almost everyone has at one time or another experimented with the
use of a magnifying glass and the sun for starting a fire. The modern
thermal-imaging furnace or heat source is merely an advanced adaptation
of this simple concept. If the sun is utilized as a heat source we have a
"solar-furnace", and if some other source of light is utilized we have a
"thermal-imaging furnace". These methods all have one concept in com-
mon; heat is produced simply by focusing or concentrating an intense
light source onto the material it is desired to heat.

It is interesting to note (Benveniste, 1956 and Gradstein, 1961/62)
that the use of lenses or mirrors for lighting kitchen fires and altar flames
was known to antiquity and that as early as the year 1540, solar furnaces
using mirrors a foot in diameter were capable of melting gold. A large
solar furnace was also built in 1774 and used by Lavoisier for a number
of chemical experiments. This furnace had an optical system composed
of two lenses, one of which was four feet in diameter. This furnace was
capable of tracking the sun and could reach temperatures of 1500°C (about
the melting point of steel). The first arc-image furnace (that is, one
using a carbon arc as the source) appears to have been demonstrated by
Tyndall (1866) in his lectures on high temperature chemistry.

Modern well engineered thermal-imaging furnaces (Field and Wagner,
1967 and 1967a) have several advantages that are important to research
and to certain Air Force applications. These are: (1) the heating process
is very clean, (2) essentially any atmosphere can be used, (3) there are
no electric or magnetic fields present, (4) very high temperatures (3000°C)
can be achieved, and (5) using the sun as a source permits the generation
of energy without the use of any other fuel. The later advantage has po-
tential applications for support facilities in remote locations.

While the author's work in this field has been mostly on single crystal
growth the method is, however, applicable to many other problems in
materials research. It is the purpose of this report to describe the state-
of-the-art, and to point out the role of thermal imaging to research and
to other applications of potential importance to the Air Force.

## 2. THE THERMAL-IMAGING FURNACE

The basis of all thermal-imaging furnaces is the simple solar furnace
shown in Figure 1. Nearly parallel rays of light coming from the sun are

focused by the parabolic mirror to form an image of the sun with the size of the image depending upon the size and design of the mirror. While the solar furnace has advantages, it is generally not satisfactory for materials research problems that require a steady application of heat for long period of time.

The type furnace that is most commonly used is the two-mirror system shown in Figure 2. The source, placed at the focal point of one parabolic mirror, produces a parallel beam of light - as in the case of a searchlight. This beam is collected by the second parabolic mirror to form an image as in the solar furnace. This design has proved quite successful for a number of studies but heats only one side of a specimen. This is a serious disadvantage for many applications, especially single crystal growth. A design (Ploetz, 1959) that circumvents this difficulty is shown in Figure 3. In this design two parabolic mirrors are placed facing each other with very little spacing between the mirrors. In this manner the focal point of each mirror is actually outside the adjacent mirror. A small hole cut in the center of each mirror allows the light from the source to completely illuminate one mirror, thereby producing the required parallel beam of light to illuminate the second mirror. The light from this second mirror is then focused out through the other hole. In this manner the point at which the light is focused (the hot-spot) is actually outside the optical system. If two clam-shell systems are placed facing each other as shown in Figure 4, both sides of a specimen can be heated. Two light sources X illuminate the two mirror systems C, which in turn heat the specimen R on both sides. The two back-up mirrors M collect a portion of the light that does not normally enter the mirror system, and refocus it back through the lamp to increase the overall efficiency. The back-up mirrors increase the thermal flux by about 25 percent.

At this point it is important to stress one vital point in relation to heating with light; that is, unless there is an absorber present there is no heating produced except that due to a small absorption of the air itself. It is, therefore, incorrect to speak of the temperature that a particular furnace can reach but rather to specify the thermal flux (energy/unit area) that can be produced. Temperature specification is sometimes helpful, however, if one remembers that it applies to an essentially flat absorber that will retain the major portion of the light that falls upon it.

The choice of the type of source to be utilized also presents another design factor to be determined. The sun is the best from the standpoint of power and attainable temperature. As sunlight can be collected over as large an area as desired, large amounts of energy can thus be collected. Very large solar furnaces (Laszlo, 1965) are capable of producing about one million watts of energy into a focal area that will permit attaining temperatures of nearly 4000°C. Such large furnaces are very expensive, require provisions for tracking the sun, and are limited by the whims of the weather. For these reasons thermal-image furnaces today utilize an artificial source of light. The carbon arc can produce a very high temperature but is not steady and, due to consumption of the electrodes, is not suitable for experiments requiring long periods of operating time.

For the reasons outlined above, the source normally used for research purposes is the high-pressure xenon lamp. A 5000-watt lamp is shown in Figure 5. These lamps have a spectral distribution of light very similar to the sun except for a series of peaks in the 0.8- to 1.0-micron range. These lamps are commercially available up to 20,000 watts, and 40,000-watt versions are in the development stage.

The high-powered laser deserves more investigation as a possible source. Such lasers can now operate at continuous power levels of approximately 9000 watts, and together with a lens or mirror system can be easily focused. Such sources should be excellent for many applications.

A double clam-shell furnace utilizing two 5000-watt lamps and three-foot parabolic mirrors is shown in Figure 6. This furnace can produce a maximum thermal flux of 1900 watts/cm$^2$ and an average flux density of 850 watts/cm$^2$ over an area of 5mm by 5mm. This value of maximum flux is approximately one-half that attainable in a good solar furnace. The attainment of such operating characteristics requires careful attention to the optical components of the system (Wagner and Field, 1967). The temperature stability in this furnace is very good. The temperature of a melt can be maintained to ±5°C with only current control of the lamps. With intensity control, the temperature variation should not exceed ±2°C.

Atmosphere control can be achieved by surrounding the specimen with a glass or quartz envelope. As quartz is quite transparent to the wavelengths of light present in the source it absorbs very little heat and is, therefore, heated mostly by reflection from the specimen. Pressures of 100 psi are easily attained, and under certain circumstances pressure up to 1000 psi should be possible.

## 3. APPLICATIONS

It is not possible to cover all present and/or possible applications of thermal imaging in a short report. Several important uses will be described and a number of others outlined in sufficient detail to indicate the potential of this method.

### 3.1 Single Crystal Growth

Single crystals serve two important functions: (1) it is from such crystals that the fundamental properties of a material can be determined, and (2) they are also the heart of such devices as the transistor, maser, laser, etc. The growth of high quality crystals is, therefore, an important function in relation to obtaining a better knowledge of materials and to the construction of many actual devices. The advantages of clean heat, atmosphere control and high temperature capability make thermal imaging a natural choice for a number of vital materials.

There are a number of methods for crystal growth but most are based upon growing either from a melt, liquid or vapor. Melt growth is essentially a process involving the melting of a mass of material and then permitting it to solidify in such a manner that a single crystal of the material results. It is this method that is most successful when thermal imaging is used as the source of heat. Growth from a melt also embraces a number of different approaches that are given various names. Two of the best and most general will be described.

The first of these methods is best described by again referring to Figure 4. Here is seen a rod R of material being melted. For the growth of a single crystal the sequence of events will be as follows: The lower portion of the rod (normally round) would be a piece of a single crystal. The top portion would be a source of supply for additional material called the feed rod. This can, for example, be a rod prepared from material of the same composition as the seed crystal. The rods are then positioned so that their ends nearly touch, and the lamps are turned on to melt the ends of the two rods. If they are sufficiently close together the two molten ends will join, forming a molten zone supported by surface tension. The rods are rotated in different directions to assure good mixing and uniform temperature in the melt. If the rods are now slowly lowered together as a unit, the molten zone will move up the rod. As the material freezes, growth of the crystal will continue. At least forty different materials have been produced by this method. Work at AFCRL has been on the ferrites, spinel, stabilized zirconia, sapphire and especially ruby (Field and Wagner, 1968).

The purpose of the work on ruby has been to develop a better material for laser applications. Thermal imaging has several advantages that should permit the production of better crystals with repeatable characteristics - the cleanliness of the process and the fact that the temperature of the molten zone can be higher than other methods resulting in an increased fluidity of the melt. The interface between the crystal and the liquid can also be easily contoured with an external heater in order to decrease the dislocation density, and by utilizing the zone leveling principle the chromium distribution in the crystal should be more uniform. One of the ruby crystals is shown in Figure 7. This crystal is approximately 1/4 by 2 inches, has a dislocation count of $10^4$ dislocations/$cm^2$, very few low angle grain boundries, a total impurity concentration of 200 parts per million, and the chromium distribution across the crystal varies by only ±1 percent. Further work should produce better crystals with improved characteristics for laser applications in communications, ranging, etc.

Another melt growth technique is the Czochralski or pulling method shown in Figure 8. This is the two-mirror, thermal-imaging furnace but in this case the optic axis of the mirrors is in the vertical position. The light from the top mirror is directed onto the material contained in a crucible. When the charge is molten, a seed crystal is lowered until it touches the top of the melt and is then slowly withdrawn. As the temperature of the seed crystal is below the melting point material will solidify on the seed, and as it is withdrawn a single crystal is formed.

Thermal imaging has one important advantage for Czochralski growth - the ability in certain cases to eliminate crucible contamination. Consider the case where the material is dense, fills the crucible, and is a good thermal insulator. The light beam can then be focused on the center of the charge in the crucible and as heat is being supplied only in this region, it is possible to melt in only this central region. In this manner there is no reaction between the charge and the crucible. Also, the melting point of the material can actually be higher than that of the crucible. For example, material that melts at 2850°C can be handled in an alumina crucible that melts at about 2000°C. A crystal can still be pulled from the central molten region as described above.

## 3.2 Other Applications to Materials Research

The characteristics of a thermal-imaging furnace also make it readily adaptable to many other physical and chemical investigations requiring very high temperatures with or without atmosphere control as: (1) melting and alloying, (2) phase determination, (3) thermal expansion, (4) purification, (5) and X-ray diffraction.

There are two basic properties of the thermal-imaging technique that are responsible for most of the above applications. First, there is the ability to direct light onto a small region of a sample. This eliminates the requirement for a container in many cases. The second point is that very rapid heating is possible. By placing a specimen directly at the focal point, materials can be heated to temperatures in the order of 3000°C in a few seconds and, since the lamps can be rapidly turned off, the sample can be quickly quenched or cooled. These two facts permit alloying, phase determinations and other experiments to be made at high temperatures in a short period of time.

The float-zone method of crystal growth that was described previously, is also one of the best for purification of many materials. It has for years been one of the main techniques for the purification of semiconductor materials such as silicon and germanium. By this process certain impurities can be "swept" out of a material. Thermal imaging provides the additional advantage of utilizing an absolutely clean source of heat; light cannot add any additional impurity.

## 3.3 Optical and Microwave Windows

Missiles and very high speed aircraft have various requirements for windows that will transmit optical and/or microwave signals. In addition to adequate mechanical and electronic properties, these windows must withstand severe heating. These conditions present a difficult problem; that is, the measurement of properties under actual operating conditions, especially at high temperature. Here again thermal-imaging techniques could provide a simple solution to this problem. The experimental setup would be as shown in Figure 9. Here there is the usual clam-shell furnace, but this time the light is injected into a device (Chen, 1963 and

Glaser et al, 1963) called a "light-pipe". The purpose of a light-pipe is to produce a more uniform distribution of thermal flux and, therefore, more uniform heating of a specimen. The increased uniformity is the result of multiple reflections within the light-pipe. The light-pipe usually has a square or rectangular cross section. The cross section may remain constant in size or may be in the shape of a truncated pyramid; that is, shaped like a horn. The window under investigation may be placed within the end of the pipe or adjacent to it as shown in Figure 9. As the thermal flux is very uniform, the temperature in the window will also be uniform with proper experimental precautions. If it is desired to heat both sides of the specimen, a similar clam-shell unit can be placed on the opposite side. However, in most applications a window is heated only from the outside by friction with the atmosphere and the arrangement shown in Figure 9 is perhaps the more realistic.

Optical transmission of a window can be determined in a simple fashion. The spectral distribution of the light emitted by the light-pipe can be directly measured. A similar measurement of the light passing through the window permits determination of the absorption of the window. The high intensity of the light provides the heating of the window.

When one considers that the light-pipe is a metal pipe generally having a polished silver interior and having a square or rectangular cross-section, one realizes that this is the ideal configuration for a wave guide. Microwave probes for injection of signals and for measurement can be inserted. The light then heats the specimen, and the light-pipe at the same time forms a microwave measuring system to evaluate the parameters of the material. Again, measurement of the microwave energy incident to the specimen and that transmitted would give the absorption. Light-pipes have been successfully operated in a variety of sizes comparable with usual microwave wavelengths, so that measurements could be made at the wavelengths of most operating systems. The high heating rates attainable with thermal imaging also can provide for proper simulation of high heating rates encountered in reentry applications.

### 3.4 Energy Conversion

No one needs to be made aware of the importance of solar cells in the space program, especially for powering unmanned satellites. But what about terrestrial applications? In remote areas or where supply functions are difficult, the sun is an often overlooked potential source of energy. While sunlight is not always available, modern batteries and/or energy storage devices can provide for periods when sunlight is absent. It is interesting to note that as far north as Boston, Massachusetts there are normally 120 days a year when the sky is clear and when solar radiation is suitable for most solar furnace work.

While many experiments have been made and various devices developed for heating and energy conversion using the sun, further work must be done to develop systems suitable to military applications. However, the results all indicate that this approach is a sound one.

When considering the use of solar cells for terrestrial applications, it has been shown (Berman, 1967 and Herchakowski, 1965) that the most efficient system is one combining a solar cell with a simple integral concentrator. Such a system is capable of providing 100 mw of power with normal solar radiation. It has been estimated that the cost for such a cell-concentrator arrangement would be less than $10.00 per watt.

Energy conversion can also be achieved by other means. Recent investigation of a solar-powered Stirling engine power unit (Trayser and Eibling, 1967) have resulted in the design of a small unit for field use. This unit can provide 50 watts of power, weighs about 15 pounds, is estimated to cost around $500.00, and is 15 x 16 x 24 inches in size when folded for shipment. These studies also resulted in the results shown in Table 1 for comparative weight and cost factors of various systems.

Table 1. Weight and Cost Factors of Power Source

| Power Source | Pounds/Watt | $ /Watt |
|---|---|---|
| Solar-Stirling Cycle | 0.32 | 10 |
| Solar Cells, Flat Plate Collector | 0.2 | 150 |
| Solar Cells, Concentrating Collector | 0.1 | 15 |
| Solar-Thermoelectric | 0.75 | 50 |
| Solar-Rankin Cycle | 2.6 | 12 |

Simple portable solar concentrators have also been developed for other applications, such as cooking food in desert areas where fuel is scarce.

Water Generation

The production of drinking water by desalinization of sea water is rapidly becoming one of world importance. It is not our intent to enter into a discussion of this problem, but rather to consider just two possible applications of thermal energy to the problem. The first is the production of small amounts of pure water by distillation of sea water, and the second is the concept of producing water from rocks.

Requirements in the order of 100 gallons or less per day in remote areas where sea water is available, are best handled by using solar heat

(Daniels, 1967). Small easily constructed and maintained plastic stills have been designed. A small plastic still of 30 square feet costing about $15 for materials can produce about 1 gallon per day. These small stills are easily constructed by unskilled labor and are very easy to maintain. An area of 50 by 50 feet is, therefore, capable of producing 100 gallons per day. For any larger amounts, some type of fuel operated system would be better.

Most rocks on the earth and possibly those on the moon may contain as much as 0.13 cubic meters of water per cubic meter of rock (Anonymous, 1968). To reclaim this water requires sufficient temperature to decompose the rock. Such heat can easily be supplied by a solar concentrator. In fact, several experiments (Anonymous, 1960) have succeeded in obtaining water from rock. Heating was performed in a solar furnace at a vacuum of $10^{-5}$ torr. The steam was then condensed in a cold trap at -40°C. Both vacuum and condensing temperatures are readily available on the moon. Solar radiation on the moon is also approximately 20 percent more intense than the maximum available on the surface of the earth. While this concept may not be logical for terrestrial use, it may be vital to the needs of any moon base. In this case, large scale operations where sunlight is readily available are not too unreasonable.

## 3.6 Radiative Parameters

Research on and design of high speed vehicles that are subject to re-entry through the atmosphere require a knowledge of the radiative parameters of the materials used in their construction. Such parameters include the amount of light and heat emitted and/or reflected from their surface. The study of such parameters requires the ability to rapidly heat a material in a controlled atmosphere to very high temperatures. Thermal-imaging can easily provide this type of environment. However, the measurement of the radiative parameters themselves presents a difficult problem. This stems from the fact that the heating is produced by light that contains a large portion of visible and infra-red radiation, and the separation of this light from that emitted or reflected from the sample is a difficult problem. There are, nevertheless, some method of measurement (Noguchi and Kazuka, 1966 and Laszlo, 1965a) that are reasonably satisfactory and can provide reasonable good results. Adequate instrumentation in this area needs one thing; namely, a good idea. It is anticipated that future research in this area may provide better methods for such measurements. Thermal imaging would then provide an excellent technique for the evaluation of such parameters.

## 3.7 Miscellaneous Applications

Under this heading we will consider a few additional applications of thermal imaging. Their listing here is not meant to indicate a lack of importance, but rather the extent to which this technique can and has been applied.

The severe heating of missile reentry can produce vaporization and ablation of nose cone materials. Many high temperature materials have been studied by this method (Laszlo, 1965b). Items determined include the vapor pressure and rates of vaporization together with the nature of the vaporized products. The ablative characteristics of a number of high-temperature materials including composites have also been measured. Thermal-imaging has the advantage of both high temperature and simulation of the actual atmosphere through which a missile travels. However, it is difficult to include mechanical effects of friction other than thermal. Ablative rates can be determined as well as the nature of the material and gases given off during ablation. The increase of temperature with time can also be controlled and measured. For extremely high temperatures, a plasma generator can be utilized as a source. In this case the process of thermal imaging can provide the temperature and spectral characteristics of the plasma without the usual contamination.

Thermal imaging has been applied to many other engineering and scientific problems, and will undoubtedly be applied to many more in the future. Such studies include: (1) the evaluation of mechanical properties of materials at high temperature for engineering applications, (2) the determination of fuel ignition characteristics, (3) the effects of thermal blast of clothing and various military items, and (4) the production of high-temperature burns on both animals and man for study of thermal blast and other biological effects. This is a partial listing, but indicates the tremendous scope of thermal-imaging research and application.

## 4. SUMMARY

It has been the purpose of this report to present the results of independent research by the authors, and at the same time emphasize the potential importance of thermal imaging to the possible solution of various Air Force problems. The results obtained on single crystal growth and the outline of other important applications, demonstrate the validity of this approach as a basic and applied technique with a bright future.

# REFERENCES

Anonymous (1960) Water from rocks, Aero-Space Lab., North American Aviation Inc., Los Angeles, California.

Anonymous (1968) Moon Water, Industrial Research, p. 22.

Benveniste, G. (1956) Burning glasses from Archimedes to Lavoisier, Sun at Work 1 (No. 2):5.

Berman, P.A. (1967) Design of solar cells for terrestrial use, Solar Energy 11:180.

Chen, M.M., Berkowitz-Mattuck, J.B. and Glaser, P.E. (1963) The use of a kaleidoscope to obtain uniform fluk over a large area in a solar or arc imaging furnace, Applied Optics 2:265.

Daniels, F. (1967) Comparative costs of distilling small amounts of sea water with fuel and with solar heat, Sun at Work 12:18.

Field, W.G. and Wagner, R.W. (1967) Thermal Imaging for High-Temperature Crystal Growth, Paper No. J7 in Program and Abstracts of American Crystallographic Association Symposium on Crystal Growth, University of Minnesota, p. 50.

Field, W.G. and Wagner, R.W. (1967a) Method for Crystal Growth of High-Melting Point Materials in Controlled Atmospheres, Program, GSA, Meeting in New Orleans, p. 65.

Field, W.G. and Wagner, R.W. (1968) Thermal Imaging for Single Crystal Growth and Its Application to Ruby, in Abstract Book, I.C.C.G., Univ. of Birmingham, England, p. 6. To be published in J. Crystal Growth.

Glaser, P.E., Chen, M.M. and Berkowitz-Mattuck, J.B. (1963) The flux redistributor, an optical element for achieving flux uniformity, Solar Energy 7:12.

Gradstein, S. (1961/1962) Radiation furnaces of past centuries, Philips Tech. Rev. 23:182.

Herchakowski, A. (1965) Solar photovoltaic systems using concentrators, Proc. 19th Annual Power Sources Conference.

Laszlo, T.S. (1965) Image Furnace Techniques, Interscience Publishers, New York, p. 26.

Laszlo, T.S. (1965a) Image Furnace Techniques, Interscience Publishers, New York, Chapter XIII, p. 103.

Laszlo, T.S. (1965b) *Image Furnace Techniques*, Interscience Publishers, New York, Chapter XIII, 123 and 138.

Noguchi, T. and Kozuka, T. (1966) Temperature and emissivity measurement at $0.65\mu$ with a solar furnace, *Solar Energy* 10:125.

Ploetz, G.P. (1959) *The Clam Shell Thermal Image Device* (Thermal Imager), AFCRL-TN-59-759.

Trayser, D.A. and Eibling, J.A. (1967) A 50-watt portable generator employing a solar-powered Stirling engine, *Solar Energy* 11:153.

Tyndall, J. (1866) Heat as a Mode of Motion, D. Appleton Publishers, New York, p. 281.

Wagner, R.W. and Field, W.C. (1967) *J. Opt. Soc. Am.* 57:1409.

## FIGURE CAPTIONS

| Fig. | Caption |
|------|---------|
| 1. | Simple Solar Furnace |
| 2. | Two-Mirror Paraboloidal System |
| 3. | Single-Compound System or "Clam-Shell" |
| 4. | Dual-Compound Thermal-Imaging Furnace.  C, compound mirror assemblies; X, xenon lamps; R, specimen; and M, backup mirrors |
| 5. | 5000 Watt High-Pressure Xenon Arc Lamp |
| 6. | Thermal-Imaging Furnace |
| 7. | Single Crystal of Ruby Grown by the Float-Zone Technique in Thermal-Imaging Furnace.  Size approximately 1/4 x 2 inches. |
| 8. | The Vertical Two-Mirror Furnace |
| 9. | Experimental Setup for Evaluation of Windows at Optical and Microwave Wavelengths |
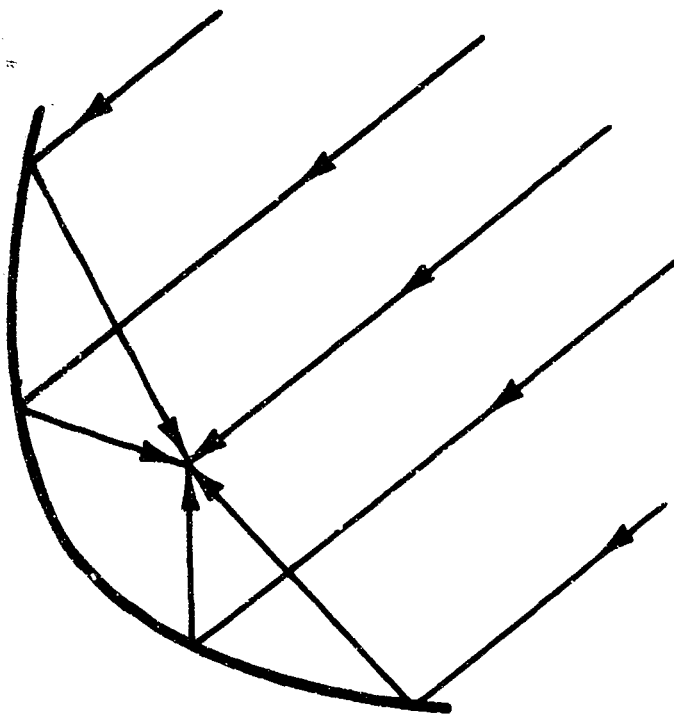
AFCRL PHOTO 98-339

Figure 1
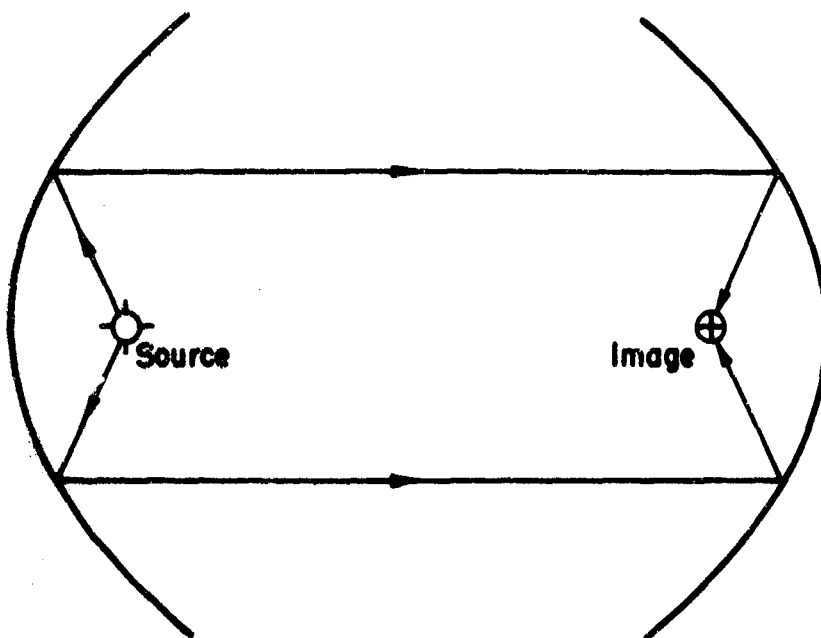


Figure 2

Source

Image

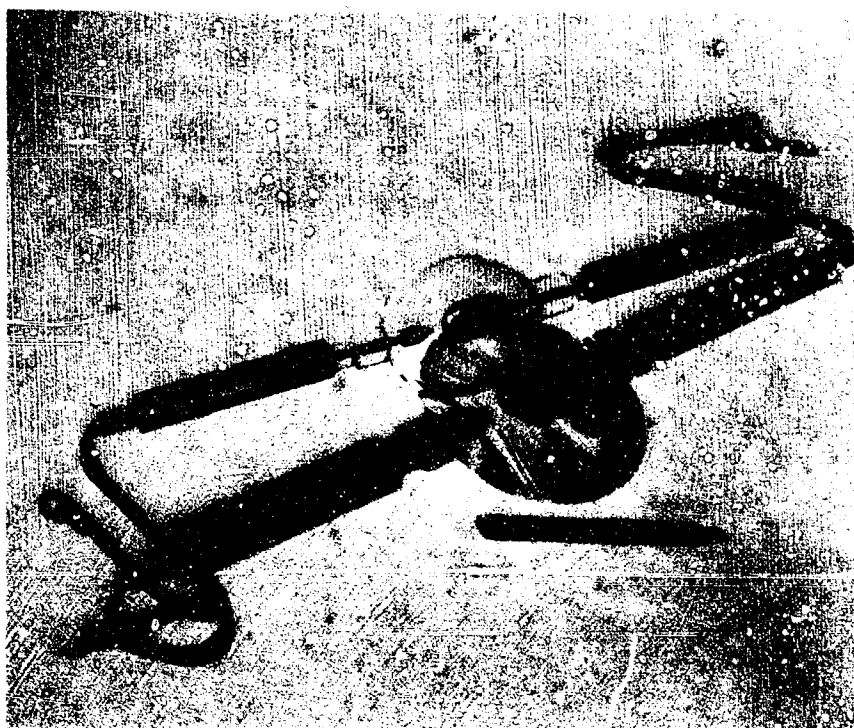Figure 3



M

M

R

C        C

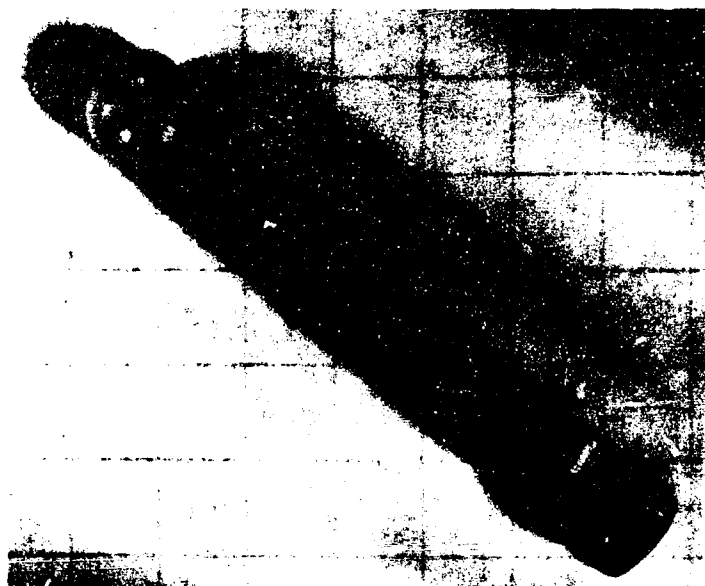Figure 4

U-17

Figure 5



Figure 6

U-18
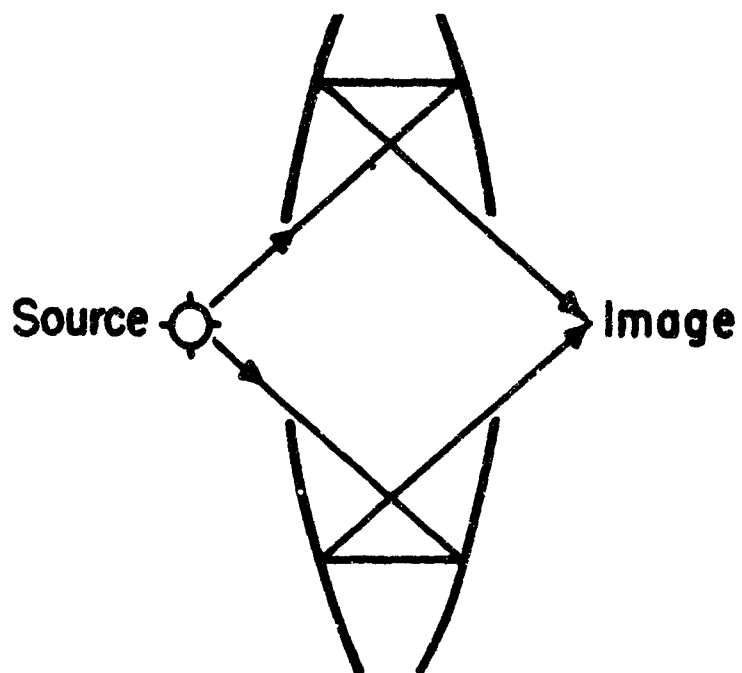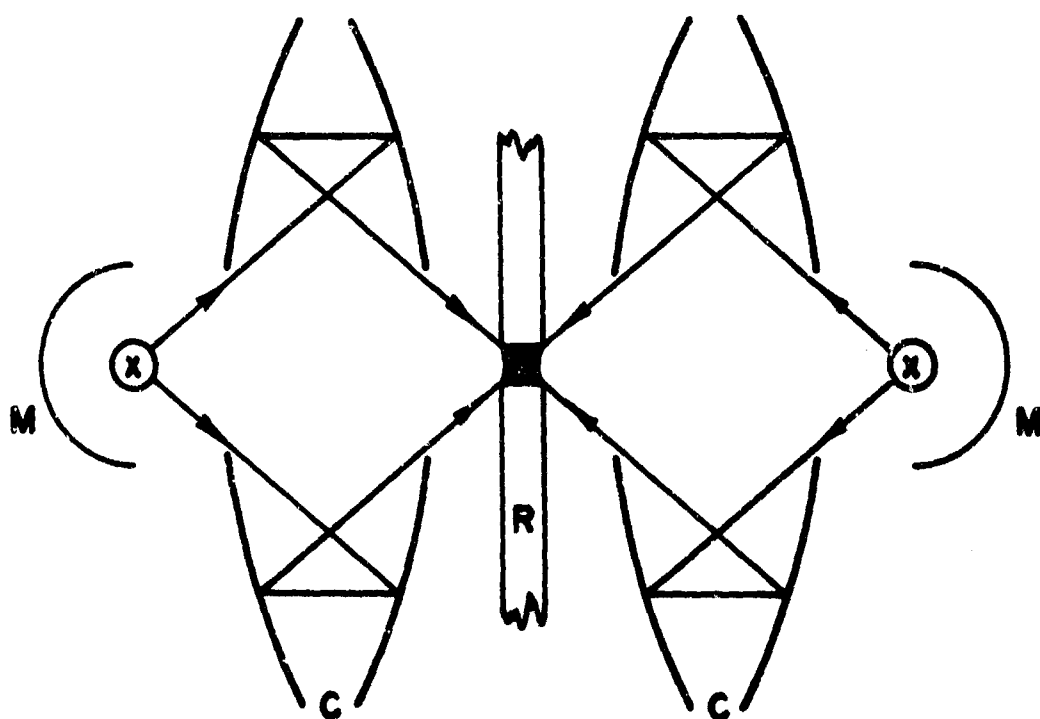
Figure 7
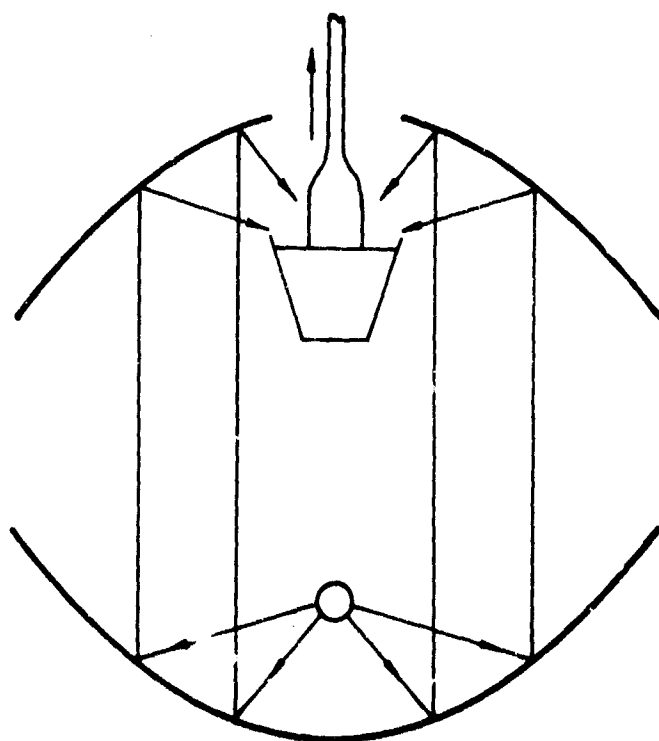


Figure 8

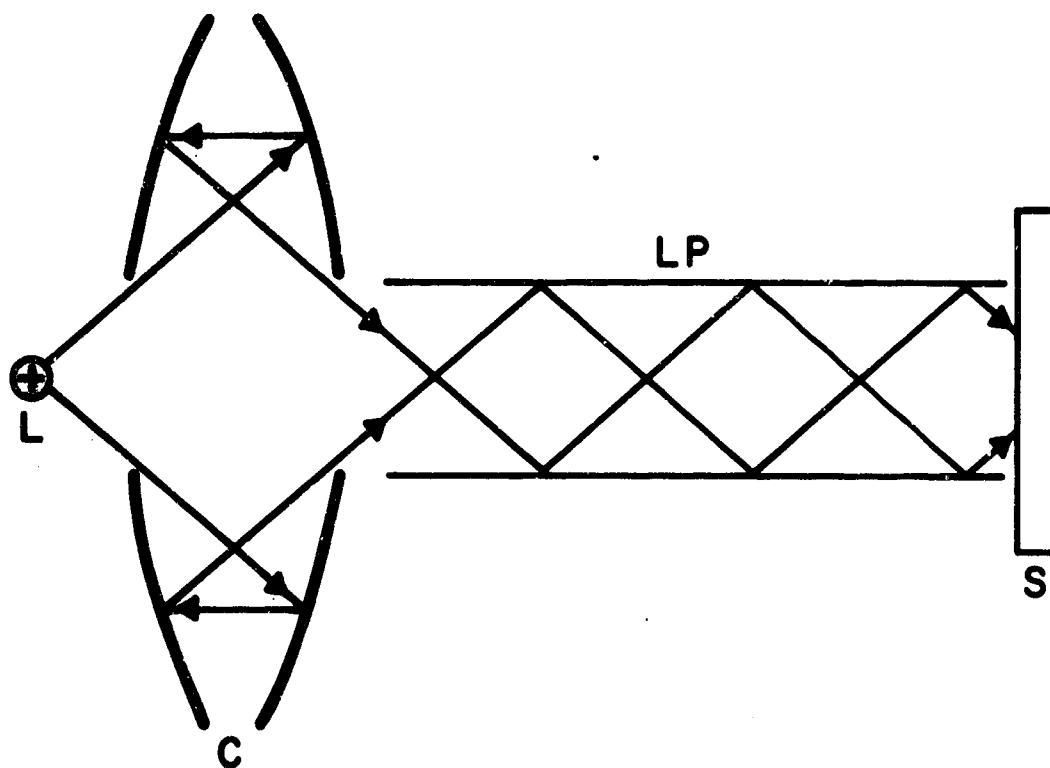Figure 9

# SIMULTANEOUS ROCKET AND RADAR BACKSCATTER STUDIES
## OF THE ELECTRICAL STRUCTURE OF THE LOWER IONOSPHERE

By

Rita C. Sagalyn

# BIOGRAPHY

Mrs. Rita C. Sagalyn was born in Lowell, Massachusetts, 24 November 1924. She received her B.A. in Physics from the University of Michigan in 1948 and her M.A. in Physics from Harvard University in 1950.

Since 1950 Mrs. Sagalyn has been engaged in studying the electrical properties of the atmosphere, the ionosphere and interplanetary gas. Experiments have been designed and flown on a variety of rockets and satellites for the study of ambient charged particle densities, electric currents and electric fields in and above the ionosphere.

Mrs. Sagalyn is the recipient of the Guenter Loeser Award in 1958 and of the Patricia Kayes Glass Award in 1966. She is a member of RESA, University Fellows, University of Michigan, and the American Geophysical Union. She has published over 40 articles in scientific journals.

# Simultaneous Rocket and Radar Backscatter Studies of the Electrical Structure of the Lower Ionosphere

ABSTRACT

In October 1967 a field program was carried out in Puerto Rico in which the electrical structure of the lower ionosphere was studied by means of simultaneous rocket-borne experiments and radar backscatter measurements made at the Arecibo Ionospheric Observatory. Charged particle densities and temperatures were measured as a function of time and spatial position over the altitude range 80 to 180 km. On the day flights electron and neutral particle temperatures were found to be nearly equal to an altitude of 125 km. Above 130 km the electron temperature was found to increase more rapidly than the neutral gas temperature exceeding it by 500°K at apogee. The electron temperature decreases rapidly with time after sunset, then a nearly isothermal temperature distribution develops between 130 and 180 km which persists through the night. Over this altitude region and at times when comparison is possible, good agreement is found between the results of the rocket-borne experiments and Thomson backscatter measurements at Arecibo, Puerto Rico.

Analysis of the daytime results shows that the diurnal variation in charged particle temperature is in fundamental agreement with the theories of Dalgarno. However, significant variations from the theory are found in the electron temperatures in the vicinity of 110 km during the day and at all altitudes at night. The significance of these results to the understanding

of ionospheric processes including heating, collision phenomena, photo-ionization, chemical, and transport processes is outlined.

During October 1967 five rockets were launched from Vega Baja, Puerto Rico with launch elevation and azimuth set to intercept the backscatter beam as illustrated in Figure 1. Four independent experiments with high precision and high sampling frequency were flown on each rocket. These included electron density and temperatures and positive ion density and temperatures. On the daytime flights Lyman α intensity was also measured. The sensors for each experiment were mounted on booms, extending four feet from the surface of the rocket to minimize disturbances introduced by the vehicle (Figure 2). These disturbances include rocket potential effects, space charge sheaths, and vehicle motion.

The Arecibo backscatter radar was operated 2 to 10 hours before and after each rocket launch. The launchings took place both day and night, the exact times having been chosen to maximize the study of special phenomena. These included:

(1) Measurement and interpretation of E- and lower F-region electron and ion temperatures.

(2) Measurement of small scale charged particle irregularities by two independent techniques.

(3) Determination of the "near field" correction for the Arecibo radar.

(4) Measurement of the rate of decay of ionization in the ionosphere after sunset when solar Xrays and ultraviolet radiations are absent.

(5) Determination of the influence of conjugate point electrons on ionospheric temperatures.

Until the investigation under discussion was conducted, there was often significant disagreement in the results of direct and indirect probing of the ionosphere. This has been particularly evident in the area of electronic structure and ion and electron temperature measurements. These experiments, carried out at the same place and time, have shown, for example, that at the times and over the altitude range where the Thomson backscatter is sufficiently sensitive the electron and ion temperatures are in very good agreement (Figure 3). The charged particle distributions are also in agreement although there are differences in detail (Figure 4). It has been shown that the fine structure differences are partly due to the large volume (approximately 16 km$^3$) sampled by the backscatter radar. The analysis also indicates that the fine structure backscatter measurements can be improved by using different pulse widths and changing integration times. The electron density and temperatures obtained one hour after local sunset on 24 October 1967 are shown in Figure 5. It is seen that shortly after sunset there is a rapid change in the temperature and density distributions. The charge density decays primarily due to the

dissociative recombination of $O_2^+$ and $NO^+$. The electron temperature becomes essentially isothermal above 120 km. Analysis shows that the electron temperatures are maintained with little change through the night because of the low frequency of elastic and inelastic collisions between electrons and the neutral gas molecules. The backscatter data became unreliable below 200 km immediately after sunset due to the very low environmental electron concentrations and relatively large receiver noise signals. This study demonstrates that, until the Thomsom scatter sensitivity is significantly improved, "in situ" rocket experiments will be particularly valuable for interpreting lower ionospheric phenomena at night.

These coordinated experiments have provided a new level of confidence in both rocket electrostatic probe techniques and in ground-based Thomson backscatter systems for ionospheric investigations. The many specific experiments carried out have contributed to the solution of several problems including: daytime ionospheric E-region heating; the source of presunrise electron temperature enhancements; and ionization production and decay measurements in the lower ionosphere.

The altitude region studied, 70 to 200 km, is important for radio wave and radar absorption and reflection. The knowledge gained will provide a basis for the interpretation of all types of ionospheric disturbances and should be useful in the prediction of many natural perturbations.

REFERENCES

Dalgarno, A., McElroy, M. B., and Walker, J. C. G. (1967) Planetary Space Science 15: 331.

Dalgarno, A. and Walker, M. B. (1967) Planetary Space Science 15: 200.

## FIGURE LEGENDS

Figure 1.   Rocket-borne and Backscatter Studies of Ionospheric Structure

Figure 2.   Location of Experiments on Nike Iroquois Nose Cone

Figure 3.   Comparison of Rocket and Backscatter Measurements of Electron Temperature $T_e$ for Launch of 24 October 1967 at 1314 Hours

Figure 4.   Comparison of Electron Densities From Rocket, Backscatter, and Plasma Line Measurements for Launch of 27 October 1967 at 1314 Hours

Figure 5.   Post Sunset Electron Temperature and Density Profile for Launch of 24 October 1967 at 1859 Hours Local Time
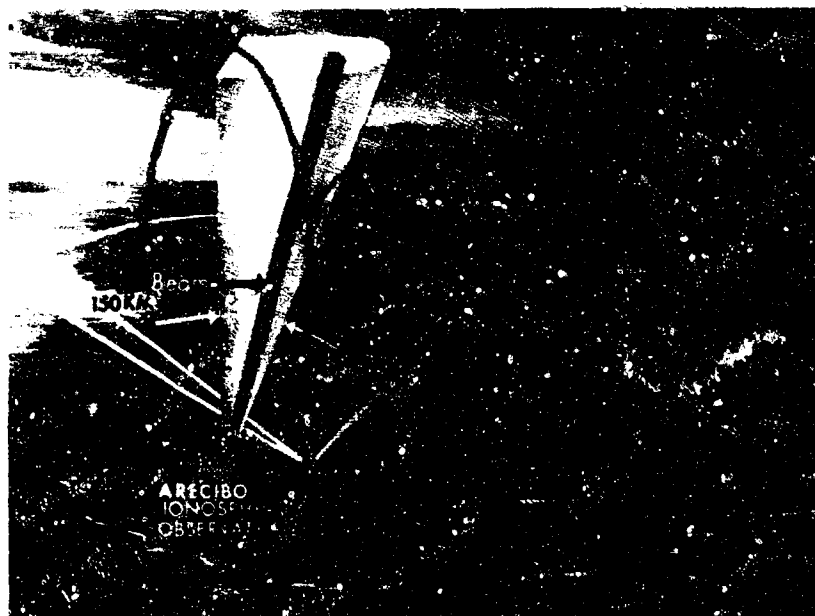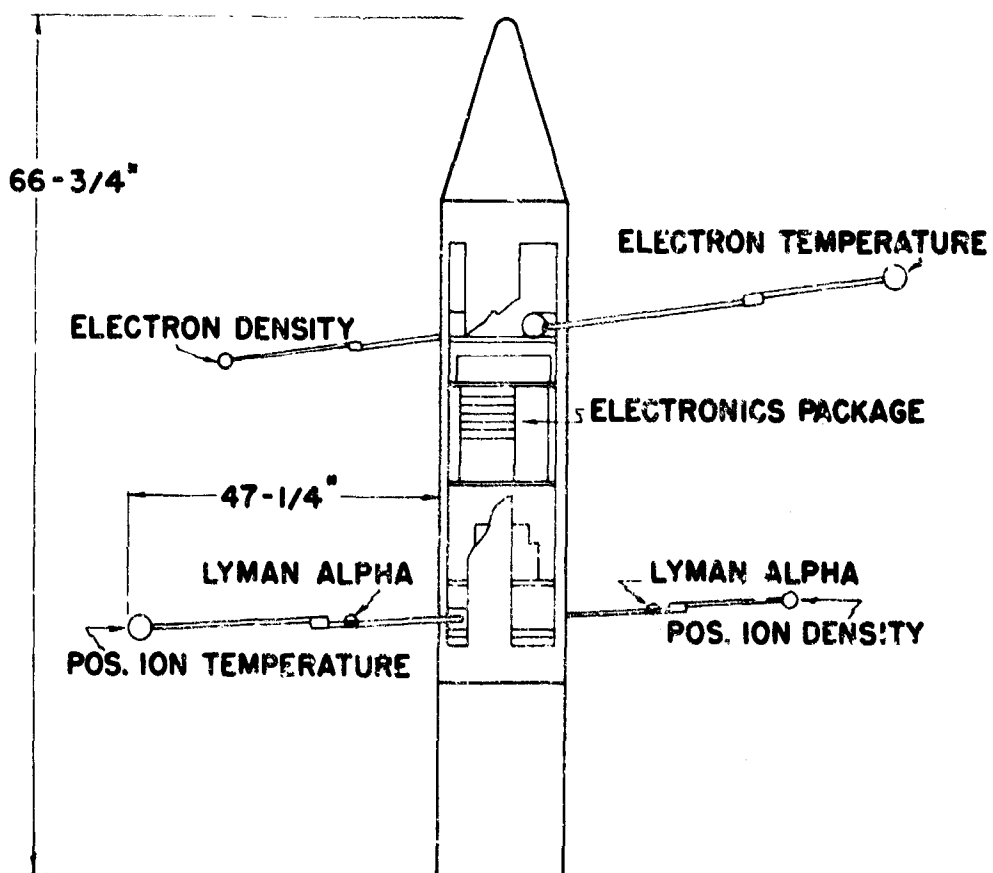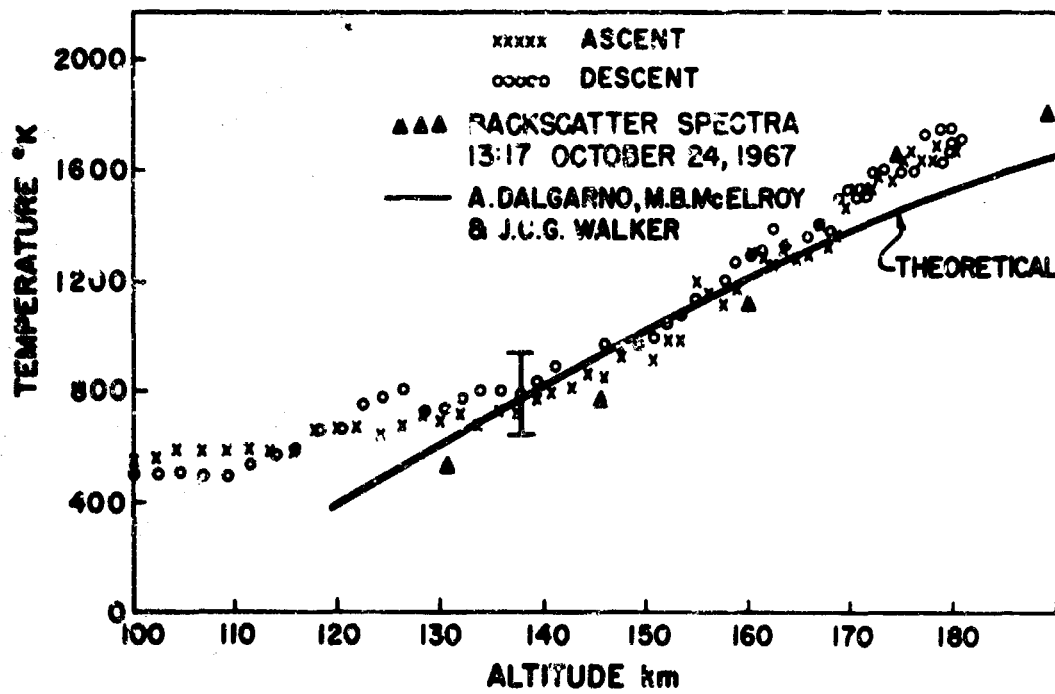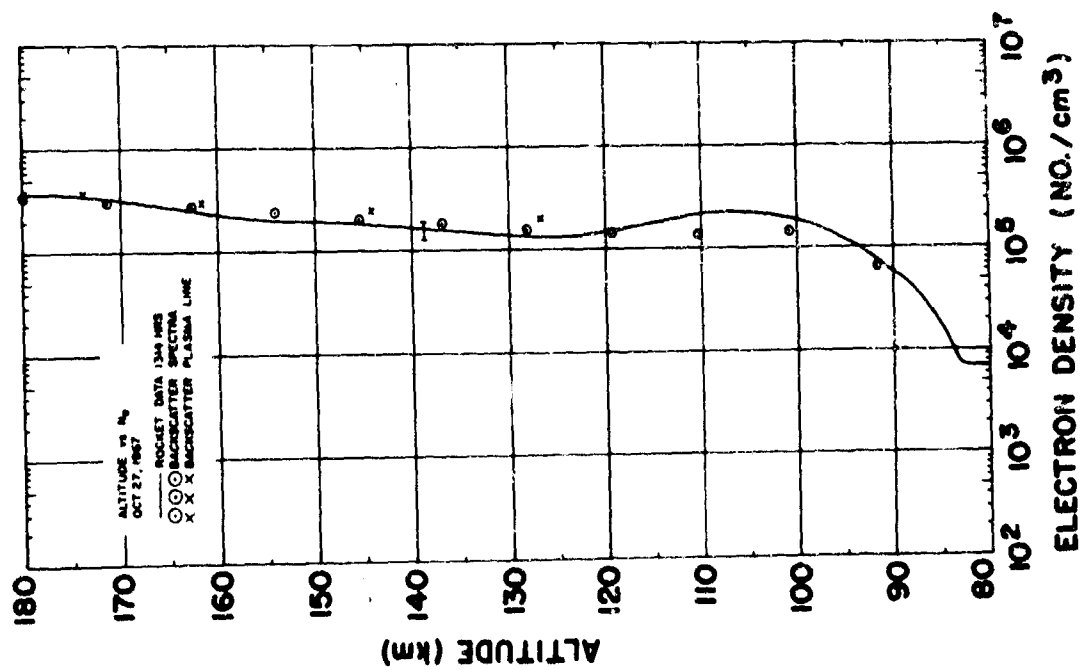
Figure 1



Figure 2
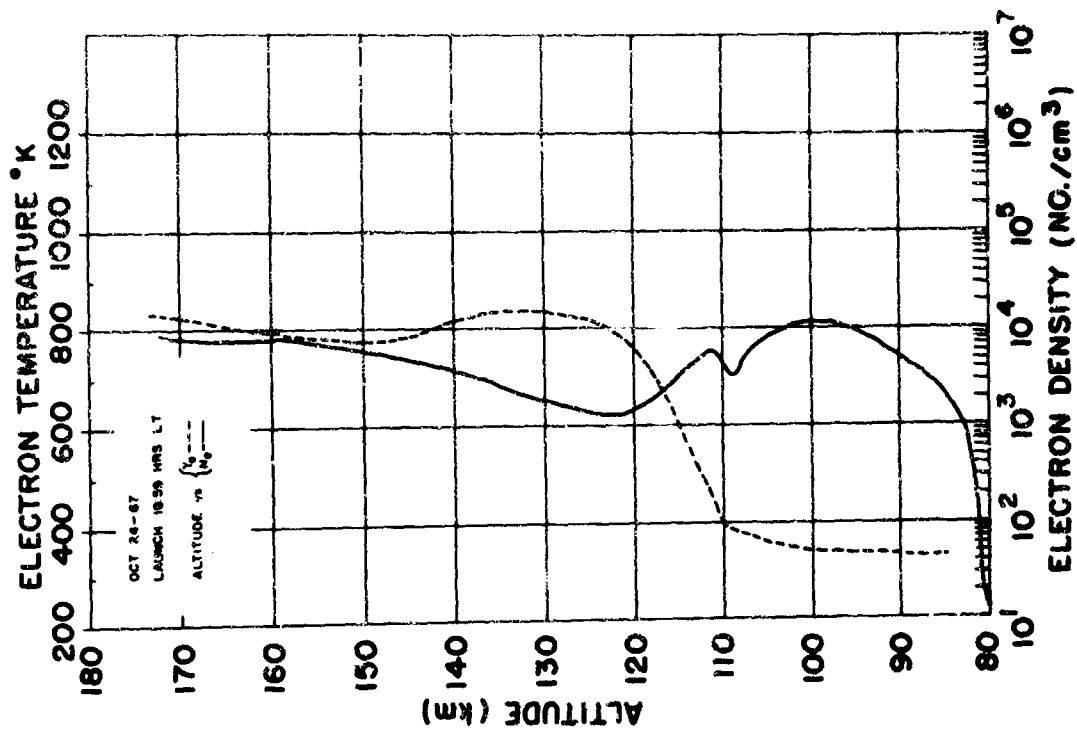
Figure 3

Figure 5



Figure 4

V-9

SIMULTANEOUS RADAR, AIRCRAFT, AND
METEOROLOGICAL INVESTIGATIONS OF CLEAR-AIR TURBULENCE

By

Kenneth M. Glover

Roland J. Boucher

Hans E. E. E. Ottersten

Kenneth R. Hardy

W-1

# Simultaneous Radar, Aircraft, and Meteorological Investigations of Clear Air Turbulence

ABSTRACT

Simultaneous studies of the lower 15 km of the atmosphere by multi-wavelength radar, jet aircraft, and special radiosondes have been conducted at the JAFNA radar facility at Wallops Island, Va. Probably the most important result is that for the particular aircraft and velocity used in these experiments, every clear air radar echo above 3 km has been associated with aircraft reports of at least some perceptible degree of turbulence. Between the altitudes of 3 and 6 km, all CAT was detected by the radars; however, the ability of the radars to detect weak CAT decreased with increasing altitude and only the more intense turbulence was detected above 12 km. The indications are that more sensitive radars than those at Wallops Island should make it possible to detect most, if not all, of the significant CAT up to altitudes of at least 15 km.

The vector wind shear appears to be the most significant meteorological factor in specifying clear air turbulence. The presence or absence of turbulence was correctly specified in 89 percent of the cases solely on the basis of shear greater than $0.9 \times 10^{-2}$ sec$^{-1}$.

# BIOGRAPHY

## Roland J. Boucher

Mr. Roland J. Boucher is a research physicist at AFCRL and is employed at the Weather Radar Branch of the Meteorology Laboratory. Mr. Boucher is concerned with the meteorological aspects of the Clear Air Turbulence study at Wallops Island, Virginia and is also conducting experiments with Doppler radar to determine the characteristics of turbulent structure within the boundary layer.

Prior to joining AFCRL Mr. Boucher was employed as a senior scientist by a private research organization in the Boston area where he conducted applied research in radar and satellite meteorology. Earlier positions include those of Research Meteorologist at Harvard University Blue Hills Observatory; District Forecaster, U. S. Weather Bureau; Research Associate at M. I. T. and NYU; and meteorologist with transoceanic airlines.

Mr. Boucher holds the degree of M.S. in Meteorology from M.I.T. and B.S. from St. Michael's College, Vermont. He is vice chairman of the AMS Committee on Radar Meteorology and has published papers on radar and satellite meteorology in the Journal of the AMS.

# BIOGRAPHY

## Kenneth M. Glover

Mr. Kenneth M. Glover is a research physicist with the Meteorology Laboratory, AFCRL. Since 1964, he has been investigating the nature of all targets responsible for radar backscattering from the clear atmosphere and the role of these scatterers as tracers of atmospheric motions. He has also conducted theoretical and experimental research in the radar backscattering properties of simulated atmospheric structure and in system analyses of several techniques for the indirect probing of atmospheric parameters. Prior to joining AFCRL in 1962, Mr. Glover was employed as a electronic scientist by a private electronics firm and also served as an instructor of mathematics in the evening school at Indiana Central College. He received an AB in mathematics and an M.S. in physics from Miami University (Ohio) in 1958 and 1960 respectively. Mr. Glover has published 14 papers in radar meteorology and related fields.

## BIOGRAPHY

### Kenneth R. Hardy

Dr. Kenneth R. Hardy is a research physicist in the Meteorology Laboratory, AFCRL, and is currently Chief of the Weather Radar Branch. Over the past three years, he has been investigating the nature of the targets responsible for radar echoes in the clear atmosphere and how these echoes may be utilized for deducing atmospheric structure. Previously, he carried out research on the structure of hurricane rain bands and on the nature of the particles within severe thunderstorms as determined by radar observations. Prior to joining AFCRL in 1963, Dr. Hardy was employed by the University of Michigan where his assignments were in research in cloud and precipitation physics, radar meteorology, atmospheric diffusion, and in teaching. In 1957 he was employed by a private meteorological consulting firm where he participated in weather modification studies, and from 1953 to 1957 he was employed by the Canadian Meteorological Service as a Meteorological Analyst and Forecaster. He received an A.B. with honors in physics in 1952 from the University of Saskatchewan, an M.A. from the University of Toronto in 1953 and a Ph.D. in meteorology from the University of Michigan in 1963. He has won the Canadian Award of the Darton Prize of the Royal Meteorology Society, and has published 17 papers in various scientific journals.

# BIOGRAPHY

## Hans Ottersten

Mr. Hans Ottersten is a research physicist with the Weather Radar
Branch of the AFCRL Meteorology Laboratory. Since joining AFCRL in 1966,
he has been investigating theoretical and experimental aspects of the
probing of the clear atmosphere with electromagnetic waves, and the radar
detection of clear air turbulence in particular. From 1961 to 1966
Mr. Ottersten was employed by the Research Institute of National Defence
in Stockholm, Sweden, where his assignments as a senior research engineer
were in theoretical and experimental studies of the influence of the
troposphere on microwave propagation in order to establish the consequences
for the performance of various electronic systems in military applications.
Mr. Ottersten received his Master of Electrical Engineering from the
Royal Institute of Technology in Stockholm, Sweden, in 1962. He is the
author or co-author of 11 papers in the field of radio meteorology and
tropospheric radio wave propagation.

# 1. INTRODUCTION

Since 1965, the sensitive multiwavelength radar facility at Wallops Island, Va., has been used to investigate the nature of clear air radar echoes, and in particular to evaluate the use of radar as a sensor for clear air turbulence (CAT). The use of radar for CAT detection has been prompted by the fact that the radar backscattering from clear air regions is related to the mean gradient of potential refractive index and to the degree of turbulence. The sharper the original mean gradient and the more violent the turbulent mixing, the stronger the inhomogeneities that will be created; consequently, the radar scattering will be increased. There is, however, a large gap between the eddy sizes that affect aircraft and those that create the inhomogeneities detectable by radar. The radars are sensitive only to refractive index variations over scales of one-half the radar wavelength. Thus, for the 10.7-cm and 71.5-cm wavelength radars at Wallops Island, eddy sizes of about 5 and 35 cm are detected. On the other hand, aircraft are responsive mainly to turbulent eddies over scales ranging from about 10 to 1000 m, the high values applicable to heavy, high-speed aircraft. Because the energy at large eddy sizes is broken down into smaller and smaller eddies, radar measurements should provide some information on the turbulent kinetic energy at the larger scales.

It is postulated that at least three conditions are necessary before turbulence of considerable intensity will develop. First, the wind shear must progress beyond the point where the shearing stresses produce a fully developed turbulent flow despite the stabilizing influence of negative buoyancy. Second, some irregularity in the flow must be present in order to initiate the transformation of energy from the mean flow into turbulent kinetic energy. The third, and most basic, condition is that the initial lapse rate must be strongly stable in order to allow a strong vertical wind shear to build up before the turbulent motion is induced. The larger the original shear, the larger will be the turbulent kinetic energy that is extracted from the mean flow, and the more violent will be the turbulence and its effect on aircraft.

The consequence of the above argument for radar measurements is that at high altitudes, a correlation between the degree of turbulence and the magnitude of the mean vertical gradient of potential temperature should be apparent in the sense that large temperature gradients are necessary for the development of strong turbulence. Large temperature gradients may of course exist even though wind shears are small, but in such a case the small-scale inhomogeneities that give rise to radar signals are not intense enough to be detected. Consequently, turbulence of considerable intensity should be associated with large stable mean vertical gradients of potential temperature. For the radar, this means that the backscattered signal intensity will be at least a crude quantitative measure of the degree of turbulence.

The preceding qualitative discussion may be described with the aid of the gradient Richardson number

$$Ri = \frac{g}{\theta} \frac{\partial\theta/\partial z}{\beta^2},$$

where $g$ is the acceleration due to gravity, $\partial\theta/\partial z$ is the lapse rate of potential temperature, and $\beta$ is the vertical wind shear. Here we are not concerned with negative Ri's because for these cases, buoyancy forces are actually contributing to the turbulent kinetic energy. We do not consider such situations to be representative of the conditions we want to discuss. The Richardson number may be taken as an indicator of the relative strength of the stabilizing influence of negative buoyancy and the turbulence-inducing forces from wind shear. Large Ri's are indicative of stability, where every turbulent disturbance or irregularity will decay rapidly with time. Small Ri's indicate that a fully developed turbulent flow will be maintained: values less than 0.5 are likely to be characteristic of developed turbulent flow. Low Ri's are a necessary condition for strong turbulence; however, it is not a sufficient condition, because a low Ri may arise from a small $\partial\theta/\partial z$ in association with small $\beta$ values indicative of weak turbulence. We consider that Ri cannot be used for any quantitative estimate of the degree of turbulence but has to be regarded as a discriminator between regions where the turbulent flow is developed and regions of high stability where every turbulent disturbance is suppressed. The additional requirement for high turbulence intensities is large $\beta$ values, which we think cannot occur except in regions of high $\partial\theta/\partial z$.

This paper deals with the results of simultaneous probes of the lower 15 km of the atmosphere for clear air turbulence (CAT) by multiwavelength radar, jet aircraft, and special rawinsondes. The experiments were conducted from December 1967 through March 1968, during which a total of 58 flights of uninstrumented aircraft of the jet fighter type (F-100, F-86, and F-4) were made in the region surrounding the Wallops radars.[*]


2. MEASUREMENT TECHNIQUE


The measurement technique is illustrated in Figure 1. Each set of observations began with with an aircraft ascent at a rate not exceeding 700 m/min, from a height of 8 km to approximately 15 km, along an 18-km-diameter spiral path. Occasionally, spirals from 3 km upward were obtained. About every 10 to 15 sec the pilots reported their altitude and qualitatively estimated the severity of any turbulence encountered; these data were recorded on tape throughout the flight. Upon completion of the spiral ascent,

---

[*]During the period of the observations, the essential radar characteristics were: minimum detectable reflectivity at 15-km range = $2.2 \times 10^{-15}$, $1.3 \times 10^{-17}$, and $1.8 \times 10^{-18}$ cm$^{-1}$; beamwidths = 0.21°, 0.48°, and 2.9°; pulse length = 2.0, 2.5, and 5 $\mu$sec; and wavelengths = 3.2, 10.7, and 71.5 cm, respectively.

the aircraft were directed to the highest altitude either reported as or suspected of being turbulent, and a ground controller then vectored the aircraft along a horizontal racetrack pattern approximately 60 km from end to end. During horizontal flight, the aircraft generally maintained a relatively constant indicated airspeed of 260 ± 10 m/sec. Upon completing each racetrack, the aircraft decreased altitude by 300 m and then resumed the racetrack course until the entire turbulent altitude region was penetrated in closely spaced vertical intervals. Each flight consisted of these horizontal passes through as many such turbulent regions as possible during the approximately 1 hr of flying time available. When necessary, aircraft soundings of the higher altitudes were given first priority. The radar procedure consisted primarily in taking slow elevation scans (1.0°/sec) at azimuths corresponding approximately to the azimuth of the aircraft as reported by an ancillary tracking radar. From photographs of the three radar displays, it was possible to determine both the location and extent of each clear air layer (Hardy et al., 1966). Aircraft probes were requested for an altitude interval extending approximately 300 m above and below each clear air radar echo. Temperature, humidity, and wind profiles representative of the conditions during the aircraft and radar observations were obtained from the ascent of a tandem pair of standard USWB radiosondes, with one sonde modified to provide a continuous record of temperature.

## 3. RESULTS

Thirty-nine aircraft flights on 31 days provided reports of CAT between the altitudes of 3 and 15 km. In general, radar and meteorological observations were taken during each flight. There were, however, some flights for which one or more data sources were inoperative. As a result, there are some slight but insignificant differences in the flights compiled in the radar and meteorological results that follow.

### 3.1 Radar and Aircraft Observations of CAT

Reports of CAT during 36 flights were broken down into a relative scale based upon the pilot's comments of none, light, moderate, and severe CAT, or combinations of these terms. Altitude profiles of turbulence intensity were constructed from these reports and compared with similar composite profiles of radar-echo height obtained from the radar photographs. The radar data were restricted to observations obtained when: (1) the aircraft was within the maximum radar range of 37 km, at which high-altitude clear air echoes are generally detected with the Wallops radars and (2) there were no clouds within 300 m of the aircraft reporting position. From these data, 176 cases were obtained. Each case consisted of a 1-km altitude characterized by the maximum CAT intensity in the interval, and the presence or absence of a corresponding clear air radar echo. For a confirmed radar detection, we required at least two successive

photographs that showed radar echoes occurring at the same altitude as the aircraft report of CAT. No further consideration was given to a particular altitude interval unless all these criteria were satisfied.

The 176 cases of simultaneous radar and aircraft observations are summarized in Figure 2, where the observed incidence of CAT and the presence or absence of corresponding radar clear air echoes are arranged according to altitude and CAT intensity intervals. The clear regions represent those cases where the aircraft and radars gave identical indications of the existence of CAT, whereas the hashed areas represent those cases in which CAT was not detected by the radars. Probably the most obvious and the most important result is that for the particular aircraft and velocity used in these experiments, every clear air radar echo above 3 km has been associated with aircraft reports of at least some perceptible degree of turbulence. At the lower altitudes, where the influence of water vapor upon the gradient of refractive index is strongest, this somewhat surprising result suggests that turbulence of a strength at least perceptible to an aircraft must be present to create detectable refractive index variations even if the mean gradient of refractive index is fairly strong.

From these data, it is quite evident that the detection capability of the Wallops radars decreases with increasing altitude. Between 3 and 6 km, the radars detected turbulent regions with a perfect score; all cases of CAT, regardless of intensity, were detected by the radars. With increasing altitude, however, the percentage of cases detected decreased; above 12 km, most regions of CAT were not detected by the radars. Such a result was to be expected since the influence of water vapor upon the mean gradient of refractive index also decreases with increasing altitude.

The percentage of cases detected within each of the individual altitude intervals has also been computed by regrouping the turbulence intensities according to two categories: (1) less than light and (2) light or greater. As shown in Table 1, these observations clearly demonstrate that as the detection capability of the radars decreases with altitude, the stronger CAT is consistently more likely to be detected than the weaker-intensity turbulence is. This general result is consistent with the thesis of Atlas et al. (1966) that at the higher altitudes, where the mean gradient of potential

Table 1. Percentage of Observed CAT Detected by Wallops Island Radars

| CAT Intensity | Altitude | | | |
|---|---|---|---|---|
| | 3-6 km | 6-9 km | 9-12 km | 12-15 km |
| Less Than Light | 100% | 38% | 21% | 0% |
| Light or Greater | 100% | 100% | 41% | 17% |

refractive index is considerably reduced, turbulence intense enough to significantly affect aircraft is a necessary condition before a clear air stratum can be detected with radars comparable to those of the Wallops Island facility.

It is not surprising that the Wallops Island radars fail to detect all turbulence at the higher altitudes. Using relationships developed by Ottersten (1968), it is possible to deduce a probable minimum value of the energy dissipation rate (a measure of the turbulence intensity) that would be detectable with these radars at high altitudes. Assuming a potential temperature gradient of $1.3 \times 10^{-4}$ °C $cm^{-1}$ and a shear of $10^{-2}$ $sec^{-1}$, the minimum detectable energy dissipation rate at a range of 15 km is 0.6 $cm^2$ $sec^{-3}$. For the aircraft velocities used in these experiments, this value would probably be classified as light-to-moderate according to a scale given by MacCready (1964). These radars are therefore not sufficiently sensitive to regularly detect light-to-moderate CAT in the upper troposphere or lower stratosphere. As also noted by Ottersten (1968), however, strong CAT at high altitudes will generally be associated with zones of increased variability in the atmospheric refractive index. This result, when added to the experimental results presented above, suggests that radars more sensitive than those at Wallops Island should make it possible to detect most, if not all, of the significant CAT up to altitudes of at least 15 km.

Radar echoes from altitudes above approximately 5 km were stratified, relatively thin (0.1 to 1.5 km), and — at 10.7-cm wavelength — somewhat patchy (horizontal dimensions on the order of 5 to 30 km). More-over, the echoes were not particularly persistent, often lasting for less than a few tens of minutes. A similar horizontal stratification and patchi-ness was evident in the aircraft encounters with CAT. The transitory nature of both the radar and aircraft observations prohibited a detailed comparison of radar echo and CAT intensities.

## 3.2 Meteorological Analysis of CAT

CAT reports from a total of 29 flights were correlated with Richardson number (Ri) and vertical vector wind shear (β) derived from the special rawinsondes released from Wallops Island USWB station. With few excep-tions, the rawinsonde observations were made during or within 1 hr of the flight time. For purposes of the meteorological analysis, the aircraft CAT reports were grouped into four categories: (1) negligible (smooth or very, very light), (2) very light, (3) light, and (4) light-to-moderate and moderate. No CAT of intensity greater than moderate was encountered. From the aircraft and rawinsonde data, 127 cases were obtained. Each case consisted of an altitude interval of about 1 or 2 km, characterized by the presence or absence of aircraft-detected CAT. Most of the turbulence episodes were contained within single intervals. Each interval consisted of two or more subordinate layers a few hundred meters in depth, having quasihomogeneous lapse rates and wind shears. Values of Ri and β were computed for each layer on the basis of the original detailed rawinsonde

records. The lowest Ri value and its corresponding $\beta$ within the interval were used to characterize the entire interval. With minor exceptions, the lowest Ri also corresponded to the highest $\beta$ in the interval.

An illustration of the method of analysis is given in Figure 3 for 26 January 1968. The diagram shows the regions of CAT, the radar layers, and the rawinsonde data. The heavy segments of the temperature curve represent the layers used in the computation of Ri, and the intervals or "cases" of CAT or no CAT with their corresponding Ri and $\beta$ are marked with vertical arrows. A profile of CAT intensity is shown at the right of the sounding. At a particular height, the indicated CAT intensity corresponds to the maximum intensity encountered by the aircraft, regardless of its horizontal position or the time spent at that altitude. For the case in Figure 3 the tropopause is irregularly developed, but the main tropopause is just above 12 km. The flight encountered two regions of CAT below this height. No definite radar detection was obtained from the region of light CAT near 12 km, but the region of moderate CAT between 10.5 and 11.2 km was detected. In the region of light CAT, there is no obvious relationship between the CAT and the meteorological profiles; however, the lower region of moderate CAT is characterized by a stable lapse rate and strong shear.

From the meteorological analysis of the 127 cases, it was found that a Richardson criterion of Ri < 2 could serve as an indicator in specifying regions of CAT. However, the data show further that the prediction of CAT improves if, in addition to the Richardson criterion, a shear criterion of $\beta \geq 0.9 \times 10^{-2}$ sec$^{-1}$ is employed. This general result is consistent with the thesis outlined in the introduction that the requirements for strong CAT are low Richardson numbers and, in addition, strong vertical wind shears.

A closer look at the data further revealed that the shear criterion, $\beta \geq 0.9 \times 10^{-2}$ sec$^{-1}$, would alone serve as well as the combined Richardson and shear criterion in specifying regions of CAT. The reason for this is that for the cases of strong shear the associated Richardson number is generally low. Once a shear criterion is applied, an additional Richardson criterion will not substantially change the specification of turbulent regions. It appears that on the basis of rawinsonde data, a shear criterion alone is a successful indicator in specifying regions of turbulence that will affect aircraft.

This result is demonstrated further in Figure 4, which is a histogram displaying the incidence of CAT in 127 cases grouped into four categories of wind shear and four categories of CAT intensity. From Figure 4 it is evident that both the incidence and intensity of CAT increase sharply as the vertical wind shear $\beta$ increases; 85 percent of the cases with $\beta < 0.5 \times 10^{-2}$ sec$^{-1}$ had negligible turbulence; 43 percent of the cases with shears between 0.5 and $1.0 \times 10^{-2}$ sec$^{-1}$ were turbulent although only 18 percent had intensities of light or greater. For wind shears between 1.0 and $1.9 \times 10^{-2}$ sec$^{-1}$, 64 percent of the cases were turbulent, with 38 percent of an intensity light or greater. For wind shears exceeding $2.0 \times 10^{-2}$ sec$^{-1}$, turbulence occurred in 75 percent of the cases, and 60 percent had

turbulence of light or greater intensity. The probabilities of CAT indicated by our data may not apply to normal level flight, however, since the project aircraft probed the regions in depth. With the particular aircraft and velocity used in our experiment, the wind shear criterion $\beta \geq 0.9 \times 10^{-2}$ sec$^{-1}$ applied to rawinsonde data specified the occurrence or non-occurrence of very light or stronger CAT correctly in 69 percent of the entire group of 127 cases from 29 separate flights, including 74 percent of the turbulent cases and 93 percent of cases involving CAT greater than light.

In our estimation, these results do not contradict earlier results, especially those of Penn and Pisinski (1967), which have demonstrated good correlation between low Richardson numbers and the incidence of turbulence and have also certainly revealed the importance of the vertical wind shear as an energy source for turbulence. Simultaneously we must emphasize that the limited resolution in our temperature and wind data prevents a quantitative comparison with the results obtained by Penn and Pisinski. Standard radiosonde measurements tend to underestimate temperature gradients and, in particular, vertical wind shear. Clear air turbulence often appears in thin layers extending vertically for about 100 m. The limited resolution in the radiosonde wind profiles prevents an accurate estimate of the vertical wind shear over such small height intervals. The deduced shear values can be severely underestimated, and consequently the estimates of Richardson's numbers will be too high.

Despite the limited resolution in rawinsonde data, it appears feasible to use wind shear criteria based on rawinsonde winds for the delineation of regions in the atmosphere, where the probability of aircraft encounters with significant turbulence is high. Further, it is interesting to note that all 14 cases of CAT with light-to-moderate or greater intensity occurred in altitude regions where the rawinsonde indicated a layer of increased stability. This is consistent with the thesis that strong vertical wind shear, which is a necessary condition for strong CAT, can develop only in the vicinity of layers of strongly stable temperature lapse rates. The consequence is that strong CAT will generally be associated with zones of increased variability in the refractive index. Since the radar backscattering from the clear air will be enhanced at these regions, it appears that radars of sufficient sensitivity should be a powerful tool in detecting CAT.

## ACKNOWLEDGMENTS

# REFERENCES

Atlas, D., Hardy, K. R., Glover, K. M., Katz, I., and Konrad, T. G. (1966) Tropopause detected by radar, Science 153: 1110-1112.

Hardy, K. R., Atlas, D., and Glover, K. M. (1966) Multiwavelength backscatter from the clear atmosphere, J. Geophys. Res. 71: 1537-1552.

MacCready, P. B., Jr. (1964) Standardization of gustiness values from aircraft, J. Appl. Meteor. 4: 439-449.

Ottersten, H. (1968) Theoretical aspects of CAT detection by radar, Proc. 13th Radar Meteorology Conf., Amer. Meteor. Soc., Boston, 252-257.

Penn, S., and Pisinski, T. A. (1967) Mesoscale Structure of the Atmosphere in Regions of Clear Air Turbulence. AFCRL-67-0115, AFSG, No. 190.
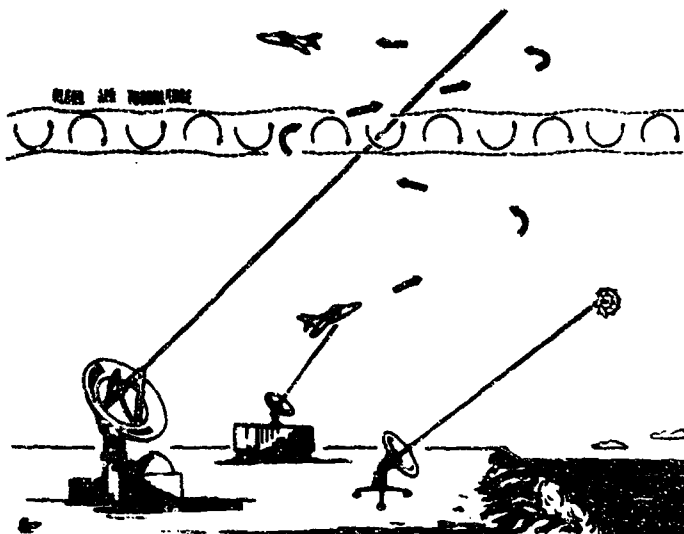
## FIGURE LEGENDS

Figure 1. Artist's concept of the simultaneous probing of the atmosphere for CAT by multiwavelength radar, jet aircraft, and special radiosondes.

Figure 2. Observed incidence of CAT and corresponding radar clear air echoes according to altitude and CAT intensity. Note that in no case was there a radar echo associated with a nonturbulent atmosphere.

Figure 3. Heights of radar echoes, reports of CAT and meteorological soundings. Clear air radar echoes are indicated by the shaded layers, and the profile of aircraft encounters with CAT is given by the heavy line to the right of the sounding.

Figure 4. Observed incidence of CAT according to vertical wind shear and CAT intensity. The magnitude of the shear is given in terms of $\beta \times 10^{-2}$ sec$^{-1}$.
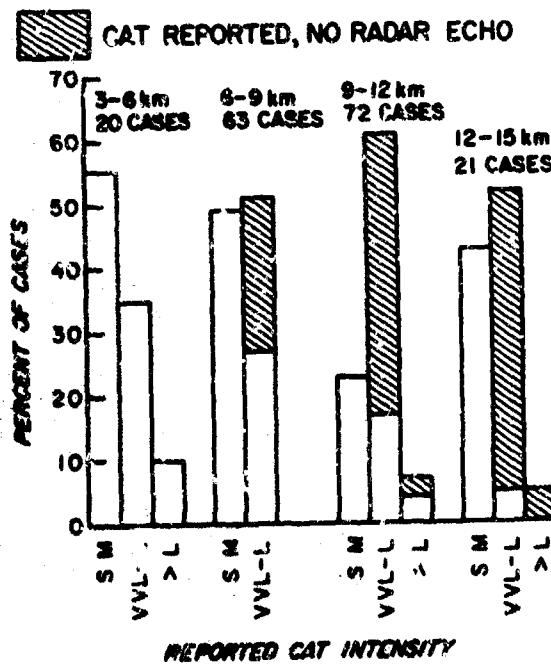
CAT EXPERIMENT

Figure 1



CAT REPORTED, NO RADAR ECHO

REPORTED CAT INTENSITY

Figure 2

Figure 3



REPORTED CAT INTENSITY
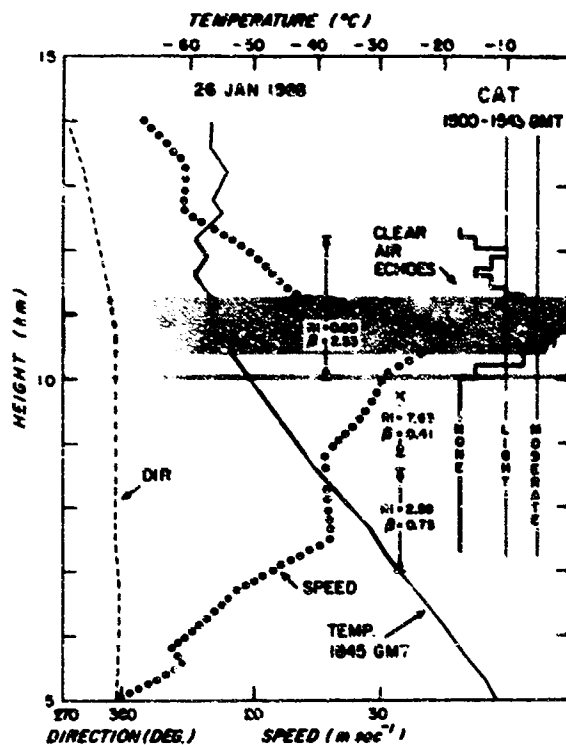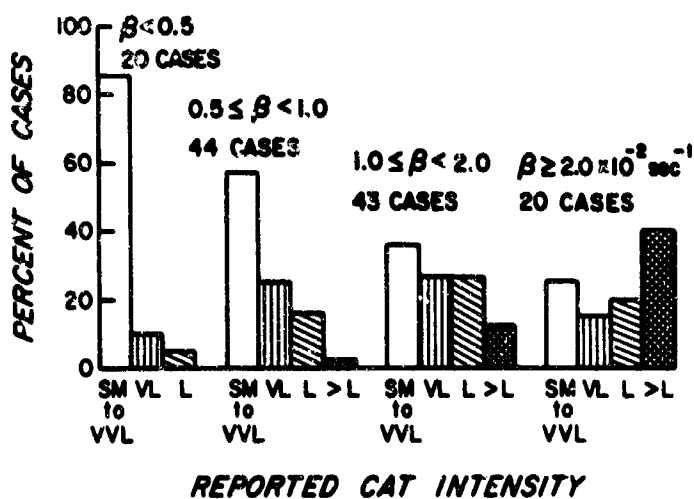
Figure 4

# BALLISTIC-IMPACT FLASH

By

Captain J. B. Abernathy
and
Major William Goldberg

Air Force Institute of Technology
Wright-Patterson Air Force Base, Ohio

X-1

# Abstract

The down range flash from the perforation of thin aluminum plates by steel and aluminum fragment simulators; one half inch diameter cylinders with hemispherical heads; was investigated to determine time, size, and temperature. By comparing the relative intensities of vibrational band structure in the AlO green system an effective vibrational temperature for the flash was determined to be between $3400°K$ and $4100°K$. The overall dimensions of the flash were found to be approximately 14 inches long and five inches in diameter. The time duration was found to be between three and five milliseconds.

## Biographies

John Billy Abernathy was born on 4 February 1936 in Cleveland, Mississippi. He attended the United States Military Academy and graduated in 1958 with a Bachelor of Science degree. After being commissioned in the Regular Air Force, he completed pilot training in 1959. He has served as a Tactical Fighter Pilot in England, Korea, Japan, Okinawa, as well as the United States. In September 1966 he returned from duty in Southeast Asia and entered the Air Force Institute of Technology. He was awarded the degree of Master of Science in Aerospace Engineering in June 1968 and is currently attending the Aerospace Research Pilot's School, Air Force Flight Test Center, Edwards AFB, California.

William Goldberg was born 26 November 1935 in Toledo, Ohio. He was awarded the Bachelor of Science degree in Engineering Physics (cum laude) by the University of Toledo in June, 1957, and commissioned in the United States Army. He served as a guided missile officer at Fort Bliss, Texas, and subsequently entered the Engineering Sciences graduate program at Purdue University. He received the Master of Science degree in June 1961 and was assigned as a research and development officer at the U.S. Army Ballistic Research Laboratories, Aberdeen Proving Ground, Maryland. In September 1964 he was commissioned in the

U.S. Air Force and returned to graduate study at Purdue University, majoring in Engineering Mechanics. He was awarded the degree of Doctor of Philosophy by Purdue University in June, 1967, and is presently assigned as an Assistant Professor of Mechanics, Air Force Institute of Technology, School of Engineering.

BALLISTIC IMPACT FLASH*

## I. Introduction

Experience has shown that modern jet aircraft are vulnerable to frag-
ments and projectiles fired by conventional air defense weapons. In order
to design survivability into an aircraft, the engineer must know the effect
of fragment penetration of thin plates. Unfortunately, research in pone-
tration mechanics historically has only been active during periods of need,
(wartime). Thus, there is still no theory available which adequately de-
scribes the process of ballistic perforation of a thin elastic plate by a
fragment. One interesting and important part of this impact and penetra-
tion process is the resulting flash. This flash or spark has been found to
be capable of causing fires in aircraft fuel systems.

The object of this investigation is, therefore, to describe one as-
pect of the impact mechanism; specifically, the flash of light resulting
from the impact of high-speed fragment simulator projectiles on thin alu-
minum plates. The temperature and duration of the flash are the primary
areas of interest.

### Background

One of the first extensive investigations of impact flash phenomena
was made by Norman Brown (Ref 7) in 1948. His method involved estimates
from still pictures and use of a high-speed framing camera to determine
time sequence and duration. In 1952 R. L. Kahler (Ref 19:1-7) observed
that an inert atmosphere reduced the impact flash, and that pure oxygen
enhanced the flash. His results confirmed Brown's finding that reduced
pressure reduced the flash. In 1952 Roland G. Bernier (Ref 4) conducted a
series of tests with various target and projectile combinations. His find-
ings related projectile mass, density, and velocity to the flash size and
duration. In 1955 W. T. Thompson (Ref 33:80) published a report on armor
penetration in which he suggested that the target-projectile interface was
molten. The existence of the molten interface formed the basis for R. F.
Recht's theory of impact failure, which he called "Catastrophic Thermoplas-
tic Shear." (Ref 29:189) He proposed that failure occurred when the local
rate of change of the temperature had a negative offect on strength which
was equal to or greater than the positive effect of strain hardening.
Joseph M. Krafft (Ref 23:1249) conducted a series of experiments to esti-
mate the percentage of projectile striking energy that was absorbed by
sliding friction. He found that for "mechanically" clean surfaces the

---

*Based on a thesis submitted by John B. Abernathy in partial fulfill-
ment of the requirements for the degree of Master of Science in Engineering
at the Air Force Institute of Technology, Wright-Patterson Air Force Base,
Ohio.

friction accounted for 3% of the energy loss, but ordinary handling introduced enough lubricant to reduce the loss to less than 1%. In 1960 D. D. Keough (Ref 20) used a photo-multiplier system to detect flashes from microparticles at higher velocities. His work was an indication of the shift in emphasis to space application and micrometeorite particle detection. He reported that reduced atmospheric pressure resulted in longer rise times for the flash luminosity although other descriptors remained unchanged. The more recent investigations have been primarily concerned with space applications and hence, have usually been in the hypervelocity range. In 1964 F. W. MacCormack (Ref 24) made a thorough investigation of the impact flash at hypervelocities and low ambient pressure. He concluded that microscopic particles of ejecta emerge, and due to high-speed aerodynamic effects heat, ablate, and radiate in the manner of meteors. A. P. Caron (Ref 10) suggested that the pyrophoric oxidation reactions of the impacted projectile and target material with gaseous oxygen were the cause of the luminosity. He used the ideas of Bull (Ref 9) and Bjork (Ref 5) to show that the impact compressed the target and projectile to high pressures and temperatures. The "excited" ejecta particles were thrown into the gaseous oxygen where oxidation could take place with the finely dispersed metal.

Backman and Stronge (Ref 2) have recently (1967) correlated luminosity with the vapor-phase-combustion process. Their conclusions are similar to those of MacCormack; the high speed flow causes the material ejecta to heat and ablate, and then burn in the oxygen atmosphere.

## II. Physical Model

The overall physical model of the flash can be divided into three phases. The material must be removed from the plate by the rupture phase. Then, because of high speeds the particles are heated, and the surfaces melt and flow during the ablation phase. Finally, the exposed surface area and the oxygen available in the atmosphere combine chemically giving the burning phase.

### Rupture Phase

Thompson's discussion of a dynamical approach to armor penetration (Ref 33), Krafft's experiments on friction (Ref 23), and Recht's thermoplastic shear (Ref 29) have presented careful documentation for increased temperatures in the particles being ejected by a ballistic impact. Although the velocities of this investigation do not qualify as hypervelocity, the qualitative arguments of Bjork and Olshaker (Ref 5) certainly are applicable in that the material has been shocked to a higher energy state and during the recovery retains a percentage of that energy. There can be little doubt that the particles torn from the target plates during the impact are at an increased temperature. The discussion by Rinehart (Ref 31) of spalling and scabbing indicates a mechanism for thrusting excited particles into a stream of down range ejecta.

## Ablation Phase

The ignition of the particles is most likely a surface burning phenomena (Ref 14:20). If the particles are subjected to high speed flow, the surrounding gas envelope would melt the material and hence ablate, continuously exposing new surface area and also providing smaller particles or droplets for the burning phase.

## Burned Ejecta Phase

T. H. Rautenberg and P. D. Johnson (Ref 28) investigated the characteristics of the Aluminum-Oxygen reaction in flashbulbs. By comparing the spectral lines of aluminum and sodium; known to be in thermal equilibrium with the other degrees of freedom in flames (Ref 13:169), they concluded that since all the temperatures observed were essentially the same, the AlO system was excited thermally rather than directly by the arc. The enhanced energy production by aluminum powders in explosives and rocket fuels led to extensive investigation of the mechanism of reaction. Irvin Glassman (Ref 14), R. W. Bartlett, et al (Ref 3), Andrej Macek (Ref 25), and Thomas Brzustowski (Ref 8) were primary workers in the field. The ultimate model for combustion appears to be a diffusion controlled flame front surrounding the solid or liquid metal core. (See Figure 1). Brewer and Searcy (Ref 6) investigated the $Al-Al_2O_3$ system in an effusion cell, and from the vapor pressure measurements they obtained a boiling point of $3800° < 200°K$ for $Al_2O_3$. Glassman asserted (Ref 14:5) that the boiling point of the oxide might be taken as the combustion temperature. Aluminum is in the category of metals which have a vaporization temperature for the oxide ($3800°K$) greater than the vaporization temperature for the pure metal ($2720°K$), and hence it follows the model of Figure 1.

### III. Spectroscopic Temperature Measurement

#### Theory

The intensity of spectral line structure in emission, $I_{em}^{nm}$, is defined as the energy emitted by the source per second. If there are $N_n$ atoms in the initial state, and if $A_{nm}$ is the fraction of atoms in the initial state carrying out the transition to $m$ per second then:

$$I_{em}^{nm} = N_n hc\nu_{nm}A_{nm} \tag{1}$$

where $hc\nu_{nm}$ is the energy of each light quantum of wave number $\nu_{nm}$ emitted in the transition. $A_{nm}$ is the Einstein transition probability of spontaneous emission and is given as:

$$A_{nm} = \frac{64\pi^4 \nu_{nm}^3}{3h} \left| \vec{R}_{nm} \right|^2 \qquad \text{(Ref 1; 7-176)} \tag{2}$$

where $\vec{R}_{nm}$ (transition moments) are the matrix elements of the electric dipole moment $\vec{R}$ of the system.

The term "band spectrum" is used to designate a spectrum which originates from either emission or absorption in the molecules of a compound. The intensity of band system structure depends on three things: (1) the frequency $v'$, (2) the number of molecules in the initial state, and (3) the transition probability.

## Frequency

The energy associated with a molecule may be separated into three elements which are: (1) electronic, due to changes in outer electronic structure; (2) vibrational, due to vibration of the component atoms relative to each other; and (3) rotational, due to rotation of the molecule as a whole about the center of gravity. To indicate the division of energy in molecular spectra, the wave number or term value expression is usually given: $T = To + G + F$ where:

$$To = \text{electronic term value}$$

$$G = \text{vibrational term value}$$

$$F = \text{rotational term value}$$

When discussing a particular transition, $v' \rightarrow v''$, the wave number corresponding to the transition is given by:

$$v = T'-T'' = (T'_e - T''_e + (G'-G'') + (F'-F''))  \qquad (3)$$

or
$$v = v_e + v_v + v_\gamma  \qquad (4)$$

For a given electronic transition $v_e$ is a constant representing the difference between the two minima of the energy states; and since, in general, F is small compared to G, $v_\gamma = (F'-F'')$ may be neglected. These simplifications result in a coarse structure of the electronic transition which may be called the vibrational structure since $v_v$ is the only variable. Hence the form of the wave number expression is:

$$v = v_e + \omega''_e(v''+1/2) - \omega''_e x''_e (v''+1/2)^2 + \ldots - [\omega''_e(v''+1/2) - \omega''_e x''_e(v''+1/2)^2 + \ldots]  \qquad (6)$$

where: $\omega_e$ = vibrational frequency (cm)
$\omega_e x_e$ = amplitude of first overtone or second harmonic

and $\omega_e x_e < \omega_e$, as are all coefficients on successive terms in the two expansions. Since there are no strict selection rules for vibrational quantum numbers, equation (5) represents all possible transitions between the different vibrational levels of the two participating electronic states.

## Population

The distribution of molecules may be determined from the Maxwell-

Boltzmann law when thermal equilibrium exists. Since only discreet values of vibrational energy are possible, the number of molecules in each of the vibrational states is proportional to the Boltzmann factor

$$\exp[-E/KT]$$

where: $E = G(v')hc$

   $G(v')$ = vibrational term value ($cm^{-1}$)

   $h$ = Planck's constant ($6.623 \times 10^{-27}$ erg-sec)

   $c$ = speed of light in vacuum ($2.998 \times 10^{10}$ cm/sec)

   $K$ = Boltzmann's constant ($1.38033 \times 10^{-16}$ erg/degree)

   $T$ = absolute temperature (degrees Kelvin)

The quantity $\exp[-G_0(v')hc/KT]$ gives the relative number of molecules in each vibrational level referred to the number of molecules in the lowest vibrational level. The total number of molecules $N$ is proportional to the sum of the Boltzmann factors over all states, (the partition function).

$$Q_{v'} = 1+\exp[-G(o)hc/KT]+\exp[-G(1)hc/KT]+... \tag{6}$$

Therefore, the number of molecules in the state $v'$ is

$$Nv' = \frac{N}{Q_{v'}} \exp[-G(v')hc/KT \tag{7}$$

## Transition Probability

The Franck-Condon principle for emission relates the transition probability to band intensity. According to the principle, (Ref 37:315) electronic transitions to lower energy states take place at constant internuclear distance (i.e. vertical lines in Figure 2). In order to avoid a discontinuity in velocity the lower state selected must also be one with the same turning point location.

In Figure 2 the transitions from A and B are more probable because the molecule spends more time near the turning points. If there is to be no change in position and velocity, immediately after the jump the molecular positions would be F and C respectively (i.e. vertically below the turning points) this would produce two vibrational intensity maxima (Ref 16:197). The wave mechanical formulation of the Franck-Condon principle rests on the assumption that the variation of $R_e$ (the electronic transition moment) with internuclear distance $\gamma$ is slow and $R_e$ may be replaced by a mean value $\overline{R_e}$. The transition probability is proportional to $[R_e]^2$ or $\overline{R_e}^2 [\int \psi_{v'} \psi_{v''} dr]^2$ where: $\psi_{v'}$ and $\psi_{v''}$ are the eigenfunctions of the wave equation for the two states involved (Ref 16:200).

X-9

So:

$$I_{em}^{\nu'\nu''} = \frac{64\pi^4}{3} c\nu_{\nu'\nu''}^4 N_{\nu'} \overline{R_e^2} [\int \psi_{\nu'} \psi_{\nu''} dr] \tag{8}$$

By properly normalizing the orthognal eigenfunctions, the sum of the squares of the integrals for all transitions can be shown to be equal to one (Ref 16:203). By summing over all transitions and rearranging, equation (8) becomes:

$$\Sigma \frac{I_{em}^{\nu'\nu''}}{\nu_{\nu'\nu''}^4} \qquad \alpha \qquad N_{\nu'} \tag{9}$$

Then, equating this sum to the population (Boltzmann distribution) and taking the logarithm gives:

$$log \left[ \Sigma \frac{I_{em}^{\nu'\nu''}}{\nu_{\nu'\nu''}^4} \right] = C_1 - \frac{G'(\nu') hc}{KT} \qquad C_1 = Constant \tag{10}$$

where the quantity $\frac{I_{em}^{\nu'\nu''}}{\nu_{\nu'\nu''}^4}$ is called the band strength. By plotting the log of the sums of band strengths, as measured in the $\nu''$ progressions ($\nu' = $ constant); against the vibrational term values $G(\nu')$ times the constants a straight line with slope ($-\frac{1}{T}$) is obtained.

## IV. Experimental Method

Since several investigators (Ref 2, 10, 35) have indicated that a minimum velocity is necessary to cause an impact flash, it was decided to use the maximum velocity consistently attainable with a powder load of 240 grains of Dupont 3031. The amount of powder did not completely fill the cartridge, so one and a half cleaning patches were used to fill the void and keep the powder density uniform. The neck on the cartridge was resized between shots, and crimp ring was pressed into the neck so that the projectile would rest at a common position for each loading. See Figure 3 for range layout and equipment. The velocities attained fall essentially into two groups, one for the steel projectiles and the other for the aluminum. The difference in velocity is due to the difference in mass of the two projectile types. The mean steel projectile was 115.4 grains with a standard deviation of 2.78 grains, and the mean aluminum projectile was 82.2 grains with a standard deviation of 2.12 grains. See Figure 4 for projectile dimensions. The projectiles were designed with a hemispherical nose so that effects of small variations from normal impact on impact flash were minimized.

A spectrograph, streak camera, and image converter camera were used to record the overall view, spectral response, and time history of the impact flash.

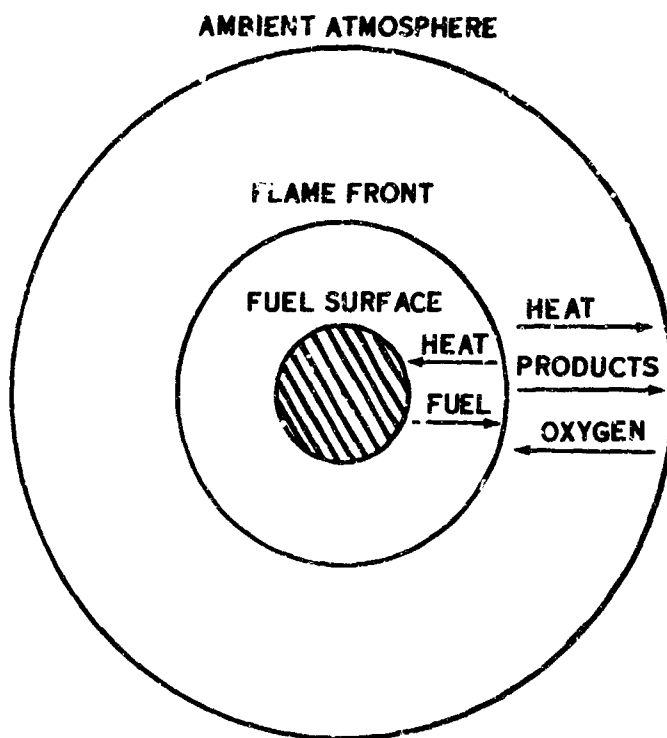The image converter camera could be used to develop a sequence of

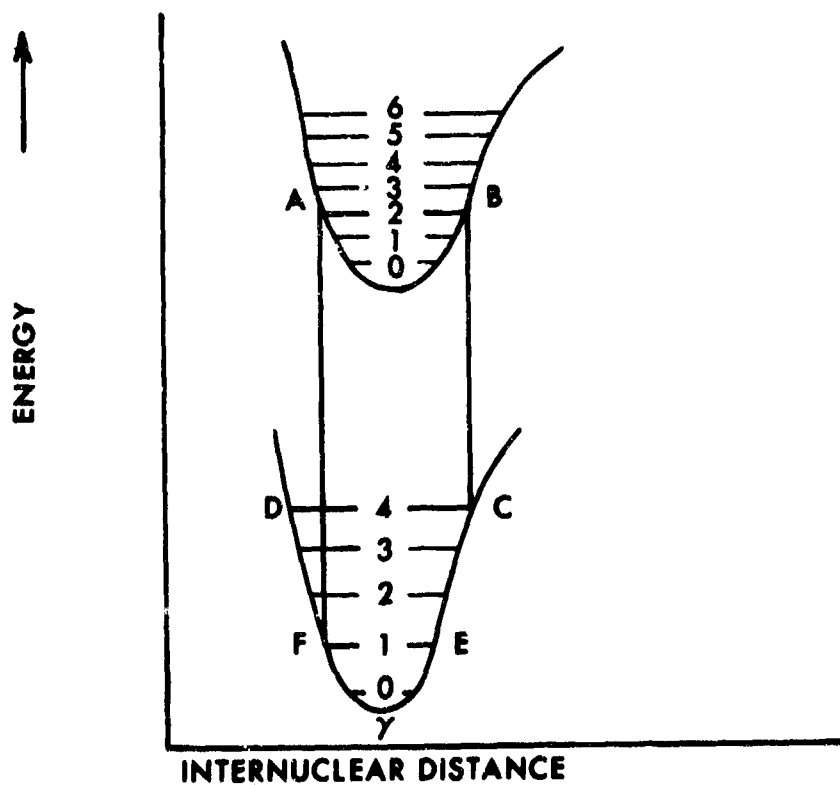Figure 1 - Diffusion Film Burning Model (Ref 14:37)
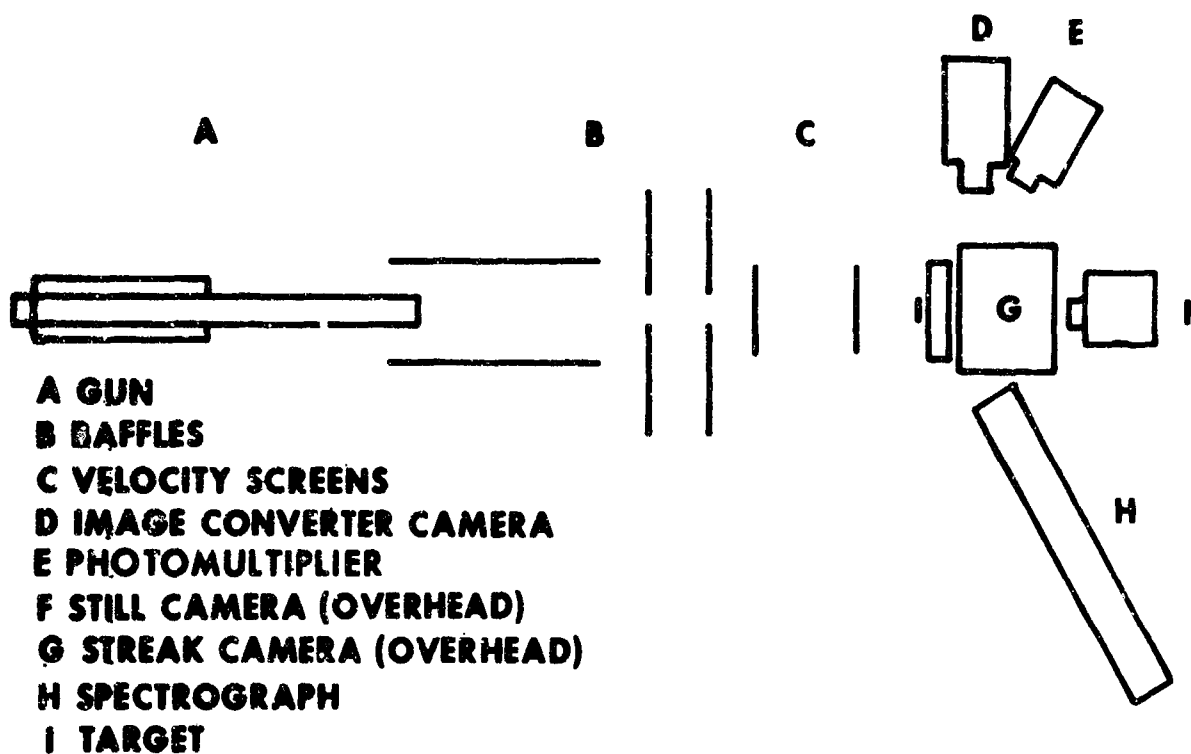


Figure 2 - Potential Energy Levels

X-11

A GUN
B BAFFLES
C VELOCITY SCREENS
D IMAGE CONVERTER CAMERA
E PHOTOMULTIPLIER
F STILL CAMERA (OVERHEAD)
G STREAK CAMERA (OVERHEAD)
H SPECTROGRAPH
I TARGET

Figure 3 - Range Layout

**ALUMINUM PROJECTILE**

.975 ± .001

.375
±
.001

.375

BEFORE IMPACT

AFTER IMPACT

**STEEL PROJECTILE**

.387 ± .001

.498
±
.001

.498
±
.001

BEFORE IMPACT

AFTER IMPACT
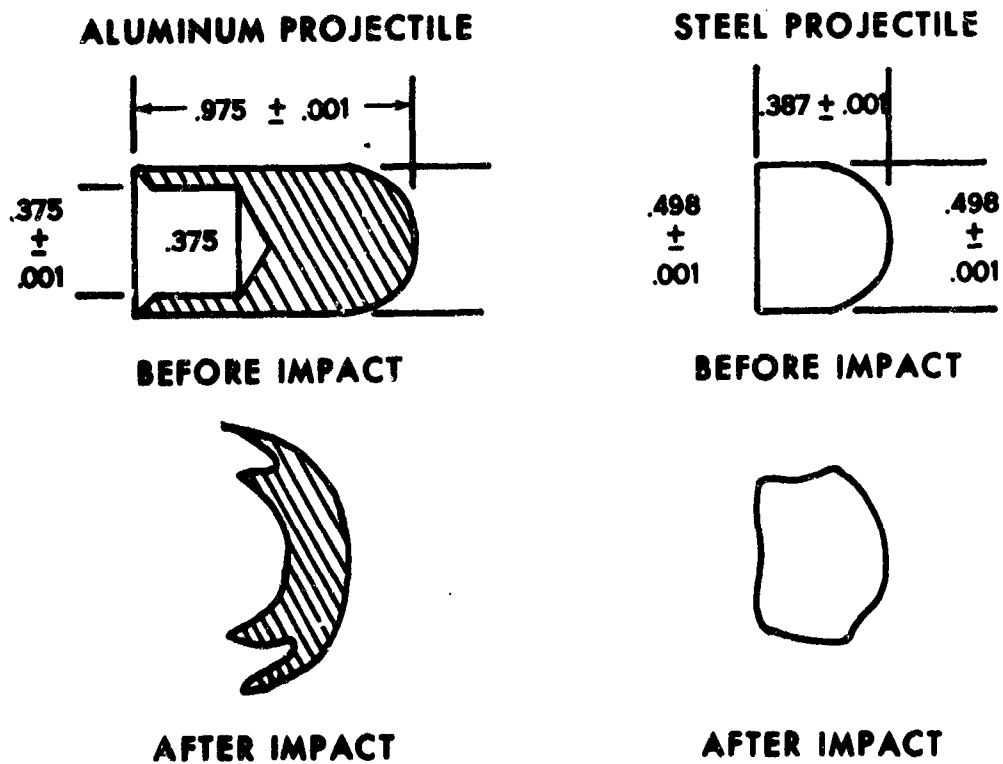
Figure 4 - Projectiles

three exposures for each event. The delay between exposures and the exposure time was adjusted so that various intensity levels were observable. The usual method employed was to limit the exposure time and aperture to the minimum in an effort to penetrate as far as possible into the luminous cloud core.



a                    b                    c
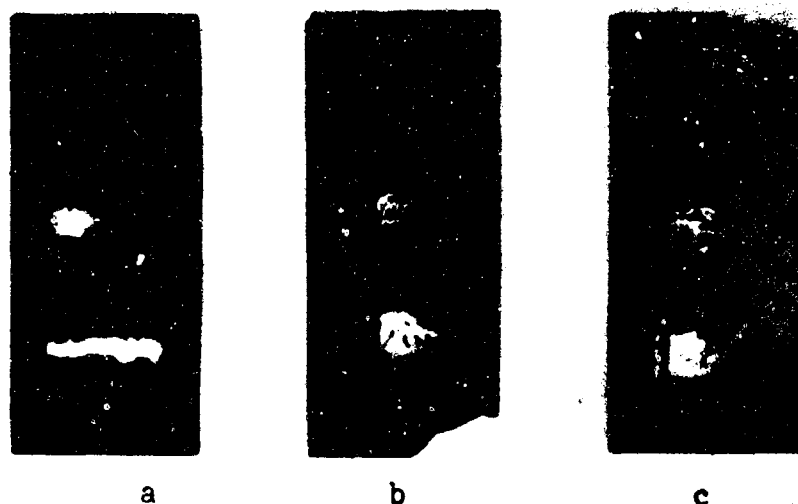
Figure 5 - Image Converter Sequences

Figure 5a, b, c show the results from experiments A10, A15, and A23, respectively. The projectile was traveling from left to right with an f11 lens setting; the exposure sequences (top to bottom) are listed in Table I.

|   | Delay (microseconds) | Exposure (microseconds) |
|---|---|---|
| 1 | 15 | 2 |
| 2 | 10 | 2 |
| 3 | 20 | 1 |

Image Converter Sequences

Table I

A distance vs. time picture of the event was produced by locating a streak camera so that the film and projectile were moving on mutually perpendicular axes. One millisecond interval timing marks were used to calculate the film speed, and a reflective tape grid was positioned to give down range distance information. Failure to move down range was indicated by a
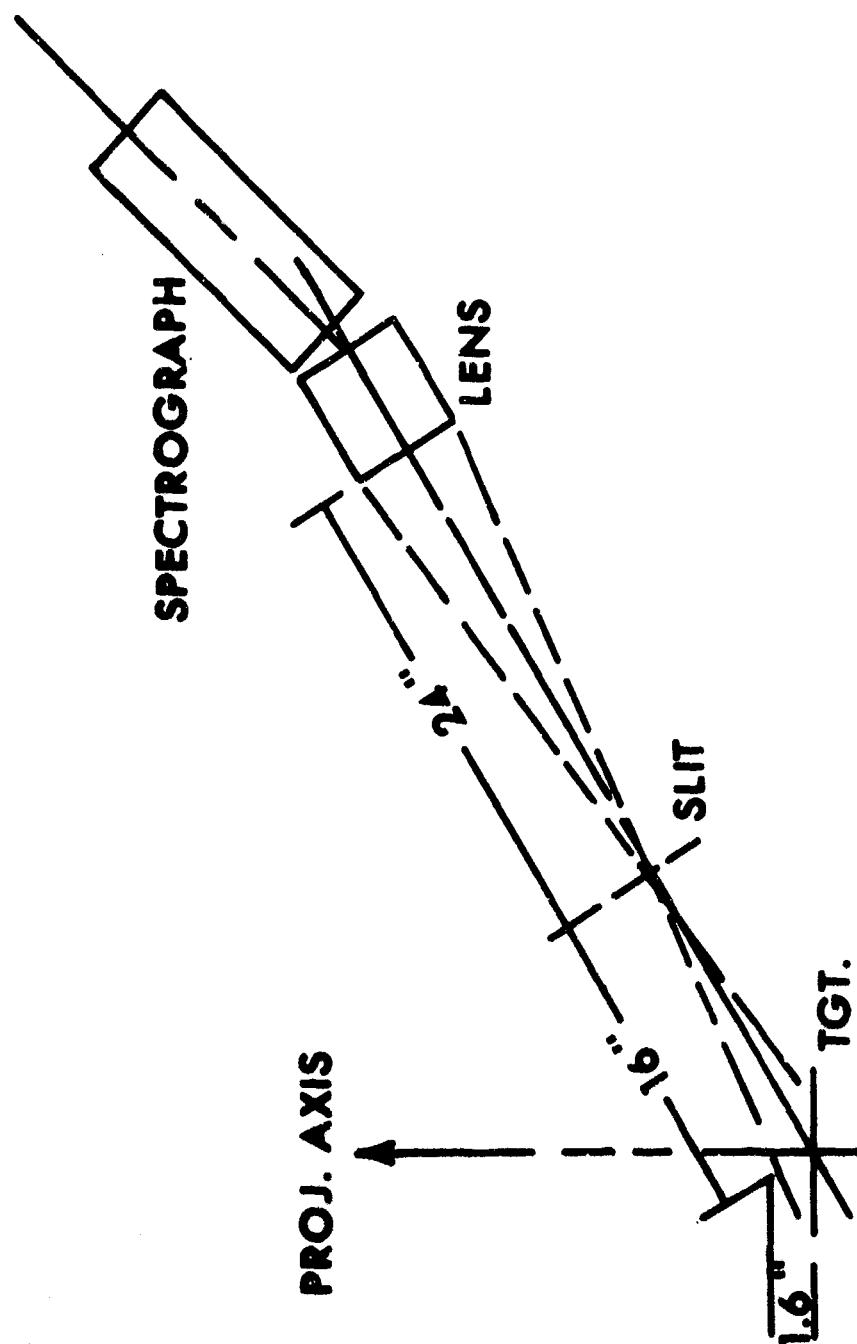
Figure 7 - Spectrographic Alignment

streak parallel to the long axis of the film. In addition, variations in
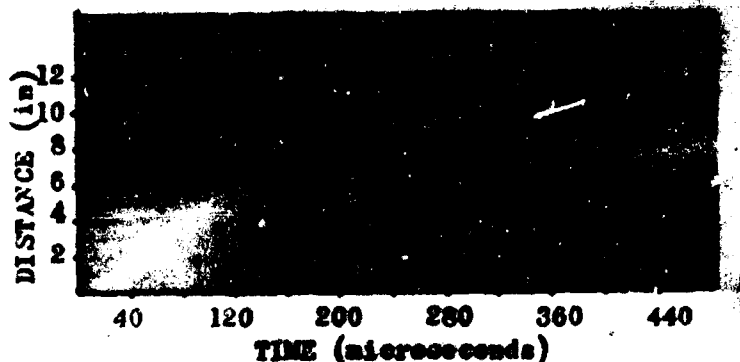intensity also were recorded by the streak camera (See Figure 6).



Figure 6 - Streak Camera Print, Experiment S6


The photographed grid system was used to calculate distances traveled
down range, and the time marks were used to calibrate the long axis of the
film so that accurate readings of distance and time could be taken.

The spectrograph was focused on the intended impact point. The field
of view extended a distance of 1.6 inches along the projectile line of
flight axis when the spectrograph slit was 16 inches from the impact aim
point. (See Figure 7). The time integrated spectral response was recorded
for each shot. The film was carefully developed, and useful film records
were measured on a Jarrell-Ash 21-050 microphotometer with a Bristol
Dynamaster Recorder. The film was calibrated using a General Electric NBS
source lamp so that relative intensity could be determined from the
spectrographic plates (Ref 15:145). The microphotometer record was then
translated into intensity using the method developed by Johnson and Tawde
(Ref 17:580). The readings were then tabulated and processed through a
computer program to form Deslandres tables of the AlO bands. Figure 8 is
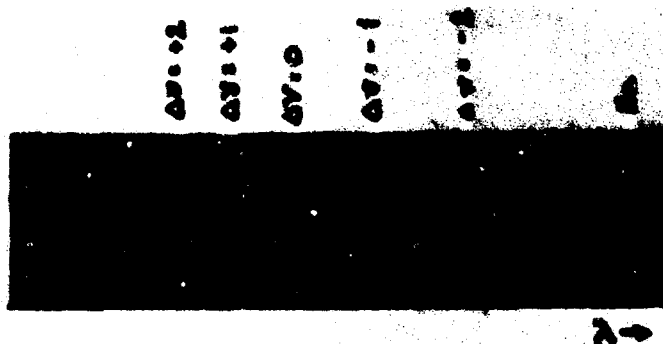a print from experiment Al9 showing the AlO green system.



Figure 8 - AlO Green System Spectrum

Table IV contains the set of relative intensities which resulted from
experiment A18. The experimental conditions are presented in Tables II
and III. The results of the spectrographic analyses were combined and
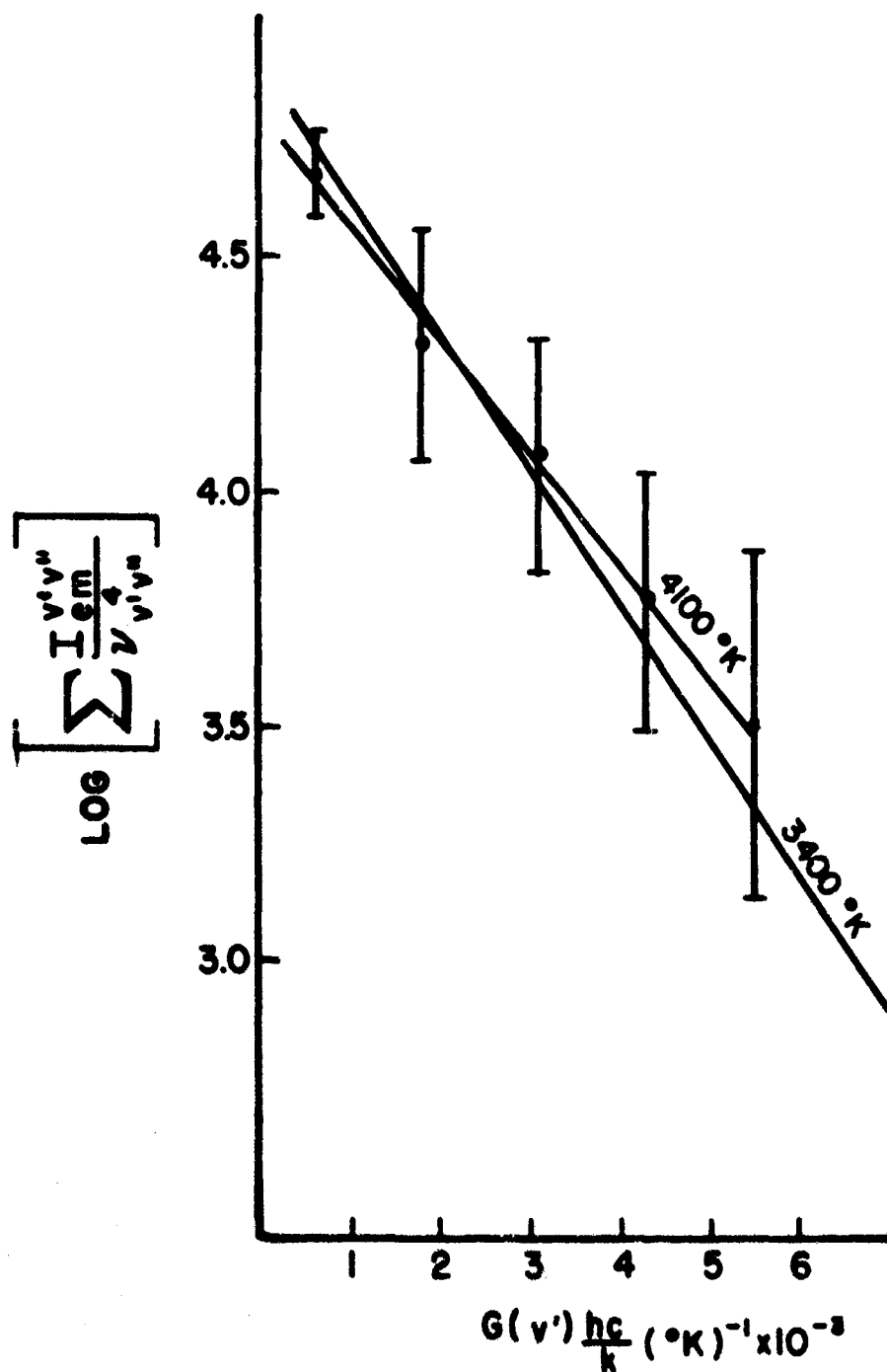are found in Figure 9. The mean value and standard deviation are indicated
for each term value.



Figure 9 - Vibrational Temperature

X-16

| Shot No. | Weight (grains) | Velocity (ft/sec) | Material | Thickness (inches) | Hole Dia. (inches) | Area H / Area P |
|---|---|---|---|---|---|---|
| A 1 | 85.2 | 4680 | 2024 T-3 | 0.063 | 0.65 | 1.69 |
| A 2 | 79.8 | 4710 | 2024 T-3 | 0.063 | 0.60 | 1.44 |
| A 3 | 80.0 | 4710 | 2024 T-3 | 0.063 | 0.60 | 1.44 |
| A 4 | 81.1 | 4670 | 2024 T-3 | 0.063 | 0.60 | 1.44 |
| A 5 | 81.1 | 4690 | 2024 T-3 | 0.063 | 0.65 | 1.69 |
| A 6 | 79.8 | 4710 | 2024 T-3 | 0.063 | a | b |
| A 7 | 79.5 | 4720 | 2024 T-3 | 0.063 | a | b |
| A 8 | 80.4 | 4690 | 1100 | 0.063 | 0.65 | 1.69 |
| A 9 | 81.0 | 4740 | 1100 | 0.063 | 0.60 | 1.44 |
| A 10 | 83.7 | 4700 | 7075 T-6 | 0.063 | 0.60 | 1.44 |
| A 11 | 84.7 | 4710 | 7075 T-6 | 0.063 | 0.65 | 1.69 |
| A 12 | 86.0 | 4780 | 7075 T-6 | 0.063 | 0.60 | 1.44 |
| A 13 | 84.6 | 4760 | 7075 T-6 | 0.063 | 0.65 | 1.69 |
| A 14 | 80.7 | 4730 | 1100 | 0.125 | 0.80 | 2.56 |
| A 15 | 80.8 | 4690 | 1100 | 0.125 | 0.85 | 2.89 |
| A 16 | 80.6 | 4780 | 1100 | 0.125 | 0.70 | 1.96 |
| A 17 | 80.0 | 4630 | 1100 | 0.125 | 0.80 | 2.56 |
| A 18 | 80.3 | 4900 | 1100 | 0.125 | 0.80 | 2.56 |
| A 19 | 83.2 | 5050 | 2024 T-3 | 0.125 | 0.80 | 2.56 |
| A 20 | 84.8 | 4800 | 2024 T-3 | 0.125 | a | b |
| A 21 | 80.0 | 5010 | 7075 T-6 | 0.125 | 0.70 | 2.89 |
| A 22 | 80.6 | 4760 | 7075 T-6 | 0.125 | 0.70 | 2.89 |
| A 23 | 85.0 | 4850 | 2024 T-3 | 0.190 | 0.75 | 2.25 |
| A 24 | 84.5 | 4780 | 2024 T-3 | 0.190 | 0.80 | 2.56 |
| A 25 | 79.8 | 4910 | 2024 T-3 | 0.190 | 0.75 | 2.25 |
| A 26 | 83.8 | 4910 | 2024 T-3 | 0.190 | 0.75 | 2.25 |
| A 27 | 84.6 | 5040 | 2024 T-3 | 0.190 | a | b |
| A 28 | 80.7 | 4960 | 7075 T-6 | 0.190 | 0.80 | 2.56 |
| A 29 | 83.2 | 4880 | 7075 T-6 | 0.190 | 0.75 | 2.25 |
| A 30 | 80.4 | 4940 | 7075 T-6 | 0.190 | 0.75 | 2.25 |
| A 31 | 84.3 | 4570 | 7075 T-6 | 0.190 | 0.75 | 2.25 |
| A 32 | 80.8 | 4760 | 7075 T-6 | 0.190 | 0.75 | 2.25 |

a - Not measured
b - Not calculated

Aluminum Projectile Data

Table II

| Shot No. | Weight (grains) | Velocity (ft/sec) | Material | Thickness (inches) | Hole Dia. | $\frac{\text{Area}_H}{\text{Area}_P}$ |
|---|---|---|---|---|---|---|
| S 1 | 121.7 | 4360 | 1100 | 0.063 | 0.55 | 1.21 |
| S 2 | 120.6 | 4330 | 1100 | 0.063 | 0.55 | 1.21 |
| S 3 | 115.2 | 4580 | 1100 | 0.063 | 0.50 | 1.00 |
| S 4 | 115.2 | 4560 | 1100 | 0.063 | 0.55 | 1.21 |
| S 5 | 115.5 | 4470 | 2024 T-3 | 0.063 | 0.50 | 1.00 |
| S 6 | 115.6 | 4490 | 2024 T-3 | 0.063 | 0.55 | 1.21 |
| S 7 | 120.3 | 4330 | 7075 T-6 | 0.063 | 0.60 | 1.44 |
| S 8 | 116.1 | 4540 | 7075 T-6 | 0.063 | 0.50 | 1.00 |
| S 9 | 114.3 | 4590 | 1100 | 0.125 | 0.65 | 1.69 |
| S 10 | 114.1 | 4460 | 1100 | 0.125 | 0.65 | 1.69 |
| S 11 | 116.5 | 4450 | 1100 | 0.125 | 0.65 | 1.69 |
| S 12 | 118.5 | 4360 | 1100 | 0.125 | 0.65 | 1.69 |
| S 13 | a | 4450 | 2024 T-3 | 0.125 | 0.55 | 1.21 |
| S 14 | a | 4450 | 2024 T-3 | 0.125 | 0.55 | 1.21 |
| S 15 | 116.7 | 4330 | 2024 T-3 | 0.125 | 0.55 | 1.21 |
| S16 | 112.0 | 4440 | 7075 T-6 | 0.125 | 0.55 | 1.21 |
| S 17 | 112.8 | 4460 | 7075 T-6 | 0.125 | 0.50 | 1.21 |
| S 18 | 112.6 | 4450 | 2024 T-3 | 0.190 | 0.60 | 1.44 |
| S 19 | 112.0 | 4510 | 2024 T-3 | 0.190 | 0.60 | 1.44 |
| S 20 | 113.1 | 4400 | 2024 T-3 | 0.190 | 0.60 | 1.44 |
| S 21 | 113.0 | 4450 | 2024 T-3 | 0.190 | 0.60 | 1.44 |
| S 22 | 113.8 | 4440 | 7075 T-6 | 0.190 | 0.55 | 1.21 |
| S 23 | a | 4500 | 7075 T-6 | 0.190 | 0.55 | 1.21 |
| S 24 | a | 4580 | 7075 T-6 | 0.190 | 0.55 | 1.21 |
| S 25 | 114.5 | 4370 | 7075 T-6 | 0.190 | 0.60 | 1.44 |
| S 26 | 113.7 | 4400 | 7075 T-6 | 0.190 | 0.60 | 1.44 |

a - Not measured

Steel Projectile Data

Table III

INTENSITY

| V'' \ V' | 0 | 1 | 2 | 3 | 4 | 5 | 6 |
|---|---|---|---|---|---|---|---|
| 0 | 100.00 | 45.95 | 10.81 | 0.00 | 0.00 | 0.00 | 0.00 |
| 1 | 16.22 | 21.62 | 35.14 | 16.22 | 0.00 | 0.00 | 0.00 |
| 2 | 32.43 | 51.35 | 18.92 | 2.70 | 10.81 | 0.00 | 0.00 |
| 3 | 0.00 | 16.22 | 32.43 | 0.00 | 21.62 | 10.81 | 0.00 |
| 4 | 0.00 | 0.90 | 18.92 | 27.03 | 0.00 | 21.62 | 13.51 |
| 5 | 0.00 | 0.00 | 0.00 | 21.62 | 10.81 | 0.00 | 16.22 |
| 6 | 0.00 | 0.00 | 0.00 | 0.00 | 16.22 | 0.00 | 0.00 |

Relative Intensity Table for Experiment A18

Table IV

## V. Discussion of Results

Due to the difference in projectile mass, the velocities attained were separated into two groups. The mean velocity for the steel projectiles was 4452 fps with a standard deviation of 78 fps, and for the aluminum projectiles was 4788 fps with a standard deviation of 121 fps. The aluminum projectiles consistently caused a larger hole in the target plate. The most probable reason was the gross deformation of the aluminum projectile during the perforation process. See Figure 4 for a recovered projectile shape.

The Rockwell hardness of the steel projectiles was approximately C54 prior to the impact and B10 afterward. An attempt was made to examine the microstructure of the steel, but no changes were detectable except for some cracks in the rear half of the projectile generally parallel to the longitudinal axis.

The overall dimensions of the flash varied considerably. The length is estimated to be 14 inches and the maximum transverse dimension approximately five inches. (See Figure 10a, b).
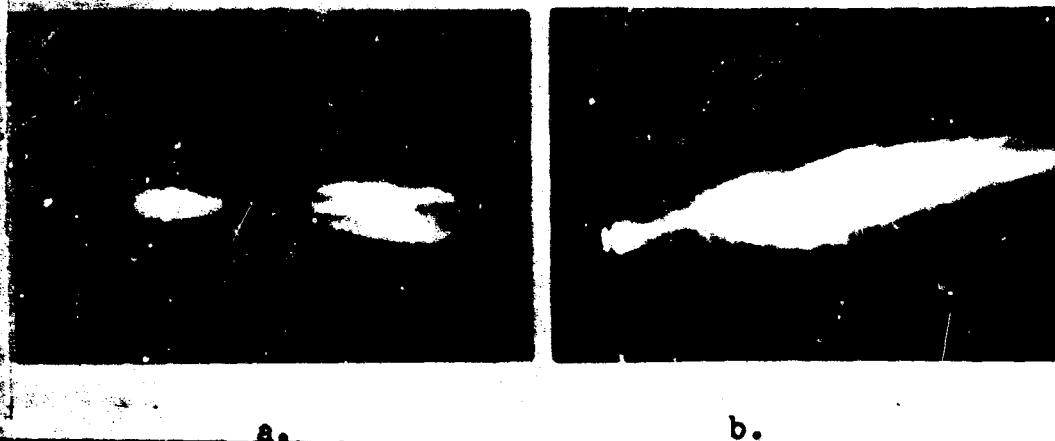
Figure 10

a. Steel Projectile   b. Aluminum Projectile

Down Range Flash


The streak camera results (See Figure 6 for typical print) indicate
that there are two flash intensity maxima. The first occurs when the pro-
jectile breaks through the target and the second is approximately 40-75
microseconds later. The still photographs and streak camera prints locate
this second maxima approximately 3-5 inches down range. Since the spectro-
graph was positioned to view the area immediately behind the plate, it
probably did not record the later increase in luminosity. This error in
viewing point selection may have accounted for the small number of useful
spectroscopic plates. Only four of 32 aluminum projectiles and one of 26
steel projectiles successfully exposed the spectrographic record. When
the atmosphere behind the target plate was a gas mixture with 96% oxygen,
the three aluminum projectiles resulted in successful exposures even though
the impact point was not as accurate as for the steel projectiles. The
increased success rate can be attributed to the additional availability of
oxygen to react with the freshly exposed aluminum surfaces.

An unsuccessful attempt was made to measure the effect of nitrogen on
the flash. A qualitative examination of the still pictures indicated that
the system did not suppress the flash. This may be attributed to a latent
gaseous oxygen content of approximately 6% at the time of the impact.
These results indicate that although increased oxygen availability enhanced
the impact flash, the removal of oxygen to suppress the flash would require
more thorough purging.

The results of the spectrographic analysis given in Figure 9 indicate
that the effective vibrational temperature (from the AlO green system) is
5100°K. As can be seen by the increasing separation of the data, the higher
term values are more difficult to locate and interpret. Herzberg (Ref 16:204)

X-20

points out that the success of the "sum rule" method of temperature deter-
mination depends on two things: first, measuring all of the bands in the
progressions used, and second, the source has to be in thermal equilibrium.
Tawde (Ref 32:734) reported that there were 34 bands of the AlO system.
His data included the sequence $\Delta v = +3$. Apparently the equipment used in
this investigation was not sensitive enough to distinquish this sequence.
Failure to include this term would lower the sum for progressions after
the third term value. Figure 9 shows the least squares fit for the first
three term value points, and also, the fit for the entire collection of
data. The temperature (as determined from a least squares fit of the
data) for the entire collection of data was $3400°K$, and the value for the
first three terms is $4100°K$. The $4100°K$ temperature is identical to that
reported by Backman (Ref 2:38) and the $3400°K$ corresponds to the findings
of Tawde (Ref 32:734) for an AlO system excited by a carbon arc. These
values also bracket the $3800° \pm 200°K$ (Ref 6:5308) for the vaporization tem-
perature of $Al_2O_3$ at atmospheric pressure. The vaporization temperature
was suggested in the model (See Section II), and the reported bounds in-
dicate that these values should be considered as reasonable estimates for
the spark temperature.

Since there was no spectroscopic evidence of anything but AlO and
sodium, (a contamination) it was decided to lump all the data points in-
cluding the steel projectile before computing the least squares fit.

## V. Conclusions

In conclusion, the results of this investigation indicate that the
impact flash produced by cylindrical projectiles with hemispherical heads
on thin aluminum targets lasts approximately 3-5 milliseconds. The di-
mensions of the flash were found to be approximately 14 inches by 5
inches. The effective vibrational temperature, determined from the AlO
green system, was found to be between $3400°$ and $4100°K$. These temperatures
agree with previously reported information (Ref 2:32) and are compatible
with the physical model.

## Acknowledgement

## Bibliography

1. American Institute of Physics Handbook (Second Edition), McGraw Hill, New York, 1963.

2. Backman, M. E. and W. J. Stronge. Penatration Mechanics and Post-Perforation Effects in an Aluminum-Aluminum Impact System. NWC- TP-4414. China Lake, California, 1967.

3. Bartlett, R. W. et.al. Estimating Metal Particle Combustion Kinetics. Combustion Kinetics. Aeronutronic Report U-1751. Newport Beach, California: Ford Motor Company, July, 1962.

4. Bernier, R. G. Aluminum and Magnesium Fragments vs. Dural Plates. Unpublished report from BRL, Aberdeen, Maryland. October, 1952.

5. Bjork, R. L. and A. E. Olshaker. The Role of Melting and Vaporization in Hypervelocity Impact. The Rand Corporation RM - 3490 - PR, May, 1965.

6. Brewer, L. and A. W. Searcy. J. A. C. S. 73 (1951) 5308.

7. Brown, N. Size and Duration of Sparks Produced by Impact of Steel and Pyrophoric Simulated Fragments on Thin Metal Plates. BRL R - 683. Aberdeen, Maryland. December, 1948.

8. Brzustowski, T. A. and I. Glassman. "Vapor Phase Diffusion Flames in the Combustion of Magnesium and Aluminum," in Heterogeneous Combustion (Progress in Astronautics and Aeronautics). Edited by Hans G. Wolfhard, et.al. 15: Academic Press, 1964. 75-158

9. Bull, G. V. et.al. "Review of Hypervelocity Impact Studies at McGill University." Report 63-15, NASW-515, December, 1963.

10. Caron, A. P. Oxidative Detonations Initiated by High Velocity Impacts AFFDL - 65-41, May, 1965.

11. Friend, W. H., et.al. An Investigation of Explosive Oxidations Initiated by Hypervelocity Impacts. AFFDL-TR-67-92. Wright-Patterson Air Force Base, Ohio: Air Force Flight Dynamics Laboratory, May, 1967.

12. Fruchtenicht, J. F. Experiments on the Impact-Light-Flash at High Velocities. NASA - CR 416. Washington: National Aeronautics and Space Administration, March, 1966.

13. Gaydon, A. G. Spectroscopy and Combustion Theory. London: Chapman and Hall Ltd., 1948.

14. Glassman, Irvin. Metal Combustion Processes. New York: Paper presented to American Rocket Society, 14th Annual Meeting, Washington, November, 1959.

15. Harrison, G. R. et.al. _Practical Spectroscopy_. Englewood Cliffs
New Jersey. Prentice-Hall, 1948.

16. Herzberg, G. _Molecula Spectra and Molecular Structure_. (Second
Edition) Princeton: D. Van Nostrand Co., 1950.

17. Johnson, R. C. and N. R. Tawde. "Intensity Distribution in Molecular
Spectra." _Proceedings of the Royal Society of London_, A 137;
575-591, September, 1932.

18. Jones, A. H. et.al. _Survey of Hypervelocity Impact Information II_.
ASRL Report 99-2. MIT: December, 1963.

19. Kahler, R. L. _Impact Flash Suppression_. Joint USAF- USN Technical
Symposium on Aircraft and Missile Vulnerability. Wright-Patterson
Air Force Base: September, 1952.

20. Keough, D. D. _Luminosity Studies of High Velocity Impact_. AFCRL -
TR - 60-415. Bedford, Massachusetts. October, 1960.

21. Kottenstette, J. P. _Impact Flash Characteristics of Triboluminescent
Material_. AFTL - TR - 65-75; Eglin Air Force Base, November, 1965.

22. Kottenstette, J. P. and E. Wittrock. _Impact Flash Characteristics
as Affected by Oxidizing Materials_. AFATL - TR - 67-2. Eglin Air
Force Base, February, 1967.

23. Krafft, J. M. "Surface Friction in Ballistic Penetra-
tion." _Journal of Applied Physics_, 26: 1955. 1248-1252.

24. MacCormack, R. W. Impact Flash at Low Ambient Pressures. NASA TN
D - 2232. Washington: National Aeronautics and Space Administration.
March, 1964.

25 Macek, A. and J. Mckenzie Semple. _Time Resolved Spectroscopy of
Single Burning Metal Particles_. Project Squid Technical Report
ARC - 10 - P. Charlottesville, Virginia: University of Virginia,
June, 1966.

26. Olshaker, A. "An Experimental Investigation in Lead of the Whipple
Meteor Bumper." _Journal of Applied Physics_, 31:2113-2120. 1960.

27. Pearse, R. W. B. and A. G. Gaydon. _The Identification of Molecular
Spectra_. (Third Edition) New York: John Wiley and Sons, 1963.

28. Rautenberg, T. H. Jr. and P. D. Johnson. "Light Production in
Aluminum-Oxygen Reaction." _Journal of the Optical Society of America_.
50:602-606, June, 196^.

29. Recht, R. F. "Catastrophic Thermoplastic Shear." _Journal of Applied
Mechanics_. 31:189-193. 1964.

30. Richmann, J. L. *Damage Assessment Technique*. AFATL - TR - 67-48. Eglin Air Force Base, Florida. May, 1967.

31. Rinehart, J. S. "On Fractures Caused by Explosions and Impacts." Quarterly of the Colorado School of Mines. 55: October, 1960.

32. Tawde, N. R. and S. A. Trivedi. "GN and AlO Bands in the Study of the Carbon Arc." *The Proceedings of the Physical Society*. 51:733-740. November, 1939.

33. Thompson, W. T. "An Approximate Theory of Armor Penetration." *Journal of Applied Physics*. 26:80, 1955.

34. White, E. L. and J. J. Ward. *Ignition of Metals in Oxygen*. DMIC Report 224. Columbus, Ohio: Defense Metals Information Center, February, 1966.

35. White, W. C. "Suppression of AlO in the Wake of Ultraspeed Pellets." *Journal of Astrophysics*. 121 (1) 1955, 271-276.

36. White, W. C. "Ablation from Aluminum Ultraspeed Pellets." *Journal of Astrophysics*. 122 (3) 1955, 559-564.

37. Zel'dovich, Ya. B. and Yu. P. Raizer. *Physics of Shock Waves and High Temperature Hydrodynamic Phenomena*. Edited by W. D. Hayes and R. F. Probstein (First English Edition). New York: Academic Press, 1966.

MEASUREMENT OF THE SPECTRAL SHIFT OF HIGH-
ENERGY RUBY LASERS WITH A PULSE SPECTROMETER


By


HAROLD D. NEWBY


DIRECTORATE OF RANGE ENGINEERING
RANGE MEASUREMENTS LABORATORY
AIR FORCE SYSTEMS COMMAND
PATRICK AFB, FLORIDA


Y-1

ABSTRACT

This paper covers a system that is designed
to measure the spectral shift and energy
output change caused by the rapid temperature
rise within the laser rod during each pulse
of a high energy pulsed ruby laser system.

PERSONAL BIOGRAPHY

Harold D. Newby
Assistant Chief, Engineering Sciences Branch
Range Measurements Laboratory
Patrick Air Force Base, Florida 32925


EDUCATION:

B.S.E.E., University of Florida, 1959
Optical Physics, UCLA, 1962
Precision Radiometry, University of Michigan, 1965
Laser Technology and Applications, University of Michigan, 1966
24 Credit Hours towards Masters, Florida Institute of Technology


EXPERIENCE:

Nine years experience in Infrared Research and Development, Missile
Launch Support and Operations, Electro-Optical System Calibration,
and Electro-Optical System Development:

1959 - 1960    Infrared Research and Development, Hughes Aircraft
               Company, Culver City, California

1960 - 1961    Missile Launch Support, Western Electric, Cape Kennedy, Florida

1961 - 1962    Mercury - Atlas Launch Operation, General Dynamics/
               Astronautics, Cape Kennedy, Florida

1962 - 1966    Electro-Optical System Calibration, Pan American World
               Airways/GMRD, Patrick Air Force Base, Florida

1966 - 1968    Electro-Optical System Development, Range Measurements
               Laboratory, Patrick Air Force Base, Florida

1968 - Present Assistant Chief, Engineering Sciences Branch, Range
               Measurements Laboratory, Patrick Air Force Base, Florida

The Range Measurements Laboratory at Patrick Air Force Base, Florida, has been assigned a special project that requires the use of a high energy pulsed ruby laser. The system to be developed required the use of very narrow spectral bandpass filters centered around the ruby wavelength of 6943 Angstroms. The question arose as to what was the minimum bandpass filter that could be utilized? The next question was, due to variations in coolant temperature, how can one control the output wavelength? It was calculated that due to the relative long periods between pulses, low duty cycle, the system would stabilize after three to five pulses at the rate of one pulse per second and a nominal 6943 Angstrom output wavelength could be maintained. However, because of the short pulse duration and the extremely low efficiencies of ruby laser systems, a rather sharp rise in temperature, within the internal structure of the ruby rod, would result every time the laser is pulsed. Exactly how much this sharp temperature rise in the ruby would detune the system from the 6943 Angstrom operating point was unknown and what the magnitude of this temperature rise as well as changes in output energy were and are still unknown.

This paper describes a system that is designed to measure the spectral and energy shifts in the output that occur in all high energy pulse lasers to date. This particular system is designed to measure the spectral and energy output shift as a function of ruby coolant temperature and pulse duration of a high energy pulsed ruby laser that is operated in the conventional mode with an output pulse width of approximately one millisecond (ms).

The term high energy pulse laser system in this paper shall refer to a laser system that has an output energy capability in excess of one hundred joules in approximately one millisecond pulse duration. Also, spectral and energy shift shall be defined as the variations in the laser output wavelength and energy for a rod coolant temperature (T) at any time ($\tau$) within that pulse.

$$\Delta \lambda (\tau, T) \; ; \; \Delta J (\tau, T)$$

The spectral and energy shift in most high energy laser systems should be predictable, within limits, after thermal equilibrium has been achieved. However, this has never been measured and can only be assumed at this time. Measurements have been made on the output energy and it does stabilize after three to five shots.

The system described in this paper is being built to measure the actual spectral and energy shift of high energy pulsed ruby lasers for a single pulse configuration to a maximum of one thousand pulses. The only limitations on the upper limit are the associated data recording equipment.

The requirement on the measurement in the spectral shift was to measure the shift in spectra to an accuracy of 0.5 Angstroms or greater with a time resolution within a single pulse of at least ten microseconds.

The approach that has been taken in the design of the Pulse Spectrometer is to use standard commercially available products wherever possible and reconfigure them to meet any of the special requirements that are unique to this system.

The instrument chosen as the dispersing instrument was the Jarrell-Ash, Model 78-466, 1.0 Meter Czerny-Turner Scanning Spectrometer/Spectrograph shown in Figures Number 1 and 2. The grating for the experiment was an 1180 groove per millimeter grating that provides a dispersion of 2.73 Angstroms per millimeter when operating in the third order and using a 10 micron slit width.

The sensor chosen to measure the variation in wavelength was a 28 element lead sulfide (Pbs) linear array. This element was chosen primarily because it was available. The individual sensors measured 0.21 millimeter by 0.21 millimeter and were arranged in a linear array of 7.0 millimeters in length. With this configuration each sensor element has a resolution of 0.68 Angstroms when placed at the focal plane of the spectrographic output of Jarrell-Ash instrument. The sensor array is shown in Figures Number 3 and 4.

Two types of temperature monitoring sensors are required. The first, which measures average coolant temperature of the ruby rods, flash lamps and cavity, were selected to have a long time constant so they would not measure the sharp rise in the rod temperature but would be used only to measure the time required for the system to reach thermal equilibrium. A photograph of these quartz thermometers is shown in Figure Number 5. The second type which measures the rapid temperature variations at the rod coolant output were selected for their short time constants and availability. These indium antimonide (InSb) sensors with narrow bandpass filters provide the detectors for an optical radiometer and are shown in Figure Number 6.

In order to insure that all required information is recorded, the calculations covered in Appendix A were performed to determine the electrical bandpass requirements to record all necessary data. The bandpass calculations show a required electrical bandpass of 1000 Hertz. The recording system was chosen as an FM multiplexed configuration with 8000 Hertz constant bandpass voltage controlled oscillators as the input device. The reproducing system, for post test data processing, was chosen to have the half power point at 4000 Hertz with a linear phase cutoff filter. This keeps the overall electronics system well within the calculated limits.

The system operation can be described very simply. Figures Number 7 and 8 show optical and electrical signal flows of the Pulse Spectrometer System. The scanning drive system of the Spectrometer remains stationary during the complete operation. The 6943 Angstrom line is on one of the sensing elements, then during the pulse period any change in the laser output spectra will be shifted across the linear array. As the output spectra is shifted across the sensor array each sensor element will produce a voltage output that is proportional to the energy incident upon its surface. This output is then amplified and applied to the input of the constant bandwidth voltage control oscillator (VCO). The outputs of the VCO's that operate at different frequencies are multiplexed together and recorded on magnetic tape. In addition to all sensor outputs being recorded a sync pulse is also recorded for later use in the data processing.

The playback signal flow shown in Figure Number 9 describes how the signal is reproduced to an analog form for insertion into a special sampler, digitizing and formating system. This system works by certain external commands generated by the previously mentioned sync pulse.

The Digital Formator will, upon command, sample the simultaneous outputs of all sensors within a time gate of $90 \times 10^{-9}$ seconds. These outputs are then digitized, placed in a predetermined format and recorded on a digital recorder. The analog tape system will return to the start point and remain there until a new start command is provided. Once the Digital Formator cycle is completed, a command to add a new delay from the sync pulse to the sample is given, followed by a new start command to the analog playback system. This cycle is repeated until all sensors have been sampled for the full pulse width. The system then goes to the next pulse and repeats the previous cycle. This system is shown in the photograph in Figure Number 10.

The signal flows for the display of the data are shown in Figure Number 11. At this time either system could be used. The type of display can either be a two dimensional or three dimensional plot or a computer listing. A typical two dimensional display may appear as shown in Figure Number 12.

The system described will provide information on the minimum bandpass optical filter useable if only the shift in laser output spectra need be considered. The system will also provide information on the coolant requirements of future laser systems if tightly controlled spectral output is a requirement as well as information on the time required for the system under test to reach thermal equilibrium.

The system described is now in its final stages of fabrication and only subcomponent testing has been completed. The first complete system test is now scheduled for the first of October 1968. Any results, as well as a discussion on the output energy shift will be presented at the presentation of this paper.

# PULSE SPECTROMETER SYSTEM BANDWIDTH CALCULATION

$f(t)$
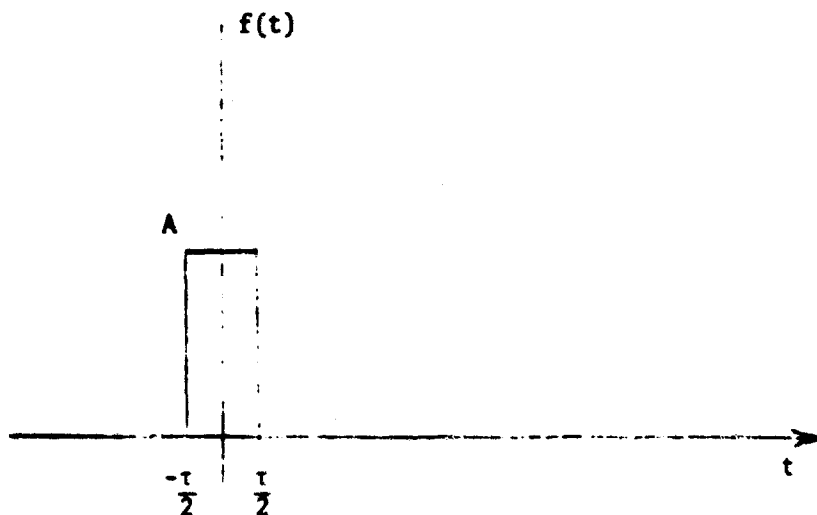


1. Determine the Fourier Series of $f(t)$. For a positive interger $T$ and $\omega_0 = 2\pi$, the terms of the sequence $\sqrt{2/T}\cos n\omega_0 t$, $(n = 0,1,2,\cdots)$ are orthonormal on the interval $[-\frac{T}{2}, \frac{T}{2}]$. Thus, we may write

$$f(t) = \sum_{n=0}^{\infty} C_n \sqrt{2/T}\cos n\omega_0 t \quad \text{on} \quad [-\frac{T}{2}, \frac{T}{2}], \text{ where}$$

$$C_n = \int_{-\tau/2}^{T/2} f(t) \sqrt{2/T}\cos n\omega_0 t\,dt$$

$$= \sqrt{2/T}\, A \int_{-\tau/2}^{\tau/2} \cos n\omega_0 t\,dt$$

$$= \frac{\sqrt{2/T}}{n\omega_0} A [\sin n\omega_0\tau/2 - \sin n\omega_0(-\tau/2)]$$

$$= \frac{2\sqrt{2/T}}{n\omega_0} A \sin n\omega_0\tau/2$$

$$= \sqrt{2/T}\, \tau A\, S_a(n\omega_0\tau/2) ; \text{ or}$$

Y-6

$$f(t) = \frac{2\tau A}{T} \left[ 1 + \sum_{n=1}^{\infty} S_a (n\omega_o \tau/2) \cos n\omega_o t \right]$$

2. Determine the number N to which is required to sum to maintain a mean square error, $\epsilon$ , of equal to or less than 0.1 per cent of $A^2 \tau$.

$$\epsilon = \int_{-T/2}^{T/2} | f(t) - S_N (t) |^2 dt \ ; \ \text{where } S_N (t) = \sum_{k=0}^{N} C_k (\sqrt{2/T} \cos k\omega_o t)$$

By Eq. (19), Pg. 465 of MATHEMATICAL ANALYSIS by T. M. Apostol

$$\epsilon = \int_{-T/2}^{T/2} f^2 (t) dt - \sum_{k=0}^{N} C_k^2$$

$$= \int_{-\tau/2}^{\tau/2} A^2 dt - \frac{2A^2 \tau^2}{T} \sum_{k=0}^{N} S_a^2 (k\omega_o \tau/2)$$

$$= A^2 \tau - \frac{2A^2 \tau^2}{T} - \frac{2A^2 \tau^2}{T} \sum_{k=1}^{N} S_a^2 (k\omega_o \tau/2)$$

$$\frac{\epsilon}{A^2 \tau} = 1 - \frac{2\tau}{T} - \frac{2\tau}{T} \sum_{k=1}^{N} S_a^2 (k\omega_o \tau/2)$$

For $\tau = 10^{-3}$, $T = 1$, $\omega_o = 2\pi$, $\epsilon \leq A^2 \tau \times 10^{-3}$ we have

$$10^{-3} \geq 1 - 2 \times 10^{-3} - 2 \times 10^{-3} \sum_{k=1}^{N} S_a^2 (k\pi \times 10^{-3}) \ , \ \text{or}$$

$$- .997 \geq - 2 \times 10^{-3} \sum_{k=1}^{N} S_a^2 (k\pi \times 10^{-3}) \ , \ \text{or}$$

$$\sum_{k=1}^{N} S_a^2 (k\pi \times 10^{-3}) \geq 498.5$$

FORTRAN PROGRAM TO SOLVE FOR N

```fortran
1    P = .0031415926

2    D = 0.0

3    G = 0.0

4    G = G+1.0

5    D = D+((SIN(G*P))/(G*P))**2

6    IF(D-498.5)4,7,7

7    N = G

8    PRINT 9,N

9    FORMAT(////12H ANSWER:  N=.15)

10   END
```

ANSWER:  N= 1537

## LIST OF ILLUSTRATIONS

Figure 1    Czerny-Turner  1.0 Meter Spectrometer

Figure 2    Spectrometer Slits and Sensor Housing

Figure 3    Pulse Spectrometer 28 Element Sensor Array

Figure 4    28 Element PbS Sensor Array

Figure 5    Hewlett Packard Quartz Thermometer

Figure 6    InSb Temperature Sensors

Figure 7    Pulse Spectrometer Optics

Figure 8    Pulse Spectrometer Data Signal Flow (Record)

Figure 9    Pulse Spectrometer Data Signal Flow (Playback)

Figure 10   Pulse Spectrometer Electronic System

Figure 11   Pulse Spectrometer Data Signal Flow (Display)

Figure 12   Typical Pulse Spectrometer Display
            (Output Wavelength vs. Time)

SPECTROMETER
SLITS AND
SENSOR HOUSING

PULSE SPECTROMETER
28 ELEMENT SENSOR ARRAY

FIGURE 3



28 ELEMENT
P b S SENSOR
ARRAY

FIGURE 4

Y-13

HEWLETT PACKARD
QUARTZ
THERMOMETER

FIGURE
5



In Sb
TEMPERATURE
SENSORS

FIGURE
6

OPTICAL FILTER

NITROGEN CRYOSTAT

PREAMP

InSb DEWAR

DC POWER SUPPLY

N₂ LINE FILTER
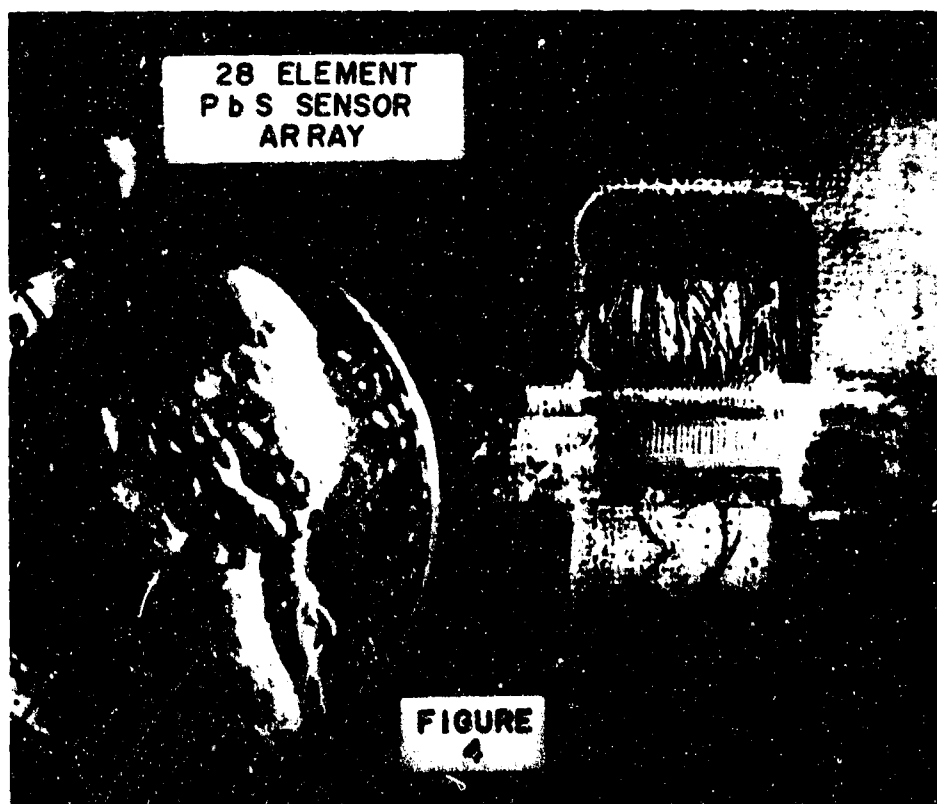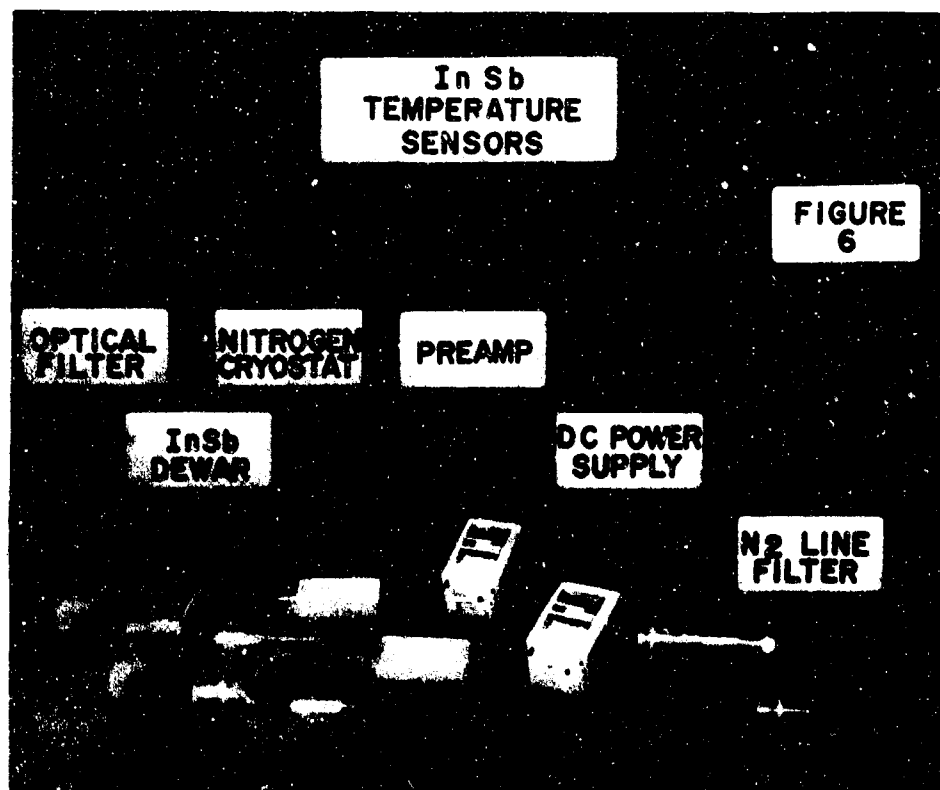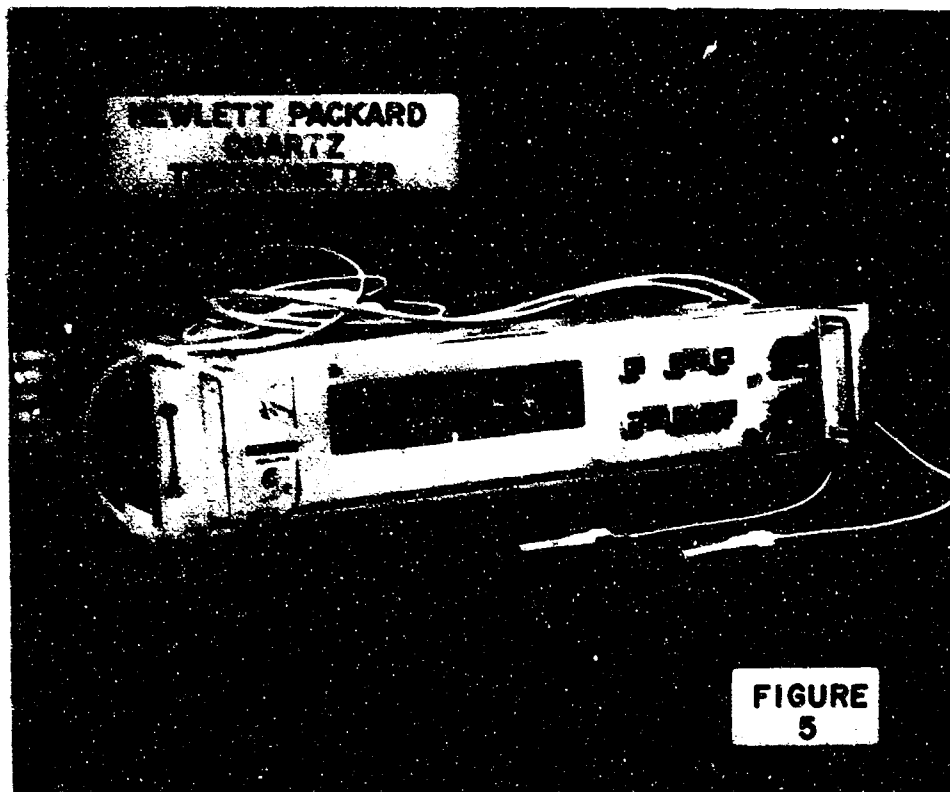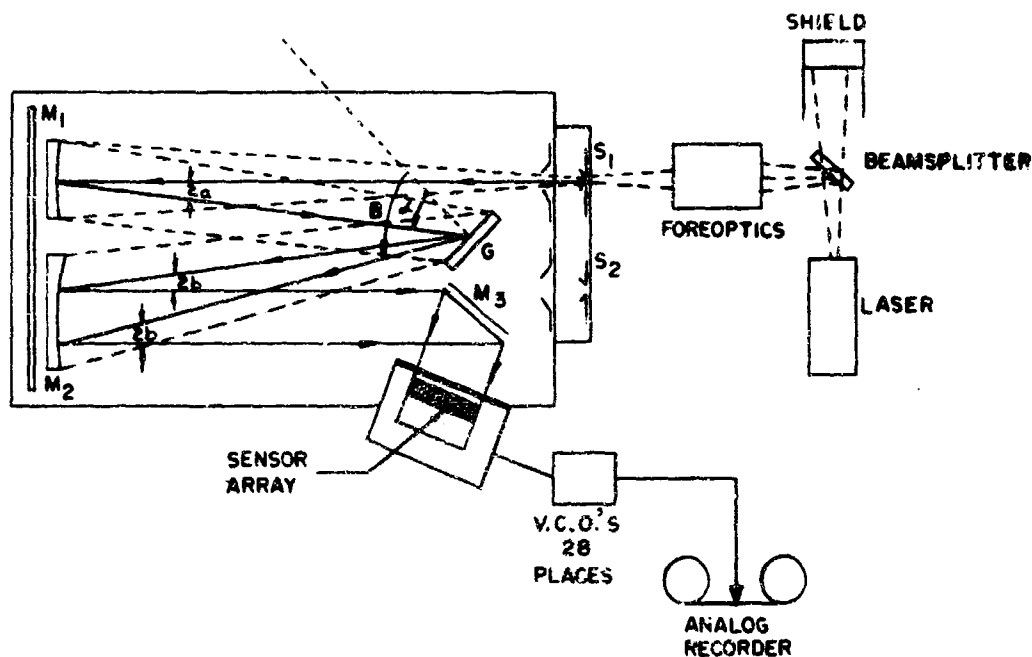
PULSE SPECTROMETER
OPTICS

FIGURE 7



PULSE SPECTROMETER
DATA SIGNAL FLOW
(RECORD)

FIGURE 8

Y-15
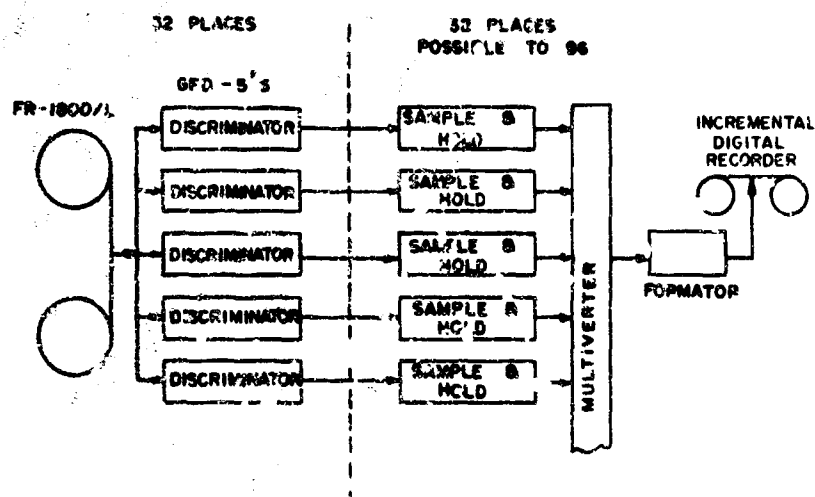
PULSE SPECTROMETER
DATA SIGNAL FLOW
(PLAYBACK)

FIGURE 9

PULSE  SPECTROMETER
DATA  SIGNAL  FLOW
(DISPLAY)
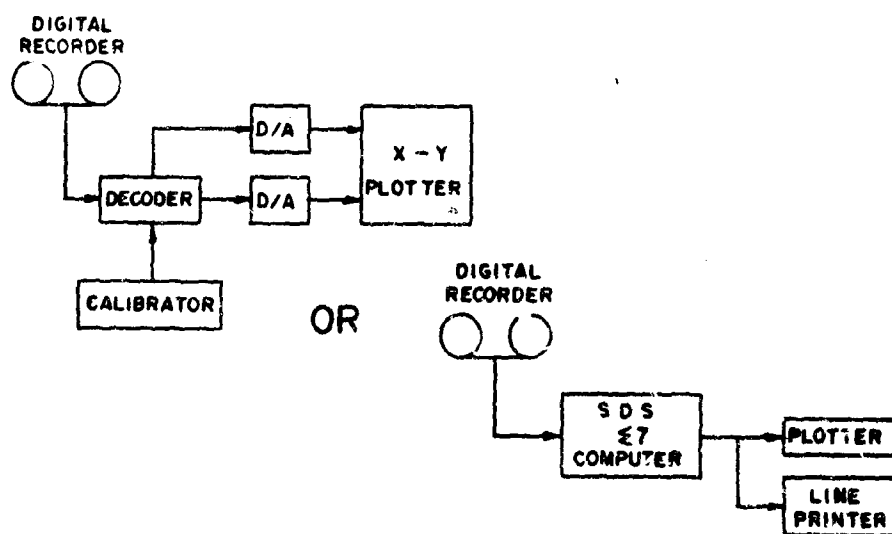
FIGURE  11



TYPICAL PULSE SPECTROMETER DISPLAY
(OUTPUT WAVELENGTH VS TIME)
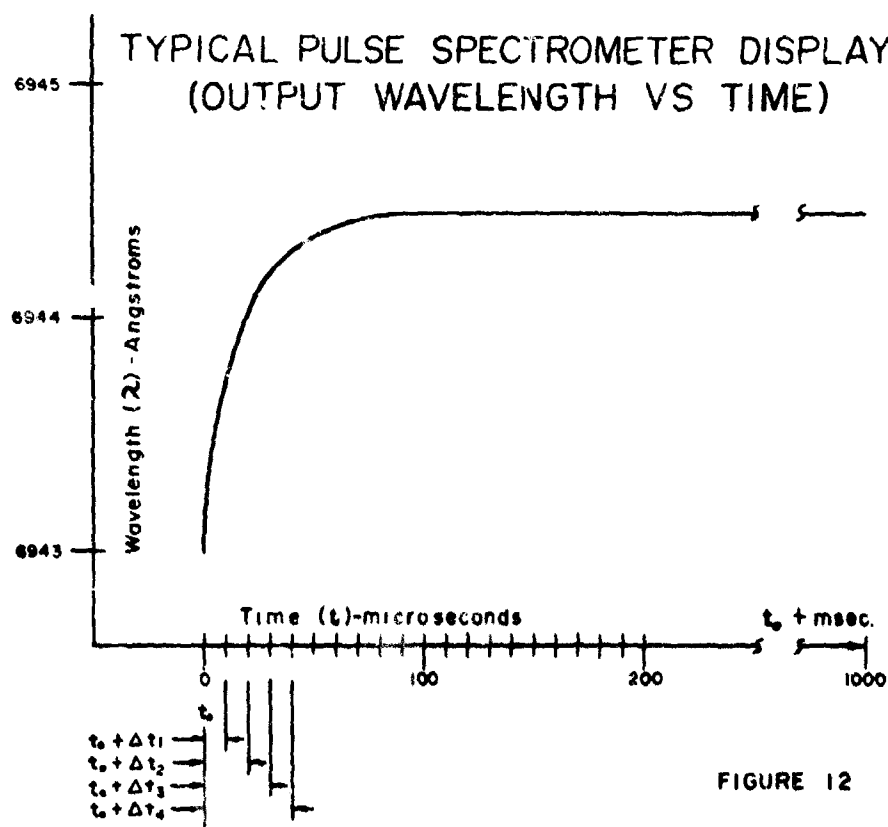
FIGURE 12

WORLDWIDE SOLAR RADIO PATROL AND
PROTON WARNING SYSTEM


By


John P. Castelli

Ionospheric Physics Laboratory
Air Force Cambridge Research Laboratories
Office of Aerospace Research
L. G. Hanscom Field, Bedford, Massachusetts

Z-1

# BIOGRAPHY

John P. Castelli was born in Lexington, Massachusetts in 1916. He received the A.B. and M.A. degrees at Boston College in 1938 and 1939. During World War II he served in the Army Air Forces as a Radar Officer. He has been with AFCRL since 1946 where until 1955 he worked mainly on rocket projects and various phases of radio systems. From 1955 until the present he has been doing microwave radio astronomy research. He has had responsibility for a number of AFCRL Solar Radio Eclipse expeditions in 1961, 1963, and 1966.

Mr. Castelli is presently leader of the Solar Section of the Radio Astronomy Branch and has responsibility for radio solar work within the Branch. This includes establishing and maintaining a solar radio facility at the Sagamore Hill Radio Observatory, Hamilton, Massachusetts, for making continuous observations of the sun throughout much of the radio spectrum, and for analyzing and reporting results of the measurement program. He maintains close contact with Air Weather Service personnel in their space forecast mission.

Mr. Castelli is married and has four children. He has authored and contributed to numerous journal articles and scientific reports in the propagation, radio astronomy, and solar measurement areas. He is a member of Commission V URSI, IEEE, and AAS.

# Worldwide Solar Radio Patrol and Proton Warning System

ABSTRACT

In 1967, the Air Force Cambridge Research Laboratories established
in Manila, Philippine Islands a second solar microwave monitoring pro-
gram to complement that at the Sagamore Hill Radio Observatory,
Hamilton, Massachusetts. Stressing burst spectral investigations gener-
ated from high-accuracy fixed-frequency measurements of flare associ-
ated radio bursts, a worldwide program of virtually continuous observa-
tions was assured. The combined effort of the two patrols provides
warning of the incidence of principal proton events. A warning system
quickly establishes, from the radio signature of the event, the fact that
an important solar event has taken place. It then employs the finite but
variable delay time between solar event and actual arrival of particles in
near-earth space for warning automated equipment and/or personnel to
take appropriate precautionary measures.

Based on the general philosophy that radio spectra reveal underlying
mechanisms, the peak flux spectra of all bursts, and in detail the spectra
of principal proton events, have been studied. It has been found that when
the traditional meter-wavelength Type IV evidence alone is used the "false
alarm" rate is very high. Even the better criterion of centimeter burst
flux, with increases $\geq$ 1000 flux units, is not satisfactory unless the
hitherto ignored signature of flux increasing in the short centimeter-

wavelength direction coupled with high burst intensity (U-shaped) is considered. This approach has been tested earlier against 1966 principal proton events and against the principal PCAs of the last sunspot cycle. It holds up equally well against more recent investigations of 1967 principal PCAs. There is evidence, therefore, that different spectral curves emerge for proton and nonproton bursts and perhaps for proton and nonproton regions.

Data collected both at Sagamore Hill and Manila Observatory are available to the Air Weather Service and to the general scientific community; daily in the case of the Air Weather Service, and monthly through ESSA and other bulletins to other users. The more important radio bursts are reported in real time to AWS Solar Forecast Center for processing and retransmission to routine users for warning purposes. The value of the research is enhanced by the reliability of the data, resulting from emphasis placed on absolute accuracy.

## INTRODUCTION

The forecasting of solar proton events has recently assumed practical significance in the prediction of hazards that may be encountered by man and equipment in space, in alerting scientific investigators to potential physical dangers in their projected space and related ground experiments.

In space travel for whatever purpose, whether to travel to the moon to study its composition or simply to orbit our planet high above the earth to study emission from cosmic space, man must know what conditions he is likely to encounter. If the elements seem to be lethal, for example, he must delay his exploration until more definite information is available.

Once having pierced the thin friendly protective mantle of our atmosphere and ionosphere, man may not be able to endure the dangers of the very things he came there to study. The bio-medical scientists are familiar with the dosages of cosmic radiation man can tolerate. Others have determined that particle radiation associated with solar proton flares may ultimately be deadly. In the judgment of some solar scientists, there will be no safe period for space exploration through 1970. Whether they are right or merely cautious, plans for manned space flight continue while others endeavor to predict safe or dangerous periods. The contributions of all researchers of solar geophysical phenomena are being weighed carefully.

Future probabilities (there is no certainty) are suggested from statistics of the past. To seek out one single piece of information which affords an infallible clue that a proton flare is likely to occur at a designated time or even that one has just occurred, before actually counting particles or observing some effect indicating that particles have arrived is absurd because it is an oversimplification of a very complex phenomenon. Yet this is precisely what radio astronomy presumes to do. Its contribution

at present is one of warning rather than prediction. Although not infallible the statistical record looks very good.

## THE PCA AS AN INDICATOR OF PROTON EVENTS

One of the reliable indicators of an important proton event as it affects the environment of the earth and the one used by AFCRL to study correlations for warning purposes is the ground-based 30-MHz Polar Cap Absorption (PCA) measurement made with riometers. This type of indication, with an average delay time from flare-burst maximum of four or five hours to first onset of particles and a much longer delay to maximum absorption, affords a measure of the severity of the event (see Figure 1). Proton flux from the 20- to 100-MeV particles can be estimated from the magnitude of the absorption.

A more direct measure of cosmic particles has in recent years become available from satellite-borne monitors. In time these will become the basic means for measurements of particle emission. Before that time arrives, valid correlations with PCAs must be established. Currently, with sensitive sensors, many so-called proton events (and electron events) are being cataloged which are not detected with riometers. The energy level of some of these is quite low. Some have direct flare association, others have nebulous association; still others represent recurring activity from active regions that earlier were responsible for important emission (Fan et al., 1968 and Anderson, 1968). Not all of these satellite-observed proton events are dangerous. Probably some of the weaker PCAs do not pose great dangers to personnel in manned orbiting laboratories. There may, however, be dangerous particle emissions associated with solar events for which there is neither PCA nor satellite indication. Deep space probes could encounter these.

## THE PCA FLARE-BURST SIGNATURE

The radio astronomy approach to warning is based on the centimeter-wavelength radio signature of large flares associated with solar disturbances on the visible disk of the sun. Invisible proton flares can apparently occur on the back side of the sun, just beyond the west limb, for example, and cause particles to spiral out in the direction of the earth. Obviously, it is impossible to give real-time warning of such an event. Even before current Air Force efforts, researchers (Webber, 1964) recognized the superior correlation between cosmic-ray events and centimeter bursts to other associations. Others recognized that centimeter-burst flux was more closely related to PCAs than "other" radioactivity (Pick-Gutman, 1961).

An example of "other" radio data often misinterpreted is the Type IV designation. The Type IV solar radio emission, as first defined by

Boischot, was a meter-wavelength phenomenon. It is a featureless type of burst in which the signal level rises to equivalent black body temperatures of up to $10^{10}$ or $10^{12}$ degrees K. Bandwidth is broad, and the intensity variation is smooth. Circular polarization is generally present. The event may last between 10 minutes and several hours, and is detected with sweep-frequency equipment. Information is usually displayed on a C.R.T. and recorded by photographic techniques. In time the Type IV definition was extended to include the centimeter-wavelength region.

A Type IV meter-wavelength indication alone without centimeter-burst association is not useful to people in need of warning information. There would be too many false alarms. If meter-$\lambda$ Type IV data is coupled with centimeter bursts, the flase-alarm rate drops greal . Even so, if one fails to take into account the centimeter-burst spectrum, although the intensity may be high in certain parts of the spectrum, false alarms will result. This fact seems to have been overlooked. If we take spectra into account, the false-alarm rate drops still further. The particular spectrum to which we refer is the so-called "U" spectrum (Castelli et al., 1967). The peak flux increase of these bursts shows a minimum in the 500- to 1500-MHz range with flux increasing in the high frequency direction to intensities $\geq 1000$ units in the 3-cm range. There is an increase also in the low frequency direction below the minimum. Typical curves for PCEs (polar cap events) in 1966 are shown in Figure 2.

SPECTRA

The validity of this type of presentation lies in the fact that in the centimeter-wavelength region burst maxima at different frequencies occur at the same time or within a very few minutes of each other and the optical flare maximum. See Figure 3 for a typical centimeter burst.

Prior to using burst spectral information in a warning system, a scheme for classification of bursts had to be worked out. AFCRL has done this using empirical plots of over 700 bursts observed at Sagamore Hill in 1966 and 1967 (see Figure 4). Although the scheme accounts for all bursts, in our warning approach we are concerned only with events in the A1 category. Actually, the percentage of all events in this group is quite small (see Figure 5). Not all of these have PCA association as we shall see.

Although events in other groupings are not associated with principal PCAs, their association with other geophysical events is becoming clearer. SCNAs (Sudden Commencement Noise Absorption), for example, are well correlated with all A groups (Castelli and Strauss, 1967), whereas SFDs (Sudden Frequency Deviations) seem to favor group C events. Negative associations are also useful in our warning system. Magnetic storm signatures are beginning to emerge.

Other spectra may be derived from single frequency observations. For example, energy spectra of bursts derived from burst mean-flux

density and duration may be plotted. The merits of this approach are being studied and compared with peak flux spectra. Errors in energy spectra might result from the inability to measure burst duration with the necessary precision. Radio astronomy leans heavily on spectral information when determining emission mechanisms.

## EQUIPMENT REQUIREMENTS

Sagamore Hill

Before a valid spectrum can be drawn, one must have a sufficient number of accurate points to plot a meaningful spectrum. Today the Air Force has this capability and is identified with precise solar radio measurements. Since early 1966, the solar section of the Radio Astronomy Branch of AFCRL has maintained a sunrise to sunset solar radio patrol at Sagamore Hill, Hamilton, Massachusetts. Fixed frequency coverage with a number of multiple frequency instrumented parabolic antennas is maintained at 606, 1415, 2695, 4995, 8800, and 15,400 MHz. All systems employ essentially a Dicke radiometric configuration. In some instances single-sideband operation is employed, in other cases dual-sideband operation is used. The i.f. bandwidth is generally 8 to 10 MHz except where radio interference (TV, radar, and so forth) is a problem; then the bandwidth is narrowed to 1 or 2 MHz.

Most of the frequencies selected operate in the vicinity of radio astronomy guard channels. There are other cogent reasons for the selected frequency ranges.

Antenna half-power beamwidth (resolution) is generally greater than 2 or 3 degrees to permit a valid total flux measurement, and especially a valid burst calibration.

Because of the importance of burst spectra and in order to be self-sufficient, AFCRL is extending its frequency coverage to the 100- to 600-MHz region, specifically to 246 MHz for a start, in the Fall of 1968. Coverage will also be extended upward to the 30,000 MHz vicinity for spectral studies.

The AFCRL solar radio patrol is also conducted in the 20- to 40-MHz range with a sweep-frequency system for the detection of classical meter-wavelength Type I to V bursts.

The data output of all systems is made available in real time to the Air Weather Service Solar Forecast group which cooperates with AFCRL in providing personnel to conduct the patrol. High absolute accuracy is emphasized in all measurements. Lack of absolute accuracy was a recognized major weakness of earlier data in many instances despite the fact that the measurements afforded quantitive flare associated data in all kinds of weather and environments.

Figure 6 is an exterior view of a portion of the Sagamore Hill Solar Radio Observatory. The project was and is supported in large measure by the Laboratory Directors Fund of AFCRL.

## Manila

Stressing the warning concept from data derived from fixed frequency centimeter-wavelength observations, a second site was established in mid-1967 at the Manila Observatory. The station is located about eleven hours west of Sagamore Hill. It is the site (one of eight) of optical solar observations conducted jointly by AWS personnel and local scientists. Although virtually full-time solar radio monitoring can be provided by the two stations, at some periods of the year there is no overlap between Manila and Sagamore Hill. At other times very low elevation data at sunrise or sunset is somewhat compromised in accuracy due to tropospheric scintillations. There is really no easy solution to these problems other than to have additional stations. In some instances needed radio data are available from non-Air Force affiliated groups. Figure 7 shows the coverage effected by the two stations.

The radio equipment used at Manila was AFCRL constructed and assembled and was excess from our solar eclipse projects of 1963 and 1966. The equipment is operated jointly by Manila Observatory and the Air Weather Service. It is, however, also under AFCRL control; accuracies and calibrations are maintained by Sagamore Hill standards. All operation methods were determined by the Sagamore Hill group. Key Filipino personnel at Manila and all AWS personnel were trained by the Sagamore Hill group.

All AWS solar observing stations including Manila have facilities for real time reporting of burst data to the AWS Solar Forecast Center at Colorado Springs. Presently the Manila patrol is a four-frequency system operating at 1415, 2695, 4995, and 8800 MHz on a single radio telescope (see Figure 8). By late 1968, 606 MHz and a 25- to 50-MHz sweep-frequency unit supplied by AFCRL will be added to the system.

The project at Manila supports both AWS requirements and AFCRL's scientific data needs. The principal reason for operating the station is to "capture" all principal proton events. One proton event with PCA association has been observed by the group. Figure 9 is a copy of 9 June 1968 radio data taken at Manila associated with this important proton event. It is fairly representative of centimeter bursts of large proton events (PCA), though there is some apparent decrease of flux at 8800 MHz. Actually none of these relatively rare events traceable to a flare has occurred in the Sagamore Hill daylight observing hours so far in 1968. Several others recorded at Sagamore Hill in 1966 and 1967 are shown in Figures 10 and 11.

Athens

A third station midway between Manila and Sagamore Hill is in operation near Athens, Greece. At present only a single 10-cm wavelength radio patrol is in operation there. Plans are being made to increase radio coverage in that area for much needed spectral data. The usefulness of the Athens site is enhanced by the optical solar patrol there, manned by the AWS.

The centimeter-wavelength solar monitoring equipment is relatively inexpensive compared to optical systems and high resolution radio mapping systems.

## DEFINING THE LIMITATIONS OF THE AFCRL PROTON WARNING SYSTEM

A significant number of all PCAs must be classified as anomalies with which we cannot cope. Earlier we quoted an example of such an event where the particle emission might be caused by a solar disturbance on the back side of the sun. Again we can not presently furnish warning of the weaker events that sometimes recur and are associated with active regions or nebulously flare-correlated weak disturbances. What we actually do is observe all centimeter bursts and, on the basis of how well they conform to the empirically derived spectral intensity criteria, give an estimate (warning) whether or not a PCA is likely to follow. Things other than the radio signature are involved in PCEs. It is recognized that the position of the disturbance on the solar disk and other directivity problems influence whether or not the earth's atmosphere sees a de facto proton event as a PCE. A flare-burst, which has all the signatures of being a proton event, may sometimes occur without any particles being actually detected. These would be classified as "false alarms" though it is suspected that there was particle emission which was either trapped in the solar atmosphere or spiralling out, simply missed the earth's direction. We are quite content to be guilty of false alarms in these few instances. Our problem is just the reverse of that of the riometer monitors. Whereas we observe certain reliable signatures and look for a PCA, riometer observers routinely record all absorptions large and small, and then try to relate them to some solar disturbances, sometimes unsuccessfully in the case of weaker events.

## APPLYING CRITERIA TO EARLIER PCA

In an earlier paper (Castelli et al., 1968), we discussed various criteria for proton events and applied our criteria to principal PCAs of 1966 and to those of the last sunspot cycle. One of the criteria often misapplied is that of meter-λ Type IV radio data. As in the case of large flares,

there are many more meter-$\lambda$ Type IVs than PCAs. From Sagamore Hill observations in 1966 we were able to show that using centimeter spectral data for that year, we could provide warning of principal PCAs with only one false alarm as compared with 23 false alarms using the meter-$\lambda$ Type IV criteria alone; 14 with meter-$\lambda$ Type IVs and any centimeter burst; and 3 with meter-$\lambda$ Type IVs and a centimeter burst greater than 1000 units, at any frequency regardless of spectrum (see Figure 12). In fact, all principal PCAs for that year, whether the associated flare burst was observed at Sagamore Hill or elsewhere, fitted well into our preferred pattern (Figure 2).

Considering also Bailey's (1964) list of principal PCAs of the last sunspot cycle both the U-shaped spectrum and centimeter-burst signatures applied very well (Castelli et al., 1968) (see Figure 13). Where exceptions occurred, we could not be sure if the PCA was in reality associated with a non-U-shaped spectrum, whether the radio data was complete and accurate, or whether the PCA-flare-burst association (always a problem) was correct. Bailey defined a principal PCA as one whose equivalent 30-MHz absorption exceeded 2.5 dB. With regard to the U-shaped spectrum, we caution against too rigid an application of this criterion in the sense that it is not presently known how far in the high-frequency direction the peak-power flux spectra increase before starting to bend back. We do know that there is a general rising trend. We are presently applying 15 GHz spectral data for 1968 to the study and will later this year include 8.6-mm burst data. When Castelli et al. (1967) first called attention to the U-shaped spectrum, we cautioned that there might be a levelling off or start to change of the spectral index direction in the 3-cm wavelength vicinity. Note also that the U-shaped spectrum reduced in intensity by an order of magnitude in the 10- to 3-cm range is possible and often found even with very large flux in the 25- to 50-cm range. These types do not conform to our definition of the U-shaped burst for proton-flare association.

## 1967 BURST DATA, SAGAMORE HILL

In reviewing 1967 spectra of bursts, recorded at Sagamore Hill in the same manner as the 1966 data (Figure 12), a similar pattern emerges. There were 37 meter-$\lambda$ Type IVs. Only 23 or 62 percent had any centimeter association. This is the identical percentage found for 1966. Among these 23 there were five events whose single-frequency centimeter flux reached 1000 units at any frequency. Two of these did not have the preferred spectrum by our criteria. One had an inverted-U spectrum C1, exceeding 1000 units at 4995 MHz but dropping rapidly to only 40 percent of this at 8800 MHz. Flare importance was 1B. The other did not have any confirmed flare association though the emission at 606 MHz (80,000 units) made it one of the most intense events of the present sunspot cycle. This left only three possibles whose spectra were of the A1 type (> 500 units at 8800 MHz) and which also exceeded 1000 flux units at 8800 MHz. This data is shown in Figure 14. One of these was related to a principal PCA on 23 May 1967 and was one of the largest radio bursts ever recorded.

The PCA was 11 dB. We have earlier seen the burst shape (Figure 11). Figure 15 shows its spectrum.

The other two possibles on 21 May and 27 February with 2B and 2N Flare association, respectively, had no apparent PCA association though we wonder why not. Hence, we would have had two false alarms for the year.

Applying Bailey's criterion of a principal PCA (> 2.5-dB absorption) to Masley's (1968) list of PCAs for 1967 we find that there were four such events. The largest, with an 11-dB absorption, was observed during Sagamore Hill daylight and met our criteria. The next largest on 28 January 1967, with a 7-dB absorption, was truly an anomaly for its effects were clearly seen with neutron monitors but with neither optical nor radio correlation. It has been suggested that this was associated with a flare beyond the west limb. The next largest, with 3-dB absorption on 28 May, was related to a flare starting about 0528 UT (Sagamore Hill nighttime). Based on available data from Nagoya (Tanaka, 1968) the centimeter event had the preferred spectrum.

A final principal PCA with 2.6-dB absorption on 2 February reportedly related to a 2B flare at 0152 UT had a very weak emission whose spectrum was almost flat in the 1000- to 10,000-MHz range. This event is truly upsetting for we would certainly not have forecast it. It is suggested that it falls in a second category of PCA bursts characterized by weak microwave emission and a gradual rise and fall burst shape (Sakurai, 1967). This same burst configuration possibly identifies weaker flare associated PCAs.


CONCLUSIONS


A careful study of centimeter flare burst data associated with principal PCAs of 1966 and 1967 leads us to believe that our centimeter peak flux intensity spectral classification is reliable for giving warning of most principal cosmic-ray events. Very few false alarms will result from this approach. We do not urge its use to the exclusion of any other type of data (the best of all disciplines must be sifted and weighed) but in view of the record, we fail to see how the Air Force can afford to ignore it.

With 1968 data, the usefulness of the Manila operation will provide much needed self-sufficiency. We visualize having, under central calibration control, enough complete solar radio patrol stations to enable us to attempt to find unambiguous flare-burst association for all proton events, even the weak ones. For the present with the addition of Manila to Sagamore Hill operation, we have virtually continuous observation. Personnel have all been trained and alerted to the same ideas and ideals. With real-time reporting of burst spectral data we can contribute vitally to warning of proton events.

# REFERENCES

Anderson, K. A. (1968) Electrons and Protons in Long-Lived Streams of Energetic Solar Particles, University of California Report, Berkeley, California, June 1968.

Bailey, D. K. (1964) Polar-cap absorption, Planetary Space Sci. 12: 495-541.

Castelli, J. P., Aarons, J., and Michael, G. A. (1967) Flux density measurements of radio bursts of proton-producing and nonproton flares, J. Geophys. Res. 72 (No. 21): 5491-5498.

Castelli, J. P., and Strauss, F. M. (1967) Correlation between sudden cosmic noise absorption and solar radio bursts observed at five microwave frequencies, Nature 216 (No. 5117), Nov. 25, 1967, pp. 776-777.

Castelli, J. P. (1968) Observation and Forecasting of Solar Proton Events, AFCRL-68-0104, Air Force Surveys in Geophysics, No. 203.

Fan, C. Y., Pick, M., Pyle, R., Simpson, J. A., and Smith, D. R. (1968) Protons associated with centers of solar activity and their propagation in interplanetary magnetic field regions corotating with the sun, J. Geophys. Res. 73: 1555-1582.

Masley, A. J. (1968) The 1967 Solar Cosmic Ray Events, Douglas Missile and Space Systems Division Paper 4662.

Pick-Gutman, M. (1961) Évolution des Émissions Radioélectriques Solaires de Type IV et leur Relation avec d'Autres Phénomènes Solaires et Geophysiques, Annales d'Astrophysique 24: 183-210.

Sakurai, K. (1967) Development of solar flares and the acceleration of solar cosmic rays, Report of Ionosphere and Space Research in Japan 21 (No. 4): 213-222.

Tanaka, H. (1968) in Monthly Solar Bulletins of the Research Institute of Atmospherics, Nagoya University, Toyokawa, Aichi, Japan.

Webber, W. R. (1964) A review of solar cosmic ray events, in AAS-NASA Symposium on the Physics of Solar Flares, Greenbelt, Md. 1963, NASA Rpt. SP-50, pp. 215-256.

FIGURE LEGENDS

Figure 1. Distribution of Principal PCAs (> 2 dB) From 1952 to 1963
(Bailey, 1964). Mean delay flare from start to flare max (24 minutes)
shown by broken line. Mean delay flare from start to PCA onset 4
hours. Mean delay PCA onset to max 18 hours

Figure 2. Radio Spectra of Proton Events Observed During 1966 at Saga-
more Hill, the Netherlands, Nagoya, Tokyo, and Dominion Observa-
tory, Canada. (The points for each event represent the maximum
flux increase at the observed frequency; the events generally occur
within a few minutes of each other and the associated optical flare.)

Figure 3. Complex Radio Burst Observed on 1 April 1967 at Sagamore
Hill Radio Observatory, Hamilton, Mass.

Figure 4. AFCRL Classification of Microwave Solar Bursts According to
Peak Flux Spectra. Curves are shown for typical events. Subclasses
are also indicated: (A) type A grouping; (B) type G grouping; (C) type
C grouping; (D) indeterminate spectra grouping. All flux shown in
units of $10^{-22}$ W M$^{-2}$ Hz$^{-1}$.

Figure 5. Percentage Distribution of All 1966 and 1967 Burst Peak Flux
Spectral Graphs According to Designated Spectral Type — Sagamore
Hill Observatory

Figure 6. An Exterior View of a Portion of the Sagamore Hill Solar Radio
Observatory

Figure 7. Solar Patrol Hours (UT) Throughout the Year. Overlap is
shown by lines on dots; dark areas are periods when neither Manila
nor Sagamore Hill can observe the sun

Figure 8. Manila Solar Radio Observatory

Figure 9. Complex Radio Burst Observed on 9 June 1968 at Manila Ob-
servatory

Figure 10. Complex Radio Burst of the Solar Proton Event, 28 August
1966, Sagamore Hill Radio Observatory (AFCRL) Hamilton, Mass.

Figure 11. Great Radio Burst of the Solar Proton Flare 23 May 1967 at
Sagamore Hill Radio Observatory, Hamilton, Mass. (Chart
reconstructed-flux values plotted at intervals of one minute or less;
flux density in units of $10^{-22}$ W M$^{-2}$ Hz$^{-1}$)

Figure 12. Meter-Wavelength Type IV Events and Distribution of Those
Associated with Centimeter Bursts

Figure 13. Principal PCAs for 1952 to 1963 (Bailey, 1964) Associated
With Microwave Burst Activity at Different Flux Density Levels

Figure 14. Sagamore Hill Meter-Wavelength Type IV Events for 1967 in Relation to Centimeter Bursts

Figure 15. Radio Spectrum, Proton Event for 23 May 1967. Points represent max flux increases. Observations at Sagamore Hill and Ottawa (2800 MHz)
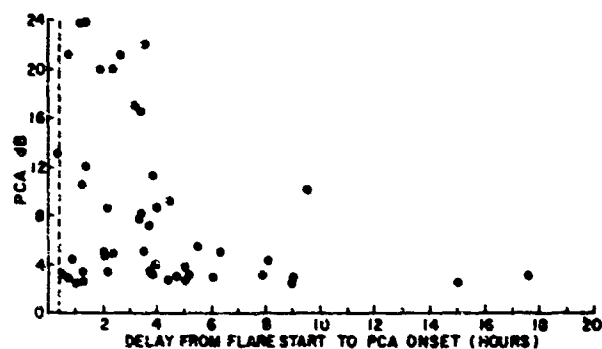
Figure 1
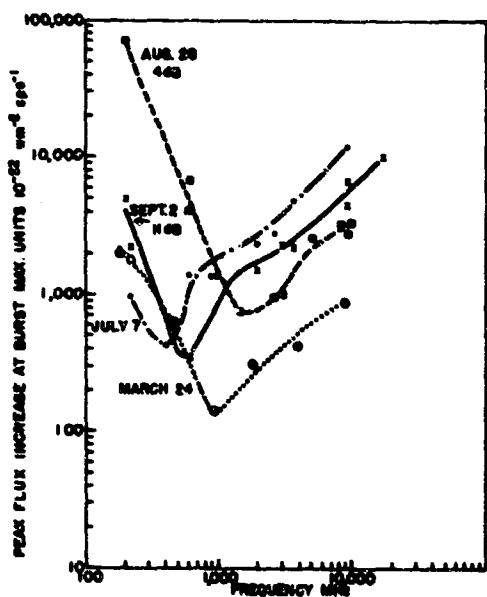


Figure 2
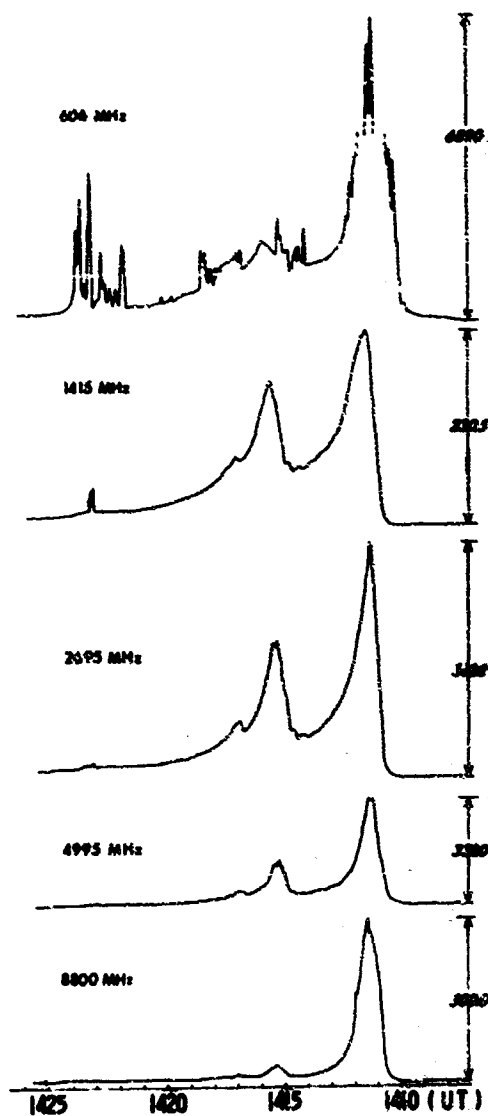


Figure 3
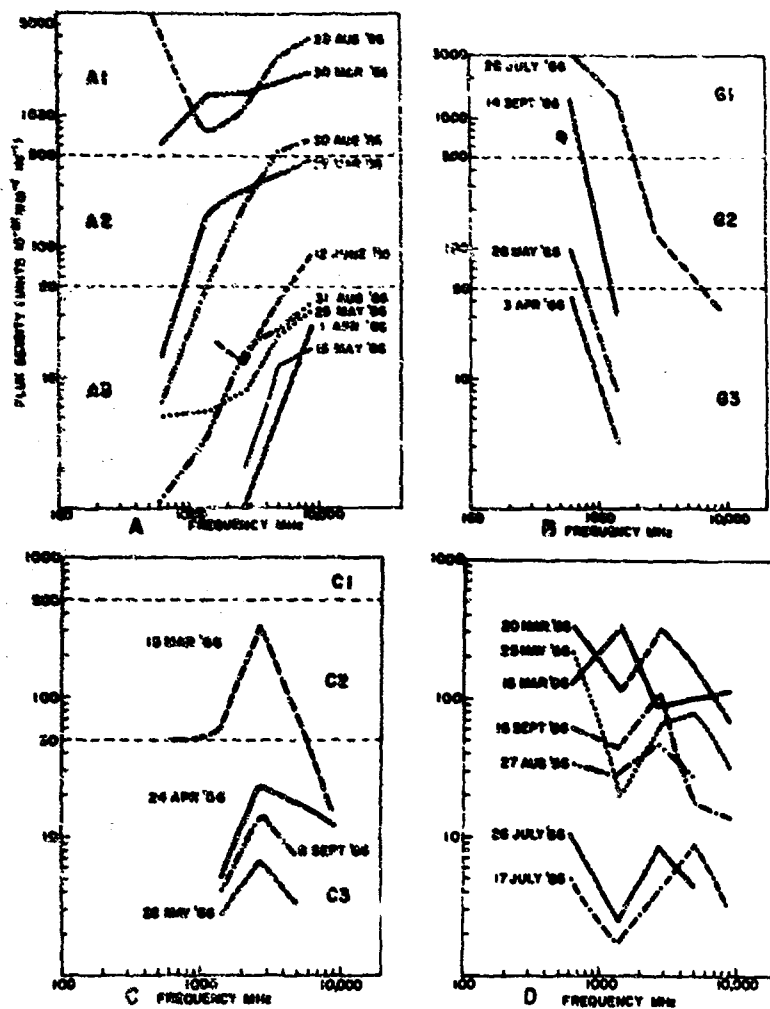
Figure 4
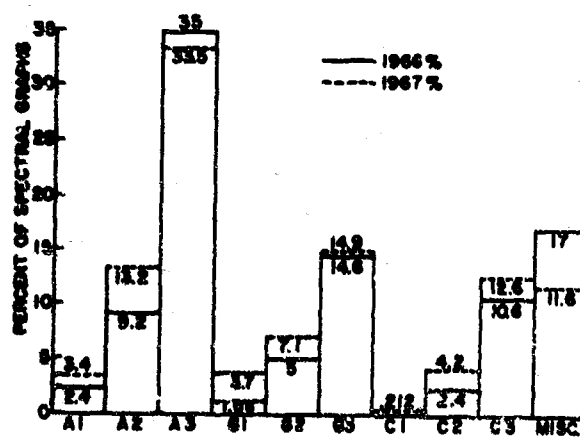


Figure 5

Figure 6

FIG. 7  DRAWING SHOWS SOLAR PATROL HOURS (U.T.) THROUGH THE YEAR.
OVERLAP IS SHOWN BY LINES ON DOTS;  DARK AREAS ARE PERIODS
WHEN NEITHER MANILA OR SAGAMORE HILL CAN OBSERVE THE SUN.

■ = SAGAMORE HILL         ▨ = MANILA

Figure 8



Figure 9

Figure 11



Figure 10

Z-19
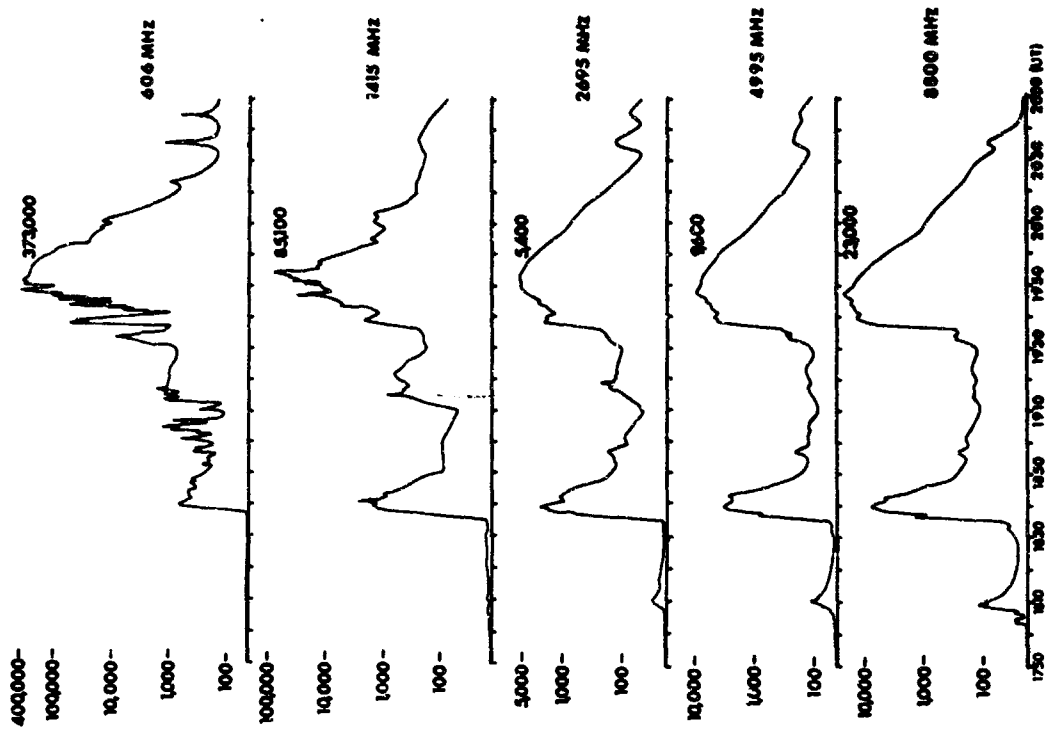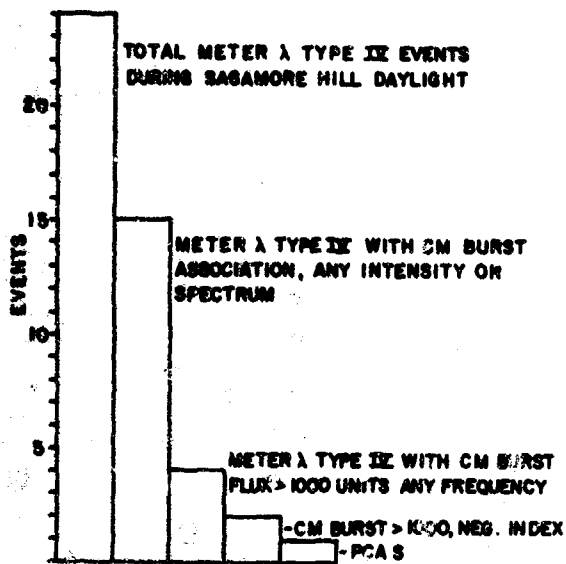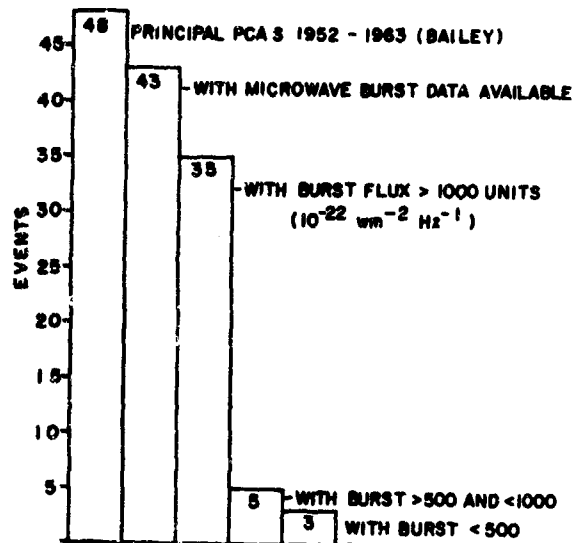
Figure 12



Figure 13
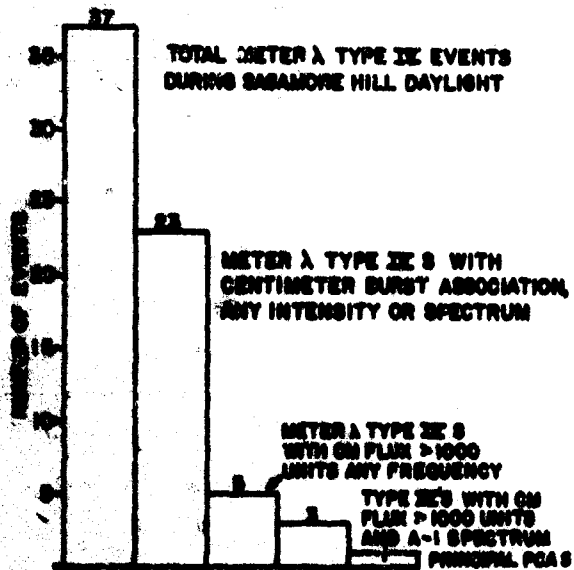


Figure 14
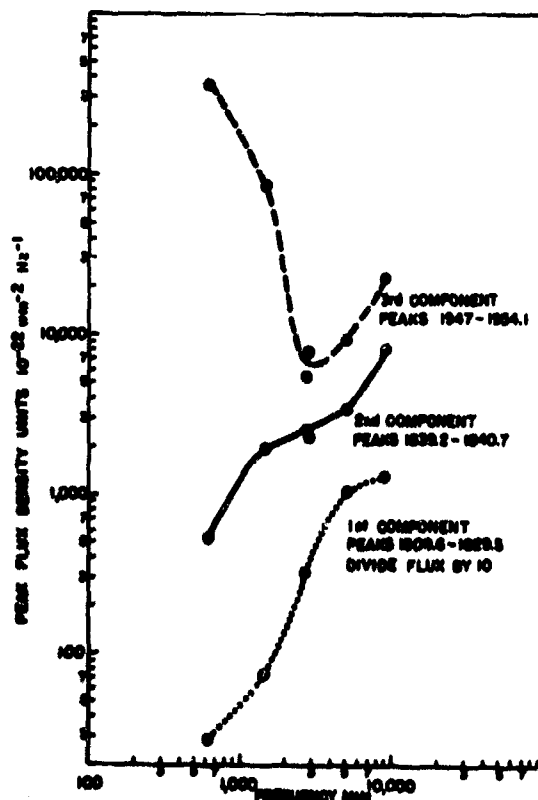


Figure 15

DEVELOPMENT OF PASSIVELY PRESSURIZED
PARTIAL-PRESSURE SUIT

By

Jefferson C. Davis, Lt Colonel, USAF, MC

Education Division
USAF School of Aerospace Medicine
Aerospace Medical Division (AFSC)
Brooks Air Force Base, Texas

AA-1

# DEVELOPMENT OF PASSIVELY PRESSURIZED
## PARTIAL PRESSURE SUIT

## ABSTRACT

Efforts to improve comfort and reliability of the partial pres-
sure suits led to the development of the passively pressurized partial
pressure suit.  The functional component of this suit is a family of
sealed tubes affixed to the inner surface of the outer layer of the
suit, running longitudinal along the extremities and torso.  These
tubes will expand according to Boyle's Law and apply mechanical or
partial pressure to the skin at any altitude up to and including a
vacuum.  Two variables affect the amount of pressure applied to the
skin at altitude:  initial volume of air sealed in each tube; tight-
ness of fit of the outer layer.  Flights to altitudes between 65,000
feet and 115,000 feet have been made with no adverse reactions.
Passive partial pressure suits should find application in any long
duration flight to altitudes above 50,000 feet where normally "shirt-
sleeve" cabin conditions prevail, but emergency protection must be
provided.

## Biographical Sketch

### Lt Colonel Jefferson C. Davis, USAF, MC

Lt Colonel Jefferson C. Davis is a native of Neosho, Missouri, where he graduated from high school in 1950. He attended the University of Missouri and the University of Missouri School of Medicine, where he received his M.D. degree in 1957. Lt Colonel Davis completed his internship at Bellevue Hospital, New York, New York in 1958.

He entered the U.S. Air Force in 1958 and attended the Primary Course in Aviation Medicine at Randolph AFB, Texas. He was assigned to duty as a flight surgeon, Ellsworth AFB, South Dakota, from 1958-1960, where he served as Director of Aerospace Medicine. He was awarded the Air Force Commendation Medal for work during this period. From 1961-1962 he was an instructor in flight medicine at the USAF School of Aerospace Medicine, Brooks AFB, Texas.

He completed Phase I of the aerospace medicine residency training program at the University of California, Berkeley, California, receiving an MPH in June 1963. Lt Colonel Davis completed Phase II of the residency training program at the USAF School of Aerospace Medicine in 1964, and the third and final year of residency at Headquarters, Strategic Air Command, was completed in June 1965. From July 1965-March 1968 he was assigned to the Aeromedical Indoctrination Branch, Education and Training Division, USAF School of Aerospace Medicine. He was medical officer for the USAF Compression Training Program during that period. At present Lt Colonel Davis is the Commander, 37th USAF Dispensary, Phu Cat AB, RVN.

Lt Colonel Davis is certified in Aerospace Medicine by the American Board of Preventive Medicine. He is a member of the Aerospace Medical Association, the American Medical Association, and the Society of USAF Flight Surgeons and is a fellow of the American College of Preventive Medicine.

AA-3

The pressurized and climate-controlled aircraft cabin and the sealed spacecraft environment provide adequate physiological parameters for man's operations in the hostile low barometric pressures of extreme altitude. With the exception of extravehicular activity in space flight and planned aircraft depressurization at high altitude, the pressure suit is worn as a back-up for these systems. Crewmember objections to existing pressure suits are most often based on encumbrance, impaired vision and loss of mobility even in the unpressurized mode during the prolonged periods when they are worn as emergency equipment, needed only in the event of loss of cabin pressurization.

A vast spectrum of protective capability is required of pressure suits for various aerospace systems. On one end of this spectrum are the extensive demands on a suit for extravehicular activity in space, where protection must include pressurization adequate to prevent both hypoxia and decompression sickness, elaborate thermal regulation and protection against radiation and micrometeorites. On the other end is the requirement for a protective garment which is unrestrictive and comfortable in the normal operation of the pressurized cabin but with the capability to automatically respond in the event of sudden failure of cabin pressurization. Our efforts have been directed toward this end of the spectrum of requirements.

There are two basic methods of providing pressure to the body at high altitude - pneumatic and mechanical. The pneumatic or full pressure suit is in reality a pressurized cabin which conforms to body contours and supplies gas pressure to the entire body equally. Recent technological advances have brought the full pressure suit to the present level of outstanding reliability and sophistication. For prolonged wear as a back-up system, however, they do pose difficulties. Because the full pressure suit is, of necessity, heavy and cumbersome even in the unpressurized mode, they add greatly to fatigue when worn for several hours.

The quest for answers to these objections was begun in the 1940s by the Royal Air Force and the United States Air Force. The basic idea was to provide a compromise garment which would provide adequate physiological protection to allow descent or corrective action in the event of an emergency, or, if possible, to allow completion of the prescribed mission at high altitude yet cause a minimum of interference during normal operations.

The search for comfortable yet adequate combinations led to a variety of garments ranging from the pressure breathing mask, pressure helmet with torso counterpressurization only to suits providing mechanical counterpressurization to the torso and extremities. Pressure breathing with torso counterpressurization only is unsatisfactory for, while the lungs are protected from damage by the high inspired oxygen pressures, fainting

AA-4

due to venous pooling occurs in most subjects after as little as 30
seconds at 55,000 feet. However, when helmet pressure is balanced with
both torso and extremity counterpressure, durations of up to 4 hours at
65,000 feet (ambient pressure 42 mm Hg) with the suit and helmet pressur-
ized to 100 mm Hg above ambient, have been attained with no ill effects.
Peak altitudes of over 198,000 feet (ambient pressure 0.3 mm Hg) have
been attained in the altitude chamber wearing mechanical pressure suits
so configured.

Mechanical pressure has been applied to the skin in two ways. In
the capstan or pneumatic lever principle, developed by Dr. James Henry
of the University of Southern California and Wright-Patterson AFB, fa-
bric is drawn tightly over the skin to apply mechanical pressure.

In the so-called bladder suits, pressure is applied by inflation of
confluent bladders covering the entire body except the hands, feet, neck,
and head. Pressures applied to the helmet are contained by a rubber dam
neck seal and balanced with the counterpressure over the rest of the body
by a regulator pre-set to provide a total pressure of 140-150 mm Hg (am-
bient + suit) regardless of altitude attained.

The partial pressure suit is thus an attempt to provide emergency
pressure protection with as near "shirtsleeve comfort" as possible in
the normal unpressurized state. With current state-of-the-art partial
pressure suits, disadvantages are the lack of environmental control
despite large body areas covered by solid bladders, vulnerability of the
large interdependent bladders to damage and loss of pressure and the
need for relatively tight-fitting of the capstan suit.

Efforts to improve comfort and reliability of mechanical or partial
pressure suits led to exploration of the use of the expansion of trapped
gases at altitude according to Boyle's Law. This was first attempted in
the form of closed cell sponge material with which it was proposed to
make a suit which would inflate automatically at decreased barometric
pressure, applying mechanical pressure to the skin. Inherent difficul-
ties with this material were thickness required even uninflated, rigid-
ity at altitude and difficulty finding a material which would produce
reproducible expansion rates upon repeated exposures to altitude. Using
this basic principle, we turned to the investigation of other forms of
flexible sealed gas containers and have successfully completed feasibil-
ity studies on the concept of the passively pressurized partial pressure
suit. The principles to be described may have application as an emer-
gency pressure suit for high-altitude aircraft flight, a constant wear
intravehicular garment for extended space flight and for crewmembers of
the proposed supersonic transport. During development of this new con-
cept, the guiding theme has been the quest for comfort in the unpres-
surized state yet with reliable protection at any altitude up to and
including a vacuum.

AA-5

The suit construction is quite simple (Figure 1). The outer layer is an inelastic, lightweight, porous fabric. The inner layer is inconsequential for its only function is to serve as a wicking material for passive cooling and to protect the tubes before donning of the suit. In our test suits, the inner layer was cotton underwear. The functional component is a family of sealed tubes, affixed to the inner surface of the outer layer of the suit, running longitudinally along the extremities and torso. Each tube is pleated in accordion fashion so that uninflated it assumes a small cross-sectional diameter yet has the potential for expansion as its contained volume of air increases at the low barometric pressure at high altitude (Figure 2). The potential volume of each tube is designed to be so great that its limit of expansion is never reached and work is not expended in stretching the tube wall as would be true with small tubes of elastic material. The inelastic outer layer of the suit thus acts as a restraining layer to direct pressure to the skin. One set of tubes extends from the wrists, across the shoulders, along the torso and to the mid-thigh. Another set extends from the ankles to the shoulders (Figure 3). Each tube is independent of all the others and is sealed with a filler valve at either the wrist or ankle to allow adjustment of gas volumes. Only two variables affect the amount of pressure applied to the skin as the subject goes to altitude: 1. the initial volume of air sealed in each tube at ground level and 2. the tightness of fit of the outer layer (Figure 4). Our studies have shown that the optimal fitting techniques for subjects of varying sizes is to vary only the initial tube volumes and leave the tightness of fit constant.

A standard partial pressure suit helmet (HGU-8/P) was modified for integration with the suit. The helmet has a standard rubber neck seal and balanced oxygen pressure to the helmet is programmed by a regulator pre-set to follow the known pressure curve of the suit (Figure 5). Tests have also shown the feasibility of a soft pressure helmet which can be worn folded back around the neck, to be donned at the time of an emergency, for use in situations where the buffeting protection afforded by the hard helmet is not required. In our studies, hands were protected by tight leather gloves only and the feet by tight boots.

During the past 3 years of development and testing manned altitude chamber flights to altitudes between 65,000 feet and 115,000 feet have been made in five test suits by nine test subjects with no adverse reactions. To test mission completion capabi'' of the suit, durations of 1 hour at 70,000 feet, 2 hour. at 65,000 feet have been achieved without ill effects. To study the possible deleterious effects of Charles Law on suit performance at the low temperatures of high altitude, a series of cold chamber tests were run. In manned flights at 65,000 feet, minus 30 degrees centigrade for 10 minutes, the pressure curves showed no significant change (Figure 6). Skin temperature dropped

sharply upon entering the cold chamber at ground level, tubes deflated, but rose toward normal at altitude with tube inflation.

Pressure measurements were made by two methods. In the first series of experiments, a liquid-filled manometer connected to a liquid-filled bladder was used to measure the pressure exerted on the skin by inflation of the tubes at altitude. Later studies showed that the easier method of monitoring air pressure in the tubes yields equivalent results.

Even the small volume of air in the tubes at ground level provides enough flotation to support the subject in water. With the largest total tube volume in the torso and upper extremities, flotation is upright.

The advantages of the passive partial pressure suit are summarized as follows:

1. It is a lightweight, loosely fitting garment offering a minimum of encumbrance and bulk at normal cabin altitudes below 20,000 feet. The first factory test model weighed only 5 pounds.

2. There are no connections to the suit as no outside pressurization source is required. This is an important factor in reducing encumbering hoses and improving reliability inasmuch as the suit operates entirely according to a law of physics.

3. Passive ventilation through the porous outer fabric and between the tubes in the uninflated state precludes the need for accessory ventilating systems. Accessory ventilating vests have been successfully tested under the suit and could be used if required. However, it is our opinion that where possible, air conditioning should be made a requirement of the aircraft cabin and not a part of the pilot's apparal in order to free him from encumbering hardware as much as possible.

4. In the inflated state at altitude, the tubes are fully confluent, covering the entire body surface with a dead air space. This provides excellent protection against the cold of extreme altitudes. Extension of this principle to the possible applications in cold water survival gear by use of special insulating tubes which could be manifolded and partially inflated by a carbon dioxide charge bears further investigation.

5. In situations where buffeting protection is not critical, the soft helmet can be worn folded back around the neck, to be closed manually or automatically with further development.

AA-7

6. Independence of each tube so that damage to one does not affect counterpressure afforded by the rest of the suit is a definite safety factor. The collapsed, pleated tubes are large enough at full expansion to allow considerable overlap should an adjacent tube be damaged.

7. Our water tests at ground level have demonstrated that there is adequate gas volume in the tubes to provide flotation for a man.

Out studies have demonstrated the feasibility and many desirable features of the concept of passive pressurization in altitude protective garments. The test suits meet the criteria for comfort in the unpressurized, normal operating mode, yet provide predictable, dependable physiological protection in the event of emergency loss of cabin pressure. With further development, passive partial pressure suits should find application in any long duration flight to altitudes above 50,000 feet where normally "shirtsleeve" cabin conditions prevail but emergency protection must be provided. An especially interesting possibility is for use by pilots of the proposed supersonic transport. Here the possibility of unexpected loss of cabin pressure will be so small with cabin environmental conditions so ideal that pilots will justifiably reject any protective garment that does not provide "shirtsleeve" comfort. However, the unlikely event of rapid decompression at altitudes above 50,000 feet would cause unconsciousness within seconds unless pressure suits are worn. If the pilots maintain the capability for emergency descent the unconscious passengers could survive.

The final chapter in altitude protective equipment will not be complete until every possible avenue has been explored. The concept of the passive partial pressure suit appears to be a fruitful direction for further studies. As man ventures into new and hostile environments, the field of aerospace medicine must provide physiological protection without so encumbering him that his ability to do useful work is impaired.

**ALTITUDE**
**(TUBES INFLATED)**
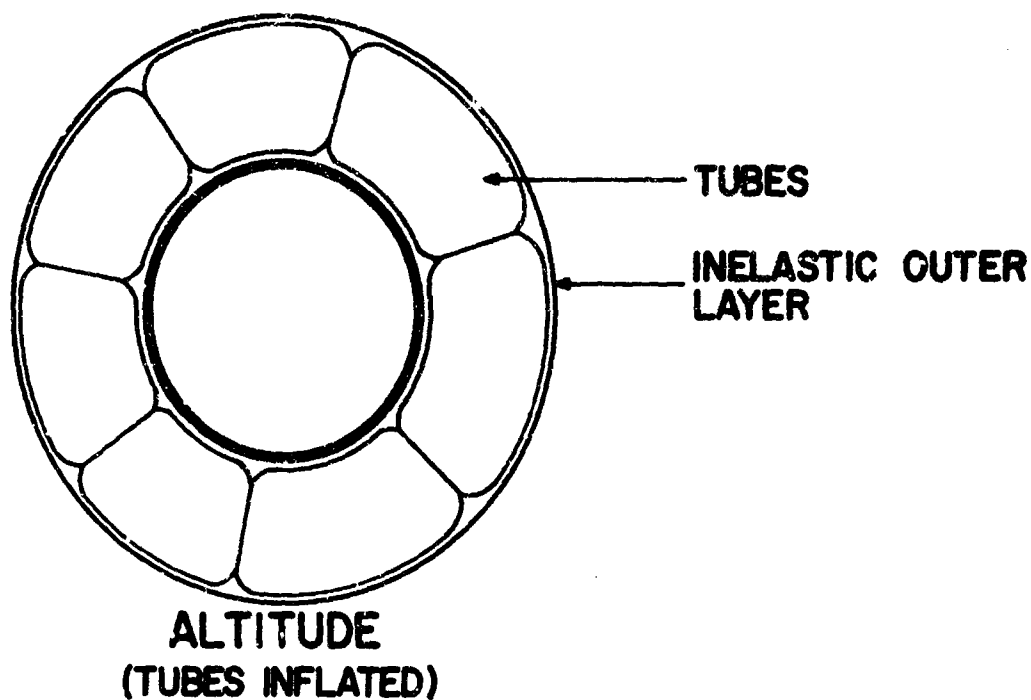
Figure 1. Diagram of cross section of the tubes, inner and outer layer at ground level.



**GROUND LEVEL**
**(TUBES DEFLATED)**
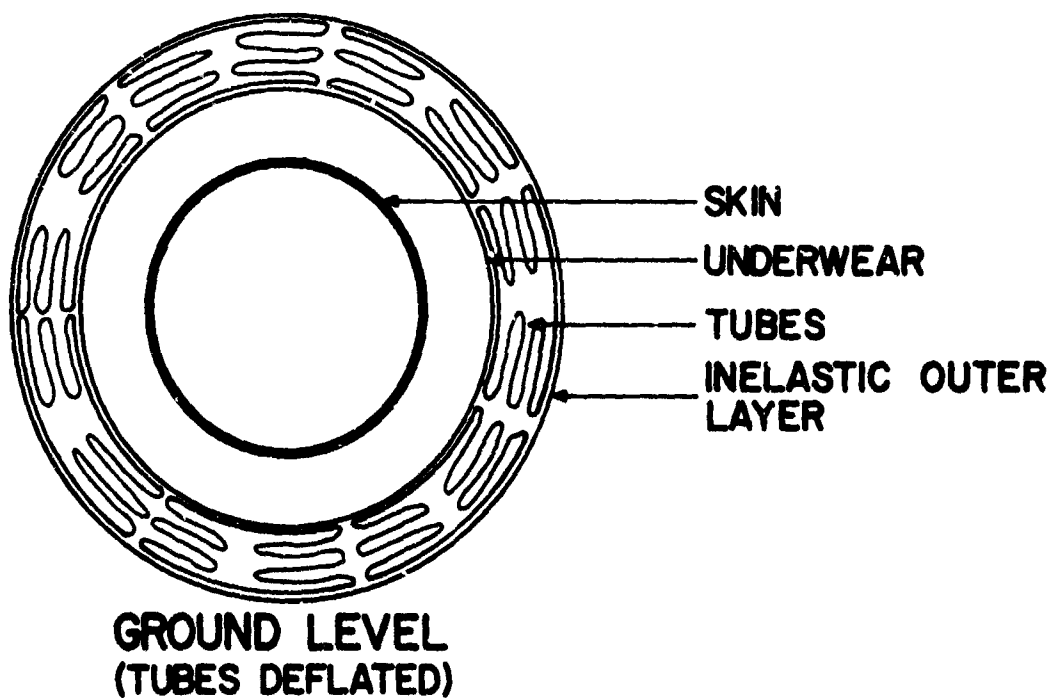
Figure 2. Diagram of cross section of the tubes (inflated), inner and outer layer at altitude.

Figure 3. Inside of torso with underwear zipped out to show tubes.

AA-10
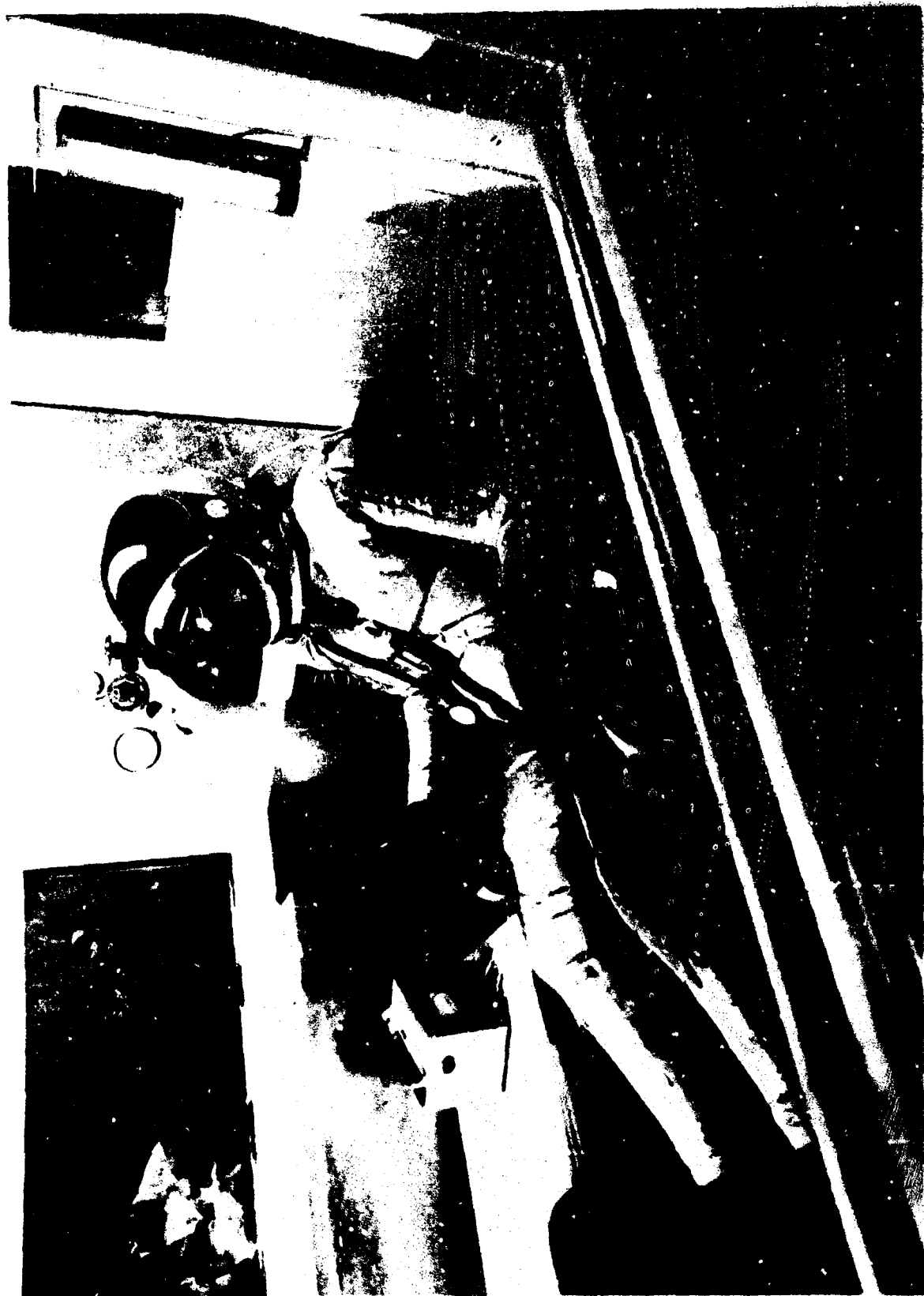
Figure 4. Overall view of the passively pressurized partial pressure suit inflated at altitude.

AA-11
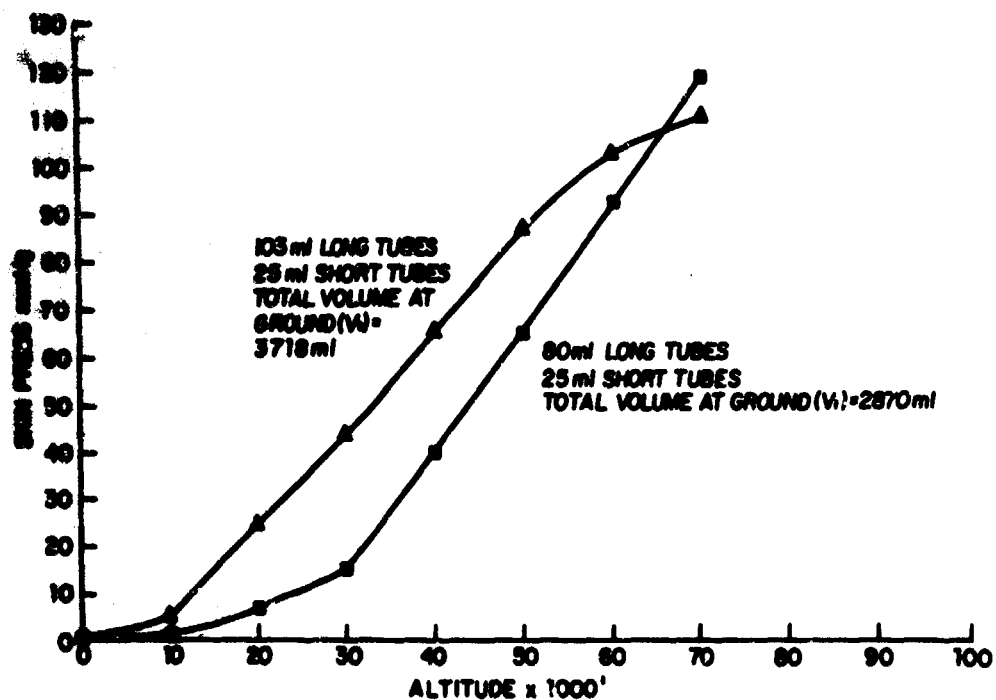
Figure 5.  80,000-foot pressure curve.
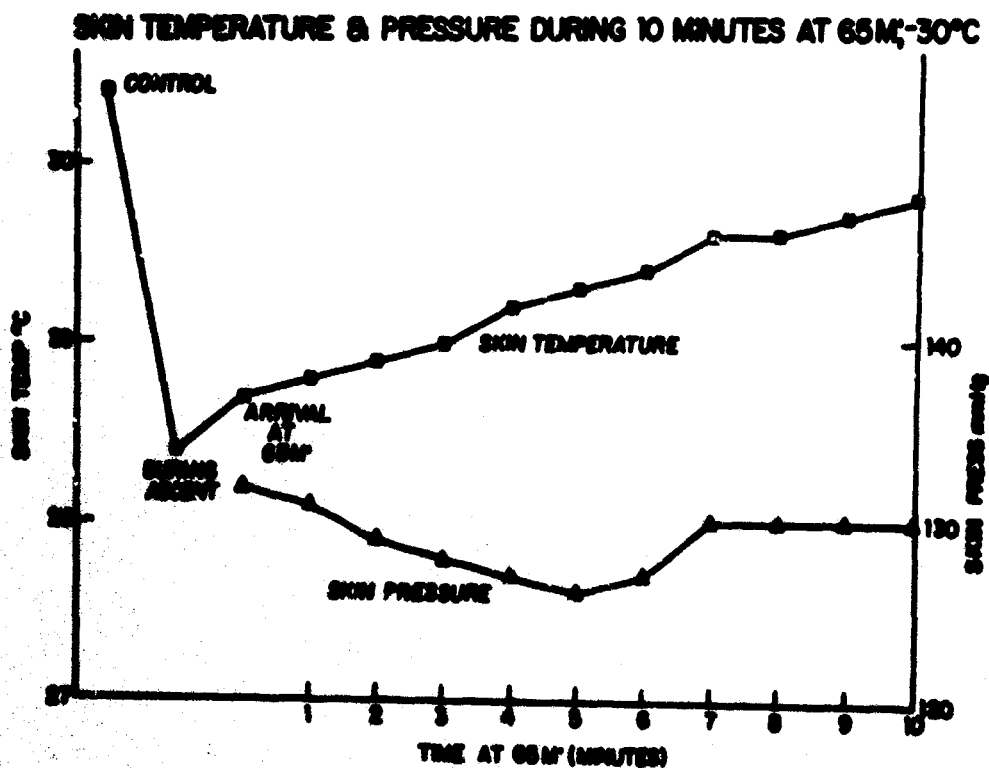


Figure 6.  Temperature-pressure curve at 65,000 feet.

# NEW CONCEPTS IN WAREHOUSING AND AUTOMATION

by

Willard L. Nelson, Chief
Industrial Engineering Branch

Industrial Engineering Branch
Management Services Division
Directorate, Supply & Transportation
Hill Air Force Base, Utah
OOAMA (OOSME)

# NEW CONCEPTS IN WAREHCUSING AND AUTOMATION

A new mechanized warehouse system, engineered and designed at
Hill Air Force Base, brings about new concepts in warehousing auto-
mation never before known to the Logistics Command. These concepts
include automatic dispensing from live storage bins; automatic routing
and consolidation of customer orders; and a unique transportation
system from storage to packaging, which basically eliminates on-base
transportation. The data which proved these concepts was developed
through the use of math models and operation simulation programs.
The simulation program revealed that approximately two-thirds of the
line items stored were less than three cubic feet and constituted 83%
of the items shipped. These small items, weighing less than 70 pounds,
can be stored in a relatively small area and are of the kind and type
that should be consolidated by consignee for economical transportation.
Having this much of our business in a concentrated area made it economi-
cally feasible to provide a sophisticated material handling system, upgrade
the facility, control personnel, and maintain surveillance over the supply
system.

## BIOGRAPHY OF WILLARD L NELSON

Born in 1924 in Mt Pleasant, Utah. Served 2 1/2 years in World War II with the US Air Force as a B-29 Flight Engineer.

He attended Snow College, Ephraim, Utah, and graduated in 1947 with a degree in Associated Science. Graduated from the University of Utah in 1949 with a Bachelor of Science Degree in Mechanical Engineering. He has participated in postgraduate work with the University of Utah in Industrial Engineering and Engineering Management.

He has been licensed as a professional engineer since 1954. He is an active member and past vice president of the American Institute of Industrial Engineers, Utah Chapter.

He holds two patents in material h    'ing equipment.

His experience includes 1 1/2 years as Field Engineer for Crane Co serving the Atomic Energy Commission; 1 year as a Geophysicist for United Geophysical Co of Canada; 2 years of consulting work in Engineered Management Programs; and 18 years with the Air Force as an Industrial Engineer. He is presently Chief of the Industrial Engineering Branch at Hill Air Force Base, Utah (OOAMA).

# NEW CONCEPTS IN WAREHOUSING AND AUTOMATION

This paper describes a mechanized warehouse system that was engineered and designed at Hill AFB as part of the Air Force Logistics Command's (AFLC) Mechanized Materials Handling Program. This project brings about new concepts in warehousing automation never before known in the Logistics Command. These concepts include automatic dispensing from live storage bins, automatic routing and consolidation of customer orders, and a unique transportation system from storage to packaging. The data which proved these concepts were developed through the use of math models and operation simulation programs. Hill AFB has been chosen as the test site for these new warehousing concepts prior to implementation AFLC-wide.

BACKGROUND--During the past few years it has become evident within the Air Force Logistics Command that our methods of handling and storing material have not kept pace with other developments in the logistics process. Sophisticated methods have been developed to requisition, account for, and distribute property by automatic data processing equipment. Transportation to destinations has been improved immensely through use of high speed aircraft and other transportation means. On the other hand, storage practices and material handling techniques have remained largely static, e.g., we store material according to cataloging classification and maintain this class integrity, disregarding physical characteristics and activity to a large extent. Most classifications of property contain both very large and very small items and items having both a high and a low activity rate. While this storage method was practical at a time preceding automated data processing equipment, it has now become outmoded. Some of the events which have contributed to this outmoding are: A change from multi to single line item documentation; from decentralized to centralized receiving, and from a separate locator file for each warehouse to a consolidated and computerized file for the entire storage complex. Automatic data processing equipment has been applied to the tasks of posting issues and receipts, preparing shipping documents, maintaining storage locations, and aggregating data for preparation of a variety of management data and reports. These changes have had a profound effect upon our workload. Workers have been relieved of routine posting and card file maintenance jobs and have become more truly Materiel Managers. All of this, plus an increased state of the art in specialized material handling equipment, has brought about reasons to challenge our basic storage philosophies. We have found that the former reasons for segregation of material in storage along catalog classification lines have disappeared to a large extent. A notable example of one that remains is the practice of taking inventory by commodity classification. While it is important to have the capability of taking a full scale inventory on all stocked items, to allow this consideration to preclude the storage of items according to their physical characteristics and activity is indefensible.

A NEW LOOK AT STORAGE CRITERIA--In serving our customers under these new logistic philosophies wherein premium transportation is

utilized, it is important that we package and ship in the most economical
way that will satisfy customer requirements. So that these economies
can be incorporated into our overall service, we must consider material
characteristics. The actual physical dimensions, the degree of fragility
and flammability, and the security requirements are the principal
factors that must be considered in pre-positioning these items into a
storage location. These characteristics determine whether or not an
item can be consolidated for economical transportation. In gathering
this item characteristic data, together with item activity, we used
electronic data processing equipment. This information, partly historical
and partly operational prediction, was processed through our computer
center, simulating as near to actual conditions as our computer system
would allow. Data were reflected for each stock item, e.g., cost category,
recoverability classification, unit of issue and weapon system applicability
(when appropriate).

An analysis of these listings reveals that issue activity patterns vary
among support categories for which we stock materials. As shown in
Figure 1, materials which are provisioned and stocked for an Inventory
Manager have a greater percentage of items in the slow moving or dormant
category. This is to be expected since Inventory Managers are the ultimate
supply source for Air Force items and they must, therefore, maintain
stocks of seldom used items. Materials stocked for direct support of a
Special Weapon System show a greater average item activity, while Base
Support Items, stocked as they are for imminent local requirements, are
the most generally active. The curves shown on Figure 1, while varying
quantitatively, generally conform at common points along the "Percent
of Line Items" axis where a significant change in attitude is evident.
Validity of the "Inventory Manager" curve, as representative, was assured
by comparison with data from a different time period. Out of eleven
computed points of reference, data for the two periods coincided at five
points and varied three activity percentage points at the extreme divergence.
Actual activity of individual line items was compared between the two time
periods. A sample of 250 items, selected to represent the whole activity
range, failed to show a high degree of stability in activity rate between
periods. As can be seen on the comparison chart (Figure 2), there is only
a general tendency of items to remain within a category of activity. It
can be concluded that while percent of activity by percent of stock items
has an excellent conformity to a pattern, individual stock items may shift
in considerable numbers among activity categories.

Having identified the activity distribution of items in our stocks, the
next step was to discover something about their physical characteristics.
We looked at items in storage which had high issue rates and at items
going into the shipment packing area. The most important finding here
was that the great majority of items being issued had small unit dimen-
sions and were of a general cargo classification. In other words, an
aggregation of small, common type items would account for more than
70% of our issue activity and, incidentally, would include virtually all of
the items which could be consolidated for shipment. Additional information
was gathered by extraction from existing records and by observation.
These additional data are not detailed here for the reason that they are
common measurements, consisting of range and distribution

characteristics for: number of items picked for off-base shipment per day; items picked for local issue; off-base single line item shipments; off-base consolidated shipments; number of items involved in consolidated shipments; number of receipts, and the number of urgent priority shipments as compared to routines. Also, a study was made of the rates at which each of these individual workloads generate during the 24 hours of the day.

DERIVATION OF REQUIREMENTS THROUGH SIMULATION-- A simulation of the proposed operation was prepared by adapting a general purpose simulation program (IBM GPSS II) to our specific requirement. Suitable data from the array previously gathered, together with standard time elements for warehouseman actions, were passed through the program. By varying the number of picking stations, the number of segregation lines, and the level of manning during a series of simulation runs, it was possible to evaluate the adequacy of the different combinations. It was also possible to identify points in the operation which would be over loaded by a given activity increase. Capacities of equipment for moving material from the shipment segregation lines to the packing area were not considered in the simulation. The segreation lines were treated as open ended for output. This is appropriate since the movement is accomplished by a direct conveyor unit which can be regulated to provide the travel rate required. The size and shape of the required operational equipment were now well defined. Consideration of how to control its function was next on the agenda.

ECONOMIC AND DIMENSIONAL SPECIFICATIONS FOR A SEMI-AUTO-MATED STORAGE FUNCTION-- The results of the simulation study revealed some stimulating facts as shown on Figure 3 (Item Activity Chart). In general, it showed that approximately 5% of the items stored at Hill AFB constitute 61% of the activity and that 45% of the material makes up 3% of the activity. In addition, 83% of the items shipped are smaller than three cubic feet and weigh less than 70 pounds. In selecting material handling systems, it was determined that:

    a. The first 5% of our items could be economically handled through automatic dispensing equipment.

    b. The next 40% could be most economically handled by a rapid mechanized stock selection system with sorting capability.

    c. The balance of the stocks should remain under conventional warehousing practices.

    In view of the gathered data, it was decided to divide our stocks into two general categories, one of which includes all non-sensitive items with a unit package size less than three cubic feet. The second category is comprised of the remainder of the items. By compressing the stock of small items within a comparatively small storage area, it is possible to concentrate approximately 70% of our storage issue and receipt activity. This concentration, in turn, makes it economically feasible to

equip the area with some fast-reacting installed material handling aids (Figure 4). A subdivision of the small items within the concentration area was made by selecting ultra-active items for storage in automated dispensing units (Figure 4). Such equipment had not been used before in an operation comparable to ours, so we procured small blocks of two different kinds of equipment. One of these is a vertical, revolving type dispenser. Various sized units of this kind can accommodate packages from envelope size up to cartons measuring 4" x 7" x 8". This block of equipment will store and dispense 150 line items. Provision for another 150 items was made in the second block of equipment. This second block has mechanisms of the conveyor type equipped with counting escapement gates, and items ranging in size from five inch cube to 24 inch cube are acceptable. Both kinds of equipment are operated by a common control console. The actuating medium is an ADPE prepared punch card. When cards are input, either singly or in decks, to the control console, they cause the dispensing of the desired quantity of particular stock items. An ability to segregate material by consignee is provided by automatic switching among three conveyor staging lines. Switching is triggered by a special card which is placed as a divider between consignee groups of cards in the input deck of cards. The capability of this semi-automated equipment to make issues rapidly is unquestionable. In the equipment acceptance test the following performance rates were attained: Envelope or similar very small items were dispensed at a rate of 100 units per minute, while larger items in the complex were dispensed at the rate of 60 units per minute. If it were possible to apply this kind of equipment over a broad range of material, it would permit two equipment operators to issue and route to packing the same amount of material that now requires 100 men.

A warehouse adjacent to the building which houses the centralized receiving and shipping functions was selected as the ideal place to locate the small items. A continuously running towveyor system, with automatic cart set-off capability, moves material from receiving bays to stations near material storage locations. For distribution of shipping documents and for transporting material to a consolidation area, equipment was selected which would traverse overhead (Figure 5). It has provision for set-off and pick-up of material tote trays. The trays are tripped off on a spur of gravity conveyor and are re-engaged for further transport by simply moving them to the far end of the spur. This selection was made because the overhead traversing rails leave the floor area unencumbered, and such equipment is adaptable to a varying number of set-off stations. It has the capability to permit routing of material from any picking station to any pre-selected segregation line. The number of segregation lines is also flexible within limits.

Operational procedure is as follows: ADPE batches shipping data by consignee and sequences the data within each batch by picking station number. This sorting and sequencing of data will occur prior to actual document preparation and thus preclude manipulation of paper work. Batched and sequenced documents will be blown to the storage complex control area by pneumatic tube. The document dispatcher will select a free segregation line for the first batch of documents and stamp this line number of each document within the batch. He will then separate the

BB-7

batch by picking station number and route the documents, via tote trays, to the picking stations involved. The tote tray will set-off at the picking station, the station personnel will pick the material, place it and the documents in the tote tray, dial the tray set-off mechanism for the line number marked on the documents, and engage the tray for transport. The tote tray will set-off on the proper segregation conveyor line. After all tote trays for the shipment consolidation have arrived on the line, the shipment will be checked for completeness and released onto a conveyor for movement to the packing area. Each segregation line will have power capability so that engaging a switch will clear the line.

FILTERING THE INPUT AND CONTROLLING OPERATIONS WITHIN THE PROCESSOR -- It was evident that performance within the storage complex could be gauged in terms of response to input. There was need then to retain information about picking documents as to the number routed to individual picking stations, and to decrease these numbers as material arrived on consolidation lines. It would also be well to have knowledge about the promptness with which completed consolidations were moving from the lines. The control panel, illustrated in the attached schematic (Figure 6), was designed to fill these needs. In practice, the panel will display document routing to individual picking stations and will decrease workloads, shown as outstanding at these stations, as material arrives on a consolidation line. The panel will also indicate lines which hold completed shipment consolidations and will, further, call attention to lines which have remained occupied beyond an acceptable period of time. Voice communication between each picking station and the control panel will be available. These facilities will be used for follow-up of delinquencies from the panel operator and for requesting assistance or reporting trouble documents, etc, to the control area. The supervisor of the entire area will be stationed adjacent to the control area and will have a group of trouble shooters at his disposal. This group will consist of unusually capable and highly skilled individuals, and their job will be as temporary fill-in wherever and whenever needed and to solve problems. The overall relationship of these storage concepts and the flow of material through our material processing area are shown on Figure 7.

OBSERVABLE BENEFITS -- We feel that this new storage concept, together with well engineered mechanization, will provide a responsive supply system commensurate with our overall logistics system. It will convert a loosely knit series of actions into an integrated function. We will have a plant which is custom tailored to our current requirements, but which is basically modular and, therefore, adjustable to future contingencies. The operation will be sensitive to control so that most of our problems will be small ones; we will know about them before they grow to serious proportions. Specific benefits we will experience are: A reduced opportunity of misrouting picking documents; an ability to provide better personnel facilities through having more of the work force in a small area; less requirement for inventory counting of stocks; reduced "load, haul, unload" activity; greater ease of accumulating

shipment consolidations; a general reduction of credit processing time from computer to transportation; a reduction of on-base transportation facilities requirements; and a reduction of requirement for non-installed material handling equipment.

# ITEM ACTIVITY BY ACCOUNT
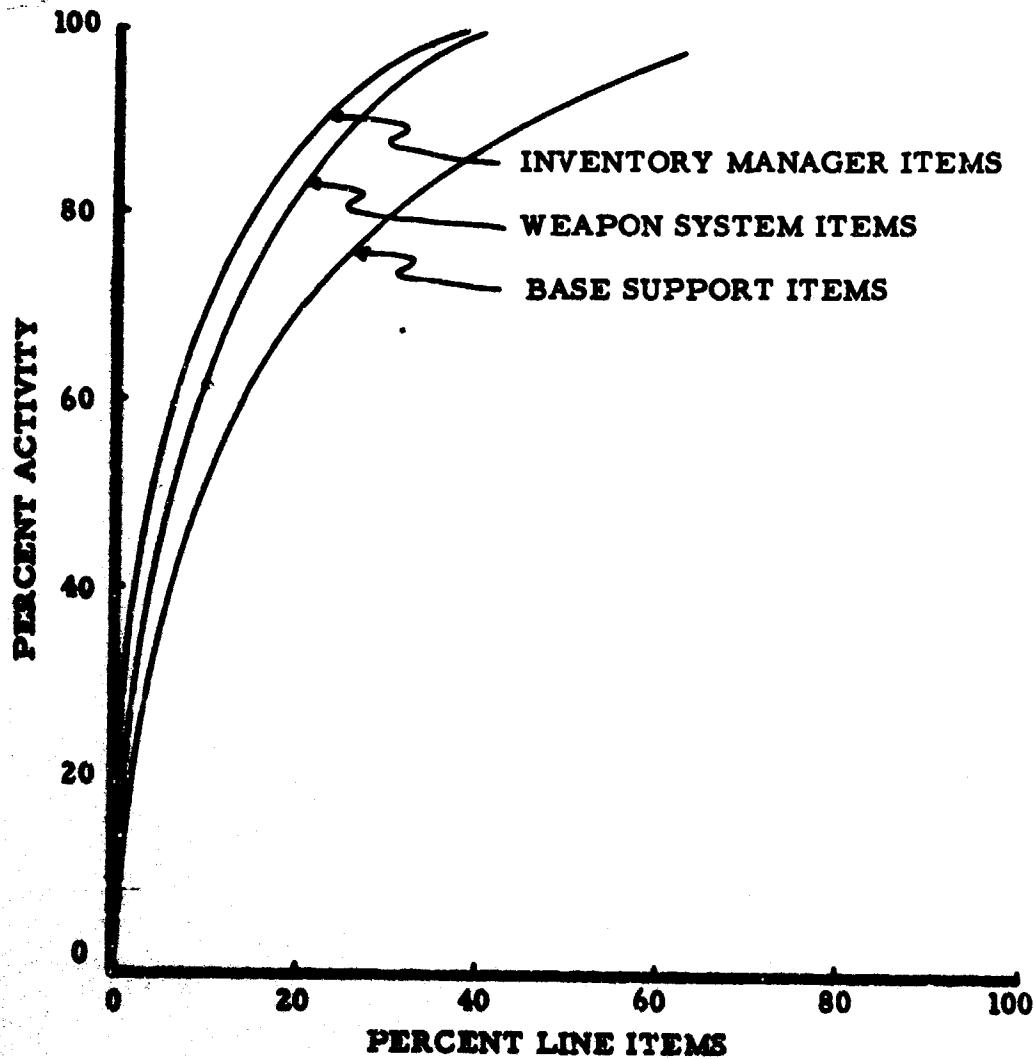


Figure 1

ITEM ACTIVITY COMPARISON

ACTIVITY, FIRST QTR. CY-66

Figure 2

# ITEM ACTIVITY



Figure 3

BB-12

SEMI-AUTOMATED WAREHOUSE
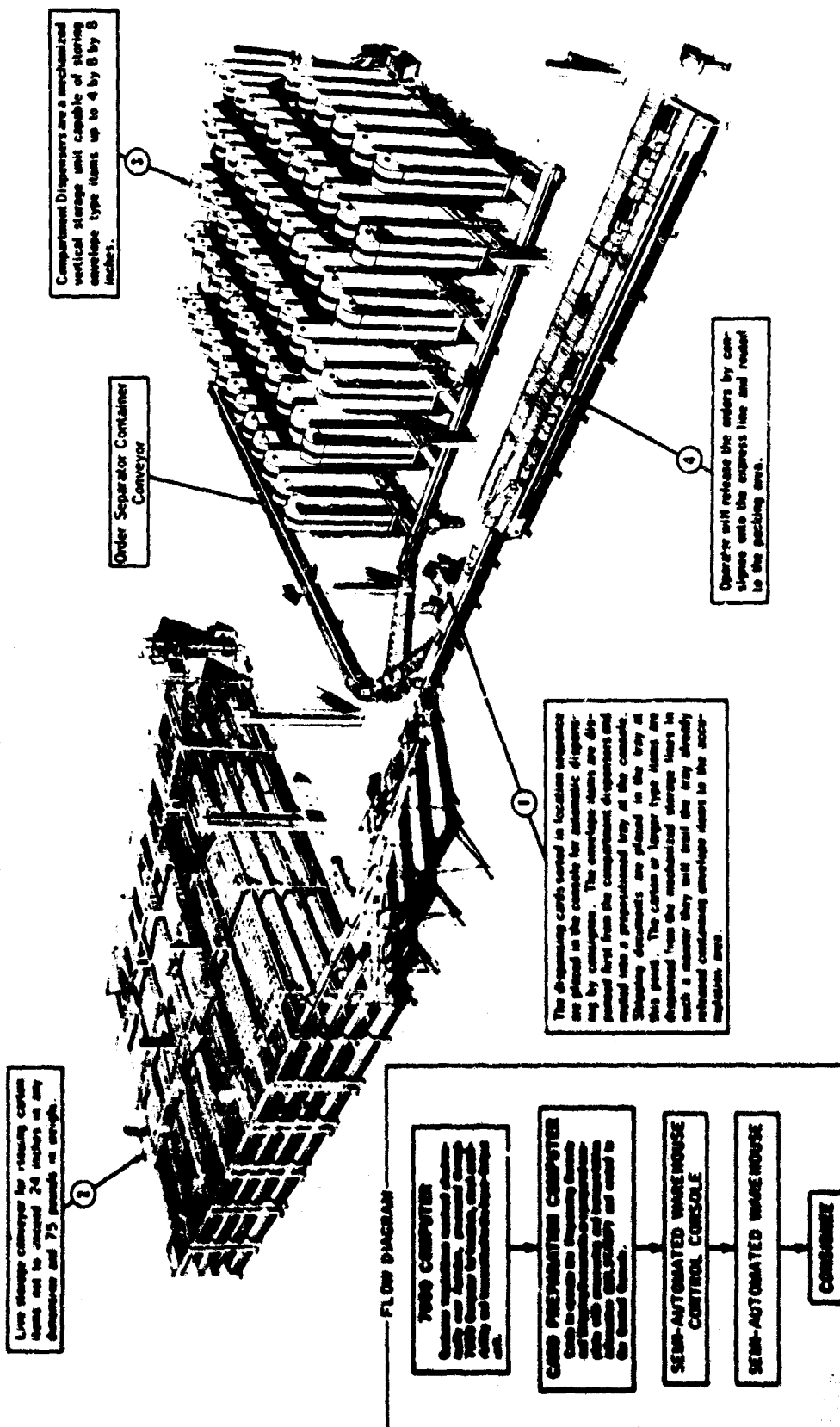
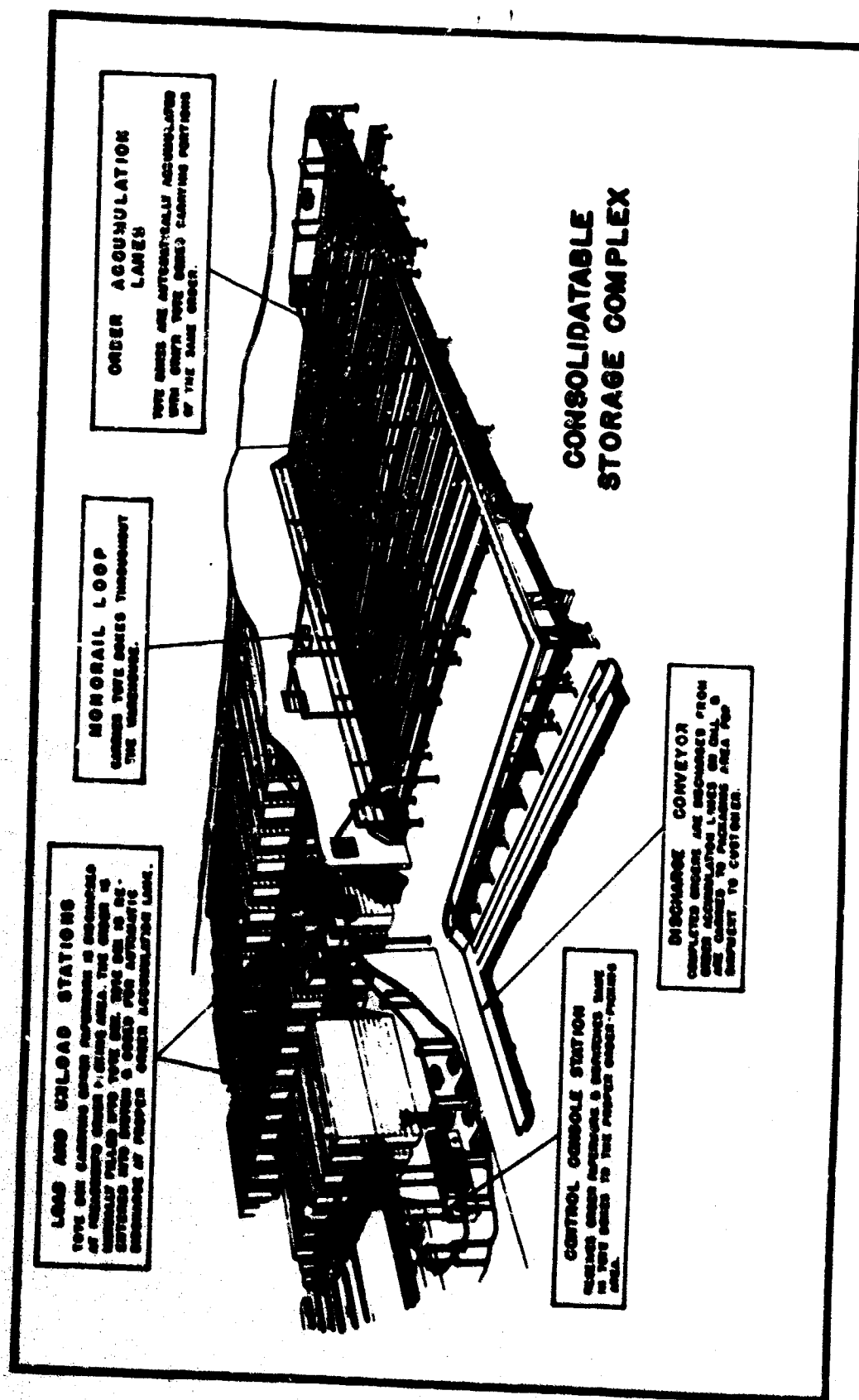Figure 4

CONSOLIDATABLE
STORAGE COMPLEX

Figure 5

# CONTROL CONSOLE



Figure 6

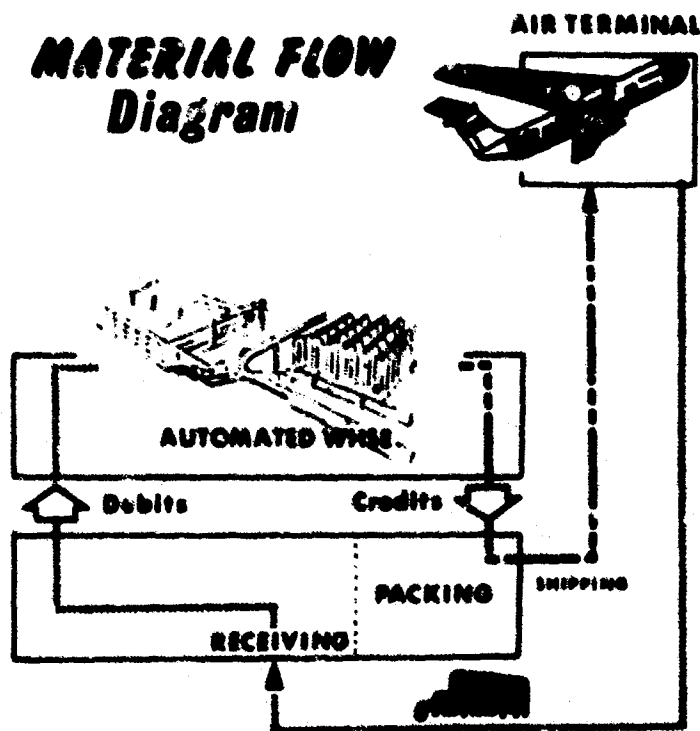## MATERIAL FLOW
### Diagram



Figure 7

A MATHEMATICAL TECHNIQUE FOR

SIMULATING TURBINE-ENGINE PERFORMANCE

ON A DIGITAL COMPUTER

BY

John S. McKinney, Captain, USAF

Air Force Aero Propulsion Laboratory
Air Force Systems Command
Wright-Patterson Air Force Base, Ohio

CC-1

## ABSTRACT

Recent advances in turbine engine technology and rising costs of turbine engines have increased the requirements for better methods of turbine engine cycle analyses. These cycle programs are used to monitor present engines, determine sensitive or critical areas in near future engines, explore the advantages and disadvantages of advanced engine cycles, and provide an economical method for obtaining engine data for aircraft mission analysis. A cycle program must meet the requirement for a fast, accurate, and inexpensive method of simulating turbine engine performance. This paper discusses the two general types of cycle analysis programs (parametric and balancing) and the differences between them. The techniques used in balancing cycle programs are also discussed, with particular attention being given to a mathematical technique recently developed within the Air Force Aero Propulsion Laboratory. The balancing technique is based upon finding a solution for a set of partial differential equations containing engine variables and errors. The variables are changed by small increments and the resulting changes in the errors are calculated. The equations are then solved, using a matrix, for the zero-error or balanced condition. This method is faster and more flexible than previous techniques used.

# BIOGRAPHY

Capt. John S. McKinney was born in Honolulu, Hawaii. He received his Bachelors degree (with Honors) in General Engineering from the University of Hawaii in 1959. Capt. McKinney was assigned as an Aircraft Maintenance Officer at Travis AFB, California from 1959 to 1962. He received his Masters degree (with Distinction) in Aerospace Engineering from the Air Force Institute of Technology in 1964. Capt. McKinney was then assigned to the Air Force Aero Propulsion Laboratory at Wright-Patterson AFB, Ohio. He is presently working as an Aerospace Engineer in the Turbine Engine Division. His primary work area is the aerodynamic and thermodynamic analysis of turbine engine cycles using digital computer techniques. He has developed several computer programs for simulating turbine engines and has participated in the evaluation of various proposed turbine engines. Capt McKinney has authored an Air Force Technical Report titled "Simulation of Turbofan Engine."

# INTRODUCTION

Undoubtedly you are all aware of the rather significant recent advances in turbine engine technology. The turbofan engines in the F-111 fighter and our new C-5 cargo transport, and the turbojet engine now under development for the supersonic transport are good examples. Although these engines, and others either proposed or under development, will be used for widely varying missions, they all have a few things in common. Besides representing significant technological improvements over present turbine engines, they all operate using complex thermodynamic and aerodynamic phenomena. Another important point they have in common is that they are all highly expensive, both in development and production.

What this means is that any trial-and-error method of developing new turbine engine cycles would almost certainly result in excessive expense. While past experiences, results, and data should still be used as guides, they should not be solely relied upon in the development of advanced engine cycles. What is needed is a simple and relatively inexpensive method for predicting, calculating, and analyzing turbine engine cycles. The basic method is available in the form of mathematical equations which describe the aerodynamic and thermodynamic processes which occur in a turbine engine. The calculations may be done by hand, but the length and complexity of the equations and the iterations involved lend themselves to a digital computer application.

There are four principal uses for turbine engine cycle analysis programs. The first is to monitor present "in-use" engines and proposed changes to these engines. For example, a cycle analysis program to simulate the TF-30 (F-111 turbofan engine) was recently developed and is being used in conjunction with actual wind tunnel tests of the engine. Another use is to determine sensitive or critical areas in near future engines now under development. A third and very important use is to explore the advantages and disadvantages of proposed advanced engine cycles for future aircraft. The fourth principal use is to provide an economical method for obtaining engine data for aircraft mission analysis. Mission analysis generally requires such a large quantity of engine data that it would be impractical to obtain it from actual engine runs.

This paper will briefly discuss the two general types of cycle analysis programs (parametric and balancing) and will then cover in more detail the techniques used in balancing cycle programs. Particular attention will be given to a mathematical technique recently developed within the Air Force Aero Propulsion Laboratory.

## PARAMETRIC CYCLE ANALYSIS PROGRAMS

The thermodynamic equations used are the same as those found in any complete textbook on thermodynamics. The heating value of the fuel is curve-fitted as a function of temperature. The properties of air and the gaseous combustion products (for example, the gas constant, molecular weight, and speed of sound) are curve-fitted as a function of temperature, pressure, and fuel-air ratio. Each engine component is treated as a "black

box"; for example, a compressor is treated as an overall pressure ratio and efficiency.

With these basic tools, it is possible to calculate the cycle performance. For a parametric cycle program, it is also necessary to have the inlet or flight conditions, and all pressure ratios, efficiencies, pressure drops, and any other cycle losses. The turbine calculations are based on the compressor requirements; that is, the work available must equal the work required. The nozzle calculations are based on the available flow. No throat area is input and complete expansion is assumed. This amounts to an infinitely variable area.

The important point to be made is that one complete pass through the engine cycle calculations is all that is required. There is no looping or balancing. The engine is not sized and is essentially completely flexible. Each point or run is equivalent to a design point, and there can be no simulation of the engine at off-design points. The parametric cycle analysis program is primarily used for optimizing a cycle for a specific single design point.

However, with multimission aircraft being emphasized increasingly and with the need for determining off-design performance, the requirement for a balancing cycle analysis program (that is, one which simulates a turbine engine at both design and off-design points) becomes definite and essential.

BALANCING CYCLE ANALYSIS PROGRAMS

The thermodynamic equations, the fuel heating value, and the gas properties required are the same as for a parametric cycle program. The calculations involved are also essentially the same. However, instead of inputing the component characteristics (pressure ratio, efficiency, etc.) for each run point, component performance maps must be made available to the program. These maps represent the performance of each component throughout its entire operating region. The basic maps required are compressor (Fig. 1), combustor (Fig. 2), and turbine (Fig. 3), but actually, maps for all components can be generated. Generally speaking, the more components that are represented by maps, the more accurate the simulation of the engine will be. The maps are usually obtained from analytical methods or component rig-testing data and are then converted into tabular or curve-fit form for use by the engine program.

The calculations begin, as in the parametric program, with the inlet or flight conditions. Also, a power setting representative of the real engine being simulated must be chosen. This power setting can be in the form of percent speed, combustor or turbine inlet temperature, or a fuel flow, depending upon the particular mode of the engine program. In addition, a set of independent - dependent variable combinations must be considered.

Enough independent variables to provide sufficient entries for all the component maps must be selected. Two good examples of independent variables are compressor speed and pressure ratio, which provide the two entries required

for a compressor map. The cycle calculations can now be accomplished, using the component characteristics obtained from each map, rather than from input values as was done for the parametric program. Now, however, the work available from the turbine can be calculated and may not necessarily equal the work required by the compressor. Similarly, a nozzle throat area is used, and a pressure required to drive the gas flow through the nozzle can be calculated. This pressure also may not necessarily equal the actual pressure of the gas stream. The differences between the turbine and compressor work, and between the required and actual nozzle pressures are used to generate errors, or dependent variables. There must be a dependent variable (error) calculated for each independent variable selected. By varying the independent variables, it is possible to change the dependent variables until they are zero. Of course, during the process, the position on each component map changes, and the cycle calculations must be computed for each change.

The final result, when the errors have been reduced to zero, is a balanced off-design point where each of the components are matched and their characteristics are compatible. There is, of course, only one unique match point for each flight condition and power setting. The balancing cycle program provides an excellent simulation of the steady-state performance of an actual turbine engine throughout its operating envelope. Calculated performance within one percent of actual performance can be expected, depending upon the accuracy of the component performance maps available.

To summarize, the three main differences between a parametric cycle program and a balancing cycle program are:

     1. The balancing program requires component maps instead of single-value inputs.

     2. The balancing program is an iterative one, looping through the cycle calculations until a match-point is reached.

     3. The parametric program can calculate only design-point performance, while the balancing program calculates both design and off-design performance and simulates a turbine engine throughout its operating envelope.

## BALANCING CYCLE TECHNIQUES

As discussed previously, the balancing cycle program can be considered mathematically as a set of independent - dependent variable combinations, and thermodynamic equations which indirectly relate the dependent variables to the independent variables. Some orderly technique must be used to vary the independent variables to arrive at the zero-error condition.

The previous technique was to handle each independent - dependent variable combination separately one at a time. The result was a set of nested balancing loops. For a turbojet, two basic loops were required (Fig. 4). The cycle calculations were done in sections corresponding to the loops. The inner loop was balanced using compressor speed as the independent variable and the work difference between compressor and turbine as the dependent variable. The outer loop was balanced using compressor pressure ratio and the pressure

required by the fixed-area nozzle. After the inner loop was balanced, the outer loop was changed in an attempt to balance it. Naturally, changes in the outer loop necessitated rebalancing the inner loop. This method, although rather crude, worked well for a simple turbojet cycle.

However, for more complex cycles, more balancing loops were required. A simple mixed-flow turbofan cycle involved four basic loops (Fig. 5). Although the method still worked, many rebalancing passes were needed for the inner loop, and computer time became excessive. ›

A new mathematical technique, which is faster and more flexible than the old, was developed within the Air Force Aero Propulsion Laboratory. The new technique handles all the independent and dependent variables as a set and is based upon finding a solution for a set of partial differential equations. In order to use the differential equations, the assumption was made that there was a direct and exact relationship between the independent and dependent variables. The fact that this assumption is not true does not affect the final result, but does mean that the set of equations must usually be solved more than once before the errors are reduced to zero.

The basic set of differential equations is based on the total derivative of $E = f(V)$, where V refers to a variable (independent variable) and E refers to an error (dependent variable) (Fig. 6). The single subscripts correspond to three variables and three errors, and the double subscripts indicate the change in a particular error (first subscript) due to a change in a particular variable (second subscript). There must be one equation for each variable-error combination. The three equations shown represent a turbojet cycle where the three errors are generated by the work difference, nozzle pressure difference, and turbine map limits exceeded. This last error had to be added to the previously discussed first two errors when it was discovered that at certain points the turbine map could not be entered as the calculated entry points were outside the turbine map limits. It is relatively easy to expand the set of three equations to one of six, as required for a turbofan cycle, or even further for more complex cycles.

If small changes in variables and errors are assumed, certain approximations can be made (Fig. 7), where B refers to a base or initial value. With these approximations and the fact that E should be zero when the cycle is balanced, the set of partial differential equations can be simplified (Fig. 8).

A pass through the entire engine cycle calculations (not just a section) will generate the required base values. Three more passes are then made through the cycle calculations, and one variable is changed by a small amount ($\Delta V$) for each pass. The change in each error due to the small change in the variables ($\Delta E/\Delta V$) can then be calculated. The set of differential equations can now be solved for $dV_1$, $dV_2$, and $dV_3$, and the new value of each independent variable can be determined. Theoretically, these new values should result in a balanced point with all errors equal to zero. However, because of the initial assumption of a direct relationship between independent variables and errors, this will probably not be the case. The errors will

be closer to zero, however, and several more passes through the entire process (where the new values become the base values for the next set of equations) will probably be necessary before the errors are reduced to zero.

A subroutine to determine the solution of a matrix is used to solve the set of differential equations (Fig. 9). After each pass through the engine cycle calculations, a matrix array is loaded with the appropriate values; after the required number of passes (base pass plus one pass for each variable) the matrix subroutine is called to solve the matrix.

As mentioned previously, this new mathematical technique for handling the independent-dependent variables of a balancing cycle program is considerably more flexible than the old method. The complexity of an engine cycle can be increased simply by increasing the size of the matrix; that is, by increasing the number of partial differential equations. For example, a basic triple-spool turbofan cycle could be represented using a matrix of nine equations. Or, a T-compressor turbofan engine such as the TF-30 (F-111 engine) would be represented using a matrix of eight equations. In addition, this new technique requires less computer memory storage and is faster (by a factor of about four) than the old method.

In short, the new technique meets the requirement for a fast, accurate, and inexpensive method of simulating the steady-state performance of a turbine engine.

(Reference AFAPL-TR-67-125, Parts I & II, "Simulation of Turbofan Engine," December 1967, by Capt. John S. McKinney.)
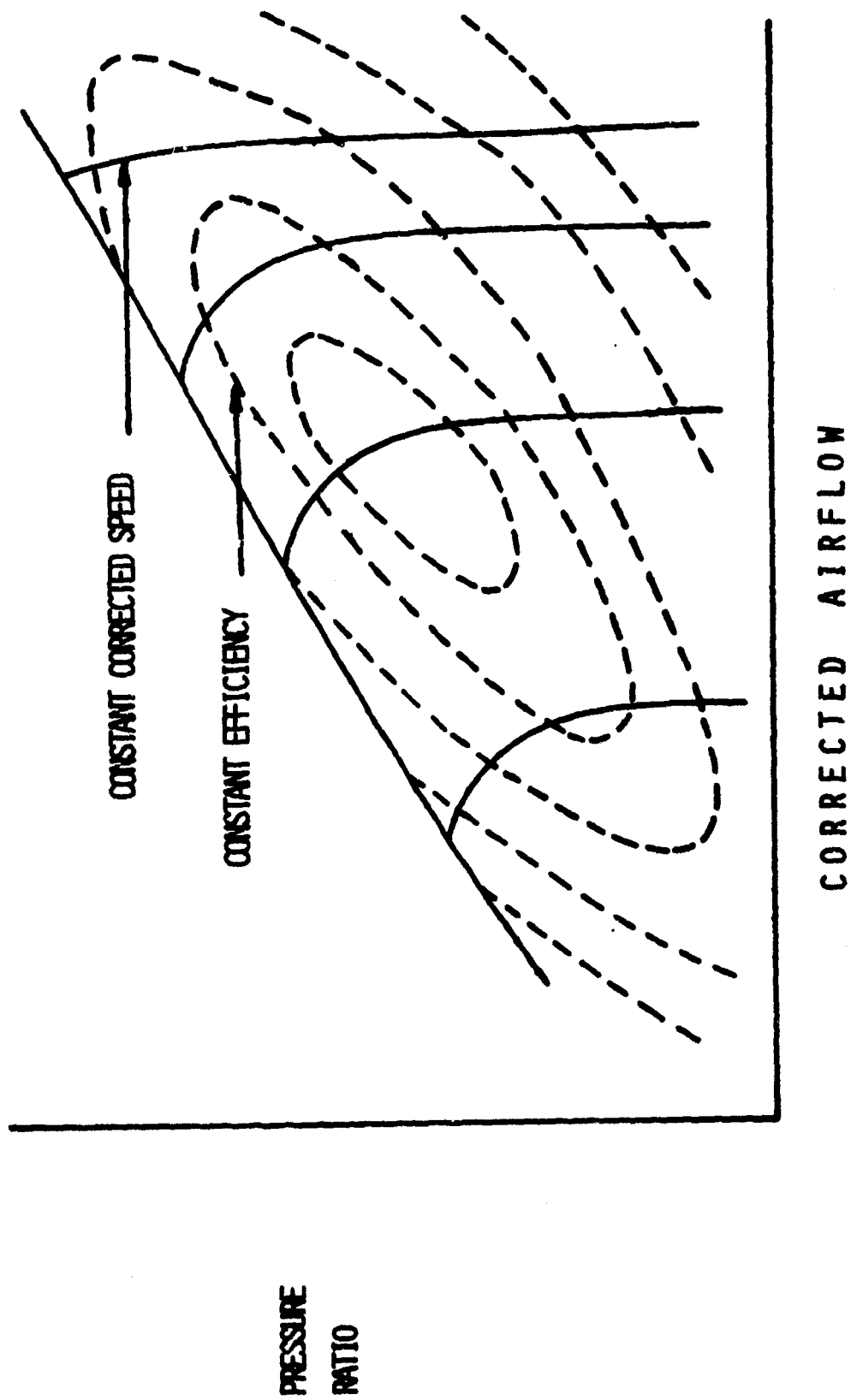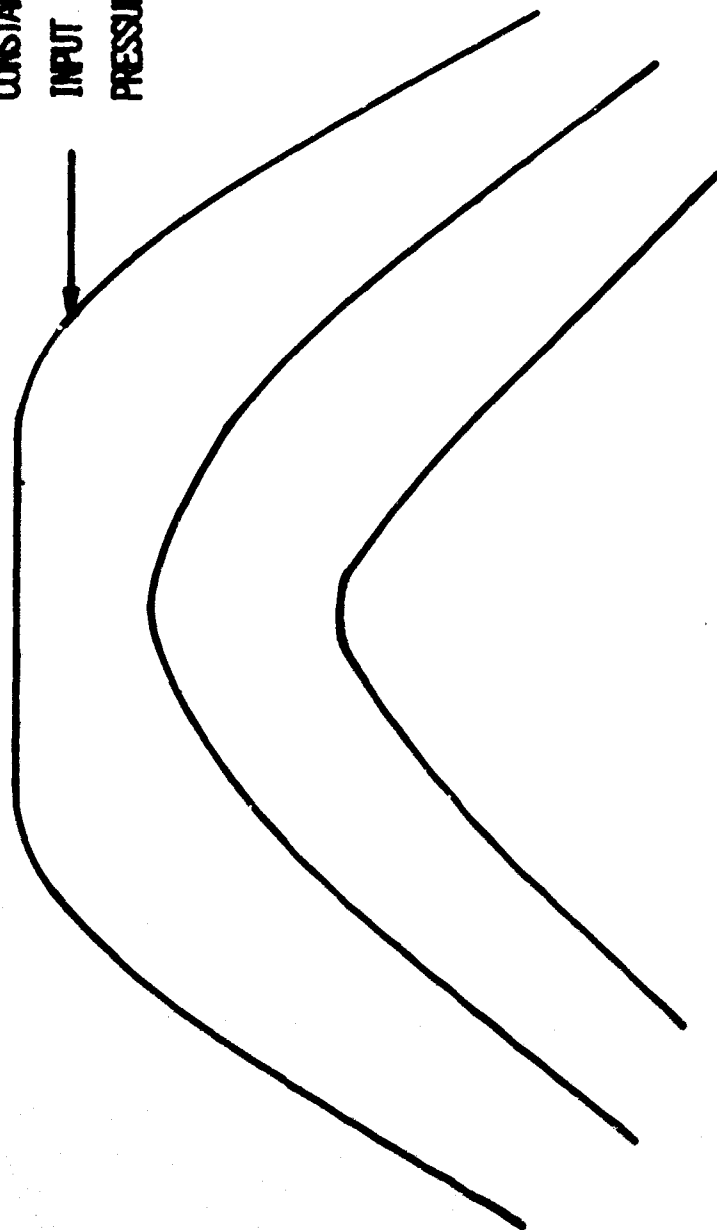
FIGURE 1 - COMPRESSOR MAP

PRESSURE
RATIO

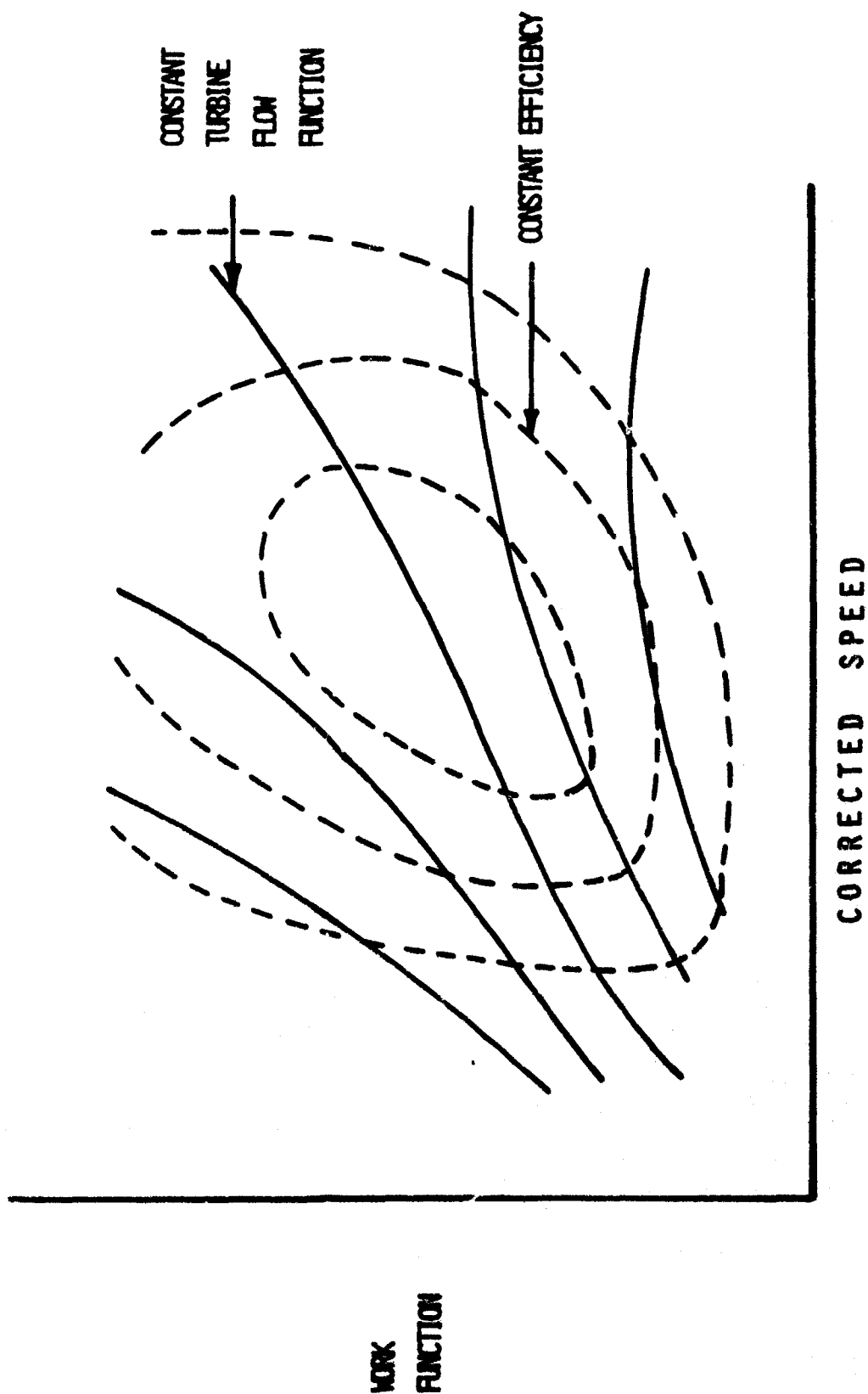CONSTANT CORRECTED SPEED

CONSTANT EFFICIENCY

CORRECTED AIRFLOW

CC-9

FIGURE 2 - COMBUSTOR MAP

CONSTANT INPUT PRESSURE

EFFICIENCY

TEMPERATURE RISE

FIGURE 3 - TURBINE MAP

CONSTANT TURBINE FLOW FUNCTION

CONSTANT EFFICIENCY

WORK FUNCTION

CORRECTED SPEED
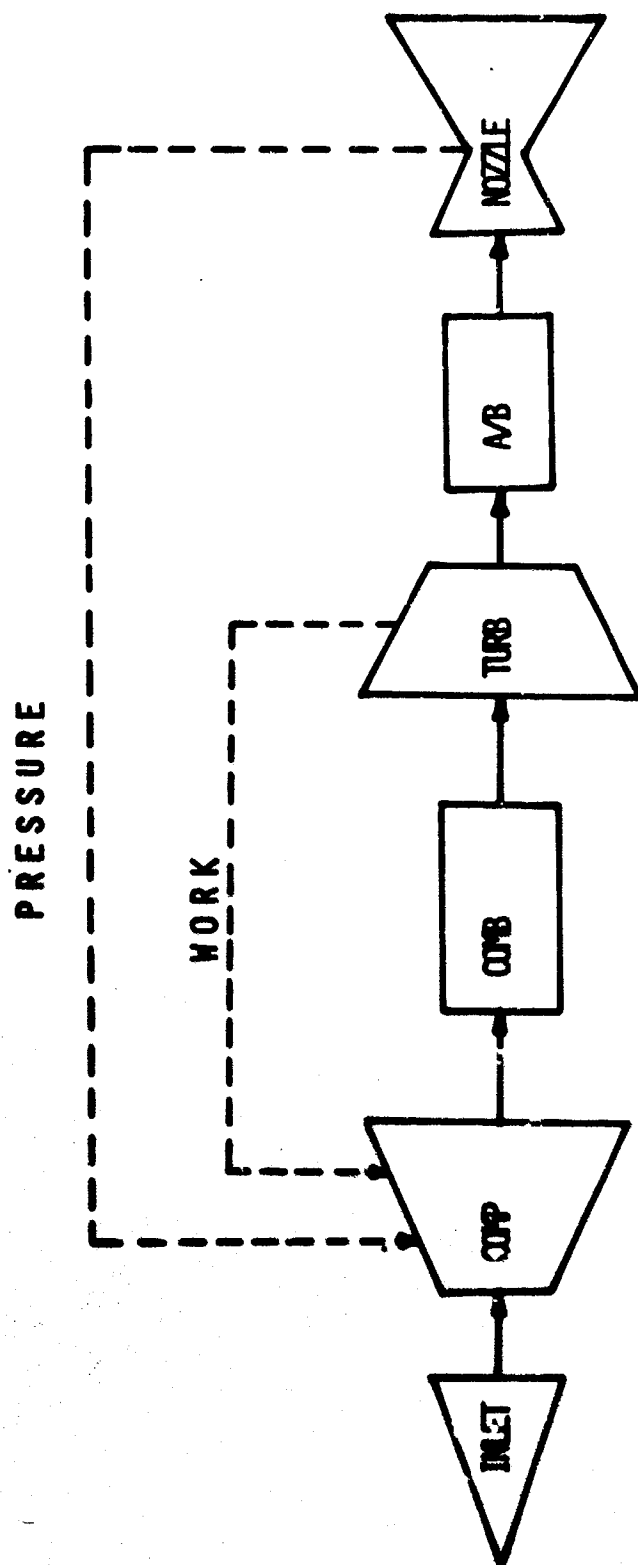
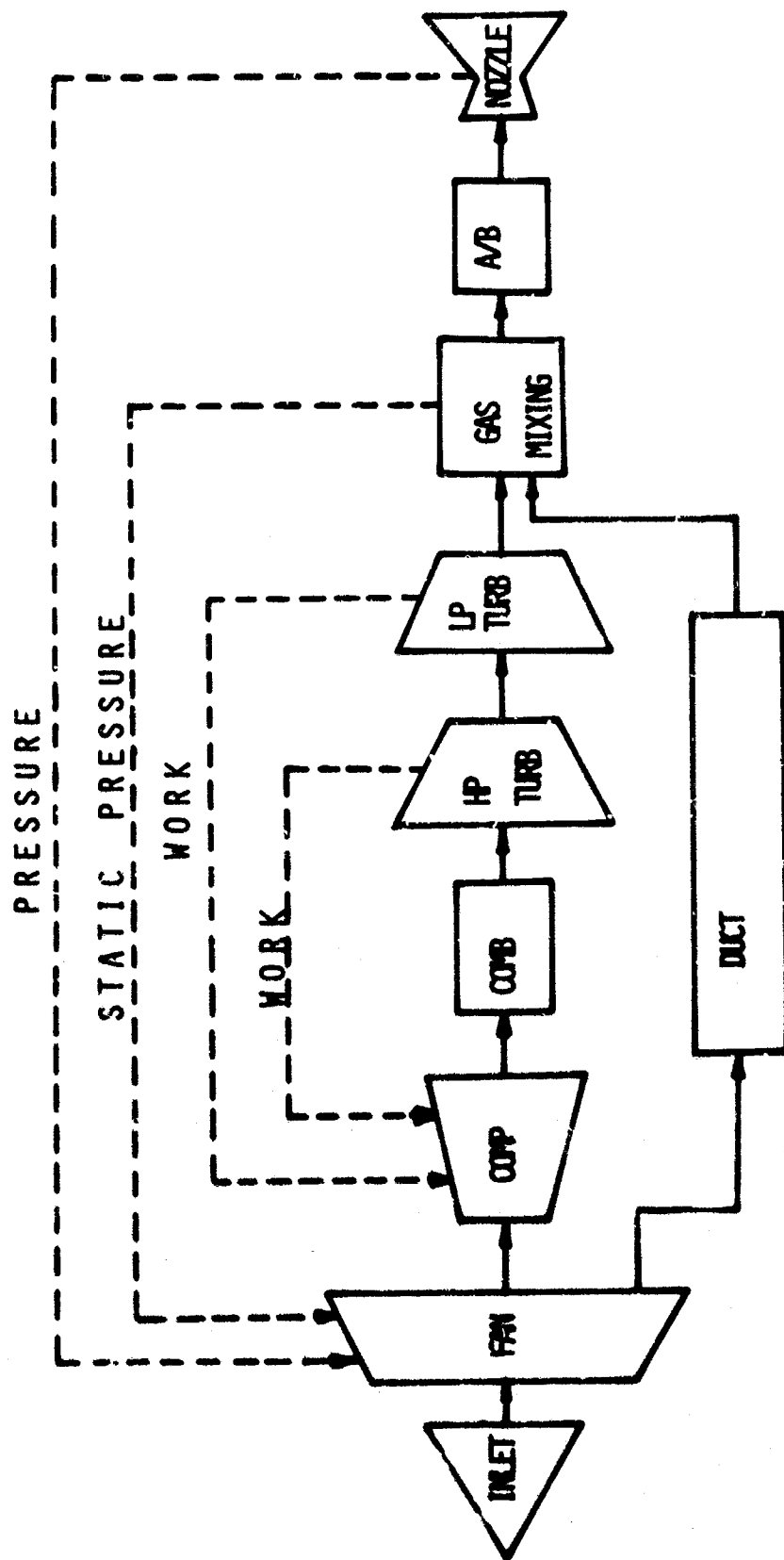FIGURE 4 – TURBOJET BALANCING CYCLE

FIGURE 5 - TURBOFAN BALANCING CYCLE

FIGURE 6 - BASIC SET OF PARTIAL DIFFERENTIAL EQUATIONS

$$dE_1 = \frac{\partial E_{11}}{\partial V_1}\, dV_1 + \frac{\partial E_{12}}{\partial V_2}\, dV_2 + \frac{\partial E_{13}}{\partial V_3}\, dV_3$$

$$dE_2 = \frac{\partial E_{21}}{\partial V_1}\, dV_1 + \frac{\partial E_{22}}{\partial V_2}\, dV_2 + \frac{\partial E_{23}}{\partial V_3}\, dV_3$$

$$dE_3 = \frac{\partial E_{31}}{\partial V_1}\, dV_1 + \frac{\partial E_{32}}{\partial V_2}\, dV_2 + \frac{\partial E_{33}}{\partial V_3}\, dV_3$$

FIGURE 7 - SIMPLIFYING APPROXIMATIONS

$$dE = E - EB$$

$$dV = V - VB$$

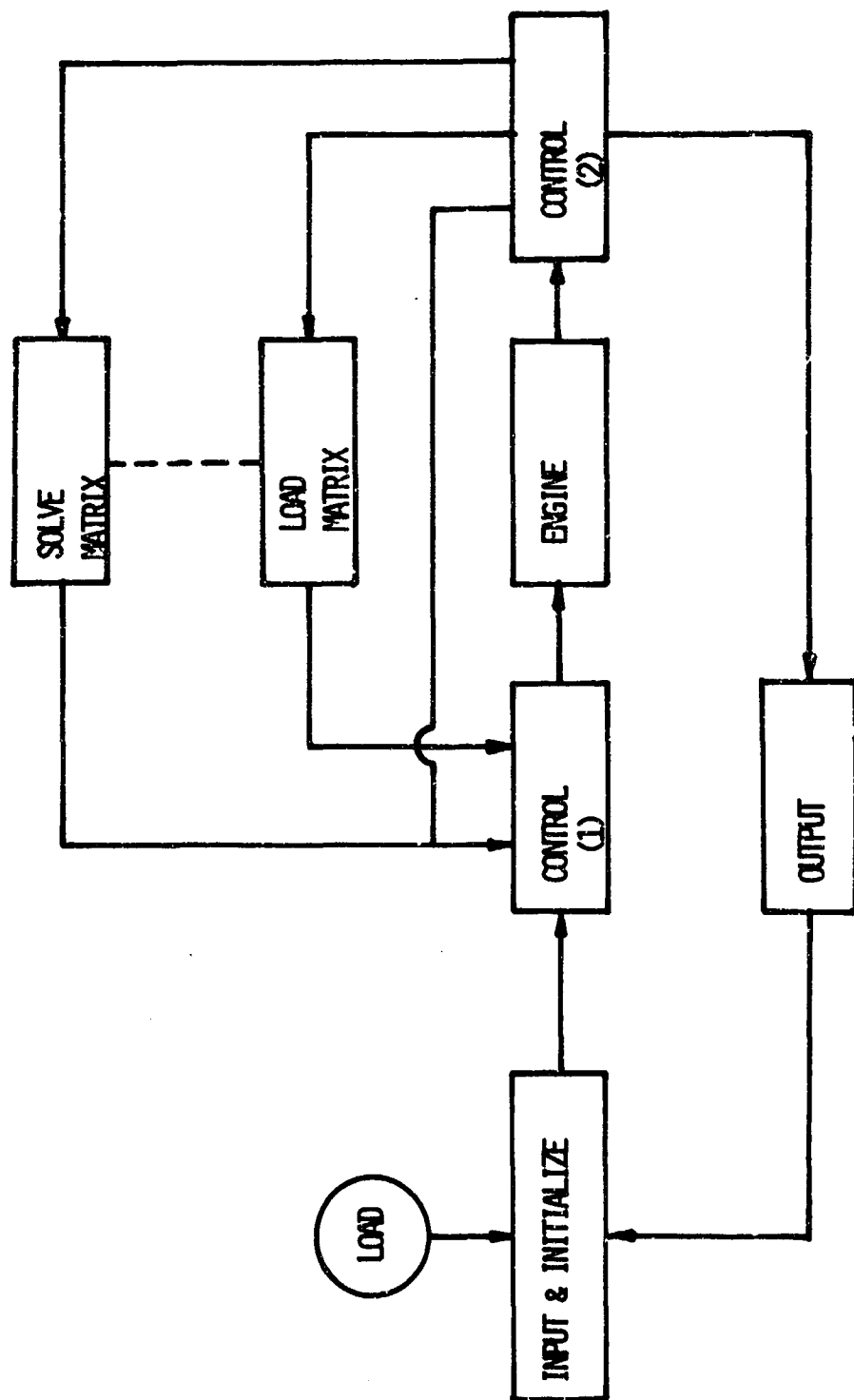$$\frac{\partial V}{\partial E} = \frac{\Delta V}{\Delta E}$$

CC-15

FIGURE 8 - DIFFERENTIAL EQUATIONS WITH APPROXIMATIONS

$$E_1 - EB_1 = \frac{\Delta E_{11}}{\Delta V_1} \, dV_1 + \frac{\Delta E_{12}}{\Delta V_2} \, dV_2 + \frac{\Delta E_{13}}{\Delta V_3} \, dV_3 = -EB_1$$

$$E_2 - EB_2 = \frac{\Delta E_{21}}{\Delta V_1} \, dV_1 + \frac{\Delta E_{22}}{\Delta V_2} \, dV_2 + \frac{\Delta E_{23}}{\Delta V_3} \, dV_3 = -EB_2$$

$$E_3 - EB_3 = \frac{\Delta E_{31}}{\Delta V_1} \, dV_1 + \frac{\Delta E_{32}}{\Delta V_2} \, dV_2 + \frac{\Delta E_{33}}{\Delta V_3} \, dV_3 = -EB_3$$

CC-16

FIGURE 9 – BALANCING CYCLE COMPUTER PROGRAM FLOW CHART

CC-17

INFRARED DETECTION, ISOLATION, AND PREDICTION

OF ELECTRONIC-EQUIPMENT MALFUNCTIONS


by


Ruth A. Herman, AB Cum Laude

DD-1

# ABSTRACT

An infrared checkout technique for the diagnosis of faults in electronic circuits is described. A radiometric system for implementation of the technique is illustrated. The technique was applied to more than 900 printed circuit panels and is shown to be effective. A discussion follows on various beneficial applications and implementation requirements.

# BIOGRAPHY


Miss Ruth A. Herman is a Senior Project Engineer in the Turbine Engine
Division, Air Force Aero Propulsion Laboratory, Wright Patterson Air Force
Base.

Miss Herman is credited with the initiation and investigation of an
original research effort utilizing thermal and infrared technques for the
automatic checkout of electronic circuits. She has received a patent for
a device to accomplish the infrared monitoring function. She is also
engaged in advancing the state-of-the-art in computer oriented mathematical
techniques for checkout purposes.

Miss Herman is a native of Dayton, Ohio. She received her bachelor's
degree in mathematics and physics (Cum Laude) in 1951 from Wittenberg
University, and did graduate work at Ohio State University. She accepted
civilian employment with the Air Force in 1960 after nine years as a
research scientist for a Government contractor.

Miss Herman is an active member of the Air Force Dayton Laboratories
Branch of the Scientific Research Society of America (RESA) and recently
received a 1967 RESA Research Award. She is also an active member of the
American Society for Nondestructive Testing, and currently she is serving
as East Region Vice Chairman, Infrared and Thermal Committee.

# INFRARED DETECTION, ISOLATION, AND PREDICTION

## OF ELECTRONIC EQUIPMENT MALFUNCTIONS

### By Ruth A. Herman, AFAPL

## INTRODUCTION

Picture America's newest air vehicle, the C-5A (Fig. 1). It is far wider than a football field, longer than twelve Cadillacs bumper to bumper, and the tail projects as high as a six story building. The C-5A will be the fastest available means of transporting large numbers of troops and their equipment to a battle area. The questions may be asked, "Just how reliable will the C-5A be?" and "What can be done to assure maximum operational effectiveness?"

Foreseeing a need for improved fault diagnosis techniques, I initiated an in-house research effort in 1961 which has continued to the present time (Fig. 2). The effort is directed toward the concept of detection, isolation, and possible prediction of malfunctions in electronic systems. The technique involves the sensing and analyzing of infrared radiation emitted by energized electronic circuits. The results of this work have far exceeded the expected advance in the state-of-the-art of checkout and maintenance test procedures.

## THE INFRARED CHECKOUT TECHNIQUE

The infrared checkout technique is based on the fact that each resistive component of any energized electronic circuit emits infrared radiation, or heat. This radiation characterizes the electrical condition and topology of the component in the circuit. As component characteristics change, so does the infrared pattern of the circuit. Observation and evaluation of this pattern change can be used to locate the electronic components (including integrated circuits) that have changed value or failed. The infrared patterns of energized electronic circuits can be illustrated by three-dimensional models (Fig. 3). The peaks illustrate the intensities of infrared being emitted by the circuit components. Each circuit condition has its own infrared signature which may be used for fault location.

My contribution to the infrared checkout technology was the concepts of monitoring the infrared pattern of complete electronic assemblies, while operating in their prescribed function, and of comparing the total pattern to, not only that of a known, acceptable assembly, but to failure patterns of various malfunctions as well. I have been granted a patent for a device which accomplishes this monitoring and diagnostic capability. Previous investigators had used infrared probing only on a piece-part basis to determine anomalies of a resistor, a diode, or other single component.

Infrared has the following advantages over conventional checkout techniques (Fig. 4):

1. Infrared is the only parameter measured
2. No physical contact is made with the circuit, therefore, the circuit cannot be damaged from probing
3. Circuit operation is not altered due to the loading effect of contact measurements
4. Checkout is accomplished of the entire printed-circuit board including components, connectors, wiring paths and coatings
5. Checkout is accomplished of both analog and digital, linear and nonlinear, integrated and discrete-element circuits, all with the same test setup.

THE RADIOMETRIC SYSTEM

The flow chart (Fig. 5) illustrates the setup required at depot level for infrared testing of electronic circuits. The circuit under test is energized using its conventional AC and DC power supplies. The radiometer detects and measures the infrared emitted by each component in the circuit under test. Note that the system is passive; that is, an active infrared source is not directed at the circuit. Tape equipment may be used to control the radiometer by providing positioning information. The tape equipment also may be used to select stored reference profiles which then are compared automatically with the output of the radiometer. The measurements and comparisons may be displayed in analog or digital form together with the diagnostic information.

Infrared testing may be implemented in three ways (Fig. 6):

1. Simply look for hot spots, or
2. Compare a circuit in known good condition with one of unknown condition and look for infrared pattern deviations, or
3. Compare a circuit of unknown condition with a library of infrared reference scans which are annotated as to failure mode. This method will identify the failed component in the shortest time.

In 1964, the Air Force initiated a contract with the Raytheon Company to conduct a detailed investigation into the feasibility of this infrared checkout technique. Based on the success of these early feasibility studies, Raytheon designed and built a radiometric system for implementing the technique. The system is called COMPARE for Console for Optical Measurement and Precise Analysis of Radiation from Electronics.

The COMPARE System is shown in the figure (Fig. 7). Printed circuit boards are loaded onto the rotary feed table and are carried under the scanning radiometer. AC and DC signals are applied to any of 16 different boards on the feed table for warm-up prior to scanning. Since 10 minutes are generally required for warm-up, the feed table greatly increases the number of circuits that can be scanned per unit time. Punched paper tape controls the Radiometric System by providing positioning information.

The tape also contains infrared reference measurements. As the detector scans a circuit board, the output signal is converted to a digital format and is stored in a magnetic core memory. A numerical printout contains sampled points of the radiometric scan that differ from the reference measurements. The printout is then matched against a diagnostic chart which will identify the faulty component. The technician then repairs the circuit.

A layout of a printed circuit board and grid overlay is shown (Fig. 8). The grid overlay is used to select the points to be sampled during the infrared scan. The dark squares in the grid define the X and Y coordinates of the points sampled for each component. An optical system sweeps the focal point of an infrared detector across the circuit and steps the scan line sequentially down the length of the circuit as each scan is completed. The total scan time is 100 seconds: 45 seconds of active scan and 55 seconds for retrace. The spacing between scan lines is 0.04 inch, the spot size of the detector. The temperature resolution is $0.05^\circ C$.

The detector used in the COMPARE System is made of mercury-doped germanium. The detection region peaks at about nine microns, or roughly $30^\circ C$ ($85^\circ F$). Therefore, its characteristics match the range of temperature expected from electronic modules and components.

INFRARED TECHNIQUE VALIDATION

In preparing to make infrared scans of printed circuit panels, a standard infrared profile of the panel in good operational condition is required. The standard infrared profile is obtained by averaging the infrared measurements from several serviceable panels. Initially all scans are compared against this standard profile. If any of the measurements differ significantly from the average, the panel containing these abnormal measurements may be suspected as faulty.

Using the Radiometric COMPARE System, the infrared technique was applied to over 900 printed circuit panels. A large number of the panels came from the Minuteman I Inertial Guidance System and were supplied by Newark AFS. More than 70% of all anomalies were spotted easily with infrared without the use of statistical data processing techniques. Applying the statistical correlation coefficient, 85% of the anomalies were diagnosed correctly. Almost 85% of the anomalies also were diagnosed correctly using conventional test methods. However, many of the anomalies found using infrared detection were not found using conventional methods, and vice versa. A significant point is that 3% of all the "serviceable" panels tested actually contained anomalies which were found using infrared testing, but these anomalies were not found using the electrical tests required by conventional test procedures. Although 3% is small, it is significant, as seen in the figure (Fig. 9). Of one group of 744 panels that had passed all electrical inspections and were ready for use, 23 anomalies were found, or approximately 3%. If these 23 anomalies were located in navigational equipment and installed in airplanes, 23 airplanes would have faulty navigational equipment!

Examples of the anomalies are shown (Fig. 10). A 500 ohm resistor was used erroneously in a transistor emitter circuit instead of the correct 5,000 ohm resistor, without being detected in electrical tests. As a result, instead of operating with the intended 75% derating, the transistor was operating at several times its normal rating, which would have caused early failure.

Another example of a defect not detected using conventional tests is a reversed electrolytic capacitor. This defect is often overlooked since it takes from 2 to 20 minutes for an electrolytic capacitor with polarity reversed to affect the electrical operation of the circuit. However, the capacitor draws enough excess current when connected backward to shorten the mean-time-between-failure calculated for the associated components and to look different to an infrared detector.

In a third example, a transistor, which was supposed to be nonconducting under one operational mode, was actually passing considerable leakage current and overheating. It is not known whether the faulty transistor slipped past the electrical tests or degraded while in storage. However, it should be noted that of 23 panels containing anomalies, approximately 65% passed electrical reinspection by the conventional test procedures even when tested for the second time.

APPLICATIONS

The infrared work accomplished by the Air Force Aero Propulsion Laboratory is directed primarily toward the location of faulty electronic components on printed-circuit boards. Other valuable applications for infrared in electronic equipment diagnosis are seen on the chart (Fig. 11). Two particularly appealing applications are those listed second and third. The reliability of the equipment can be improved if the topological locations of circuit components are chosen according to the best heat distribution patterns. For example, if two hot-components are placed too near one another, neither receives adequate cooling and their lifetimes may be shortened. Some components have been found to be operating at 120 to 150°C above ambient. This high operating temperature was a surprise to the design engineers.

Furthermore, the third item on the chart: the use of infrared in acceptance testing, both of circuits coming into the Air Force inventory and of circuits being maintained, will enable the location and rejection of many electronic-equipments that contain anomalies not now detected by conventional tests. As part of the acceptance tests for quality control, the Air Force could routinely make an infrared scan of the circuit boards of each manufacturer's electronic equipment considered for the Air Force inventory. At present, suppliers "qualify" by submitting a sample electronic equipment. The equipment is tested and either accepted for future purchase or rejected. After the items are accepted and placed in our inventory, they often are found to have a low mean-time-between-failure. The causes of the incipient troubles very often are: (1) underrated components (for

example, a 1-watt rather than a 2-watt resistor) or (2) a poor heat dissipation ability (for example, several high dissipation components grouped together). These anomalies cannot be spotted with conventional testing, but they can be spotted using infrared detection. The infrared scans can be made quickly and easily. No special skill is required to interpret the scans for equipment acceptance or rejection. One need only look for hot spots in this case. This method is proven effective. Many equipments which contain anomalies not now detected would be rejected during acceptance testing. Thus, only the more reliable equipments would reach the Air Force inventory, and the subsequent requirement for many maintenance manhours, spare parts, and redesigns would be reduced.

Infrared testing provides an important byproduct advantage beyond those already cited. When a circuit board contains a faulty component, one or more other components may be overstressed for extended periods of time without actually failing. When the faulty component is located, it is usually the only one replaced, even though the future life of the overstressed components may have been seriously compromised. This secondary overstress often cannot be determined using conventional test procedures. With infrared testing, these overstressed components may be spotted and replaced along with the failed components. The consequences of not replacing these overstressed components could later prove to be catastrophic to an Air Force mission such as that of the C-5A. Using infrared testing, a manufacturer or depot can compile a list to show an unskilled operator which components will be subjected to secondary overstress for every catastrophically failed component in the circuit.

A set of specifications have been defined for use as a starting point for the implementation of the infrared inspection technique by the government services. These specifications are included in detail in the technical report AFAPL-TR-68-84, "Infrared for Electronic Equipment Diagnosis." The specifications were kept as general as possible, but they contain all the elements necessary in order to make an infrared checkout system effective.

IMPLEMENTATION

The U. S. Air Force is now on the threshold of applying the infrared checkout technology to circuits in its inventory. Personnel of the AFLC Maintenance Technology Office have stated that they are interested in applying the technique to perform incoming inspections on electronic circuits received at the depot. All that remains prior to implementation is the development of a practical radiometric system (hardware, software, and peripheral equipment) which possesses an acceptable degree of accuracy, stability, maintainability, and versatility (Fig. 12). This system should be capable of application to all current and projected Air Force electronic hardware through CY 1973.

Present commercially available radiometers generally are satisfactory for mapping the thermal profile of an energized discrete element circuit. However, with the continued introduction into the Air Force inventory of microelectronic circuitry, which characteristically operates at lower power

levels, the noise-equivalent-power (NEP) characteristics of the radiometer need to be enhanced. Also, techniques for displaying the infrared scan data need to be improved. Digital data handling capability generally is not included in present radiometric systems, and considerably more work must be done to provide efficient, accurate data processing techniques. I am performing a comprehensive in-house investigation to provide the required data processing techniques. Current technology limitations also include the means of stimulating and loading the circuits under test and pretest conditions, with the achievement of maximum flexibility and speed. The correction of these limitations is certainly feasible and within the state-of-the-art.

PAYOFF

It is well known that the maintenance of military electronic systems is complex and expensive (Fig. 13). In 1964 the Deputy Director for Electronics, Department of Defense stated that 150,000 military personnel are engaged in maintaining communications electronic equipment and electronic portions of weapon systems. This amounts to $850 million in labor costs alone per year. In the electronic defense industry, production test efforts account for 20% of the overall cost and 50% of the manufacturing spread time. Approximately 80% of the total test time is spent in fault isolation. New and improved fault-diagnosis techniques are required in order to save manpower and money and to shorten downtime.

The application of infrared checkout techniques to electronic circuits is feasible (Fig. 14). It will lead to improved performance and reliability, the reduction of testing time, maintenance manhours, spare parts redesign, and associated costs. The advantages of better first article testing and quality control promise improved electronic equipment reliability as well as better maintenance of equipment in the inventory. When infrared testing is fully implemented in industry and in Air Force maintenance facilities, operations and maintenance savings will be substantial. The use of this technique may make the difference between success and failure of many costly future missions.
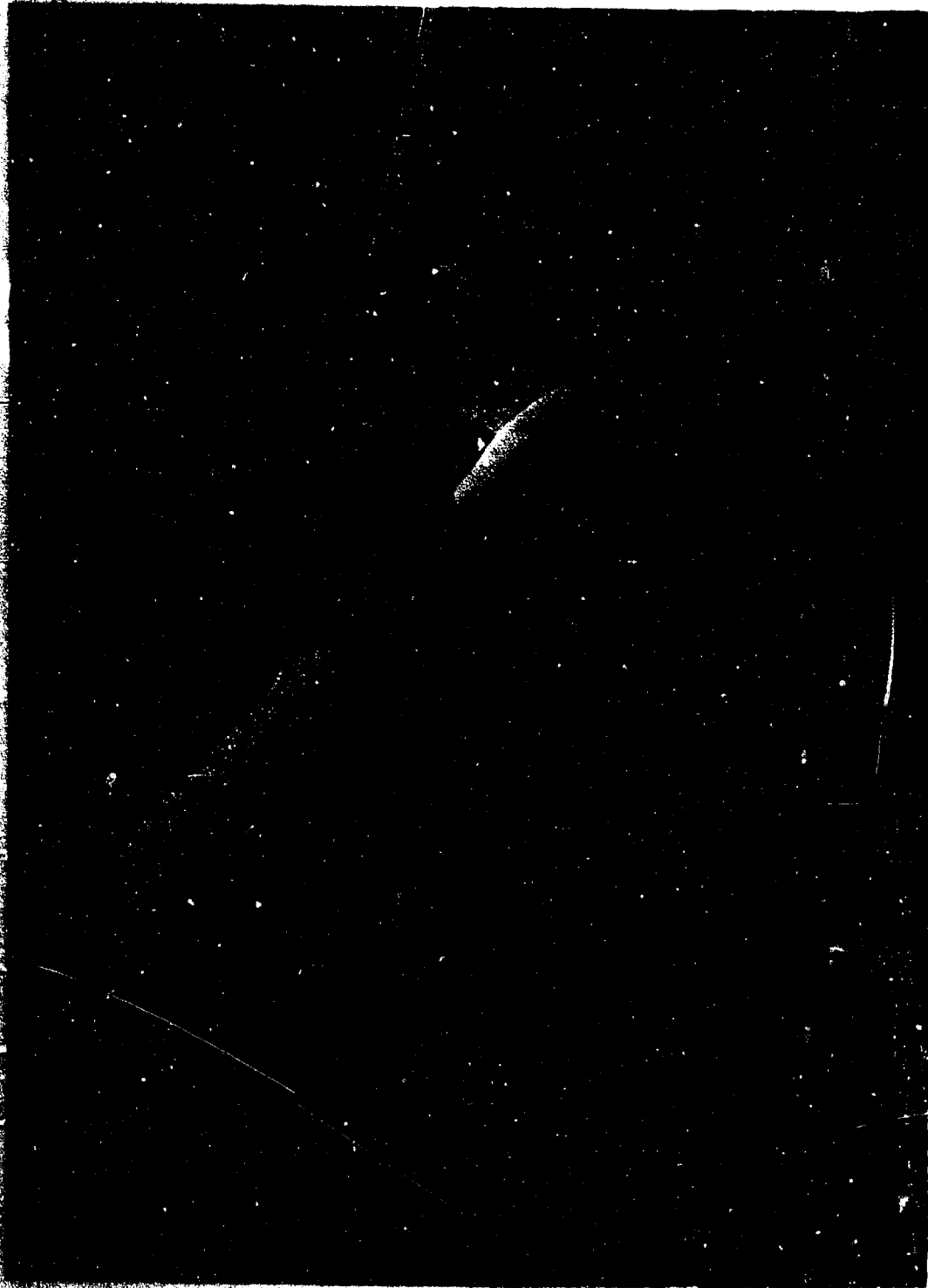
Fig. 1 - The C-5A

DD-10

Fig. 2 - Background

Fig. 3 - Infrared Maps of Energized Electronic Circuits

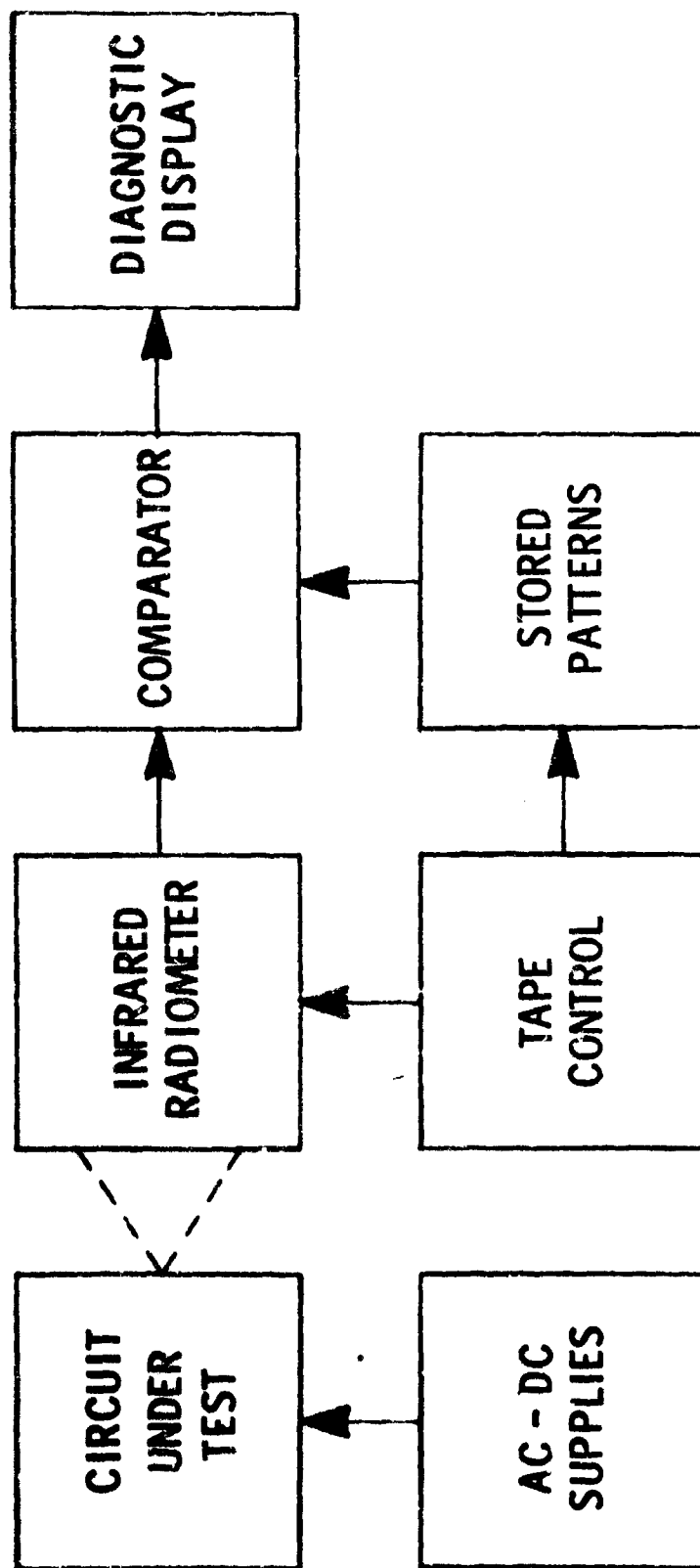Fig. 4 - Infrared Advantages

339-894 O - 69 - 19

# INFRARED TEST SETUP



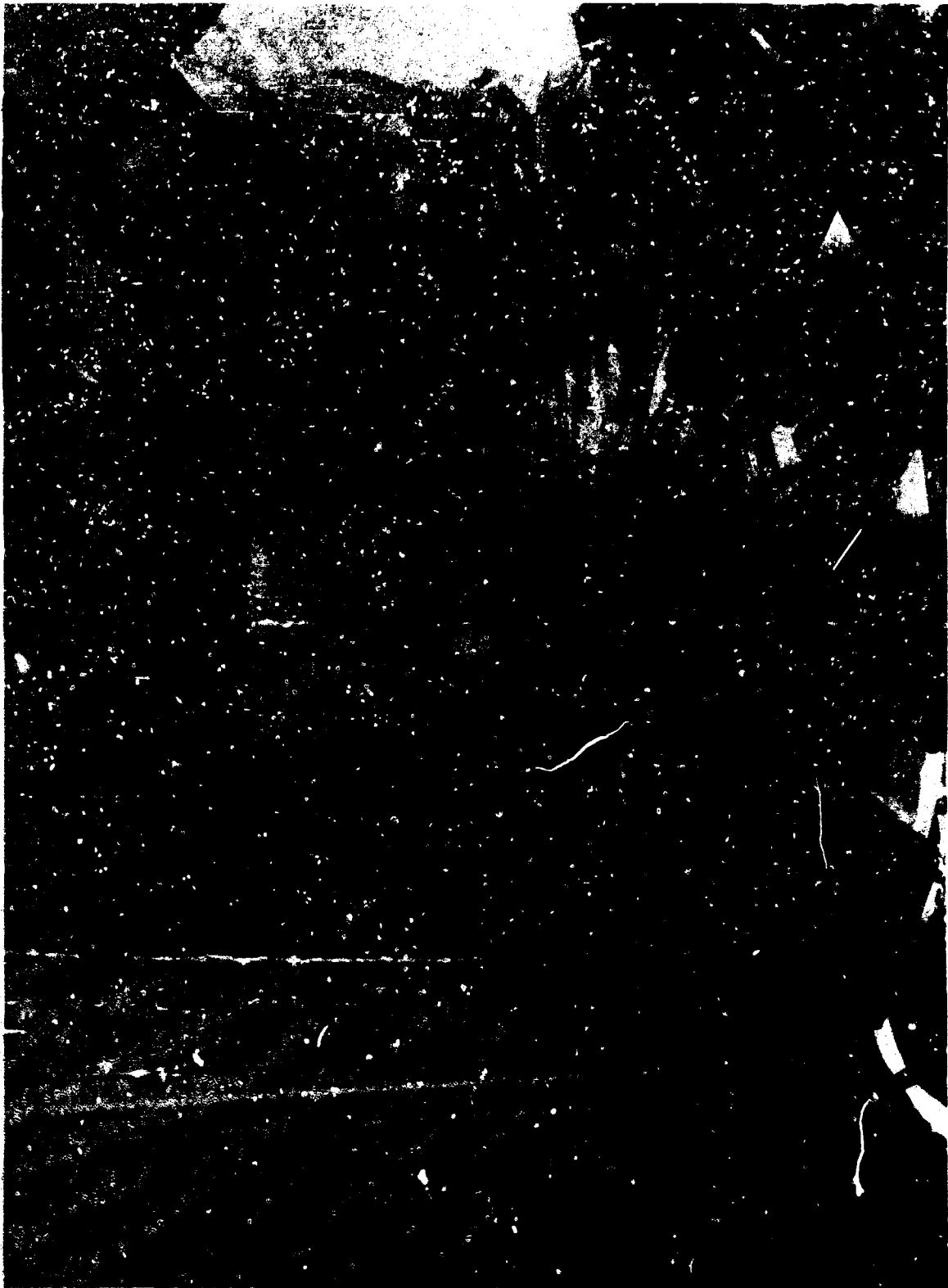Fig. 5 – Infrared Test Setup

Fig. 6 - Test Implementation
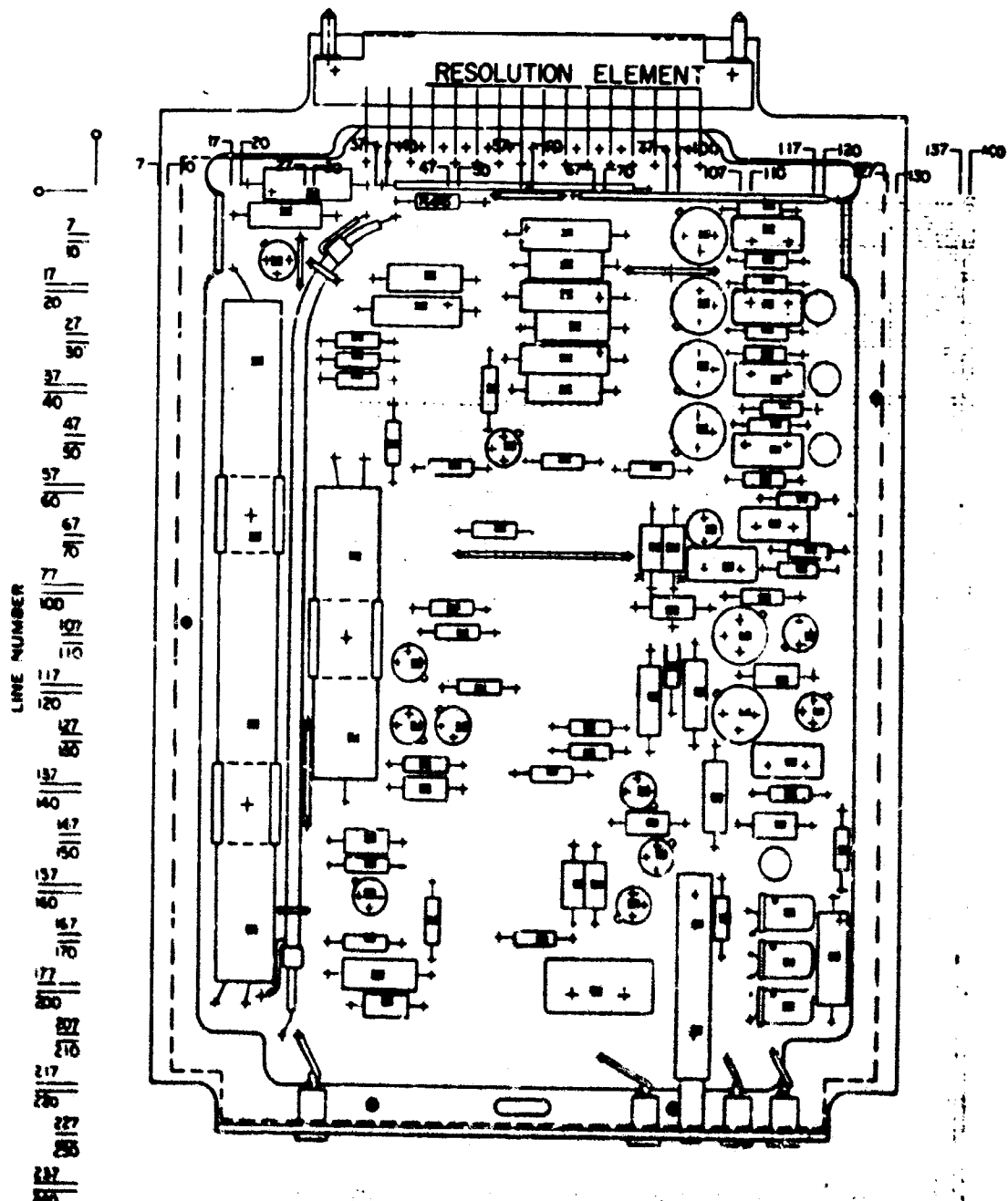
Fig. 7 - Radiometric COMPARE System

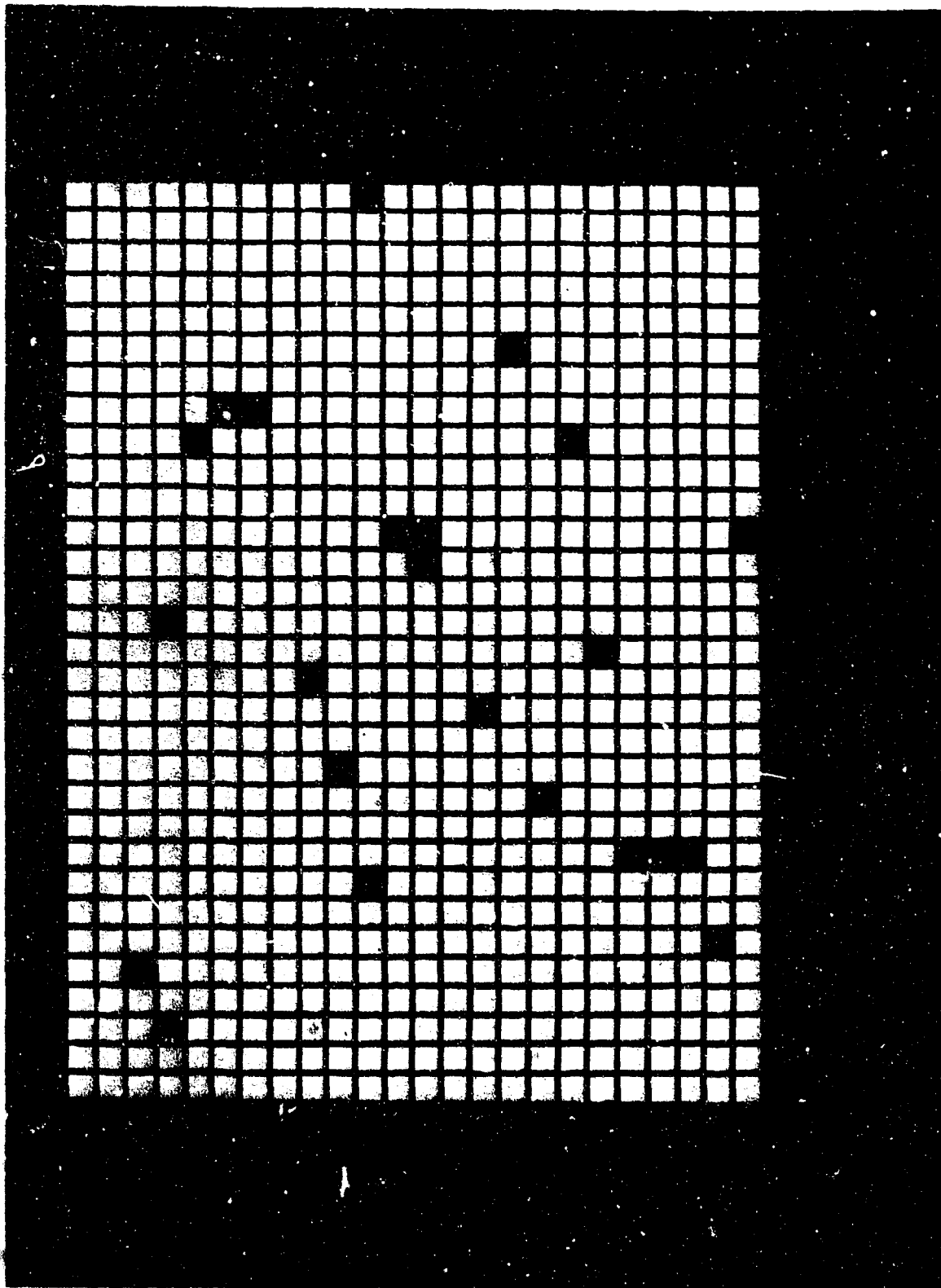Fig. 8 - Panel Showing Points Sampled During Infrared Scan

Fig. 9 – 744 Electrically Acceptable Panels
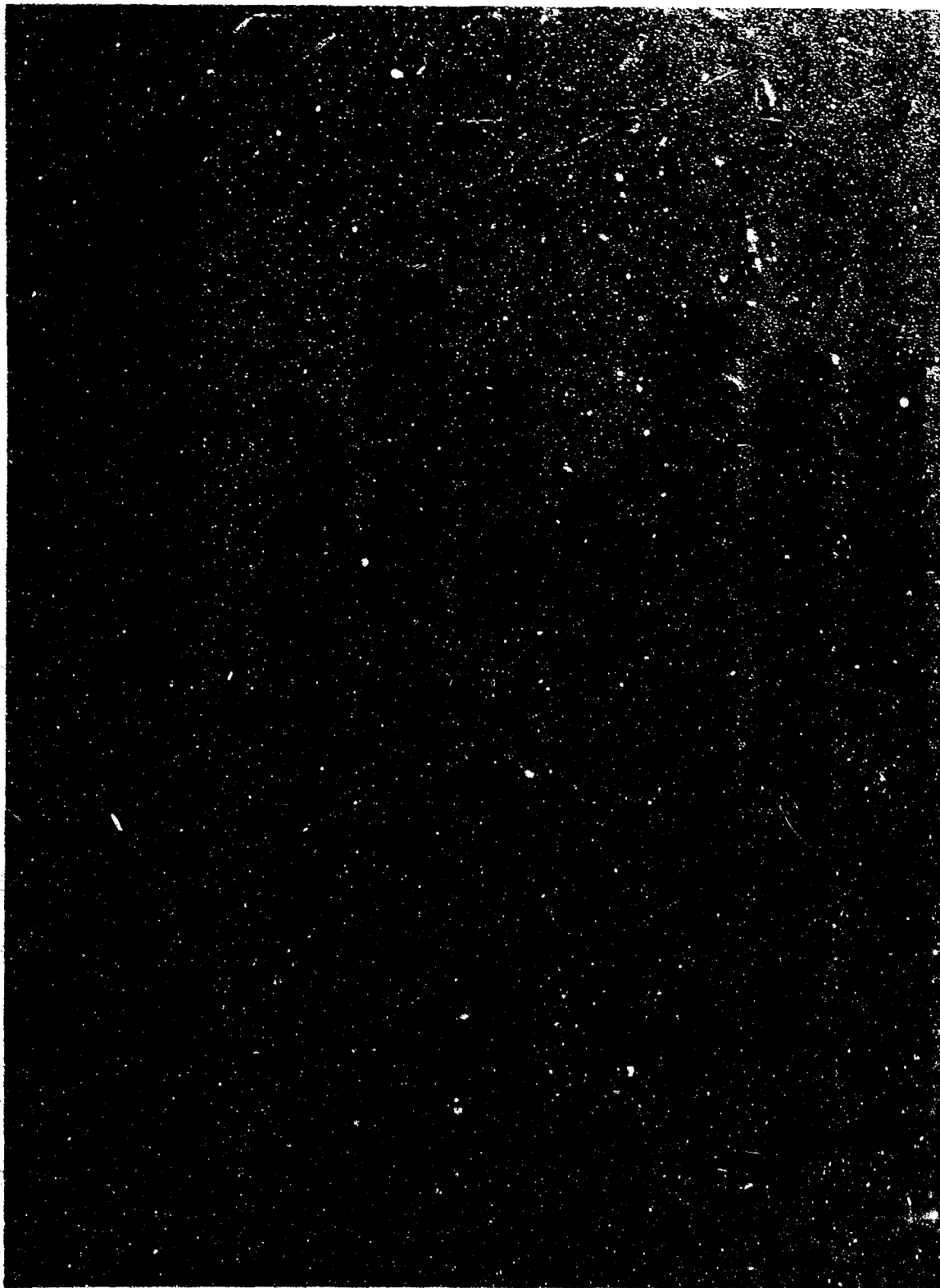
**ANOMALY TYPES**

Fig. 10 – Anomaly Types

Fig. 11 - Infrared Applications

# DEVELOPMENTAL REQUIREMENTS

- ACCURACY, STABILITY, VERSATILITY
- IMPROVED NOISE-EQUIVALENT-POWER
- IMPROVED DISPLAYS
- IMPROVED DATA PROCESSING
- VERSATILE POWERING AND LOADING FOR TEST CIRCUITS

DD-21

Fig. 12 - Developmental Requirements

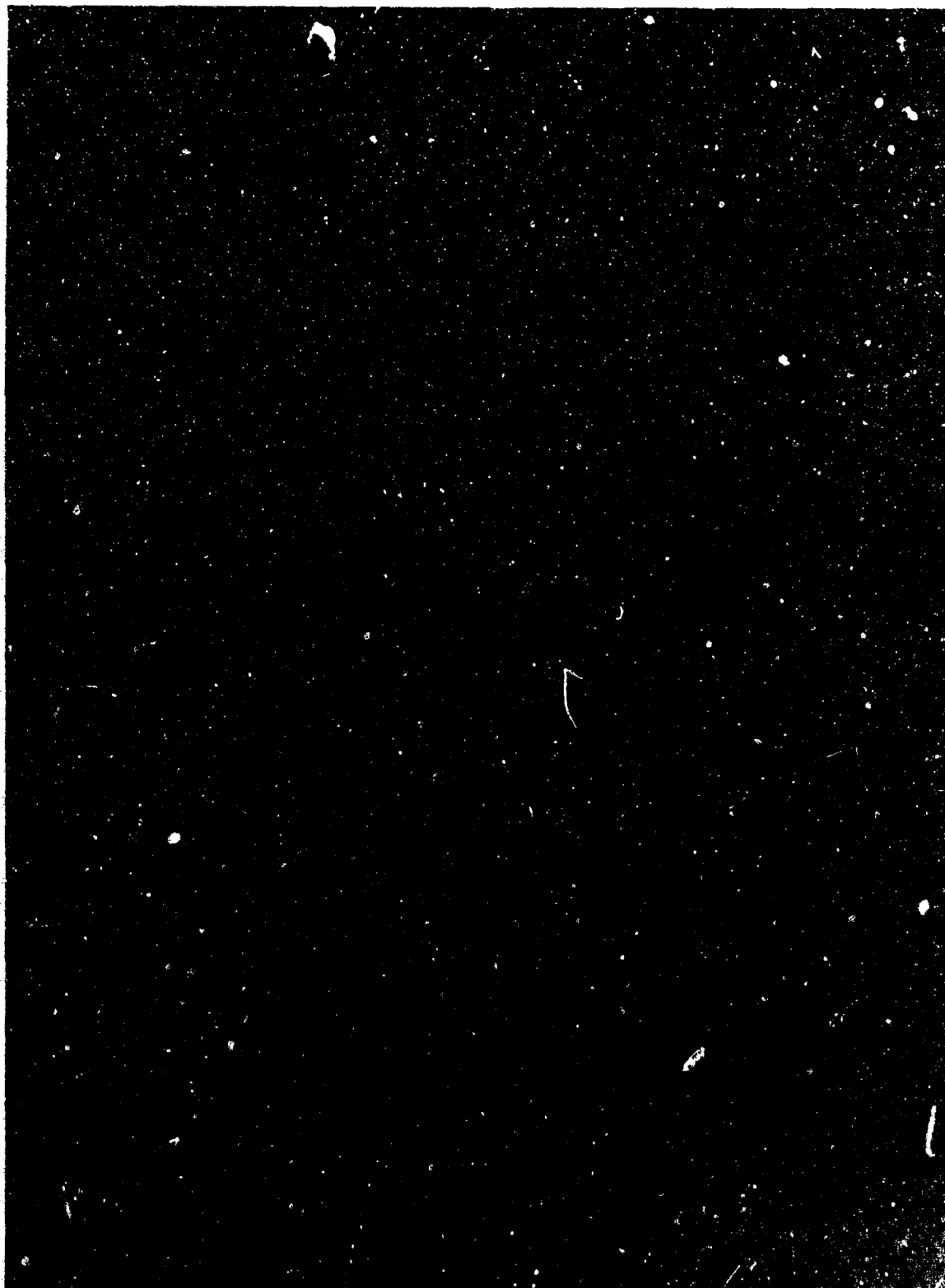Fig. 13 -- Checkout

Fig. 14 - Summary

DD-23

**DOCUMENT CONTROL DATA - R & D**

*(Security classification of title, body of abstract and indexing annotation must be entered when the overall report is classified)*

| 1. ORIGINATING ACTIVITY (Corporate author) | 2a. REPORT SECURITY CLASSIFICATION |
|---|---|
| Hq Office of Aerospace Research<br>1400 Wilson Boulevard<br>Arlington, Va. 22209 | UNCLASSIFIED |
| | 2b. GROUP<br>N/A |

3. REPORT TITLE

PROCEEDINGS OF THE 1968 AIR FORCE SCIENCE AND ENGINEERING SYMPOSIUM, VOLUME II

4. DESCRIPTIVE NOTES (Type of report and inclusive dates)

Scientific Annual 1968

5. AUTHOR(S) (First name, middle initial, last name) Donald I. Carter, Henry B. Whitmore, Judith G. Koestler, Dietrich W. J. Langer, C. Martin Stickley, Harvey Miller, Edmund E. Hoell, C. C. Gallagher, Rudolph A. Bradbury, William G. Field, Robert W. Wagner, Rita C. Sagalyn, Kenneth M. Glover, Roland J. Boucher, Hans E. E. K. Ottersten, Kenneth R. Hardy, John R. Abernethy, William Goldberg, Harold D. Newby, John R. Castelli, Jefferson C. Davis, Willard L. Nelson, John S. McKinney, Ruth A. Herman

| 6. REPORT DATE | 7a. TOTAL NO. OF PAGES | 7b. NO. OF REFS |
|---|---|---|
| March 1969 | 277 | N/A |

| 8a. CONTRACT OR GRANT NO. N/A | 9a. ORIGINATOR'S REPORT NUMBER(S) |
|---|---|
| b. PROJECT NO. N/A | N/A |
| c. N/A | 9b. OTHER REPORT NO(S) (Any other numbers that may be assigned this report) |
| d. N/A | OAR 69-0004    AD 686 101 |

10. DISTRIBUTION STATEMENT
1. This document has been approved for public release and sale; its distribution is unlimited.

| 11. SUPPLEMENTARY NOTES | 12. SPONSORING MILITARY ACTIVITY |
|---|---|
| N/A | Hq OAR (RROA)<br>1400 Wilson Boulevard<br>Arlington, Va. 22209 |

13. ABSTRACT

This is the second of two volumes containing the unclassified papers presented at the 1968 Air Force Science and Engineering Symposium. The papers in this volume are as follows: "Fire Protection in Oxygen-Enriched Atmospheres - Prevention and Extinguishment"; "In-House Contributions to Design and Construction of Devices for Biomedical Monitoring, Training and Experimental Support"; "A New Method for Determining Gyroscope Short-Term-Drift Characteristics"; "Probing the Electronic Properties of Crystals by Pressure"; "Output Energy Decay Observations in Ruby Lasers"; "Modern Thermal-Imaging Techniques for High-Temperature Research"; "Simultaneous Rocket and Radar Backscatter Studies of the Electrical Structure of the Lower Ionosphere"; "Simultaneous Radar, Aircraft, and Meteorological Investigations of Clear-Air Turbulence"; "Ballistic-Impact Flash"; "Measurement of the Spectral Shift of High-Energy Ruby Lasers with a Pulse Spectrometer"; "Worldwide Solar Radio Patrol and Proton Warning System"; "Development of Passively Pressurized Partial-Pressure Suit"; "New Concepts in Warehousing and Automation"; "A Mathematical Technique for Simulating Turbine-Engine Performance on a Digital Computer"; "Infrared Detection, Isolation, and Prediction of Electronic-Equipment Malfunctions."

DD FORM 1473

| 14. KEY WORDS | LINK A | | LINK B | | LINK C | |
|---|---|---|---|---|---|---|
| | ROLE | WT | ROLE | WT | ROLE | WT |
| Fire Protection in Oxygen-Enriched Atmospheres | | | | | | |
| Devices for Biomedical Monitoring, Training, and Experimental Support | | | | | | |
| Gyroscope Short-Term Drift | | | | | | |
| Electronic Properties of Crystals | | | | | | |
| Output Energy Decay in Ruby Lasers | | | | | | |
| Thermal-Imaging Techniques | | | | | | |
| High-Temperature Research | | | | | | |
| Rocket and Radar Backscatter Studies | | | | | | |
| Electrical Structure of the Lower Ionosphere | | | | | | |
| Clear-Air Turbulence | | | | | | |
| Ballistic Impact Flash | | | | | | |
| Spectral Shift of High-Energy Ruby Lasers | | | | | | |
| Pulse Spectrometer | | | | | | |
| Solar Radio Patrol | | | | | | |
| Proton Warning System | | | | | | |
| Passively Pressurized Partial-Pressure Suit | | | | | | |
| Warehousing and Automation | | | | | | |
| Computer Simulation of Turbine-Engine Performance | | | | | | |
| Infrared Detection, Isolation, and Prediction of Electronic-Equipment Malfunctions | | | | | | |